Polarization-Preserving Quantum Frequency Conversion for Trapped-Atom based Quantum Networks

Dissertation

zur Erlangung des Grades
des Doktors der Naturwissenschaften
der Naturwissenschaftlich-Technischen Fakultät
der Universität des Saarlandes

von

Matthias Bock

Saarbrücken

2020

Tag des Kolloquiums:	03.09.2021
Dekan:	Prof. Dr. Jörn Walter
Berichterstatter/innen:	Prof. Dr. Christoph Becher Dr. Benjamin P. Lanyon Prof. Dr. Wolfgang Tittel
Vorsitz:	Prof. Dr. Albrecht Ott
Akad. Mitarbeiter:	Dr. Herbert Wolf

Abstract

The scope of this thesis is the development of efficient and low-background polarization-preserving quantum frequency converters (PPQFC) and their integration into trapped-atom based quantum network nodes to demonstrate building blocks of a quantum network (QN). We constructed four PPQFC devices to transduce the emission wavelengths of single trapped $^{40}Ca^{+}$-ions at 854 nm and neutral ^{87}Rb-atoms at 780 nm to the low-loss telecom bands between 1260 nm and 1625 nm. Upon the conversion process, the quantum information encoded in the photon polarization has to be preserved. To this end, we rely on difference frequency generation in ridge waveguides, which are inserted into polarization interferometers arranged in Sagnac- or Mach-Zehnder-type configuration. For the conversion of single and entangled photons we achieved external device efficiencies between 26.5 % and 57.4 %, low background levels, which allow for signal-to-background ratios above 20, and process fidelities > 99.5 %. Employing the PPQFC devices, we were able to demonstrate several key elements of long-distance QNs: photon-photon entanglement over 40 km of fiber via 2-step QFC with a fidelity of 98.9 %, ion-telecom-photon entanglement with high fidelities up to 97.8 %, an atom-to-telecom-photon state transfer, and the distribution of atom-photon entanglement over 20 km of fiber with a fidelity of 78.9 %. These results hold great promise to extend small QNs with ≥ 2 nodes to a metropolitan scale.

Kurzdarstellung

In dieser Arbeit werden effiziente und hintergrundarme polarisationserhaltende Quantenfrequenzkonverter (PPQFC) entwickelt und in Quantennetzwerkknoten basierend auf gefangenen Atomen integriert, um Bausteine eines Quantennetzwerks (QN) zu demonstrieren. Wir haben vier PPQFC gebaut um die Emissionswellenlängen von einzelnen $^{40}Ca^{+}$-Ionen bei 854 nm und neutralen ^{87}Rb-Atomen bei 780 nm in die verlustarmen Telekombänder zwischen 1260 nm und 1625 nm umzuwandeln. Im Konversionsprozess muss die Quanteninformation, kodiert in der Polarisation der Photonen, erhalten bleiben. Dazu nutzen wir Differenzfrequenzerzeugung in Kantenwellenleitern, welche in Polarisationsinterferometer in Form von Sagnac- oder Mach-Zehnder-Aufbauten integriert werden. Für die Konversion einzelner und verschränkter Photonen erreichten wir externe Geräteeffizienzen zwischen 26.5 % und 57.4 %, geringe Hintergrundbeiträge, die Signal-zu-Hintergrund-Verhältnisse über 20 ermöglichen, sowie Prozess-Fidelities > 99.5 %. Mit Hilfe der Konverter konnten wir eine Reihe von Kernelementen von langreichweitigen QNn zeigen: Photonen-Photonen-Verschränkung über 40 km Faser mittels 2-Schritt QFC mit einer Fidelity von 98.9 %, Ion-Telekom-Photon-Verschränkung mit hohen Fidelities bis zu 97.8 %, einen Atom-zu-Telekom-Photon Zustandstransfer, und die Verteilung von Atom-Photon-Verschränkung über 20 km Faser mit einer Fidelity von 78.9 %. Diese Resultate sind vielversprechend um kleine QN mit $\geq$ 2 Knoten auf die Längenskala einer Stadt auszuweiten.

Contents

1 Introduction **1**

2 Fundamental concepts **11**
2.1 Quantum frequency conversion 11
2.1.1 Nonlinear optics in waveguides 12
2.1.2 Background processes in QFC 19
2.1.3 Schemes for polarization-preserving frequency conversion 25
2.2 Quantum states and processes 29
2.2.1 Description of quantum states 29
2.2.2 Description of quantum processes 33
2.2.3 Tomographic reconstruction of quantum states 35
2.2.4 Tomography of quantum processes 40
2.2.5 Bell test experiments 44
2.3 Integrating QFC devices into quantum networks: Challenges, requirements and figures of merit 46

3 Polarization-preserving quantum frequency conversion of $^{40}Ca^{+}$-resonant photons to the telecom bands **49**
3.1 Polarization-preserving QFC from 854 nm to the telecom O-band 50
3.1.1 Implementation of PPQFC in a single-crystal Mach-Zehnder configuration 51
3.1.2 Path length stabilization 59
3.1.3 Single-photon detectors for telecom wavelengths 63
3.1.4 Conversion of arbitrarily polarized light 65
3.2 Polarization-preserving QFC from 854 nm to the telecom C-band 71
3.2.1 Experimental setup 72
3.2.2 Trichroic waveguide coupling 76
3.2.3 Performance of the device 81
3.3 QFC of polarization-entangled photons from a SPDC source 84
3.3.1 Narrowband entangled photon pair source at 854 m 85
3.3.2 Experiment and results 86
3.4 Summary and discussion 91

4 High-fidelity entanglement between a trapped ion and a telecom photon via quantum frequency conversion 95
4.1 Quantum node based on single trapped $^{40}Ca^{+}$-ions 96
4.1.1 Trapping and coherent manipulation of single ions 96
4.1.2 Ion-photon entanglement at 854 nm 99
4.2 Preservation of ion-photon entanglement during QFC 111
4.3 Summary and discussion 116

5 Direct quantum state transfer from a trapped ion onto a telecom photon 119
5.1 Protocol and experimental sequence 120
5.2 Results 123

6 PPQFC system for an elementary Rubidium-atom based quantum network link 129
6.1 Design criteria of the QFC system 130
6.2 Master laser system 133
6.3 Polarization-preserving QFC for the Rubidium D2-line 136
6.3.1 Nonlinear waveguide chips 137
6.3.2 Investigation of Raman background 138
6.3.3 Narrowband spectral filtering system 140
6.3.4 Sagnac-type PPQFCD and Bell-state measurement 145
6.4 Summary and discussion 149

7 Long-distance distribution of atom-photon entanglement at telecom wavelength 151
7.1 Single trapped Rubidium atoms as quantum nodes 152
7.1.1 Overview 152
7.1.2 Generation and analysis of atom-photon entanglement 154
7.2 Atom-photon entanglement over up to 20 km of fiber 160
7.2.1 Experimental setup 160
7.2.2 Results 162
7.3 Summary and discussion 166

8 Summary and Outlook 169
8.1 Summary 169
8.2 Outlook and future prospects 172

Appendices 181

A Calculation of the process matrix from the Choi-matrix 183

B Infrared-pumped optical parametric oscillator at 2456 nm 185

C Density matrices of photon-photon entanglement without background-subtraction 187

D Photographs of the QFC system for Rb-atom wavelengths **189**

References **193**

Publications **219**

Chapter 1

Introduction

The discovery of quantum mechanics and the development of a mathematical framework to describe the related physical effects at the beginning of the 20th century is one of the great achievements in modern science and opened a large number of new research fields ranging from atomic, nuclear and particle physics to modern solid-state physics or quantum chemistry. Apart from this, quantum mechanics enabled the development of ground-breaking technologies, which have become an integral part of our everyday lives. Two prominent examples are the semiconductor-based classical information processing or the laser, both being an outcome of modern solid-state, atomic and optical physics. Due to the enormous impact of these inventions, they are sometimes referred to as the result of the "first quantum revolution". However, although quantum mechanics is certainly the underlying physical principle of these technologies, they do neither incorporate the isolation, control and manipulation of individual quantum objects, such as single atoms, photons or artificially-created atom-like systems in solid-state materials, nor the specific preparation, processing and measurement of nonclassical states, e.g. coherent superposition or entangled states. This has only been achieved during the last 30 years, triggered by major breakthroughs mainly in atomic physics, laser physics, material science and high-speed low-noise electronics. It enabled the experimental implementation of theoretical proposals originating from a new research field labeled as quantum information processing (QIP) [1]. In analogy to classical information processing, where information is encoded in bits being the basic unit with the two logical values 0 and 1, QIP relies on quantum bits (qubit) formed by two orthogonal basis states, which are commonly represented by the state vectors $|0\rangle$ and $|1\rangle$. While the state of classical bits is restricted to the values 0 or 1, qubits can also take arbitrary coherent superposition states $|\Psi\rangle = \alpha|0\rangle + \beta|1\rangle$ with α and β being complex coefficients that satisfy $|\alpha|^2 + |\beta|^2 = 1$. Moreover, in the case of more than one qubit, they can form an entangled state, for instance a two-qubit maximally entangled Bell state $|\Psi^-\rangle = 1/\sqrt{2}\,(|01\rangle - |10\rangle)$. The above mentioned individual quantum objects may serve as qubits if they can provide at least two distinct energy levels, which form the computational basis states $|0\rangle$ and $|1\rangle$. On top of this, these levels have to fulfill several requirements related to the initialization and readout capability of the state, its coherence time, and the possibility to perform gates between different qubits (for details see

the DiVincenzo criteria [2]). The availability of physical qubits and the possibility to prepare them in superposition or entangled states allows for the realization of several novel and promising applications, thus, we refer to this quantum technology as "second quantum revolution" [3]. In the context of an European initiative to boost quantum technology, the so-called "Quantum Flagship" [4, 5], the applications were organized in four categories: quantum computation, simulation, sensing/metrology and communication, which we will explain in more detail in the following.

- **Quantum computation:** A quantum computer employs a large number of qubits and a set of universal one- and two-qubit gates to implement various quantum algorithms, which commonly provide – for a certain well-defined task – a significant advantage or speedup compared to classical algorithms [6]. These algorithms typically rely on the controlled quantum interference between components of large entangled superposition states to amplify the desired result. Prominent examples are Shor's algorithm for prime number factorization [7] or Grover's algorithm for database search in large, unsorted lists [8]. Currently, the most advanced approaches to realize a quantum computer are based on superconducting qubits [9,10] or trapped-ion qubits [11,12] and driven forward by academic groups as well as several startup and established digital market companies (e.g. IBM, Google, Alibaba, AQT or IonQ to name a few).

- **Quantum simulation:** The idea of quantum simulation goes back to a visionary lecture by Richard Feynman [13]: he underlined the problem of simulating interacting quantum many-body systems with classical computers due to an unfavorable scaling of the required computational power and memory with the number of particles N in the system (the number of coupled equations scales with 2^N). These systems are, however, interesting if one wants to approach e.g. the physics of (exotic) quantum materials [14] or tackle quantum chemistry calculations of molecules [15]. Feynman suggested to design an artificially well-controlled quantum many-body system to simulate the dynamics of the target system instead. Over the past years, experimental progress allowed for the simulation of various physical models (e.g. Ising or Hubbard models) with different hardware platforms, among them trapped ions [16], cold atoms in optical lattices [17], Rydberg atoms in optical tweezer arrays [18], or photonic circuits [19].

- **Quantum sensing/metrology/imaging:** The field of quantum-enhanced sensing, metrology and imaging covers a much broader range of applications than simulation or computing. The general characteristics are that sensors are constructed from single or ensembles of quantum objects, which are potentially prepared in nonclassical states, and provide an advantage in terms of precision, sensitivity or measurement speed. The physical platforms for quantum sensing are manifold: they range from optical single-ion or optical-lattice atomic clocks [20] to gravitation-wave detectors enhanced by squeezed light [21], phase estimation beyond the standard quantum limit with ensembles of atoms/ions [22] or photons [23], magnetic-field sensing and imaging with solid-state spins in color centers in diamond [24, 25] and many others.

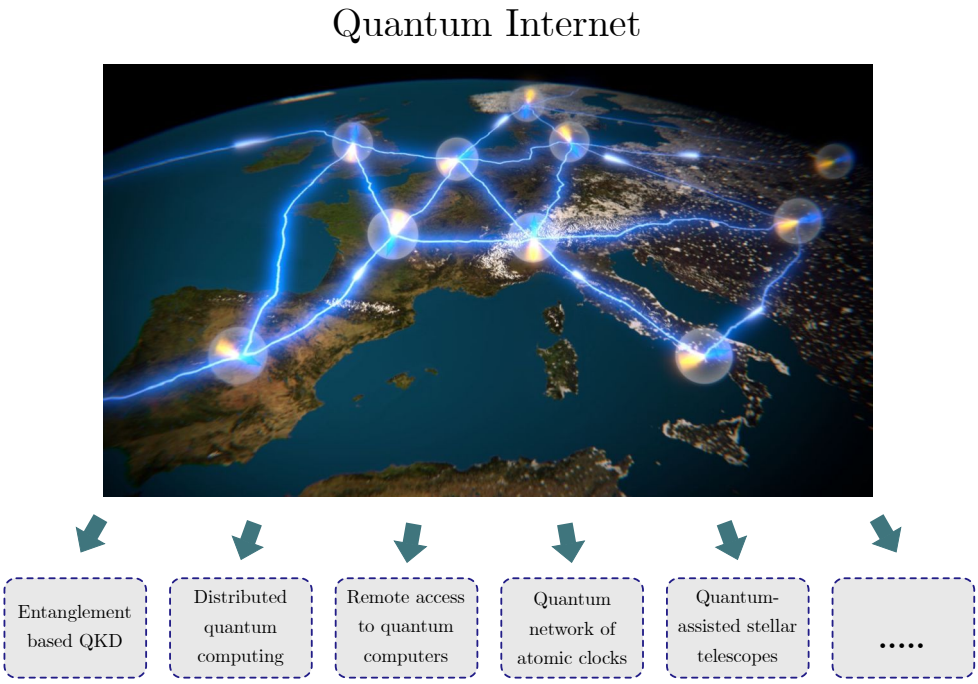

Figure 1.1. Artist impression and possible applications of the quantum internet. The artist impression has been adapted from a news article of QTech, Delft [31].

- **Quantum communication:** In this field quantum information is distributed between remote locations by means of so-called flying qubits – usually photons at optical wavelengths – which are transmitted through quantum channels connecting the distant places. In the near future, the main application is quantum cryptography being a cryptography method whose security is approved by the laws of quantum mechanics [26–28]. It combines quantum random number generators (QRNGs) to generated secret keys and quantum key distribution (QKD) to broadcast them in a secure way [4]. On a longer perspective, the vision is the realization of a quantum network or quantum internet to distribute entanglement between remote locations, which could be employed as resource for various applications [29, 30]. Since the main purpose of this thesis is the development of tools for quantum networks, we will take a closer look at this in the following.

Quantum Networks and Repeaters

An artist's impression of a quantum network spanned across Europe is shown in Fig. 1.1: it consists of stationary quantum network nodes (QNN) where quantum information is stored or processed. These nodes are interconnected by quantum channels in order to distribute entanglement between the nodes by means of photonic qubits. As soon as entanglement between QNNs is established, it can be employed as resource for interesting applications, among them entanglement-based QKD schemes [32–35] with the most advanced one being fully device-independent QKD [36–38]. The latter relies on a

loophole-free Bell test and copes with minimal assumptions on the experimental apparatus enabling the highest security so far. Furthermore, one can imagine the connection of spatially separated quantum computers (distributed quantum computing) [39, 40], remote access to quantum computers/blind quantum computing [41–43] or a quantum network of atomic clocks [44,45] or stellar telescopes [46,47], where entanglement distribution enables an improvement of the performance of these devices. A major limiting factor for the achievable entanglement rates in a quantum network – and also for the secret key rates in QKD – are transmission losses in the quantum channels. It has been shown by Takeoka et al. [48,49], that there is an ultimate limit of the rate – the so-called TGW-bound – which solely depends on the channel loss and is independent of the particular scheme (one exception is the recently developed twin-field QKD protocol [50], which allows for rates slightly above this bound). In practical fiber-based QKD implementations, where the losses scale exponentially with the distance, this results in a limit of a few hundreds of kilometer. Higher distances could be achieved with satellites: here the loss does not occur isotropic over the channel, but is mainly located in the atmosphere [35,51]. However, satellites also have some drawbacks such as the enormous costs and technical effort or the limited broadcasting time due to the movement of the satellite with respect to the ground stations. While the problem of attenuation in optical fibers is solved in classical communication with repeater stations realized by in-line Erbium-doped fiber amplifiers, this is not applicable in quantum communication due to the no-cloning theorem [52]. To this end, Briegel et al. suggested in 1998 the so-called quantum repeater [53]. To understand the general idea, we consider one possible scheme of such a repeater, which is the one we aim for in this work, and illustrated in Fig. 1.2 (adapted from [54]). The elementary building block is a repeater node consisting of two QNNs. Each QNN emits a photon being entangled with an internal degree of freedom of the QNN. The photons from both sides are sent to a central station where a projective Bell state measurement (BSM) is performed [55]. This results in the entanglement of the two QNNs with each other, being known as entanglement swapping [56,57]. In the next step, several repeater nodes are cascaded. By performing further entanglement swapping steps, either via local projective measurements of two QNNs or the re-emission of photons in combination with further BSMs, entanglement is finally generated between the outer QNNs. The benefit is that the photons must not travel along the whole distance, but solely along the the distance between two adjacent QNNs, i.e. it is possible to break the rate-distance limit in case of highly-efficient individual building blocks. It is important to note that the advantageous scaling with the distance is not provided if the entanglement creation between the QNNs in each repeater node must succeed in a synchronous way, i.e. at the same time in each node. Instead, the entanglement creation must be asynchronous and heralded: this means the detection of two photons at the BSM heralds entanglement between the QNNs, which has to be maintained or stored until each repeater node reports successive entanglement generation.

In the last years, many different physical systems were investigated as candidates for QNNs, and elementary building blocks and protocols such as light-matter entanglement or photon-mediated matter-matter entanglement were demonstrated. One class of QNNs relies on single isolated quantum systems, among them single trapped

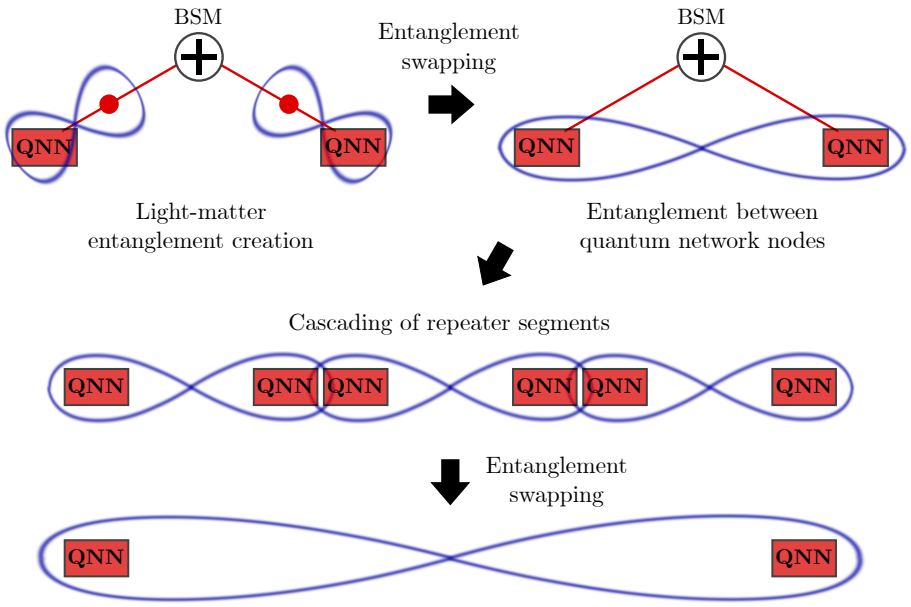

Figure 1.2. Principle idea of quantum repeaters. The scheme the work in this thesis aims at starts with repeater nodes consisting e.g. of two stationary quantum network nodes (QNN) and a central photonic Bell-state measurement (BSM). First, entanglement between the QNNs and flying qubits is generated. A photonic BSM swaps the light-matter entanglement to a matter-matter entanglement. In the next step, several repeater nodes are cascaded and via further swapping operations (e.g. again by the emission of photons or by local gates between two QNNs) entanglement between the outer QNNs is established.

ions [58–61], single trapped atoms [62–65], color centers in diamond [66–71] or quantum dots [72–75]. These systems are particularly interesting for the repeater scheme presented in Fig. 1.2. However, it should be mentioned that a plethora of alternate repeater schemes such as the DLCZ-protocol [76] as well as schemes combining single- or entangled-photon sources with absorptive memories, which allow for temporal, spectral or spatial multiplexing of the stored photons [77–79], exist. These schemes typically employ ensembles of quantum systems, e.g. atomic clouds [80–83] or rare-earth ions in crystals [84–86].

Atomic Systems as Quantum Network Nodes

Over the course of this work, we utilize single trapped neutral atoms or ions as QNNs. They can be considered as natural qubits in contrast to artificially-created qubits e.g. in solid-state materials. Trapped ions are widespread and intensively explored in QIP, for instance in quantum simulators or computers [11, 16], but also as QNNs due to a whole range of appealing benefits. Among them are a good protection from the environment, the high level of control over their electronic and motional quantum states or the fact that ions of the same species are truly identical and feature the same optical properties

(a feature, which is indeed unique for ions and atoms, as solid state systems typically suffer from effects such as spectral diffusion, dephasing or crystal strain rendering those systems distinguishable to a certain degree). In the context of QNNs, trapped ions offer well-controlled light-matter interfaces, either in free-space [58,61,87–89] or enhanced by optical cavities [59, 90, 91] as well as high coherence times up to 1 hour [92–95]. Moreover, it is possible to load more than one ion into the trap. The combination with single-qubit addressing enables high-fidelity quantum gates, either between the same ion species [96–98] or mixed-species [99], which are useful for local operations in quantum repeaters, entanglement distillation (a similar scheme as in [100] for solid-state qubits), decoherence-free subspace encoding [101] or the combination of different ion species optimized for communication and memory tasks [102]. However, it should be mentioned that not all of these properties can be accessed at the same time (at least up to now), and they are not unique for trapped ions. Moreover, ions also suffer from drawbacks related to scalability and miniaturization, or lower repetition rates compared to competitive solid-state systems. In analogy to trapped ions, neutral atoms are another well-established candidate for QNNs. They avoid one particular drawback of almost all ions species, namely the efficient generation of Fourier-limited photons: the optical transitions which allow for this task are typically located in the blue or ultraviolet (UV) spectral region where losses in optical fibers are huge ($> 50\,\mathrm{dB}$). On top of this, we will see at a later point that photons in this spectral region are quite unfavorable for the frequency conversion techniques developed in this thesis. Wavelengths above 600 nm are much better for this task, but suffer from poor branching ratios, i.e. lifetime-limited photon generation is quite inefficient in free-space, making optical cavities inevitable. Regarding this issue, neutral atoms - in particular Rubidium and Cesium - proved to have an advantage, since they enable the emission of near-Fourier-limited photons entangled with the atom at 780 nm and 852 nm, respectively [62]. Apart from this, the light-matter interface can also be enhanced via cavity-coupling [65,103] (even strong coupling to a cavity has been demonstrated [104–106]), and multiple atoms can be trapped close to each other where quantum gates can be implemented either via photons mediated by an optical cavity [107] or by exciting the atoms to Rydberg states [108–110]. We will see later in this thesis that – in comparison to trapped ions – neutral atoms suffer from shorter trapping times and lower fidelities of the state preparation and readout. Thus, both approaches have their advantages and drawbacks and are worth to further develop.

Telecom Interfaces for Network Nodes

All above mentioned experiments represent important steps towards the realization of a quantum repeater. However, they share a common drawback: the wavelengths of the optical transitions on which photons are emitted or absorbed are not at telecom wavelengths between 1260 nm and 1625 nm where attenuation losses in fibers are minimal. Instead, we find wavelengths between 350 nm and 1000 nm, i.e. in the UV, visible or near-infrared (NIR) spectral region. To get an idea about the order of magnitude: in the telecom C-band at 1550 nm the loss in Corning's SMF-28 ultra-low loss fiber [111] is $0.17\,\mathrm{dB/km}$, i.e. the transmission through 20 km is roughly 46 %. In contrast, at

780 nm and 640 nm, the photon wavelengths of the network links in [112] and [68], we find losses of 4.0 dB/km and 8.0 dB/km corresponding to transmissions of 10^{-6} % and 10^{-14} %, respectively. In fact, already the distances of 700 m [112] and 1.3 km [68] reduce the entanglement generation rate by factors 0.5 and 0.09, which makes the use of longer fibers impossible. One way out are QNNs with transitions at telecom wavelengths. A prominent example are Erbium ions in a solid-state matrix, with those several promising experiments were recently performed: on the one hand quantum memories were demonstrated with ensembles of ions in fibers, waveguides or nanophotonic structures [113–115], however, up to now they still reveal lower efficiencies and coherence times compared to other approaches. On the other hand, Purcell-enhanced photon emission from single (or only a few) Erbium ions coupled to nanophotonic, fiber or bulk cavities has been demonstrated [116–119], but with a limited control of the internal degrees of freedom of the ions. Apart from Erbium ions, transitions in the telecom can be found between higher-lying states in neutral Rubidium atoms, which can be used e.g. for cavity-assisted heralded absorption schemes [120] or frequency conversion of an incident red photon to telecom wavelengths as demonstrated in cold atomic clouds via a stimulated four-wave mixing process [121,122]. Quantum dots grown with specific semiconductor materials [123,124] as well as defects centers in silicon carbide [125] allow for single-photon emission at telecom wavelengths, however, their performance is not yet competitive to their counterparts emitting between 800 nm and 1000 nm. Furthermore, quantum dots suffer from short spin coherence times ($< 10\,\mu$s) so far. Apart from these approaches, the gap between the telecom regime and the network nodes can be bridged by frequency non-degenerate (entangled) photon pair sources with one photon at telecom wavelengths and one resonant to the transition of the QNN [126–130]. The combination of pair sources with absorptive quantum memories or heralded-absorption schemes [131] also allows for the realization of quantum repeaters in modified schemes [54].

Quantum Frequency Conversion

In the scope of this thesis, we tackle the issue of telecom compatibility by another approach: we modify the spectral properties of single photons via quantum frequency conversion (QFC) based on $\chi^{(2)}$-nonlinear optical interactions in solid-state crystals [132,133]. The general idea is to transduce the center wavelength of an incoming photon wavepacket between two specific wavelengths by means of a tailored nonlinear process stimulated by strong classical light fields without affecting the remaining classical and nonclassical properties of the photons (e.g. first- and second order coherence, temporal shape, phase, polarization or orbital angular momentum). After the first experimental demonstration in 1992 [133], it took roughly twenty years of development in order to achieve a suitable performance of the QFC devices to allow for the preservation of nonclassical properties of photons from quantum emitters at reasonable conversion efficiencies. These developments include waveguide structures in $\chi^{(2)}$- or $\chi^{(3)}$-media, which allow for conversion efficiencies >10 % of the total device, and techniques to suppress background at the single-photon level induced by the strong classical field [134, 135]. Employing $\chi^{(2)}$-based QFC devices, the preservation of first- and second-order coher-

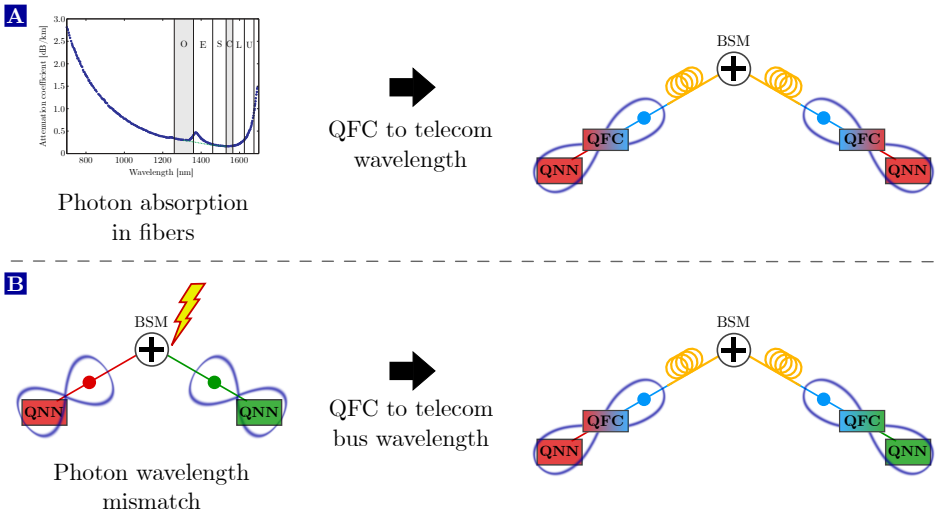

Figure 1.3. Quantum frequency conversion as a tool in quantum networks. **(A)** Quantum frequency conversion (QFC) from transition wavelengths of the QNNs in the visible or NIR spectral region to telecom wavelengths helps to minimize attenuation in optical fibers. **(B)** Dissimilar QNNs, whose light-matter interfaces do not operate the same wavelengths, can be connected via QFC to a common bus wavelength, ideally in the telecom regime.

ence properties [136–141], nonclassical temporal photon-photon correlations [142–144], energy-time entanglement [145, 146], photon-photon time-bin entanglement [147], indistinguishability between consecutive photons from the same emitter [148–150], orbital angular momentum entanglement [151], nonclassical temporal correlations between photons and atomic ensembles [152–154], or light-matter entanglement [72, 155] has been demonstrated. In a recent impressive experiment [82] a complete quantum repeater node including kilometer long fibers (scheme see Fig. 1.3a) was demonstrated: two ensemble-based memories were entangled over up to 50 km of fiber by translating the emitted photons to telecom wavelength employing two independent QFC devices and a subsequent BSM. Another benefit of QFC is shown in Fig. 1.3b: in principle it is not possible to connect QNNs, which operate at different system wavelengths, since the BSM relies on Hong-Ou-Mandel (HOM) interference and is only efficient for perfectly indistinguishable photons. This can be solved via QFC to a common bus wavelength in the telecom regime. First promising experiments in this direction showed HOM interference after frequency conversion between previously distinguishable photons [156, 157] and a quantum state transfer from a cold-atom DLCZ memory operating at 780 nm to a solid-state atomic frequency comb memory with a system wavelength of 606 nm via the telecom C-band [158]. Note that also $\chi^{(3)}$-based QFC devices consisting of ring resonators in Si_3N_4 were recently developed and combined with quantum light sources [159–161].
A downside of the $\chi^{(2)}$-based approach is its polarization dependency: only one polarization component can be efficiently converted, while the efficiency of the second component is virtually zero. This prevents the conversion of photonic qubits encoded in the polarization degree of freedom. However, polarization qubits are widely-used and well-established in QIP since the polarization state can be easily measured and

manipulated, and the polarization state is independent of the acquired optical phase. Furthermore, in particular Zeeman qubits in neutral atoms or ions can be mapped quite well to photonic polarization qubits and vice versa. One solution is the conversion of polarization qubits to time-bin qubits employing unbalanced Mach-Zehnder interferometers and electro-optical modulators [82, 147], however, this creates additional losses and complexity. Therefore, we decided to follow a second route: the development of polarization-preserving quantum frequency converters (PPQFC), being the main experimental work in this thesis. This approach has been chosen by several other groups around the world resulting in a series of PPQFC devices, which differ by the respective configuration to achieve polarization independence, the wavelength combinations, and the overall performance [162–168]. In combination with sources of nonclassical light, these devices enabled the preservation of photon-photon [163, 167] and light-matter entanglement [165, 166] after PPQFC as well as the distribution of the latter over km long fibers [90, 168].

Aim and Outline of this Thesis

The work in this thesis builds on earlier work by A. Lenhard, who constructed in his PhD thesis a polarization-dependent QFC device connecting 854 nm, a transition wavelength in a trapped $^{40}Ca^{+}$-ion, to the telecom O-band at 1310 nm and performed first experiments combining the QFCD with an ion trap and a SPDC source [169]. This converter is completely rebuilt to allow for polarization-preserving operation as well as an improved efficiency and background. Subsequently, elementary building blocks of a quantum repeater such as atom-telecom-photon entanglement and atom-to-telecom-photon quantum state transfer are demonstrated to verify the functionality and feasibility of our approach. Based on the experience with this prototype converter, an improved QFC device for conversion of Ca^{+} photons at 854 nm to the telecom C-band is designed, constructed and tested with entangled photons from a SPDC source. As a first step to scale-up our approach, a complete QFC system for an elementary Rb-atom quantum network link consisting of two QNNs is presented. The thesis is completed by a first test of this system, namely the distribution of atom-photon entanglement over 20 km of fiber. The contents of this thesis is organized as follows:

- In Chap. 2 we provide the fundamental concepts required to understand the experiments and data analysis of the thesis. We focus on the basics of QFC, in particular on nonlinear three-wave mixing processes in waveguides, the processes inducing background at the single-photon level, and several schemes to enable polarization-preserving operation. In the second part, we briefly introduce the mathematical description of quantum states and processes as well as the tomographic reconstruction methods to characterize them. The chapter is completed by a list of figures of merit and requirements to scale-up QFC for quantum networks.
- Chap. 3 is divided in three parts: in the first part we thoroughly describe the setup and alignment of our prototype PPQFCD connecting 854 nm to the telecom O-band at 1310 nm. We determine important figures of merit and prove polarization-

preserving operation by means of quantum process tomography. Furthermore, we introduce the single-photon detectors for telecom wavelengths utilized throughout this thesis. The second part is dedicated to a revised and improved converter for 854 nm, which transduces photons to the telecom C-band at 1550 nm. We perform a similar characterization as for the O-band converter with a focus on the technical novelties. Finally, we employ the C-band converter in combination with a source of polarization-entangled photon pairs at 854 nm to demonstrate entanglement preservation during PPQFC. On top of this, the advantage of QFC to the telecom regime is proven by the distribution of photon-photon entanglement over up to 40 km of spooled fiber.

- In Chap. 4 we present a complete device generating entanglement between a trapped-ion Zeeman qubit and the polarization state of the frequency-converted photon at 1310 nm. First, we take a closer look at the trapping and coherent manipulation of $^{40}Ca^{+}$-ions as well as the experimental sequence to create ion-photon entanglement at 854 nm. The latter is characterized in terms of state fidelity, generation rate and signal-to-background ratio (SBR). Next, we combine the ion trap with the PPQFCD connecting 854 nm to the telecom O-band, verify the preservation of light-matter entanglement during PPQFC and compare the results before and after conversion.

- Chap. 5: employing the same experimental setup as in Chap. 4, we here implement a different protocol, namely a direct quantum state transfer from a trapped-ion qubit onto the polarization state of a telecom photon. After the description of the general idea and sequence, the functionality of the protocol is verified by quantum process tomography.

- The QFC system to extend an elementary Rb-atom based quantum network link is presented in Chap. 6. Starting from the requirements of the final goal – atom-atom entanglement over several km of fiber – we derive design criteria and specifications of the system. Subsequently, we provide design and characterization of the individual components of the system, namely a master laser system, two PPQFCDs, a narrowband spectral filtering stage, and a BSM for telecom wavelengths.

- In Chap. 7 an experiment to establish entanglement between a single trapped Rb-atom and a telecom photon traveled through up to 20 km of fiber is described. We first take a look at the Rb-atom QNN, in particular the Rb level scheme, setup and trapping techniques, the sequences to generate entanglement and readout the atomic state, as well as the coherence properties of the atomic qubit. Subsequently, we proceed with the combined setup including atom trap and PPQFCD and the analysis of atom-photon entanglement over 50 m, 10 km and 20 km of fiber with respect to fidelity, success probability and SBR.

- Finally, we summarize the results of this thesis and provide an outlook on further technical developments and potential future experiments in Chap. 8.

Chapter 2

Fundamental concepts

In this chapter we present the fundamental concepts required to understand the experiments in this thesis as well as a series of analysis techniques to process experimental data. The chapter is organized as follows: in Sect. 2.1 we first introduce the basic nonlinear optical processes to implement quantum frequency conversion. Two prominent challenges in QFC are concerned with their efficiency and conversion-induced background (CIB). Thus, we take a closer look at both in Sect. 2.1.1 and 2.1.2, respectively. In this context, we will find out that the underlying nonlinear processes of QFC are inherently polarization-dependent, preventing conversion of polarization qubits. Thus, we give in Sect. 2.1.3 an overview of a series of experimental schemes to modify QFC devices for polarization-preserving operation.
In Sect. 2.2 we investigate quantum states and processes starting with a brief overview of their mathematical description and visual representation (Sect. 2.2.1 and 2.2.2). The basic technique to measure and quantify quantum states and processes utilized in this thesis is full tomographic reconstruction combined with maximum-likelihood estimation, which we introduce for states and processes in Sect. 2.2.3 and 2.2.4, respectively. If we intend to verify a special class of entangled states, the so-called Bell states, a valuable tool are Bell test experiments offering certain advantages compared to tomographic reconstruction. A brief introduction is given in Sect. 2.2.5.
As mentioned in the introduction, we develop quantum frequency conversion devices (QFCDs) to install them in small-scale quantum network experiments, which comes along with some challenges and requirements. Thus, we identify a plethora of requirements and figures of merit in order to assess QFC devices in this context in Sect. 2.3.

2.1 Quantum frequency conversion

The central goal of QFC is to transduce light at the single-photon level efficiently between two frequencies or wavelengths, respectively. Within the scope of this thesis, one wavelength is determined by atomic transitions in the near-infrared (NIR) spectral region around 780 nm and 854 nm, while the second is located in the telecom bands between 1310 nm and 1550 nm where the attenuation in optical fibers is lowest. The energy difference between the two regimes still corresponds to optical wavelengths, i.e.

it is appealing to choose an all-optical approach based on nonlinear optical interactions in solid-state materials. In the following section we introduce the relevant nonlinear processes, namely difference frequency generation, sum frequency generation and spontaneous parametric down-conversion, as well as some important fundamental concepts in nonlinear optics. In order to render those processes efficient, waveguide (WG) structures are required. Thus, we take a look at the WG geometry and the resulting spatial modes in which light can propagate. Sect. 2.1.1 follows the textbooks of Boyd [170], Suhara/Fujimura [171] and Marcuse [172]. A much more detailed introduction to nonlinear optics in waveguides in the context of QFC can be found in the PhD theses of A. Lenhard [169] and S. Zaske [173].

2.1.1 Nonlinear optics in waveguides

Basics of three-wave mixing

As already mentioned, nonlinear interactions between light and matter are the key to implement frequency conversion. In classical electromagnetic field theory, the response of a dielectric material to a time-dependent incident electromagnetic field $\vec{E}(t)$ is represented by the polarization $\vec{P}(t)$. Its i'th component is determined by $\vec{E}(t)$, and the material-dependent dielectric susceptibility χ is given by the following equation:

$$P_{\mathrm{i}}(t) = \epsilon_0 \sum_j \underbrace{\chi^{(1)}_{\mathrm{ij}}}_{\substack{\uparrow \\ \text{Linear optics}}} E_{\mathrm{j}}(t) + \epsilon_0 \sum_{j,k} \underbrace{\chi^{(2)}_{\mathrm{ijk}}}_{\substack{\uparrow \\ \text{2nd-order nonlinear opt.}}} E_{\mathrm{j}}(t) E_{\mathrm{k}}(t) + \underbrace{\mathcal{O}\left(\vec{E}^3(t)\right)}_{\substack{\uparrow \\ \text{higher-order} \\ \text{nonlinear opt.}}} \tag{2.1}$$

The first term linearly depends on the electric field and gives rise to the complex refractive index; hence it is responsible for phenomena such as refraction, absorption, dispersion, or birefringence. However, if the strength of the electric field increases, terms quadratically depending on $\vec{E}(t)$ as well as higher order terms become relevant. For our application we are solely interested in the quadratic term and neglect higher-order terms from now on. Note that the second-order susceptibility $\chi^{(2)}$ has non-zero elements merely for materials with a broken inversion symmetry. In general, $\chi^{(2)}$ is a 3rd-rank tensor with 27 elements, which couples all electric field components to all polarization components. Due to symmetries, this number is reduced to 10 independent elements, though. Furthermore, for lithium niobate (LN, $LiNbO_3$), which is the nonlinear material utilized in this thesis, many of these elements are zero. In fact, we end up with no more than three non-zero elements stated in the reduced d_{il}-notation : $d_{33} = \frac{1}{2}\chi^{(2)}_{333} \approx 25\,\mathrm{pm/V}$, $d_{22} = \frac{1}{2}\chi^{(2)}_{222} \approx 2.1\,\mathrm{pm/V}$ and $d_{31} = \frac{1}{2}\chi^{(2)}_{311} = \frac{1}{2}\chi^{(2)}_{131} = \frac{1}{2}\chi^{(2)}_{113} \approx 4.3\,\mathrm{pm/V}$ [174,175]. Note that the exact absolute values depend on the wavelength combination and material properties (e.g. doping, stoichiometry, etc.). However, the crucial point is that d_{33} is exceeding the other two elements by roughly one order of magnitude. We can access d_{33} if $\vec{E}(t)$ and $\vec{P}(t)$ are oriented in z - direction, i.e. if all fields are linear polarized in parallel to the c-axis of the crystal. It follows that nonlinear interactions are considerably reduced if all fields are linear polarized but perpendicular to the c-axis (d_{22}), or if one field is oriented in parallel and the other two perpendicular (d_{31}). This

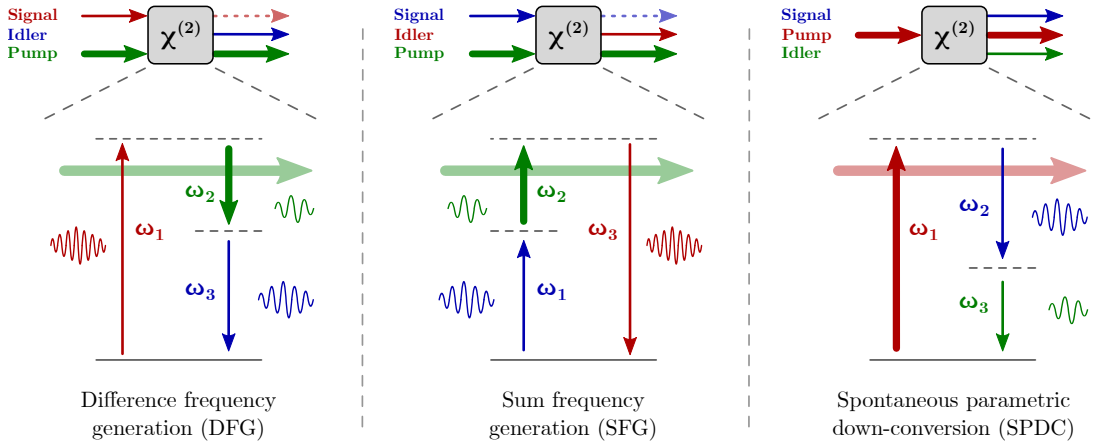

Figure 2.1. Quantum and classical three-wave mixing in nonlinear media. Energy diagrams of the three-wave mixing processes relevant for the experiments in this thesis. The QFCDs mainly utilize difference frequency generation (DFG) to down-convert input photons with frequency ω_1 to the target frequency ω_3 stimulated by a strong classical pump field at $\omega_2 = \omega_1 - \omega_3$. The inverted process is called sum-frequency generation (SFG), where lower energy input photons are up-converted due to mixing with the pump field. A purely quantum-mechanical process is spontaneous parametric down-conversion (SPDC): An input photon at ω_1 spontaneously decays with small probability ($< 10^{-5}$) to two lower energy photons, which are non-classically correlated in time.

fact is the physical origin of the polarization selectivity of the frequency conversion process under consideration, and constitutes one of the main experimental challenges in this thesis. Note that even though the nonlinear interaction is nonzero for orthogonal polarization, we cannot simultaneously access d_{33} and d_{22} due to a phenomenon called phasematching, as we are about to see. Therefore, we restrict our description to d_{33} and the second-order nonlinear polarization simplifies to

$$P_{\mathrm{z}}^{(2)}(t) = 2\epsilon_0 d_{33} E_{\mathrm{z}}^2(t). \tag{2.2}$$

In the context of QFC, we are interested in so-called three-wave mixing processes, which we observe if an electric field with two frequency components ω_1 and ω_2 described as $E_{\mathrm{z}}(t) = E_1 e^{-i\omega_1 t} + E_2 e^{-i\omega_2 t} + \mathrm{cc}$. propagates through the nonlinear crystal. The E-field introduces a nonlinear polarization $P_{\mathrm{z}}^{(2)}(t)$, which in turn results in a third electric field $E_3 e^{-i\omega_3 t}$ oscillating in phase with $P_{\mathrm{z}}^{(2)}(t)$. We compute $P_{\mathrm{z}}^{(2)}(t)$ as

$$P_{\mathrm{z}}^{(2)}(t) \propto 2\epsilon_0 d_{33} \cdot [E_1^2 e^{-i2\omega_1 t} + E_2^2 e^{-i2\omega_2 t} + \mathrm{cc}. \qquad \text{(SHG)} \tag{2.3}$$

$$+ 2E_1 E_2 e^{-i(\omega_1+\omega_2)t} + \mathrm{cc}. \qquad \text{(SFG)} \tag{2.4}$$

$$+ 2E_1 E_2 e^{-i(\omega_1-\omega_2)t} + \mathrm{cc}. \ + \ldots \,] \qquad \text{(DFG)} \tag{2.5}$$

We find that $P_{\mathrm{z}}^{(2)}(t)$ has contributions oscillating at new frequencies ω_3, which are for instance twice the original frequencies $\omega_3 = 2\omega_1 \vee 2\omega_2$ denoted as second-harmonic generation (SHG), the sum $\omega_3 = \omega_1 + \omega_2$ or difference $\omega_3 = \omega_1 - \omega_2$ of the original

frequencies labeled as sum- and difference frequency generation (SFG/DFG), respectively. In the context of QFC, the processes of interest are DFG and SFG. Both are illustrated in Fig. 2.1 along with the corresponding energy diagrams. We employ DFG to down-convert photons at an input frequency ω_1 in the NIR spectral region ("signal") to a lower energy target photon at telecom wavelengths with frequency $\omega_3 = \omega_1 - \omega_2$ ("idler") stimulated by a classical pump field with frequency ω_2 ("pump"). We can already infer from the energy diagram that energy conservation has to be fulfilled[1], implying that down-conversion of one photon from input to target frequency generates a photon at the pump frequency, too. For convenience, we rename the signal as input field and the idler as target or converted field in the following. Although the majority of our QFCDs are designed to down-convert photons to the telecom band, the inverse process, in which photons are up-converted to a higher energy by means of SFG, is also interesting for some quantum network schemes relying on photon-mediated quantum state transfer. We will demonstrate in Sect. 3.3 that QFCDs can be bi-directional, i.e. they simultaneously support DFG and SFG.

We can understand DFG as a stimulated process since we require the classical pump field with comparably large intensity to stimulate the conversion of an input photon to two lower energy output photons. However, the process also spontaneously occurs with a low probability of $< 10^{-5}$, which is known as spontaneous parametric down-conversion (SPDC). The corresponding energy diagram can be found in Fig. 2.1; note that for SPDC the historical attribution of signal, idler and pump is usually permuted as the field with the highest energy stimulates the process. It is important to mention that SPDC can be solely described by quantum mechanics: in this picture we consider SPDC still as a stimulated process, but instead of a classical field it is stimulated by the vacuum field. The process is widely used in quantum optics since the two down-converted photons possess interesting nonclassical properties. For instance, signal and idler photons are correlated in time and frequency due to energy conservation and their simultaneous creation. Moreover, they are entangled with respect to energy and time, and for special nonlinear crystals also in the polarization degree of freedom. Within the scope of this thesis, we use SPDC to characterize our nonlinear crystals and to generate polarization-entangled photon pairs.

In the next step, we derive quantitative predictions on the electric field and intensity of the converted field exemplarily for the DFG process. To this end, we have to solve - in analogy to linear optics - Maxwell's equations in matter. We start from the wave equation for optical nonlinear, non-magnetic dielectric media

$$\frac{\partial^2}{\partial z^2}E(z,t) - \frac{n^2}{c^2}\frac{\partial^2}{\partial t^2}E(z,t) = \mu_0 \frac{\partial^2}{\partial t^2}P^{(2)}(z,t), \tag{2.6}$$

which we solve for all three scalar frequency components of the electric fields E_m with $m = 1$ (input), 2 (pump) or 3 (target) using the ansatz

$$E_\mathrm{m}(z,t) = A_\mathrm{m}(z)e^{ik_\mathrm{m}z-\omega_\mathrm{m}t} + cc. \tag{2.7}$$

[1] This is proven in nonlinear optics by the Manley-Rowe-relations, see [170].

The variables ω_m and k_m are connected to each other by the dispersion relation $k_\mathrm{m} = {}^{n_\mathrm{m}\omega_\mathrm{m}}/_{c}$ with $n_\mathrm{m} = n\left(\omega_\mathrm{m}\right)$ being the frequency-dependent linear refractive index. Inserting Eq. 2.7 into 2.6 yields the so-called coupled amplitude equations

$$\begin{aligned}
\frac{\partial A_1(z)}{\partial z} &= i\kappa_1 \cdot A_2(z)A_3(z) \cdot e^{-i\Delta k' z} \\
\frac{\partial A_2(z)}{\partial z} &= i\kappa_2 \cdot A_1(z)A_3^*(z) \cdot e^{i\Delta k' z} \\
\frac{\partial A_3(z)}{\partial z} &= i\kappa_3 \cdot A_1(z)A_2^*(z) \cdot e^{i\Delta k' z}
\end{aligned} \tag{2.8}$$

with $\kappa_\mathrm{m} = {}^{2\omega_\mathrm{m} d_\mathrm{eff}}/_{n_\mathrm{m} c}$ and the effective nonlinear coefficient $d_\mathrm{eff} = d_{33}$. The parameter $\Delta k'$ is the so-called phase mismatch

$$\Delta k' = k_1 - k_2 - k_3 = \frac{n_1\omega_1}{c} - \frac{n_2\omega_2}{c} - \frac{n_3\omega_3}{c} \tag{2.9}$$

and commonly interpreted as momentum conservation of the DFG-process. In general, the coupled amplitude equations have to be solved numerically, yet we can analytically calculate the intensity of the converted field $I_3(L)$ behind a crystal of length L with only a few assumptions. If the amplitudes of the incoming fields A_1 and A_2 remain unaltered in the crystal, i.e. in the limit of small conversion efficiencies, we get

$$I_3(L) \propto |A_3(z)|^2 = \kappa_3^2 \left|A_1\right|^2 \left|A_2\right|^2 L^2 \mathrm{sinc}^2\left(\frac{\Delta k' L}{2}\right). \tag{2.10}$$

We find that the converted intensity $I_3(L)$ is maximal if the phase mismatch equals zero, while conversion quickly becomes inefficient for $\Delta k' \neq 0$. We can understand this as follows: if $\Delta k' = 0$ is not fulfilled, the converted field runs out of phase with respect to the incoming fields. Hence, the converted wavelets created at different positions z along the crystal destructively interfere, which is depicted in Fig. 2.2a: the black curve represents $I_3(z)$ for $\Delta k' \neq 0$ and reveals an oscillatory behavior with a period of $2L_\mathrm{c} = 2\pi/\Delta k'$. In the case of perfect phasematching ($\Delta k' = 0$) the sinc^2-term equals one and $I_3(z)$ increases quadratically with the position z in the crystal (red curve). However, perfect phasematching (PM) is in general not possible as energy and momentum conservation cannot be fulfilled simultaneously for dispersive media with $n_1 \neq n_2 \neq n_3$ (see Eq. 2.9).
To this end, we rely on the well-established technique of quasi-phasematching (QPM) [176]. In QPM, the permanent ferroelectric domains, which are the physical origin of the nonlinear polarization in d_eff - direction, are periodically flipped by means of high electric fields applied to the crystal. This results in a periodic sign change of the nonlinear coefficient d_eff, and in turn leads to a π phase shift of the converted electric field. If the poling period Λ equals $2L_\mathrm{c}$, the wavelets constructively interfere and I_3 increases with z (see blue curve in Fig. 2.2a). In the momentum conservation picture, QPM adds an additional term $2\pi/\Lambda$ resulting in $\Delta k = k_1 - k_2 - k_3 - 2\pi/\Lambda$, i.e. by choosing an appropriate poling period the phase mismatch can be compensated for a particular wavelength combination. Note that QPM reduces d_eff by a factor $2/\pi$,

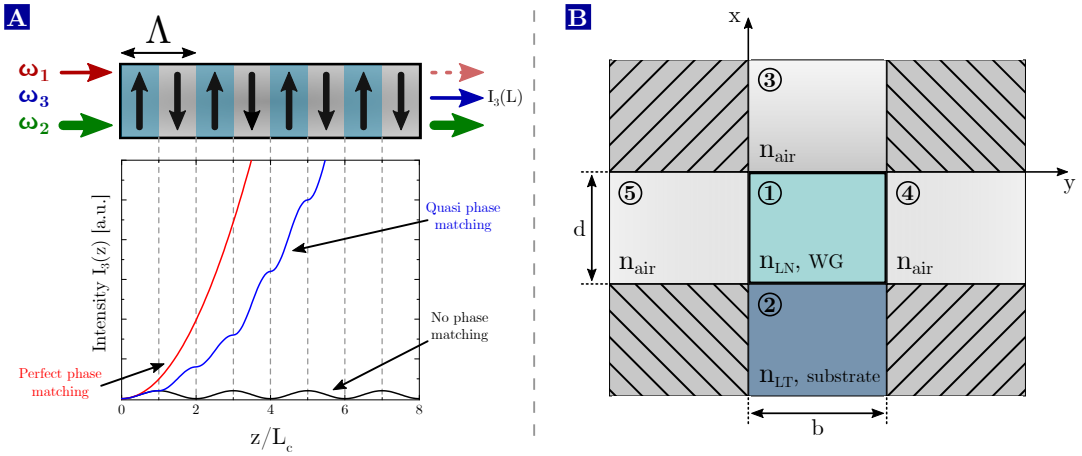

Figure 2.2. Quasi-phasematching and waveguide geometry. **(A)** illustrates the principle of quasi-phasematching (QPM). Without PM, the converted intensity oscillates in the crystal with a period $2L_c$ determined by the phase mismatch $\Delta k'$ while it increases quadratically for perfect PM ($\Delta k' = 0$). The idea of QPM is to periodically invert the ferroelectric domains with a periodicity $\Lambda = 2L_c$. This results in a periodic sign change of d_{eff} and accordingly in a π phase shift of the converted field every $z = L_c$. Thus, we obtain constructive interference and the intensity of the converted field monotonically increases with z. **(B)** Geometry of our ridge waveguides (WGs) with height d and width b. Important for the mode calculation are 5 regions: The WG made of lithium niobate (LN, region 1), the substrate made of lithium tantalate (LT, region 2), and the surrounding air (region 3,4,5).

therefore it is less efficient than ideal PM (see Fig. 2.2a).
We mentioned earlier that PM hinders conversion of orthogonal polarizations since we cannot simultaneously access d_{33} and d_{22}. This can be explained by the birefringence of lithium niobate: the two orthogonal polarizations possess different refractive indices resulting in dissimilar phase mismatches. Thus, it is very unlikely that PM is achieved for both polarizations in a crystal with a single poling period.

The assumptions mentioned above to solve the coupled amplitude equations are not suitable to describe quantum frequency conversion since the input field does not stay constant but is depleted during conversion. To cover the (desirable) regime of high conversion efficiencies, we now consider a weak input field $A_1(z) \ll A_2(z)$ with the initial condition $A_1(z = 0) = A_{\text{in}}$, a strong pump field that does not experience depletion ($\partial A_2(z)/\partial z = 0$), a weak converted field with $A_3(z = 0) = 0$, and perfect phase matching $\Delta k = 0$. We find the solutions

$$\begin{aligned} A_1(z) &= A_{\text{in}} \cdot \cos\left(\sqrt{\kappa_1\kappa_3|A_2|^2}\, z\right) \\ A_3(z) &= A_{\text{out}} \cdot \sin\left(\sqrt{\kappa_1\kappa_3|A_2|^2}\, z\right), \end{aligned} \tag{2.11}$$

that enable us to define the conversion efficiency as the ratio between the converted

intensity behind the crystal $I_3(L)$ and the input intensity I_{in}. We obtain

$$\eta_{\text{con}} = \frac{I_3(L)}{I_{\text{in}}} = \frac{|A_3(L)|^2}{|A_{\text{in}}|^2} = \frac{P_{\text{out}}}{P_{\text{in}}} \cdot \sin^2\left(\sqrt{\eta_{\text{nor}} P} L\right) \tag{2.12}$$

with $P = |A_2|^2$ being the pump power and $\eta_{\text{nor}} = \kappa_1 \kappa_3$ a normalized coupling constant. Typically, we are not interested in the the power conversion efficiency but rather the photon-to-photon conversion efficiency, which we simply calculate as $\eta_{\text{con,pho}} = \eta_{\text{con}} \times {}^{\omega_1}/_{\omega_3}$. In the ideal case, $\eta_{\text{con,pho}}$ equals one when $\sin^2\left(\sqrt{\eta_{\text{nor}} P} L\right) = 1$, but becomes reduced in realistic setups because of unavoidable losses or non-perfect spatial mode overlap. Hence, we introduce an additional parameter $\eta_{\max}$ yielding the pump-power dependent photon-to-photon conversion efficiency

$$\eta_{\text{con,pho}} = \eta_{\max} \cdot \sin^2\left(\sqrt{\eta_{\text{nor}} P} L\right). \tag{2.13}$$

We find that the efficiency increases up to a certain power $P = \frac{1}{\eta_{\text{nor}}} \left(\frac{\pi}{2L}\right)^2$ and subsequently decreases due to back-conversion. Note that a quantum mechanical treatment of DFG where classical field amplitudes are replaced by ladder operators yields the same result [173].

Lithium niobate as material platform

The material of choice for all our QFCDs as well as for an homebuilt cw optical parametric oscillator (OPO) is LN for several reasons: it offers one of the highest nonlinear coefficients d_{eff} among nonlinear solid-state materials [174] and possesses a high transparency over a broad spectral range from $\approx 350\,\text{nm}$ to $> 4\,\mu\text{m}$ [177]. Its ferroelectricity allows for QPM via periodic poling [178] and manufacturing methods are well-matured so that high-quality WG structures are commercially available. A common problem in nonlinear optics for many years was photorefractivity; to avoid this our LN crystals are doped either with Zn or MgO ($\approx 5\,\text{mol}\%$) [179,180]. Note that all our crystals are z-cut, i.e. the highest d_{eff} can be accessed if all light fields are polarized perpendicular to the cut crystal surface and propagate in in-plane direction.

Waveguides

Up to now, we considered nonlinear processes in bulk material. In order to achieve conversion efficiencies around unity in bulk material, pump powers in the order of $> 50\,\text{W}$ are required. This is rather inconvenient, in particular if we deal with pump wavelengths $> 2\,\mu\text{m}$. To this end, we enhance the power efficiency by utilizing optical waveguides, which spatially confine all light fields in transverse directions. Waveguides offer two advantages: on the one hand the small mode volume results in higher pump field amplitudes $A_2(z)$ at a given power compared to bulk. On the other hand, if the WGs are designed and manufactured to enable spatial single-mode operation of input, target and pump field, we attain a large mode overlap of all three fields along the entire crystal. Note that the latter is impossible to achieve with focused beams in bulk crystals. In the

following section we briefly derive the spatial distributions of guided modes in WGs. We employ so-called ridge waveguides, which are bonded on a substrate made of lithium tantalate and surrounded by air on the three remaining sides. There is no full analytical solution of Maxwell's equations for this geometry, however, with some approximations an analytical solution can be found [172, 181]. To this end, we consider the geometry sketched in Fig. 2.2b: the WG is assumed to be rectangular with width b and height d. The whole cross section is split in five relevant regions, in which Maxwell's equations are analytically solved. The calculations reveal that within the WG core (region 1) vertically and horizontally polarized guided modes exist. In the context of QFC we are merely interested in the vertical modes, though. Their relevant field components are calculated by

$$E_\mathrm{x} = \frac{iA}{\kappa_\mathrm{x}\beta}\left(n_\mathrm{ln}^2 k^2 - \kappa_\mathrm{x}^2\right)\sin\left(\kappa_\mathrm{x}\left(x+\xi\right)\right)\cos\left(\kappa_\mathrm{y}\left(y+\eta\right)\right)$$

$$H_\mathrm{y} = iA\sqrt{\frac{\epsilon_0}{\mu_0}}n_\mathrm{ln}^2\frac{k}{\kappa_\mathrm{x}}\sin\left(\kappa_\mathrm{x}\left(x+\xi\right)\right)\cos\left(\kappa_\mathrm{y}\left(y+\eta\right)\right) \tag{2.14}$$

with A being the amplitude, k the vacuum wavenumber and $\beta = \sqrt{n_\mathrm{ln}^2 k^2 - \kappa_\mathrm{x}^2 - \kappa_\mathrm{y}^2}$ the effective refractive index taking WG dispersion into account. The transverse wavenumbers κ_x and κ_y as well as the displacement factors ξ and η are fully determined by the geometry and refractive indices of all five regions. They are obtained by numerically solving the following equations deduced from the boundary conditions

$$\tan\left(\kappa_\mathrm{x} d\right) = \frac{n_\mathrm{ln}^2\kappa_\mathrm{x}\left(n_\mathrm{air}^2\gamma_2 + n_\mathrm{lt}^2\gamma_3\right)}{n_\mathrm{lt}^2 n_\mathrm{air}^2\kappa_\mathrm{x}^2 - n_\mathrm{ln}^4\gamma_2\gamma_3}$$

$$\tan\left(\kappa_\mathrm{y} b\right) = \frac{\kappa_\mathrm{y}\left(\gamma_4+\gamma_5\right)}{\kappa_\mathrm{y}^2 - \gamma_4\gamma_5} \tag{2.15}$$

with the parameters γ_i defined as

$$\begin{aligned}
\gamma_2^2 &= \left(n_\mathrm{ln}^2 - n_\mathrm{lt}^2\right)k^2 - \kappa_\mathrm{x}^2 \\
\gamma_3^2 &= \left(n_\mathrm{ln}^2 - n_\mathrm{air}^2\right)k^2 - \kappa_\mathrm{x}^2 \\
\gamma_4^2 &= \gamma_5^2 = \left(n_\mathrm{ln}^2 - n_\mathrm{air}^2\right)k^2 - \kappa_\mathrm{y}^2.
\end{aligned} \tag{2.16}$$

In general, there exist multiple solutions for κ_x and κ_y, each connected to different guided modes. For the lowest κ_x and κ_y corresponding to the relevant fundamental mode we compute ξ and η to

$$\tan\left(\kappa_\mathrm{x}\xi\right) = -\frac{n_\mathrm{air}^2\kappa_\mathrm{x}}{n_\mathrm{ln}^2\gamma_3} \qquad \text{and} \qquad \tan\left(\kappa_\mathrm{y}\eta\right) = -\frac{\gamma_5}{\kappa_\mathrm{y}}. \tag{2.17}$$

Eventually, we obtain the spatial intensity distribution of the fundamental mode via the z-component of the Poynting vector

$$S_\mathrm{z} = \frac{1}{2}\mathrm{Re}\left(E_\mathrm{x}H_\mathrm{y}^* - E_\mathrm{y}\underbrace{H_\mathrm{x}^*}_{=0}\right) = \frac{1}{2}E_\mathrm{x}H_\mathrm{y}^*. \tag{2.18}$$

The calculated intensity distributions for each wavelength are of particular interest since we will employ them to optimize the coupling of free-space beams to the WG in Sect. 3.2.2.

2.1.2 Background processes in QFC

It is well known that the strong pump laser with powers in the order of few hundreds of milliwatts induces background at the single-photon level leaking both into the input and converted output channel. If the background is too strong, it will alter or even erase the classical and nonclassical properties of the converted photons [182], such as first- and second-order coherence, indistinguishability or entanglement. Moreover, background generated around the input wavelength propagates backwards and might disturb the performance of QNNs, e.g. by provoking infidelities in fluorescence-based atomic-state readout schemes or by directly interacting with the nodes[2]. The origin of conversion-induced background (CIB) is manifold: on the one hand the pump laser itself, being roughly 16 orders of magnitude more intense than the converted photons, can leak into the output channel. Although its wavelength is different, the single-photon detectors may still respond to it. On the other hand, a series of processes generate background in a broad spectral region, and potentially exactly at or in close proximity to the target wavelength. Typically, those processes are quite inefficient, however, if we assume for instance an efficiency of 10^{-10} we are still about six orders of magnitude above the single-photon flux. In this section, we therefore introduce the relevant processes and conclude with some techniques to suppress background in QFCDs.

Raman scattering

A prominent background source in QFC is spontaneous Raman scattering, which has been observed in LN for the first time in [183] and investigated in QFCDs in-depth in [134,135,173,184]. The basics of Raman scattering are illustrated in Fig. 2.3a. Stokes Raman (SR) scattering of the pump laser releases a scattered photon at lower energy $\nu_{\mathrm{sr}} < \nu_{\mathrm{pump}}$ and one phonon, while anti-Stokes Raman (ASR) scattering annihilates a phonon yielding a higher energy photon $\nu_{\mathrm{asr}} > \nu_{\mathrm{pump}}$. Both processes can affect QFC as sketched in Fig. 2.3c: the strong pump field stimulates conversion of input photons to the target wavelength. Depending on the wavelength combination, either the pump or target wavelength is the longest wavelength, hence ASR or SR scattering is present at the target wavelength. The spectrum of Raman scattering is characterized by multiple peaks with Lorentzian line shapes [185]. Measurements of Raman spectra in LN waveguides revealed that the center positions of the peaks are reliable and in agreement with literature values obtained in bulk LN [173]. However, the number of peaks occurring in the spectrum as well as their relative heights and widths depend on a plethora of parameters, e.g. excitation wavelength and polarization, stoichiometric

[2] This may occur in particular for QNNs relying on cavity QED in the strong coupling regime, which are sensitive to incident single photons [70, 105]

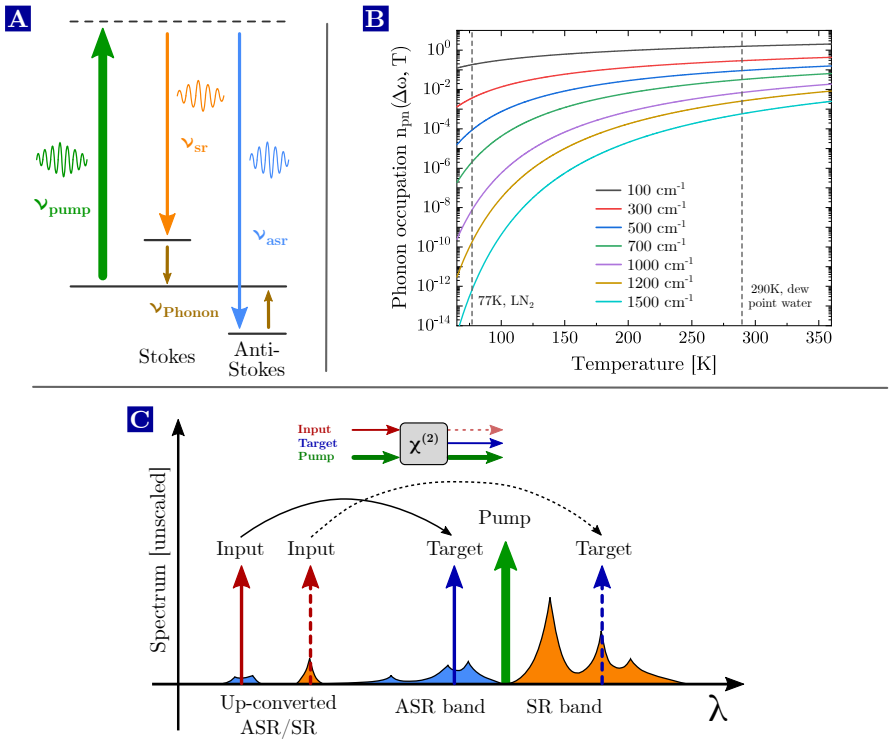

Figure 2.3. Conversion-induced background due to Raman scattering. **(A)** Energy level diagrams of the two elementary Raman scattering processes of the pump field. Stokes Raman (SR) scattering creates phonons and lower energy photons whereas anti-Stokes Raman (ASR) scattering annihilates phonons and generates photons at higher energies. **(B)** The temperature-dependent phonon occupation probability n_{pn} for different phonon energies $|\Delta\nu| = |\nu_{\mathrm{pump}} - \nu_{\mathrm{sr/asr}}|$. ASR scattering is proportional to n_{pn} while SR scattering scales with $1+n_{\mathrm{pn}}$. **(C)** Schematic spectrum showing a QFC process affected by background due to Raman scattering. Depending on the wavelength combination, the target wavelength is affected either by SR or ASR background.

composition, crystal orientation, doping of the nonlinear material or crystal temperature. Particularly interesting for the selection of wavelength combinations of QFCDs is the range of the Raman spectra. In [173] SR and ASR scattering have been observed until $\approx 1100\,\mathrm{cm}^{-1}$. However, Pelc et al. [135] measured even an extended range of ASR scattering ranging at least until $-1600\,\mathrm{cm}^{-1}$. They stated that the occurrence of ASR from $-1000\,\mathrm{cm}^{-1}$ to $-1600\,\mathrm{cm}^{-1}$ cannot not be explained by their model, since they did not observe peaks but a "Raman pedestal" featuring a lower slowing rate than expected from a Lorentzian fit to the multi-peak structure below $-1000\,\mathrm{cm}^{-1}$. These observations lead to two conclusions relevant for QFC: first, if possible it should be avoided to choose target wavelengths located within the peak structure, i.e. with a separation $< 1000\,\mathrm{cm}^{-1}$ from to pump wavelength. Second, in case of separations above $1000\,\mathrm{cm}^{-1}$ Raman background cannot be completely excluded, but its intensity is significantly lower (roughly two orders of magnitude) compared to the peaks.
So far we discussed the situation for DFG. Nevertheless, SFG is prone to Raman back-

ground, too. While ASR background is usually not present anymore at the higher energy target wavelength for the majority of viable wavelength combinations in LN, a frequently observed effect is up-converted Raman background (see Fig. 2.3c). This effect appears if SR or ASR background is generated around the lower energy input wavelength. Once it is generated in the WG, it will be subsequently up-converted and we obtain broadband background around the target wavelength. Its bandwidth is determined by the Raman spectrum and the acceptance bandwidth of the SFG process (in the order of few tens of GHz).
The relative peak heights in Fig. 2.3c insinuate that the ASR scattering rate is lower than the SR scattering rate, which is related to the temperature. While SR scattering creates phonons, ASR annihilates them and hence requires the presence of phonons. If we decrease the temperature, we start to freeze out phonons, i.e. higher energy phonon states are not occupied anymore, lowering the ASR rate at these phonon energies. In the extreme case of $T = 0\,\mathrm{K}$, ASR background is completely suppressed. To quantify this, we consider the spontaneous Raman scattering rates R_{sr} and R_{asr} [186]. Both rates depend on the occupation of the relevant phonon modes determined by the Bose-Einstein distribution $n_{\mathrm{pn}}\left(|\Delta\nu|, T\right) = \left(\exp\left(\hbar|\Delta\nu|/k_{\mathrm{B}}T\right) - 1\right)^{-1}$ with the crystal temperature T and the phonon mode energy $|\Delta\nu| = \left|\nu_{\mathrm{pump}} - \nu_{\mathrm{sr/asr}}\right|$. For the rates we obtain

$$R_{\mathrm{sr}} \propto \nu_{\mathrm{sr}}^4 \left(1 + n_{\mathrm{pn}}\left(|\Delta\nu|, T\right)\right) = \nu_{\mathrm{sr}}^4 \cdot \frac{1}{1 - e^{-\frac{\hbar|\Delta\nu|}{k_{\mathrm{B}}T}}}, \tag{2.19}$$

$$R_{\mathrm{asr}} \propto \nu_{\mathrm{asr}}^4 \cdot n_{\mathrm{pn}}\left(|\Delta\nu|, T\right) = \nu_{\mathrm{asr}}^4 \cdot \frac{1}{e^{\frac{\hbar|\Delta\nu|}{k_{\mathrm{B}}T}} - 1}, \tag{2.20}$$

$$\frac{R_{\mathrm{asr}}}{R_{\mathrm{sr}}} = \frac{\nu_{\mathrm{asr}}^4}{\nu_{\mathrm{sr}}^4} \cdot e^{\frac{-\hbar|\Delta\nu|}{k_{\mathrm{B}}T}}. \tag{2.21}$$

We find that R_{sr} and R_{asr} scale in a different way with the phonon occupation, and their ratio is determined by the Boltzmann factor. While this is hardly relevant for low phonon energies or high temperatures, it becomes crucial in the opposite situation: for $T \to 0\,\mathrm{K}$ or $|\Delta\nu| \to \infty$ the anti-Stokes scattering rate approaches zero whereas the Stokes rate converges to a constant non-zero value. Even at room temperature ASR is still significantly weaker than SR scattering. As an example we consider the DFG-process 1/710 nm - 1/1550 nm = 1/1310 nm realized in a QFC experiment in our group [137]. For a phasematching temperature of 22 °C and $\Delta\nu = 35.4\,\mathrm{THz}$ the ratio $R_{\mathrm{asr}}/R_{\mathrm{sr}}$ is approximately 0.014. Note that the Raman scattering spectrum is also temperature-dependent, however, in the temperature range we are interested in, the phonon occupation is the dominant effect [187].
In this context, it seems promising to take advantage of the temperature dependence in order to reduce ASR background by deceasing the crystal temperature [188]. To estimate the achievable gain, Fig. 2.3b shows the phonon occupation probability n_{pn} in dependence on the temperature at different phonon energies. Two important temperatures are highlighted: in our standard free-space configuration we are able to cool to the dew point of water around 290 K for our lab conditions – which should not be undershot to prevent damage of the WG – by means of thermoelectric elements. In an advanced

evacuated setup cooling down to 77 K would be possible with liquid nitrogen (LN_2). We find that n_{pn} and therefore R_{asr} indeed decrease with temperature as expected. Nevertheless, we find that the effect is comparably weak for lower phonon energies. This is not surprising since lower temperatures are necessary to freeze-out low energy phonons. As an example we consider two DFG-processes implemented in this thesis: 1/854 nm - 1/1904 nm = 1/1550 nm with $\Delta\nu = -1200\,\mathrm{cm}^{-1}$ and 1/780 nm - 1/1600 nm = 1/1522 nm with $\Delta\nu = -320\,\mathrm{cm}^{-1}$. Decreasing T from 323 K to 290 K reduces ASR background by a factor of 1.84 (1.17) for the 854 nm- (780 nm)-process, and cooling with LN_2 to 77 K results in factors of 2.61×10^7 and 91.0, respectively. Thus, large spectral separations between pump and target offer two benefits: first, the temperature scaling of ASR background is more favorable, i.e. we strongly suppress the background by decreasing temperature. Second, we pick up less ASR background at larger separations (higher phonon energies) in general as indicated by Eq. 2.20. A further remark: the wavelengths in our QFCDs are typically fixed. As a consequence, this strategy is only applicable if poling periods to achieve phasematching at low temperatures are available.

Nonlinear processes

A second class of background processes arises from undesired nonlinear interactions caused by fabrication tolerances of the QPM grating. The effect has been discovered and investigated thoroughly in [184, 189, 190]. In a perfect QPM grating with poling period Λ the domains are inverted every $l = \Lambda/2$ resulting in the predicted $\mathrm{sinc}^2(\Delta kL/2)$ behavior of the converted intensity $I_3(L)$ (see Eq. 2.10). Due to fabrication tolerances, random duty-cycle (RDM) errors occur, though. This means the position of the n-th domain boundary z_{n} randomly deviates from its ideal position $z_{\mathrm{n},0} = nl$. Accordingly, the length of the n-th domain is $l_{\mathrm{c}} = z_{\mathrm{n}+1} - z_{\mathrm{n}}$ and the length deviation is given by $\delta l = l_{\mathrm{c}} - l$. In the case of RDM, the length variation is assumed to be Gaussian distributed with a standard deviation σ_{c}. Hence, the converted intensity from Eq. 2.10 needs to be modified [184] to

$$I_3(L) \propto e^{-\pi^2\sigma_{\mathrm{c}}^2/2l^2} \cdot \mathrm{sinc}^2\left(\frac{\Delta kL}{2}\right) + \frac{1}{N}\left(1 - e^{-\pi^2\sigma_{\mathrm{c}}^2/2l^2}\right). \tag{2.22}$$

The first term describes the typical $\mathrm{sinc}^2(\Delta kL/2)$ behavior with an efficiency reduced by the factor $\exp\left(-\pi^2\sigma_{\mathrm{c}}^2/2l^2\right)$. The second term is independent of Δk and inversely proportional to the number of domain boundaries N. For $\sigma_{\mathrm{c}} \neq 0$ this term is nonzero and we get a flat QPM pedestal across the entire spectral region. The pedestal is several orders of magnitude (> 4) weaker than the sinc^2-peak but stronger than the sinc^2-wings far away (> 50nm) from the central peak. This means we observe background over the whole spectral region because of a series of weakly phasematched processes induced by the pump light.

A prominent background process is broadband SPDC generated at energies below the pump light ranging until the edge of the transmission window of LN ($> 4\,\mu$m). As illustrated in Fig. 2.4a SPDC background affects QFC wavelength combinations where $\lambda_{\mathrm{pump}} < \lambda_{\mathrm{target}}$ (see e.g. in [141, 142, 191, 192]). Note that, in analogy to Raman scattering, SPDC background can also appear around the higher-energy input wavelength

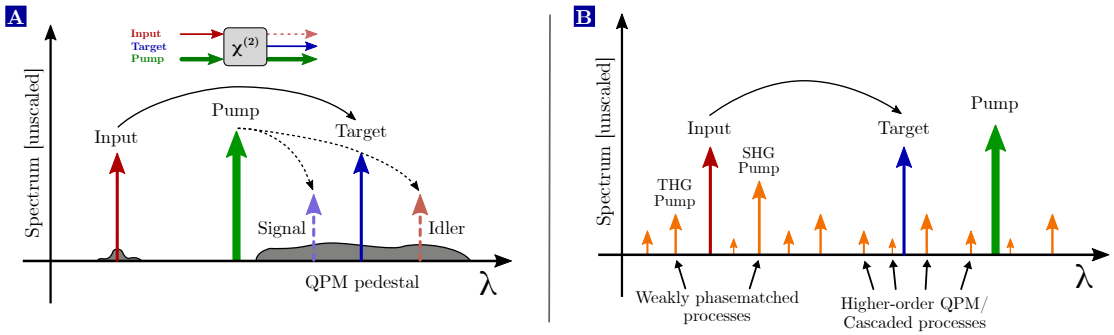

Figure 2.4. Conversion-induced background due to nonlinear-optical processes. **(A)** Random duty-cycle errors in the QPM grating lead to a broadband phase matching pedestal, which supports SPDC of pump photons even though with low probability. This may overlap with the target wavelength in the case of $\lambda_{\text{pump}} < \lambda_{\text{target}}$. **(B)** A plethora of narrow lines distributed over the whole Vis/NIR spectral region appears because of weakly phasematched processes due to random duty-cycle errors in the QPM grating, higher-order quasi-phasematched processes or even cascading of both.

by means of up-conversion.

Apart from SPDC, nonlinear interactions cause a plethora of narrow peaks in the spectrum as sketched in Fig. 2.4b. Among those are weakly phasematched SHG or third-harmonic generation of the pump field enabled by the QPM pedestal. Further narrow peaks can arise from nonlinear processes phasematched by higher-order QPM. Typically, we only consider first-order QPM where the additional term in the momentum conservation is $k_{\text{qpm}} = 2\pi/\Lambda$. In higher-order QPM this term equals $2\pi m/\Lambda$ with $m \geq 2$ and therefore enables phasematching for different wavelength combinations with a reduced efficiency. A third possibility are cascaded processes combining all nonlinear processes and Raman scattering. Although each step lowers the overall efficiency, cascaded processes could still be relevant at the single-photon level. Depending on the individual contributing effects, cascaded processes lead to narrow peaks as well as broadband background.

Techniques for background suppression in QFC

With the knowledge about potential background sources we present in this section two techniques to substantially reduce CIB below the level of the single-photon input signal. Note that this does not necessarily imply that the rate of detected background photons R_{bg} is lower than the converted telecom photon rate R_{con}. The majority of the photon sources in this thesis are synchronous, i.e. the arrival time of each photon is – within its lifetime – exactly determined by an external trigger. Hence, it is possible to detect the converted photons in a gated fashion with a short time window Δt (typ. $< 1\,\mu\text{s}$). In turn, any generated background photon arriving at the detector outside the detection gate does not contribute to the overall background. In this case, the signal-to-background ratio (SBR) is not determined by the detected photon rates, but by the probability to detect a background photons within Δt given as $p_{\text{bg}} = R_{\text{bg}} \cdot \Delta t$. Since

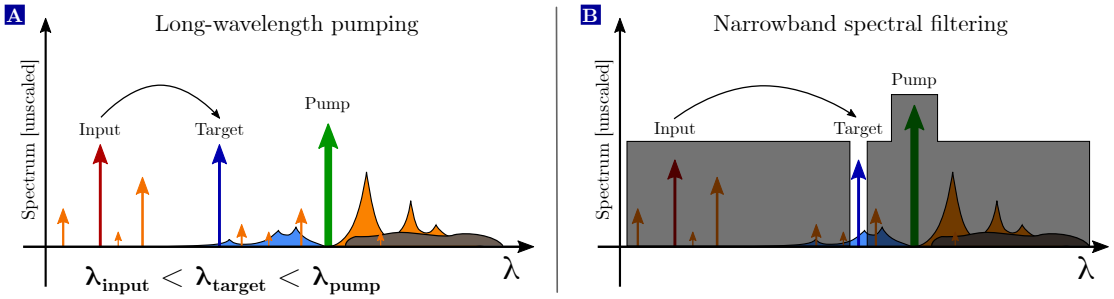

Figure 2.5. Background suppression techniques **(A)** Long-wavelength pumping ensures that two dominant background sources, Stokes Raman background and SPDC background appearing at lower energies with respect to the pump, do not overlap with the target wavelength. Thus, we can easily cut them off by standard bandpass filters due to the comparable large spectral distance ($>80\,\mathrm{nm}$). **(B)** Background at or in close proximity to the target wavelength is reduced by narrowband spectral filtering. A broadband suppression outside the filter window guarantees cancellation of a plethora of background sources, which are far away from the target wavelength, but still within the detection window of our single-photon detectors.

the generation of background photons is typically unconditional, which means that they are not correlated with the converted photons but occur uniformly distributed instead, R_{bg} can be much larger than R_{con} and still yield a SBR $\gg 1$ provided proper gating.
The first technique for background suppression is long-wavelength pumping, i.e. $\lambda_{\mathrm{pump}} > \lambda_{\mathrm{input}}/\lambda_{\mathrm{target}}$. Fig. 2.5a shows the main advantage: Stokes Raman scattering and SPDC background located at lower energies compared to the pump do not appear at or around the target wavelength. Thus, our devices are merely affected by ASR and nonlinear background. Furthermore, we mentioned in Sect. 2.1.2 the benefits of a large spectral separation between pump and target in terms of ASR. Although this approach is highly recommended, we will see in Chap. 6 that it cannot be realized for each device due to fixed input wavelengths and technical limitations regarding the pump laser systems.
The second technique is strong spectral filtering featuring a narrowband transmission window and a broadband suppression region outside of it as sketched in Fig. 2.5b. "Narrowband" here implies filter bandwidths between few tens of MHz and few tens of GHZ while "broadband" spans a region $>1000\,\mathrm{nm}$. The latter is required to eliminate all background sources far away from the target wavelength (e.g. SR or SHG background), which are still within the detection window of our single-photon detectors ranging roughly from 700 nm to 1800 nm. In particular, this includes the pump field being much stronger than all other contributions, which makes a suppression of $>200\,\mathrm{dB}$ feasible. With the narrowband filter we reduce the amount of ASR and nonlinear background in the proximity of the target wavelength. The required bandwidth is usually determined by the amount of background for a given wavelength combination as well as by the brightness and spectral width of the photon source. Typically, we need to find a trade-off between small filter bandwidths, which are beneficial in terms of background, and large bandwidths to avoid filtering out the converted photons. Thus, the filter bandwidth has to be separately determined for each QFCD to achieve a sufficiently large SBR and feasible measurement periods.

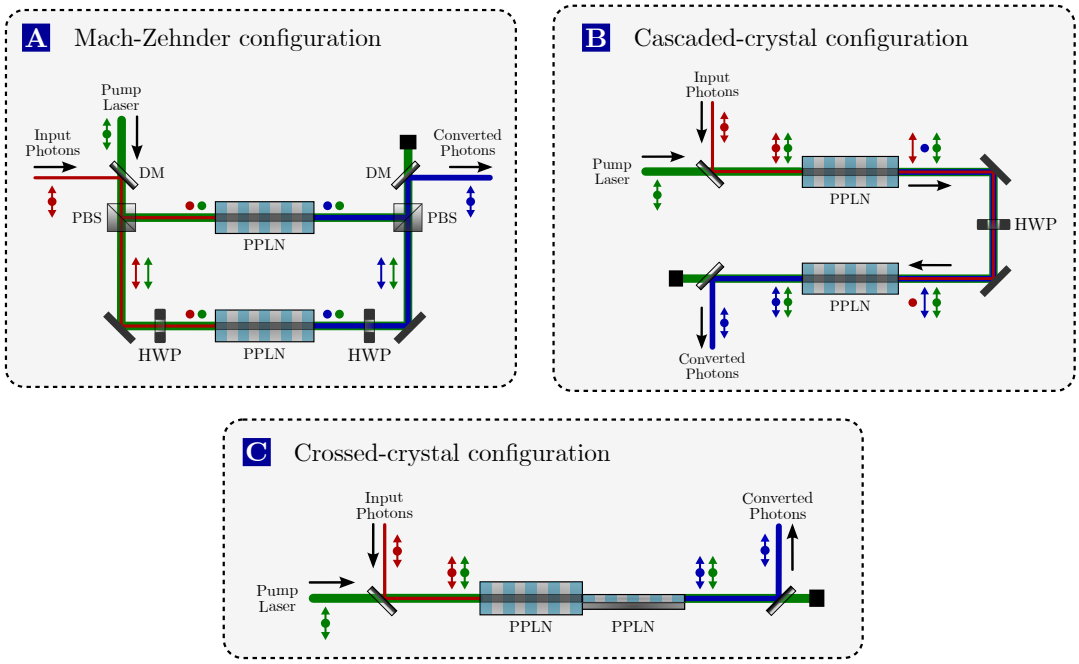

Figure 2.6. Two-crystal schemes. Three possible schemes for PPQFC utilizing two nonlinear crystals. The polarization of each beam at different positions is marked by dots (V-polarized with respect to the optical axis) and arrows (H-polarized). The c-axis of the PPLN crystal points into the plane, i.e. conversion is allowed for V-polarized light. The functionality of each configuration is described in the main text. The figures are adapted from experimental setups by Kaiser et al. [167] (Mach-Zehnder config., **A**), Krutyanskiy et al. [164] (Cascaded crystal config., **B**) and Ramelow et al. [163] (Crossed-crystal config., **C**).

2.1.3 Schemes for polarization-preserving frequency conversion

One of the main objectives of this thesis is the implementation of polarization-preserving quantum frequency conversion to accomplish conversion of photonic polarization qubits. We know from Sect. 2.1.1 that the underlying three-wave mixing processes are inherently polarization-dependent. Although our WGs support guided modes for both orthogonal polarizations, conversion is only enabled for V-polarized light, whose electrical field component oscillates perpendicular to the substrate plane. To overcome the polarization dependence, various schemes have been developed during the last years by our group and other groups around the world. In this section we introduce six possible schemes and present advantages and disadvantages of each. Based on the number of required nonlinear crystals, the schemes are divided in two categories: one-crystal and two-crystal schemes. We start with the two-crystal schemes depicted in Fig. 2.6.

Mach-Zehnder configuration. The most intuitive scheme is the polarization Mach-Zehnder configuration (PMZC) sketched in Fig. 2.6a. Arbitrarily polarized input light and the diagonally (D) or anti-diagonally (A) polarized pump laser are overlapped with a dichroic mirror (DM). Both fields are split into their orthogonal polarization components

(H-polarization corresponds to arrows and V-polarization to dots) by an achromatic polarizing beamsplitter (PBS) and coupled into two separate nonlinear WGs. To ensure conversion of both components, the not convertible V-pol. is rotated to H by means of an achromatic half-wave plate (HWP). This operation is inverted behind the WG and both converted components are overlapped again on a second PBS. The advantage is that both interferometer arms are independent of each other, i.e. it is possible to align each arm individually and equalize conversion efficiencies for H and V quite easily. Besides, each polarization component needs to pass only a single WG, which is a benefit in terms of efficiency. A disadvantage is the rather high demand for optical components, though. Moreover, to preserve the phase of arbitrary superpositions of H and V, the path length difference between the interferometer arms has to be sub-wavelength stable, which requires an active stabilization and therefore increases complexity. The PMZC has been experimentally realized by Kaiser et al. in a fully fiber-based approach [167].

Cascaded-crystal configuration. The cascaded-crystal configuration (CaCG, Fig. 2.6b) relies on the fact, that ridge WGs support guided modes of H- and V-polarized light. Both input polarization components and the D-polarized pump laser pass two cascaded WGs; while the V-component is converted in the first WG, the H-component is converted in the second. To this end, the polarizations of all three fields have to be rotated by 90° between the WGs either by an achromatic HWP or geometrically with a Fresnel rhomb. Clear advantages are a reduced demand for optical components (compared to the PMZC) and the absence of an interferometer, hence the phase relation between H and V is intrinsically stable if the pump laser possesses a sufficiently high frequency stability. However, the CaCG is rather prone to coupling losses as all three fields transmitted through the first WG must be recoupled to the second WG. This might be lossy in particular if the spatial profiles of H- and V-modes do not perfectly overlap due to a non-symmetric WG geometry. The experimental implementation of the CaCG by Krutyanskiy et al. can be found in [164].

Crossed-crystal configuration. This configuration (CrCG) is quite similar to the CaCG. Instead of using a HWP to rotate the polarization of all three fields by 90°, the second WG itself is rotated by 90°. The CrCG, as depicted in Fig. 2.6c, has been implemented by Ramelow et al. [163] with two bulk crystals, hence the conversion efficiency is roughly a factor 500 lower than for WG structures. However, there is no reason preventing the use of WGs in this configuration[3]. The advantages and disadvantages are identical to those of the CaCG.

We conclude that all presented two-crystal schemes enable PPQFC, which has been demonstrated in the respective publications. The schemes of the second category require merely a single WG crystal; their setups are displayed in Fig. 2.7. At the beginning of this work we were restricted to those schemes since we had only a single WG crystal

[3]Note that an arrangement of both WGs in close contact as shown in Fig. 2.6c might become intricate. It might be preferable to arrange the WGs in a similar way as in the CaCG.

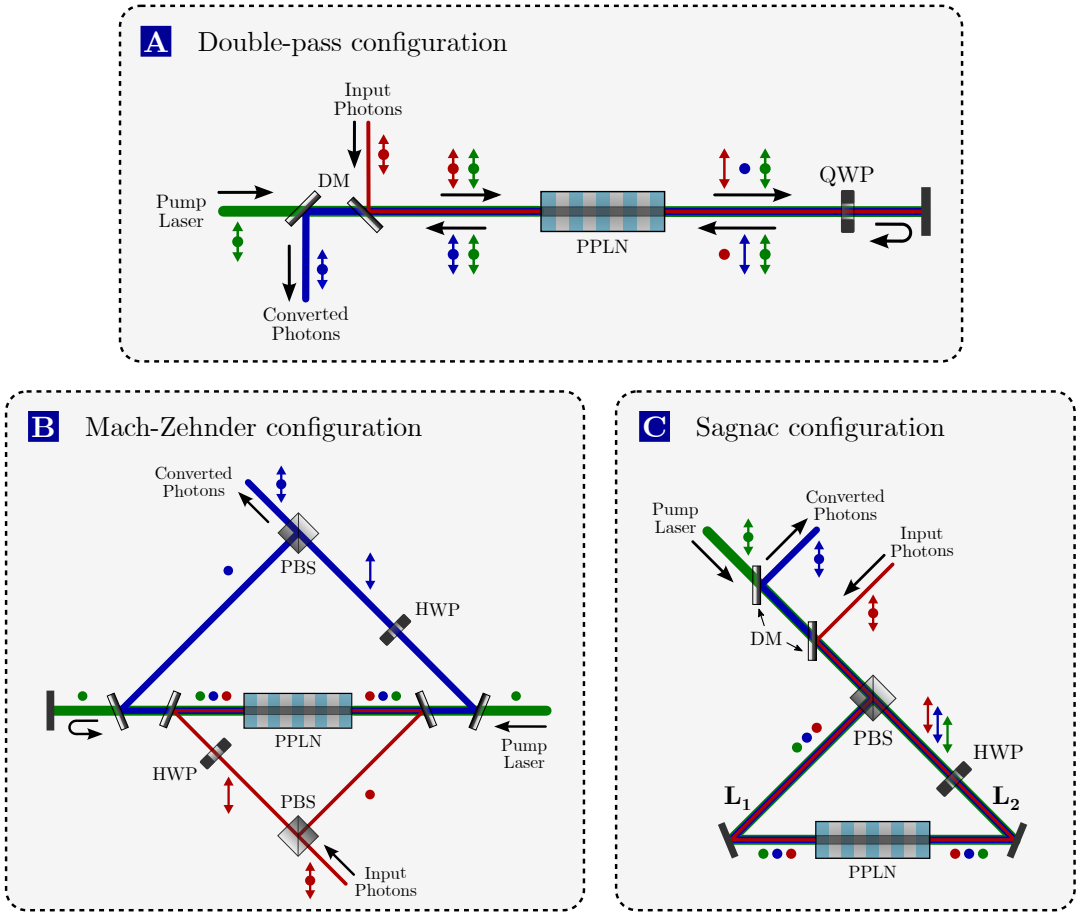

Figure 2.7. Single-crystal schemes. Three possible schemes for PPQFC utilizing a single nonlinear crystal. The polarization of each beam is again indicated by dots (V-polarized) and arrows (H-polarized); frequency conversion is merely allowed for V-polarized light. In the scope of this thesis, we implemented single-crystal Mach-Zehnder **(B)** as well as Sagnac **(C)** configurations, while double-pass configuration (**A**, figure adapted from Albota et al. [162]) could not be realized for technical reasons.

available. However, over the course of this work, we became aware of several convincing advantages of single-crystal schemes, thus, all our QFCDs are based on these.

Double-pass configuration. The double-pass configuration (DPC) sketched in Fig. 2.7a can be considered as a folded version of the CaCG. Both both input components are coupled along with the D-polarized pump laser to the WG, enabling conversion of the V-component. Instead of using a second crystal, all fields are backreflected and recoupled to the same WG. The required 90° polarization rotation of all three fields to convert the H-component in the second pass is guaranteed by an achromatic quarter-wave plate (QWP) acting as HWP in double-pass. Due to its similarity with the CaCG, advantages and disadvantages are the same except a reduced demand for optical components. The DPC was implemented in the experiment by Albota et al. [162] in a slightly different

setup using a bulk crystal embedded in an enhancement cavity for the pump laser.

Single-crystal Mach-Zehnder configuration. In the single-crystal version of the polarization Mach-Zehnder interferometer (SCMZC, see Fig. 2.7b) both polarization components are coupled into the same WG from opposite directions instead of using two separate WGs in both arms. To enable conversion in both directions, the V-polarized pump laser is coupled from one side into the WG and its transmitted fraction is subsequently backreflected and recoupled in opposite direction. In principle, it is possible and advisable for symmetry reasons to couple the pump laser also via an interferometer loop featuring a PBS into the setup. However, this requires roughly twice as much pump power (which is not available in our experiment) since we have to divide the power among both arms. The SCMZC features the same advantages as the PMZC (individual alignment for both arms and a single pass through the WG for each component) but with fewer optical components and a reduced demand for pump power. Nevertheless, the SCMZC still necessitates active stabilization of the interferometer path length. Moreover, we will see in Sect. 3.1.1 that the asymmetric pump laser setup causes the attainable conversion efficiency to decline. Note that our first PPQFC device designed to convert photons emitted by $^{40}Ca^{+}$-ions at 854 nm to the telecom O-band at 1310 nm, is constructed in a SCMZC (see Sect. 3.1).

Sagnac configuration. Fig. 2.7c illustrates PPQFC in a Sagnac interferometer. In this scheme, there is only a single interferometer loop for all three fields. Input and D-polarized pump are overlapped with dichroic mirrors and subsequently split into their polarization components using an achromatic PBS for all three wavelengths. The H-component is rotated by 90° and all fields are coupled into the same WG from opposite directions. The converted light propagates along the same path as the pump light until they are separated by a DM. In fact, we are most in favor with this configuration since it unites the advantages of all other schemes. It enables the best possible conversion efficiencies for three reasons: **(I)** each polarization component passes the WG only once **(II)** all modes in the WG have the same polarization, which avoids losses caused by different spatial modes, and **(III)** the setup is highly symmetric minimizing dissimilar losses of both polarization components. Moreover, it requires the least number of optical components and - more important - since all three fields propagate along the same path, the interferometer is intrinsically phase-stable. This means the phase between H and V is independent of the interferometer path length as well as the frequency stability of the pump laser. To prove this, we consider the two - in general unequal - path lengths L_1 and L_2 ranging from the PBS to the WG facet. Due to phasematching, the phase of the converted light is determined by the initial phases of input and pump in the following way:

$$\phi_{\text{con, init}} = \phi_{\text{inp}} - \phi_{\text{pump}} \tag{2.23}$$

with constant offsets being neglected for simplicity. Thus, we find for the total phase acquired by the converted light in the H- and V-arm

$$\begin{aligned}\phi_{\text{con, H/V}} &= k_{\text{con}} L_{1/2} + \phi_{\text{con, init, H/V}} \\ &= k_{\text{con}} L_{1/2} + k_{\text{inp}} L_{2/1} - k_{\text{pump}} L_{2/1} + \phi_{\text{disp, H/V}}(\lambda, T)\end{aligned} \tag{2.24}$$

with the factor $\phi_{\text{disp, H/V}}(\lambda, T)$ taking all dispersive elements (PBS, HWP, WG) with wavelength- and temperature-dependent refractive indices into account. We calculate the phase difference $\Delta\phi_{\text{con}} = \phi_{\text{con,H}} - \phi_{\text{con,V}}$ with $\Delta L = L_1 - L_2$ and the momentum conservation $k_{\text{con}} = k_{\text{inp}} - k_{\text{pump}}$ to

$$\begin{aligned}\Delta\phi_{\text{con}} &= k_{\text{con}} \Delta L - k_{\text{inp}} \Delta L + k_{\text{pump}} \Delta L + \phi_{\text{disp, H}}(\lambda, T) - \phi_{\text{disp, V}}(\lambda, T) \\ &= \phi_{\text{disp, H}}(\lambda, T) - \phi_{\text{disp, V}}(\lambda, T)\,.\end{aligned} \tag{2.25}$$

We find that the phase difference is independent of the interferometer arm lengths L_1 and L_2. Only large wavelength or temperature changes introduce dispersion resulting in phase shifts varying in time. Due to the mentioned advantages, all PPQFC devices except the one presented in Sect. 3.1[4] connecting 854 nm to 1310 nm are implemented in Sagnac configuration. In parallel to our work, PPQFC in Sagnac configuration was achieved by Ikuta et al. [166].

2.2 Quantum states and processes

With the basic knowledge on PPQFC, we will focus in this section first on quantum states - in particular one- and two-qubit states - and later on quantum processes being the framework to describe the action of PPQFC on quantum states. We briefly introduce the mathematical and graphical description of states and processes, and define the parameters used in the experimental chapters to assess the quality of both. The required experimental techniques to characterize states and processes and to measure the parameters are subsequently explained. The section is based on the textbooks of Chuang & Nielsen [1] and Fox [193] as well as on [194] and [195]. A more detailed introduction to quantum states and tomographic techniques in the context of quantum information can be found in [196], while further details on process tomography are explained in [197].

2.2.1 Description of quantum states

Single qubits exist in a two-dimensional Hilbert space spanned by the two orthogonal basis states $|0\rangle = (1,0)^T$ and $|1\rangle = (0,1)^T$, which correspond to the states 0 and 1 of a classical bit in computer science. In contrast to classical bits, qubits are allowed to be in any coherent superposition of the basis states

$$|\Psi\rangle = \alpha|0\rangle + \beta|1\rangle \tag{2.26}$$

[4] Implementation of this device in Sagnac config. was hindered by technical limitations. Details will be given in Sect. 3.1.

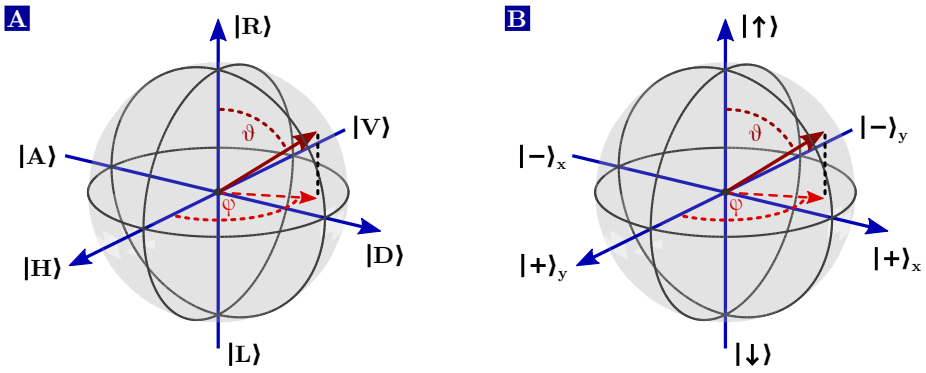

Figure 2.8. Bloch sphere representation of photonic and atomic qubits. **(A)** The Bloch sphere (or Poincaré sphere) for photonic polarization qubits. The six basis states are composed of the two eigenstates right- and left-circular ($|R\rangle = |0\rangle$ and $|L\rangle = |1\rangle$) located at the poles and the superposition states $|H\rangle$, $|V\rangle$, $|D\rangle$ and $|A\rangle$ on the equator. Pure quantum states are represented as Bloch (Stokes) vectors with length one and angles ϑ and φ. **(B)** The Bloch sphere of atomic qubits. The eigenstates are $|\uparrow\rangle$ and $|\downarrow\rangle$ while superposition states in x- and y-direction are denoted as $|+\rangle_{x/y}$ and $|-\rangle_{x/y}$, respectively.

with complex numbers α and β satisfying the normalization condition $|\alpha|^2 + |\beta|^2 = 1$. We can express the qubit state $|\Psi\rangle$ also in a geometrical form by two real parameters ϑ and φ:

$$|\Psi\rangle = \cos(\vartheta/2)\,|0\rangle + e^{i\varphi}\sin(\vartheta/2)\,|1\rangle \tag{2.27}$$

This gives rise to a very useful graphical representation of quantum states on the so-called Bloch sphere, which is illustrated in Fig. 2.8 for photonic polarization qubits (a) and atomic qubits (b). Each state $|\Psi\rangle$ is represented by a vector $\vec{r}$ pointing on the Bloch sphere surface with polar coordinates $(|\vec{r}| = 1, \vartheta, \varphi)$, i.e. all possible qubit states reside on the surface of the Bloch sphere. The basis states $|0\rangle$ and $|1\rangle$ are commonly located at the poles while the superposition states with equal coefficients $|\alpha| = |\beta| = 1/\sqrt{2}$ are on the equator. Note that the Poincaré-sphere known from classical optics to visualize the polarization of light is mathematically equivalent to the Bloch sphere. In the case of polarization qubits, we choose right-circular ($|0\rangle = |R\rangle$) and left-circular ($|1\rangle = |L\rangle$) as basis states. In principle, this choice is arbitrary, but it will prove convenient later on when dealing with joint states of atomic and photonic qubits. Accordingly, the four linear polarization states being collinear with the two axes of the coordinate system within the equatorial plane are defined as $|H\rangle = {}^{1}/_{\sqrt{2}}(|R\rangle + |L\rangle)$, $|V\rangle = {}^{-i}/_{\sqrt{2}}(|R\rangle - |L\rangle)$, $|D\rangle = {}^{(1-i)}/_{2}(|R\rangle + i|L\rangle)$ and $|A\rangle = {}^{(1+i)}/_{2}(|R\rangle - i|L\rangle)$. Atomic qubits are represented by the two electronic states $|\uparrow\rangle$ and $|\downarrow\rangle$ (e.g. Zeeman states in trapped ion), the superposition states in x- and y-direction are likewise defined as $|+\rangle_x = {}^{1}/_{\sqrt{2}}(|\uparrow\rangle + |\downarrow\rangle)$, $|-\rangle_x = {}^{-i}/_{\sqrt{2}}(|\uparrow\rangle - |\downarrow\rangle)$, $|+\rangle_y = {}^{(1-i)}/_{2}(|\uparrow\rangle + i|\downarrow\rangle)$ and $|-\rangle_y = {}^{(1+i)}/_{2}(|\uparrow\rangle - i|\downarrow\rangle)$.

The description is valid for pure quantum states, which might occur in a closed system completely decoupled from the environment. In realistic experimental conditions, qubits couple to the environment resulting in decoherence of the state. We take this into ac-

count by using the density matrix formalism describing an ensemble of quantum states. In fact, this represents quite well what is actually done in the experiment: to measure quantum states we repetitively generate the state in a huge number of experimental runs, perform projective measurements in each run, and subsequently reconstruct its density matrix, which we then assign to the state. Hence, we consider quantum states as a statistical mixture ρ of pure quantum states $|\Psi_\mathrm{i}\rangle$ occurring with probability p_i according to

$$\rho = \sum_\mathrm{i} p_\mathrm{i} |\Psi_\mathrm{i}\rangle\langle\Psi_\mathrm{i}| \tag{2.28}$$

with $\sum_\mathrm{i} p_\mathrm{i} = 1$ and $p_\mathrm{i} > 0$. A physically meaningful density matrix has to fulfill the conditions: **(I)** ρ is normalized: $\mathrm{Tr}(\rho) = \sum_\mathrm{j} \rho_\mathrm{jj} = 1$, **(II)** ρ is a Hermitian operator with $\rho = \rho^\dagger$ and **(III)** ρ is a positive semidefinite operator, i.e. all eigenvalues are non-negative. We call ρ a pure state if we have only a single term with $p_\mathrm{i} = 1$, hence $\rho = |\Psi\rangle\langle\Psi|$, and a mixed state if more than one term contributes with $p_\mathrm{i} < 1$.
In order to visualize density matrices on the Bloch sphere, we rewrite ρ as a linear combination of the Pauli matrices

$$\sigma_I = \begin{pmatrix} 1 & 0 \\ 0 & 1 \end{pmatrix} \quad \sigma_x = \begin{pmatrix} 0 & 1 \\ 1 & 0 \end{pmatrix} \quad \sigma_y = \begin{pmatrix} 0 & -i \\ i & 0 \end{pmatrix} \quad \sigma_z = \begin{pmatrix} 1 & 0 \\ 0 & -1 \end{pmatrix}, \tag{2.29}$$

which form a complete basis of the complex vector space of 2×2 Hermitian matrices. With $\vec{\sigma} = (\sigma_x, \sigma_y, \sigma_z)^T$ we decompose ρ as

$$\rho = \frac{1}{2}\left(\sigma_I + \vec{r}\cdot\vec{\sigma}\right) \quad \text{with} \quad \vec{r} = \begin{pmatrix} \langle\sigma_x\rangle \\ \langle\sigma_y\rangle \\ \langle\sigma_z\rangle \end{pmatrix} = \begin{pmatrix} \mathrm{Tr}\left(\rho\sigma_x\right) \\ \mathrm{Tr}\left(\rho\sigma_y\right) \\ \mathrm{Tr}\left(\rho\sigma_z\right) \end{pmatrix}. \tag{2.30}$$

We find that the Bloch vector $\vec{r}$ is determined by the expectation values of the Pauli operators $\langle\sigma_{x/y/z}\rangle = \mathrm{Tr}\left(\rho\sigma_{x/y/z}\right)$, which correspond to the Stokes parameters $S_{1/2/3}$ in the Poincaré sphere. In case of pure states, $\vec{r}$ is identical to the vector with polar coordinates $(|\vec{r}| = 1, \vartheta, \varphi)$ mentioned above. For mixed states we get $|\vec{r}| < 1$, i.e. the Bloch vector lies within the sphere (a maximally mixed state is characterized by $|\vec{r}| = 0$). Note, that in the Pauli-matrix decomposition the particular choice for the linear superpositions on the x- and y-axis becomes clear: the states $|H/V\rangle$ and $|D/A\rangle$ are the eigenstates of the σ_x- and σ_y-matrices, respectively.
For two qubits, we expand the two-dimensional Hilbert spaces of the single qubits $\mathcal{H}_{1,2}$ to a four-dimensional Hilbert space by means of the tensor product. For the total Hilbert space $\mathcal{H}_\mathrm{tot}$ and accordingly any state $|\Psi_\mathrm{tot}\rangle$ we obtain

$$\mathcal{H}_\mathrm{tot} = \mathcal{H}_1 \otimes \mathcal{H}_2 \quad \text{and} \quad |\Psi_\mathrm{tot}\rangle = |\Psi_1\rangle \otimes |\Psi_2\rangle. \tag{2.31}$$

However, a class of two-qubit states exists, which we cannot factorize as a product of states of the individual subsystems, i.e. $|\Psi_\mathrm{tot}\rangle \neq |\Psi_1\rangle \otimes |\Psi_2\rangle$ although the total Hilbert space is the tensor product of the subsystem Hilbert spaces. These states are called entangled states, which we mentioned already in the introduction to be of

particular interest as resource in quantum network applications and quantum computers. A prominent and important example of two-qubit entangled states is given by the four maximally entangled Bell-states

$$|\Psi^-\rangle = \frac{1}{\sqrt{2}}\left(|01\rangle - |10\rangle\right) \qquad |\Psi^+\rangle = \frac{1}{\sqrt{2}}\left(|01\rangle + |10\rangle\right)$$
$$|\phi^-\rangle = \frac{1}{\sqrt{2}}\left(|00\rangle - |11\rangle\right) \qquad |\phi^+\rangle = \frac{1}{\sqrt{2}}\left(|00\rangle + |11\rangle\right). \tag{2.32}$$

One criterion why the Bell states are maximally entangled is the amount of mixedness in the individual subsystems, which is quantified via the reduced density matrices. The Bell states themselves are obviously pure states. The situation is different, though, if we measure only the state of one qubit and ignore the second one. Mathematically, this corresponds to a partial trace over the measured qubit yielding the reduced density matrix of the remaining qubit. If we trace-out the second qubit from the Ψ^- Bell-state

$$\begin{aligned}\mathrm{Tr}_2\left(|\Psi^-\rangle\langle\Psi^-|\right) &= \frac{1}{2}\mathrm{Tr}_2\left(|01\rangle\langle 01| - |01\rangle\langle 10| - |10\rangle\langle 01| + |10\rangle\langle 10|\right)\\ &= \frac{1}{2}\left(|0\rangle\langle 0| + |1\rangle\langle 1|\right)\end{aligned} \tag{2.33}$$

we find a maximally mixed state. We obtain the same result if we partially trace-out the first qubit, hence, maximally entangled states are characterized by maximally mixed states of the individual subsystems. A second criterion proving that the Bell states are maximally entangled is the Bell parameter, which we introduce in Sect. 2.2.5.
In the following experimental chapters we will generate one- and two-qubit states - in particular entangled states - and measure their respective density matrices. To assess their quality we employ two parameters, the fidelity $\mathcal{F}$ and purity $\mathcal{P}$. The latter is defined as

$$\mathcal{P}(\rho) = \mathrm{Tr}\left(\rho^2\right) \tag{2.34}$$

and quantifies the amount of mixedness of a density matrix. In case of pure states we find $\rho^2 = \rho$ and the purity equals one, while for maximally mixed states we get $\mathcal{P} = 1/2^N$ with N being the number of qubits. In contrast, the fidelity $\mathcal{F}(\rho, \rho')$ is a relative measure and denotes the probability to find a measured state ρ compared to the desired state ρ', i.e. we interpret $\mathcal{F}(\rho, \rho')$ as the overlap between two quantum states. The fidelity is generally defined as

$$\mathcal{F}\left(\rho, \rho'\right) = \left[\mathrm{Tr}\left(\sqrt{\sqrt{\rho'}\rho\sqrt{\rho'}}\right)\right]^2, \tag{2.35}$$

and also valid for two mixed states. Within the scope of this thesis, the desired state is always a pure state $\rho' = |\Psi\rangle\langle\Psi|$. Hence, Eq. 2.35 simplifies to

$$\mathcal{F}\left(\rho, \rho'\right) = \left[\mathrm{Tr}\left(\sqrt{|\Psi\rangle\langle\Psi|\rho|\Psi\rangle\langle\Psi|}\right)\right]^2 = \left[\sqrt{\mathrm{Tr}\left(\rho'\rho\right)}\mathrm{Tr}\left(\sqrt{|\Psi\rangle\langle\Psi|}\right)\right]^2 = \mathrm{Tr}\left(\rho'\rho\right) \tag{2.36}$$

using $\rho' = \sqrt{\rho'}$ (related to $\rho'^2 = \rho'$ for pure states). In fact both measures are of particular interest for us. The fidelity is well-suited to asses how close our generated entangled states are for instance to a desired Bell state. Nevertheless, the fidelity might be illusive, since unitary rotations, which are commonly caused by the experimental setup, decrease the fidelity while the purity is only weakly affected or even unaltered. Thus, it is helpful to calculate the maximum achievable fidelity $\mathcal{F}_{\max}$ for a given purity to get an idea if the non-perfect fidelity is mainly caused by unitary rotations or an imperfect purity. To this end, we model the density matrix as

$$\rho = \mathcal{F}_{\max}|\Psi\rangle\langle\Psi| + (1 - \mathcal{F}_{\max})\,|\Psi_\perp\rangle\langle\Psi_\perp| \tag{2.37}$$

with the desired pure state $|\Psi\rangle$ and its orthogonal pure state $|\Psi_\perp\rangle$ [128]. We easily verify that ρ fulfills $\mathrm{Tr}\,(|\Psi\rangle\langle\Psi|\rho) = \mathcal{F}$. We calculate the purity of ρ as

$$\mathcal{P} = \mathcal{F}_{\max}^2 + (1 - \mathcal{F}_{\max})^2 \tag{2.38}$$

and subsequently the maximum achievable fidelity for a given purity with

$$\mathcal{F}_{\max}(\mathcal{P}) = \frac{1}{2}\left(1 + \sqrt{2\mathcal{P} - 1}\right). \tag{2.39}$$

2.2.2 Description of quantum processes

Next we take a closer look at quantum processes. Imagine the situation illustrated in Fig. 2.9: we prepare photonic qubits in a certain input polarization state ρ_{in} and send them through a PPQFC device yielding the converted output state ρ_{out}. In quantum mechanics the transformation from one state to another one is typically represented by unitary operations. However, these operations are not suitable for us since the PPQFC device might introduce decoherence (e.g. due to phase fluctuations in interferometric schemes), which is a non-unitary operation. Additionally, unequal conversion efficiencies for different polarization states result in polarization-dependent or qubit-state-dependent loss, being a non-trace-preserving operation, actually. A formalism to describe quantum processes also involving non-unitary transformations in a correct way is based on the concept of completely positive maps $\mathcal{E}$. They map the input state to the output state according to

$$\rho_{\mathrm{out}} = \mathcal{E}(\rho_{\mathrm{in}}) = \sum_{\mathrm{i}} E_{\mathrm{i}}\,\rho_{\mathrm{in}}\,E_{\mathrm{i}}^\dagger \tag{2.40}$$

in the so-called operator-sum representation with the Kraus operators E_{i}. However, from an experimental point of view it would be desirable to have a set of numerical parameters instead of several non-fixed operators E_{i}. To this end, we choose the Pauli matrices as fixed operators and rewrite ρ_{out} using $E_{\mathrm{i}} = \sum_{\mathrm{m}=1}^{4} e_{\mathrm{im}}\sigma_{\mathrm{m}}$ to

$$\rho_{\mathrm{out}} = \sum_{\mathrm{m,n}\,=\,1}^{4} \chi_{\mathrm{mn}}\,\sigma_{\mathrm{n}}\,\rho_{\mathrm{in}}\,\sigma_{\mathrm{m}}^\dagger \tag{2.41}$$

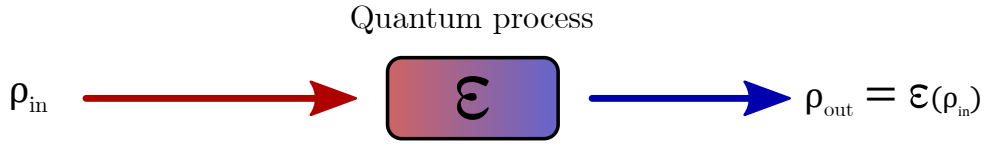

Figure 2.9. Principle of quantum processes. An input quantum state ρ_{in} is sent through a device represented by the process $\mathcal{E}$ yielding the output state $\rho_{\text{out}} = \mathcal{E}(\rho_{in})$.

where the $\chi_{\text{mn}} = \sum_{\text{i=1}}^{4} e_{\text{im}} e_{\text{in}}^{*}$ are the entries of the so-called process matrix, a positive semidefinite and Hermitian matrix. The process matrix completely describes the process, i.e. as soon as we know all entries χ_{mn} we are able to predict the output state for arbitrary input states. In our case, the quantum process ideally represents the identity operation: then all entries of χ are zero except $\chi_{00} = 1$. All unitary operations and decoherence effects result in a decrease of χ_{00} and an increase of the remaining elements. To quantify how close a process is to a desired operation, we calculate the process fidelity $\mathcal{F}_{\text{pro}}$. It denotes the overlap between a measured process matrix χ_{meas} and the ideal matrix χ_{id} according to

$$\mathcal{F}_{\text{pro}}\left(\chi_{\text{meas}}, \chi_{\text{id}}\right) = \left[\text{Tr}\left(\sqrt{\sqrt{\chi_{\text{id}}}\chi_{\text{meas}}\sqrt{\chi_{\text{id}}}}\right)\right]^{2} \underset{\chi_{\text{id}} = \mathbb{1}}{=} \chi_{\text{meas,00}}. \tag{2.42}$$

Hence, if the desired operation is the identity, the process fidelity equals the χ_{00}-entry. A further measure to assess quantum processes is the average fidelity $\mathcal{F}_{\text{avg}}$. To this end, we choose six input states arranged in an regular octahedron on the Bloch sphere (an obvious choice are the six basis states) and calculate for each the overlap fidelity between the measured output state and the ideal one related to the identity operation [198]. The average fidelity is defined as the mean value of the six overlap fidelities

$$\mathcal{F}_{\text{avg}}\left(\mathcal{E}_{\text{meas}}\left(\rho_{\text{in}}\right), \mathcal{E}_{\text{id}}\left(\rho_{\text{in}}\right)\right) = \frac{1}{6}\sum_{\text{n=1}}^{6} \mathcal{F}\left(\mathcal{E}_{\text{meas}}\left(\rho_{\text{in,n}}\right), \mathcal{E}_{\text{id}}\left(\rho_{\text{in,n}}\right)\right). \tag{2.43}$$

Interestingly, process fidelity and average fidelity are directly related to each other [199] by the equation

$$\mathcal{F}_{\text{avg}} = \frac{2\mathcal{F}_{\text{pro}} + 1}{3}, \tag{2.44}$$

in the case of a single-qubit process. Typically, we use this relation as a consistency check to validate our reconstruction methods.

We mentioned above that the process does not necessarily have to be trace-preserving, e.g. in case of qubit loss. If the process does not alter the state but only introduces isotropic loss η_{loss}, we expect the identity process matrix with $\chi_{\text{meas,00}}$ to be decreased by the factor η_{loss}. For state-dependent loss, e.g. polarization-dependent loss of the state $|R\rangle$, additional entries in χ become non-zero since all superposition states $\alpha|R\rangle + \beta|L\rangle$ are pulled towards $|L\rangle$. However, in the experiment we typically apply post-selection. This means we consider only those photons which we detect. Implicitly, this correspond

to a normalization of the non-trace-preserving process matrix since the reconstructed density matrix of the output state has a trace of one [200]

$$\rho_{\text{out}} = \frac{\mathcal{E}(\rho_{\text{in}})}{\text{Tr}(\mathcal{E}(\rho_{\text{in}}))}. \tag{2.45}$$

In this context, the trace of $\mathcal{E}(\rho_{\text{in}})$ can be interpreted as the probability not to loose the photon. If the losses are isotropic, i.e. $\text{Tr}(\mathcal{E}(\rho_{\text{in}}))$ is the same for all input states ρ_{in}, we find that $\rho_{\text{out}} \propto \mathcal{E}(\rho_{\text{in}})$. Hence, isotropic loss does not alter the state and we still consider this as a trace-preserving process. In contrast, state-dependent losses where $\text{Tr}(\mathcal{E}(\rho_{\text{in}}))$ depends on the input state remain non-trace-preserving. Due to the normalization in Eq. 2.45 we cannot easily identify a non-trace-preserving contribution. We will see later in this chapter how to reconstruct such a process based on post-selected data.
The Bloch sphere representation introduced for quantum states is well-suited to visualize quantum processes, too. We will further investigate this in Sect. 2.2.4.

2.2.3 Tomographic reconstruction of quantum states

So far we know that quantum states and processes are described by their corresponding density or process matrix. In the next two sections we want to investigate how we obtain the respective matrices by means of tomographic reconstruction methods combined with maximum-likelihood estimation. Starting with quantum states, we remember Eq. 2.30 where the density matrix is determined by the expectation values of the Pauli matrices

$$\rho = \frac{1}{2}\left(\sigma_I + \sum_{\text{i}=x,y,z} r_{\text{i}}\,\sigma_i\right) \quad \text{with} \quad r_{\text{i}} = \langle\sigma_i\rangle = \text{Tr}(\rho\sigma_i). \tag{2.46}$$

Thus, we are able to infer quantum states of single qubits by measuring expectation values in the three bases σ_{x}, σ_{y} and σ_{z}, in analogy to a polarization measurement of classical light via the Stokes parameters. To this end, we frequently repeat the state preparation to obtain a large number of identical copies, and perform projective measurements with respect to six projectors $\Pi_{\text{k}} = (|R\rangle\langle R|, |L\rangle\langle L|, |H\rangle\langle H|, |V\rangle\langle V|, |D\rangle\langle D|, |A\rangle\langle A|)$, which are described as positive-operator valued measures (POVM). Similarly, the projectors of atomic qubits are $\Pi_{\text{k}} = (|\uparrow\rangle\langle\uparrow|, |\downarrow\rangle\langle\downarrow|, |+\rangle_{\text{x}}\langle+|_{\text{x}}, |-\rangle_{\text{x}}\langle-|_{\text{x}}, |+\rangle_{\text{y}}\langle+|_{\text{y}}, |-\rangle_{\text{y}}\langle-|_{\text{y}})$. A projective measurement implies that we record detection events N_{k} for each projector and normalize them with the total number of detected events per basis setting N_{basis}. We obtain the relative frequencies f_{k} according to

$$f_{\text{k}} = \frac{N_{\text{k}}}{N_{\text{basis}}} = \frac{N_{\Pi_{\text{k}}}}{N_{\Pi_{\text{R/H/D}}} + N_{\Pi_{\text{L/V/A}}}} \quad \text{with} \quad \text{k} = R, L, H, V, D, A, \tag{2.47}$$

which denote the probability to find the respective projector Π_{k}. The relative frequencies enable us to calculate the expectation values to

$$\langle\sigma_x\rangle = f_{\text{H}} - f_{\text{V}} \qquad \langle\sigma_y\rangle = f_{\text{D}} - f_{\text{A}} \quad \text{and} \quad \langle\sigma_z\rangle = f_{\text{R}} - f_{\text{L}} \tag{2.48}$$

and subsequently the density matrix according to Eq. 2.30. This method is called "quantum state tomography" (QST). Keep in mind that we have to perform projective measurements in certain directions on the Bloch sphere. We will clarify in the following experimental chapters how to implement those for atomic and polarization qubits.
Being a procedure to measure single-qubit states, we can straightforwardly extend it to multiple qubits. As an example for 2-qubit states, the density matrix is decomposed as

$$\rho = \frac{1}{4}\left(\sigma_I^{(1)} \otimes \sigma_I^{(2)} + \sum_{\mathrm{i,j}=1}^{3} r_{\mathrm{ij}}\, \sigma_i^{(1)} \otimes \sigma_j^{(2)}\right) \quad \text{with} \quad r_{\mathrm{ij}} = \left\langle \sigma_i^{(1)} \otimes \sigma_j^{(2)} \right\rangle . \tag{2.49}$$

The r_{ij} are the expectation values of the joint Pauli operators $\sigma_i^{(1)} \otimes \sigma_j^{(2)}$ acting on the 2-qubit Hilbert space. We find that we have to perform projective measurements in $3^2 = 9$ different basis settings corresponding to $6^2 = 36$ POVMs $\Pi_{\mathrm{k}} = \Pi_{\mathrm{i}} \otimes \Pi_{\mathrm{j}} = (|RR\rangle\langle RR|, |RL\rangle\langle RL|, ..., |AD\rangle\langle AD|, |AA\rangle\langle AA|)$. We obtain the expectation values and subsequently the density matrix in a similar fashion as in the single-qubit case.
The linear reconstruction of density matrices according to Eq. 2.30 and 2.49 suffers from a distinct disadvantage: due to experimental imperfections such as count rate fluctuations, finite statistics or calibration errors in the projective measurements, the reconstructed density matrix occasionally becomes unphysical, i.e. it might have negative eigenvalues or Bloch vectors outside the sphere with $|\vec{r}| > 1$. For this reason, we avoid linear reconstruction and apply maximum-likelihood estimation (MLE) instead.
The idea of MLE is to identify the physical density matrix ρ_{est}, which fits best to the experimental data by finding extrema of a likelihood functional $\mathcal{L}$

$$\rho_{\mathrm{est}} = \arg\max_{\rho} \mathcal{L}\left(f_{\mathrm{k}}, p_{\mathrm{k}}(\rho)\right). \tag{2.50}$$

The functional $\mathcal{L}$ incorporates the measured relative frequencies f_{k}, the estimated frequencies $p_{\mathrm{k}}(\rho) = \mathrm{Tr}(\rho\Pi_{\mathrm{k}})$, and the required constraints to force the estimated state to be physical. Note that this could turn out to be a disadvantage of MLE since the result is always physical even if the data does not support this. Especially for noisy data or poor counting statistics, even the closest physical matrix can be still "far away" from the measurement data, i.e. the estimated frequencies significantly differ from the measured ones. Thus, it is always advisable to keep track of the discrepancies between measured and estimated frequencies as a validation of the reconstructed matrix.
The MLE algorithm implemented in this thesis is based on an iterative approach developed by Ježek et al. [195] and relies on the likelihood functional

$$\mathcal{L}\left(f_{\mathrm{k}}, p_{\mathrm{k}}(\rho)\right) = \sum_{\mathrm{k}} f_{\mathrm{k}} \ln\left(p_{\mathrm{k}}\right) - \mu \mathrm{Tr}\left(\rho\right). \tag{2.51}$$

The distance between f_{k} and p_{k} obeys the form of a log-likelihood measure, which has proven to be well-suited for this task [195, 201]. The parameter μ is a Lagrange multiplier to ensure that the trace of the estimated density matrix is equal to one. According to Eq. 2.50 we have to maximize $\mathcal{L}$ with respect to ρ, however, a numerically

less demanding procedure is to find the maximum from an extremum condition by varying $\mathcal{L}$ with respect to ρ. We obtain a set of nonlinear equations

$$R_{(n)} = \sum_{\mathrm{k}} \frac{f_{\mathrm{k}}}{p_{\mathrm{k}}\left(\rho_{(n)}\right)} \Pi_{\mathrm{k}}$$

$$\mu_{(n)} = \sqrt{\mathrm{Tr}\left(R_{(n)}\rho_{(n)}R_{(n)}\right)}$$

$$\rho_{(n+1)} = \mu_{(n)}^{-2} R_{(n)}\rho_{(n)}R_{(n)} \tag{2.52}$$

which are artificially symmetrized to meet the constraints on Hermitian and positive-semidefinite density matrices. Eq. 2.52 can be iteratively solved with Matlab starting from an unbiased completely mixed density matrix $\rho_{\mathrm{init}} = 1/2^N \mathbb{1}$ with N being the number of qubits. We compute the estimated state in less than a second for 1- and 2-qubit states.
Finite statistics of the measured detection or coincidence events results in statistical errors of the reconstructed density matrix as well as the deduced fidelity and purity. We obtain error bars by means of Monte Carlo simulations [202]. To this end, we assume Poissonian statistics of the detection/coincidence events (i.e. the standard deviation is given by the square root of the number of events) and simulate new sets of frequencies f_{k} from Poissonian-distributed random numbers. Hence, we obtain several equally probable density matrices from which we calculate mean value and standard deviation of all entries as well as fidelity and purity.
A final remark regarding the number of measured projectors for 1- and 2-qubit QST: in principle it is sufficient to measure a subset of selected projectors corresponding to the number of independent parameters of the density matrix [194]. Since the density matrix is Hermitian and has a trace of one, it possesses 4^N - 1 independent parameters, hence we need 4^N measurements taking normalization with the total number of detected events into account. However, we typically rely on complete QST with 6^N projector measurements since this offers the advantage of a symmetric likelihood functional $\mathcal{L}$. For incomplete QST further modifications of the MLE to counteract the asymmetry are necessary [203].

Influence of the signal-to-background ratio on quantum states

An inevitable opponent during measurements of quantum states - in particular in case of photonic qubits - are background events. Typically, these events are uncorrelated in time and independent of the current measurement basis setting. Hence, they occur as white noise altering the reconstructed states and fidelities towards statistical mixtures. In this section, we show exemplary for 2-qubit QST that we are able to determine the SBR and precisely quantify its effect on the reconstructed fidelities and purities during post-processing. Moreover, we briefly explain how to subtract background from raw data in order to reconstruct background-corrected density matrices.
To estimate the influence of the SBR on fidelity and purity, we recall the model for

background-free density matrices (Eq. 2.37)

$$\rho_{\mathrm{bgf}} = \mathcal{F}_{\mathrm{bgf}} \left|\Psi\right\rangle\!\left\langle\Psi\right| + (1 - \mathcal{F}_{\mathrm{bgf}}) \left|\Psi_{\perp}\right\rangle\!\left\langle\Psi_{\perp}\right| \tag{2.53}$$

with the desired state $|\Psi\rangle$, its orthogonal state $|\Psi_{\perp}\rangle$ and the background-free fidelity $\mathcal{F}_{\mathrm{bgf}}$. If the state is subjected to background, we get an additional term $\frac{1}{4}\mathbb{1} \cdot \mathrm{SBR}^{-1}$, which represents white noise and is proportional to the inverse SBR and the maximally mixed 2-qubit density matrix $1/4\,\mathbb{1}$. This makes sense if we imagine for instance SBR = 1: then we have equal contributions of a maximally mixed state and the background-free state ρ_{bgf}. We calculate the normalized state with background ρ_{wbg} as

$$\begin{aligned}\rho_{\mathrm{wbg}} &= \frac{\mathcal{F}_{\mathrm{bgf}} \left|\Psi\right\rangle\!\left\langle\Psi\right| + (1 - \mathcal{F}_{\mathrm{bgf}}) \left|\Psi_{\perp}\right\rangle\!\left\langle\Psi_{\perp}\right| + \mathrm{SBR}^{-1} \cdot \frac{1}{4}\mathbb{1}}{\mathrm{Tr}\left(\mathcal{F}_{\mathrm{bgf}} \left|\Psi\right\rangle\!\left\langle\Psi\right| + (1 - \mathcal{F}_{\mathrm{bgf}}) \left|\Psi_{\perp}\right\rangle\!\left\langle\Psi_{\perp}\right| + \mathrm{SBR}^{-1} \cdot \frac{1}{4}\mathbb{1}\right)} \\ &= \frac{\mathcal{F}_{\mathrm{bgf}} \left|\Psi\right\rangle\!\left\langle\Psi\right| + (1 - \mathcal{F}_{\mathrm{bgf}}) \left|\Psi_{\perp}\right\rangle\!\left\langle\Psi_{\perp}\right| + \mathrm{SBR}^{-1} \cdot \frac{1}{4}\mathbb{1}}{1 + \mathrm{SBR}^{-1}}.\end{aligned} \tag{2.54}$$

From this, we obtain the fidelity $\mathcal{F}_{\mathrm{wbg}}$ in dependence on the background-free fidelity (and vice-versa)

$$\mathcal{F}_{\mathrm{wbg}} = \mathrm{Tr}\left(\rho_{\mathrm{wbg}} \left|\Psi\right\rangle\!\left\langle\Psi\right|\right) = \frac{\mathcal{F}_{\mathrm{bgf}} \cdot \mathrm{SBR} + \frac{1}{4}}{1 + \mathrm{SBR}} \tag{2.55}$$

$$\mathcal{F}_{\mathrm{bgf}} = \frac{\mathcal{F}_{\mathrm{wbg}} \cdot (1 + \mathrm{SBR}) - \frac{1}{4}}{\mathrm{SBR}}. \tag{2.56}$$

As an example, we consider two extreme cases: if SBR $\to \infty$ we calculate $\mathcal{F}_{\mathrm{wbg}} = \mathcal{F}_{\mathrm{bgf}}$ as expected. In contrast, a SBR of zero results in $\mathcal{F}_{\mathrm{wbg}} = 1/4$, which is the fidelity between pure and maximally mixed 2-qubit states. Furthermore, we find that the highest absolute loss of fidelity occurs for $\mathcal{F}_{\mathrm{bgf}} = 1$. During experiments it is quite helpful to get a rough estimation on the loss of fidelity for a given SBR without prior knowledge about the fidelities. Hence, we set $\mathcal{F}_{\mathrm{bgf}} = 1$ and obtain the following equation denoting the worst-case decrease in fidelity

$$\mathcal{F}_{\mathrm{wbg}} \underset{\substack{\uparrow \\ \mathcal{F}_{\mathrm{bgf}}=1}}{=} \frac{4 \cdot \mathrm{SBR} + 1}{4\,(1 + \mathrm{SBR})} = 1 - \frac{3}{4\,(1 + \mathrm{SBR})}. \tag{2.57}$$

The dependence of the purity on the SBR is computed in a similar way; with the background-free purity $\mathcal{P}_{\mathrm{bgf}} = \mathcal{F}_{\mathrm{bgf}}^2 + (1 - \mathcal{F}_{\mathrm{bgf}})^2$ we compute

$$\mathcal{P}_{\mathrm{wbg}} = \frac{\mathcal{P}_{\mathrm{bgf}} \cdot \mathrm{SBR}^2 + \frac{1}{2} \cdot \mathrm{SBR} + \frac{1}{4}}{(1 + \mathrm{SBR})^2}. \tag{2.58}$$

Another possibility to calculate background-free fidelities and purities is to subtract the background from the number of coincidences in each basis before the quantum state reconstruction. Within this thesis, we typically apply both methods in order to cross-check our results. First, we investigate how to determine the signal S and background

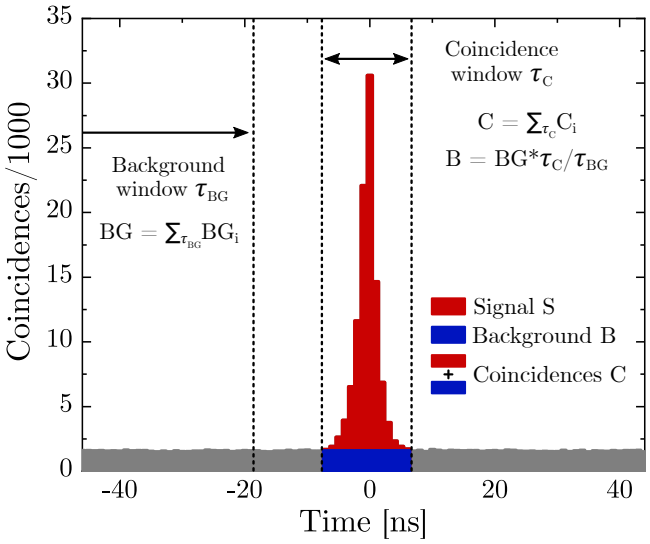

Figure 2.10. Coincidence measurement from 2-qubit QST. Time-correlated detection events of a large number of photonic qubits from a 2-qubit QST. The relevant signal coincidences are in the central peak while we observe uncorrelated background coincidences outside. We get the number of coincidences C by integrating over the time window τ_c. In contrast, the background coincidences B are obtained by integrating over a large time window τ_{bg} outside the correlation peak, and rescaling the result with the factor τ_c/τ_{bg}. Signal coincidences are accordingly calculated to $S = C - B$.

coincidences B from experimental data. During 2-qubit QST we record time-resolved detection events of qubit 1 and 2 for a large number of prepared 2-qubit states in different basis settings. The time tags of the detection events are correlated with each other yielding the number of coincidences in a certain time window from which we calculate the relative frequencies. Fig. 2.10 displays an exemplary temporal correlation function where the coincidences are sorted into time-bins of 1 ns width. We find an uncorrelated background floor (gray bars) and a bunching peak containing the relevant coincidences S. We first determine the total number of coincidences C by adding up all coincidences in a certain time window τ_c, which incorporates the whole bunching peak. In order to get the number of background coincidences B (blue bars), we sum up coincidences in a large window $\tau_{bg} \approx 10\,\tau_c$ sufficiently far away from the bunching peak. Subsequently, we rescale the number with the factor τ_c/τ_{bg}. The large window is advantageous in case of non-perfect statistics to obtain small error bars of the mean value. Accordingly, the signal coincidences are calculated as $S = C - B$ and the SBR as S/B. Note that to estimate the SBR of a 2-qubit QST, we commonly sum-up the correlation functions obtained in all measurement basis settings.

At first view it might be obvious to simply subtract B from C. However, an issue arises if we consider a projector for which we do not expect any signal coincidences, e.g. $|HH\rangle\langle HH|$ for a Ψ^- Bell-state. In the case of low event numbers and non-perfect counting statistics, we might calculate a larger mean value of B than the number of coincidences C, which results in negative values for S. To avoid this, the background sub-

traction (BGS) needs to take into account the finite statistics (which is unfortunately disregarded surprisingly often in literature). The method we apply is thoroughly described in the appendix of S. Kucera's PhD thesis [204], i.e. we explain it only briefly. Signal and background events are considered as independent processes, hence the probability to measure S' signal and B' background coincidences is $P(S' \wedge B') = \mathrm{P_S}(S') \cdot \mathrm{P_B}(B')$ assuming Poissonian distributions $\mathrm{P_S}$ and $\mathrm{P_B}$ with mean values S and B, respectively. The probability to get C coincidences is given by the sum of all possible combinations $B' + S' = C$

$$\mathrm{P}(C) = \sum_{B'+S'=C} \mathrm{P_S}(S') \cdot \mathrm{P_B}(B') = \sum_{S'=0}^{C} \mathrm{P_S}(S') \cdot \mathrm{P_B}(C - S'). \tag{2.59}$$

Subsequently, we calculate the expectation value of the signal coincidences with the assumption that the number of signal coincidences are equally distributed ($\mathrm{P_S} = \text{const.}$) to

$$\langle S \rangle = \sum_{S=0}^{C} S \cdot P_{\mathrm{B}}\left(C - S\right). \tag{2.60}$$

This method has the advantage that $S = \langle S \rangle$ is always positive and the minimum value of S cannot be smaller than its standard deviation determined by C and B. Thus, we never underestimate S by chance in case of bad statistics. Instead, good statistics are a prerequisite to measure small values of S at all.

2.2.4 Tomography of quantum processes

The process matrix χ is measured by a similar tomographic technique as quantum states. The idea is to prepare multiple input states ρ_{in}, apply the unknown process $\mathcal{E}$, and reconstruct the corresponding output states $\rho_{\mathrm{out}} = \mathcal{E}\left(\rho_{\mathrm{in}}\right)$ by means of single-qubit QST. For a single-qubit process, χ is a 4×4 matrix, which is determined by 2×16 complex $\widehat{=}$ 32 real parameters. However, χ is Hermitian, which reduces the number of independent parameters to 16, and for trace-preserving matrices we end up with 12 parameters. Thus, a set of four input states incorporating each principle axis of the Poincaré-sphere (e.g. $|H\rangle$, $|V\rangle$, $|D\rangle$, $|L\rangle$) is enough to reconstruct χ via linear inversion [205], since each state provides three expectation values. In analogy to quantum states, linear inversion is prone to experimental imperfection resulting in non-physical process matrices, so we again make use of MLE.
We mentioned in Sect. 2.2.2 that state-dependent loss is described by non-trace-preserving process matrices. We will see below that the reconstruction of such processes is possible with a modified MLE algorithm. However, if χ is non-trace-preserving, the number of independent parameters is increased by four to 16. One possibility to handle these additional parameters is to measure the efficiency, which corresponds to the first Stokes parameter S_0 of each input state. Typically, S_0 is not specified in quantum information since all density matrices are assumed to be trace-preserving. Measurements of the efficiency are quite sensitive to intensity fluctuations, though. A

more reliable alternative is a complete quantum process tomography (QPT) with six input states equally distributed over the Poincaré sphere, e.g. the six basis states $|H\rangle$, $|V\rangle$, $|D\rangle$, $|A\rangle$, $|R\rangle$, $|L\rangle$. Note that this offers – in analogy to QST – the additional advantage of a symmetric likelihood functional in the MLE. Thus, all QPTs performed in this thesis rely on six input states.

MLE of trace-preserving processes

The MLE algorithm proposed in [195] relies on an alternative description of quantum processes employing a positive-semidefinite operator S, which is isomorphic to the map $\mathcal{E}$ (referred to as Choi-Jamiołkowski isomorphism [206]). The Choi-matrix representation features the advantage that MLE can be realized in a very similar way as for quantum states. In this formalism, we assume input states ρ_{in} in the Hilbert space $\mathcal{H}$ and output states ρ_{out} in a separate Hilbert space $\mathcal{K}$. While $\mathcal{E}(\rho_{\text{in}})$ maps the input state to the output state according to Eq. 2.41, S acts as an operator on the higher-dimensional Hilbert space $\mathcal{H} \otimes \mathcal{K}$. We obtain the output state by applying S to the input state $\rho_{\text{in}}^T \otimes \mathbb{1}_{\mathcal{K}}$ in the $\mathcal{H} \otimes \mathcal{K}$-space and partially tracing-out over the input space $\mathcal{H}$

$$\rho_{\text{out}} = \mathcal{E}(\rho_{\text{in}}) = \text{Tr}_{\mathcal{H}}\left[S\left(\rho_{\text{in,m}}^T \otimes \mathbb{1}_{\mathcal{K}}\right)\right]. \tag{2.61}$$

The index m denotes the input states $\rho_{\text{in,m}}$ with $m = 1...6$. The trace-preservation constraint on $\mathcal{E}$ requires that $\text{Tr}_{\mathcal{H}}(\rho_{\text{in}}) = \text{Tr}_{\mathcal{K}}(\rho_{\text{out}})$ for every possible input state, i.e. the constraint on S is given by $\text{Tr}_{\mathcal{K}}(S) = \mathbb{1}_{\mathcal{H}}$. We obtain the estimated S-matrix by maximizing the likelihood-functional

$$\begin{aligned} S_{\text{est}} &= \arg\max_{S} \mathcal{L}(f_{\text{mk}}, p_{\text{mk}}(S)) \\ \text{with} \qquad \mathcal{L}(f_{\text{mk}}, p_{\text{mk}}(S)) &= \sum_{\text{m,k}} f_{\text{mk}} \ln(p_{\text{mk}}) - \text{Tr}(\Lambda S) \end{aligned} \tag{2.62}$$

where f_{mk} are the relative frequencies measured via single-qubit tomography. The index k denotes the respective POVM $\Pi_{\text{mk}} = (|R\rangle\langle R|, ..., |A\rangle\langle A|)$. The estimated frequencies $p_{\text{mk}}(S)$ are given by

$$p_{\text{mk}}(S) = \text{Tr}_{\mathcal{K}}(\rho_{\text{out,m}}\Pi_{\text{mk}}) = \text{Tr}\left[S\left(\rho_{\text{in,m}}^T \otimes \Pi_{\text{mk}}\right)\right]. \tag{2.63}$$

The term $\text{Tr}(\Lambda S)$ in Eq. 2.62 with $\Lambda = \lambda \otimes \mathbb{1}_{\mathcal{K}}$ takes into account the trace preservation; i.e. λ is a matrix of Lagrange multipliers. Varying the likelihood functional with respect to S yields the set of equations

$$\begin{aligned} K_{(n)} &= \sum_{\text{m,k}} \frac{f_{\text{mk}}}{p_{\text{mk}}\left(S_{(n)}\right)} \left(\rho_{\text{m}}^T \otimes \Pi_{\text{mk}}\right) \\ \Lambda_{(n)} &= \sqrt{\text{Tr}_{\mathcal{K}}\left(K_{(n)} S_{(n)} K_{(n)}\right)} \otimes \mathbb{1}_{\mathcal{K}} \\ S_{(n+1)} &= \Lambda_{(n)}^{-1} K_{(n)} S_{(n)} K_{(n)} \Lambda_{(n)}^{-1}, \end{aligned} \tag{2.64}$$

which are again iteratively solved starting from a completely mixing process matrix $S_{\text{init}} = 1/2^N \mathbb{1}_{\mathcal{H}} \otimes \mathbb{1}_{\mathcal{K}}$ (for an N-qubit process). Error bars are obtained analogous to quantum states via Monte-Carlo simulation. Eventually, we have to calculate the process matrix from the estimated S-matrix. The Choi-matrix can be described in the χ-matrix representation using a different basis (instead of the Pauli basis). Hence, we obtain the process matrix via basis transformation, which is described in Appendix A.

MLE of non-trace-preserving processes

The algorithm presented above is also capable of reconstructing non-trace-preserving process matrices if we drop the respective constraint by eliminating the term $\mathrm{Tr}\,(\Lambda S)$ in Eq. 2.62. Accordingly, the iteration step for S simplifies to $S_{(n+1)} = K_{(n)} S_{(n)} K_{(n)}$. However, if we omit the trace-preservation, the MLE might reconstruct process matrices with a trace larger than one, i.e. some input states are amplified instead of attenuated. To guarantee $\mathrm{Tr}(\chi) \leq 1$ we have to normalize the highest efficiency – associated to the state that does not suffer from state-dependent loss – to one (remember that isotropic does not affect the process matrix due to the normalization according to Eq. 2.45). To this end, we divide the S-matrix by the highest eigenvalue of $\mathrm{Tr}_{\mathcal{K}}(S)$ after each iteration step

$$S_{(n+1)} = S_{(n+1)} / \max\left[\mathrm{ev}\left(\mathrm{Tr}_{\mathcal{K}}\left(S_{(n+1)}\right)\right)\right]. \tag{2.65}$$

Furthermore, we have to take into account another issue: of course the input states have $\mathrm{Tr}\,(\rho_{\text{in}}) = 1$, and due to post-selection – by means we do the evaluation conditioned on an event – the output density matrices have a trace of one, too. This means the trace is apparently "preserved", although the process might be non-trace-preserving. However, as we performed a complete QPT with six input states, we can extract the individual efficiencies of each measured output state (the Stokes parameter S_0) and rescale it with the respective efficiency. The procedure is as follows: the iterative MLE algorithm is embedded in an additional outer loop. During the first iteration step we estimate the matrix $S^{(1)}$ using the relative frequencies $f_{\text{mk}}^{(0)}$ of the measured output states. Subsequently, we calculate the expected output states and the respective efficiencies $\eta_{\text{m}}^{(1)}$ from $S^{(1)}$ given by the trace of each state

$$\eta_{\text{m}}^{(1)} = \mathrm{Tr}\left(\rho_{\text{exp,m}}^{(1)}\right) = \mathrm{Tr}\left[S^{(1)}\left(\rho_{\text{in,m}}^{T} \otimes \mathbb{1}_{\mathcal{K}}\right)\right]. \tag{2.66}$$

Next we rescale the measured output states $f_{\text{mk}}^{(1)} = \eta_{\text{m}}^{(1)} \cdot f_{\text{mk}}^{(0)}$ and proceed to the next iteration steps until all efficiencies η_{m} converge. This procedure yields the correctly scaled output states, which we expect from state-dependent loss, and the corresponding non-trace-preserving process matrix χ. Finally, we divide the χ-matrix by its trace according to Eq. 2.45 to account for the post-selection issue in experiments. Note that the normalized χ-matrix does not represent any physical process anymore, it merely mimics the post-selection process and, hence, delivers correct results for our experimental data.

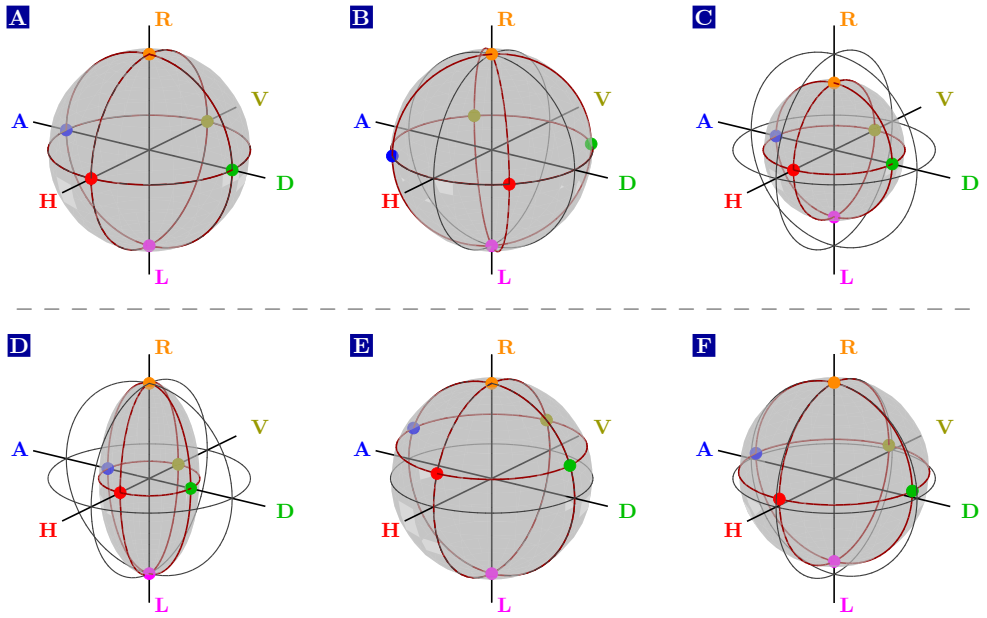

Figure 2.11. Representation of quantum processes. **(A)** - **(F)** Bloch sphere representations of exemplary chosen quantum processes. If we choose the six basis states as input, the colored dots denote the respective output states. In case of non-unity processes, the whole sphere will be rotated, shrunken, displaced or distorted. In detail, the spheres represent the following processes: **(A)** Identity operation. **(B)** Unitary $\pi/4$-rotation around the R - L axis. **(C)** Isotropic depolarization. **(D)** Pure dephasing without population transfer between the eigenstates. **(E)** and **(F)** State-dependent qubit loss of 50 % for L - polarized light. In this case the sphere is mapped to itself, but the superposition states are distorted as shown in **(E)**. The process does not preserve the trace, however, assuming trace-preservation in the reconstruction algorithm outputs a wrong estimation, see **(F)**.

Visualization of quantum processes

To represent a given quantum process matrix on the Bloch sphere, we first simulate a large number of input states equally distributed over the sphere. Next we calculate according to Eq. 2.41 the output states and plot a new Bloch sphere, which might be – depending on the process – rotated, shrunken, displaced or distorted with respect to the input sphere. Fig. 2.11a - f illustrates some examples for different processes. The gray spheres are the output Bloch spheres and the colored dots represent the six basis states. The process matrices describing these examples are obtained by employing the above explained reconstruction methods with the six basis states of the Poincaré-sphere as input states and the respective theoretically calculated output states. Fig. 2.11a displays the identity operation where the sphere and all states are mapped to themselves. Fig. 2.11b is an example for a unity rotation around the z-axis corresponding to a $\pi/4$-shift of the qubit-phase. Isotropic depolarization introduces mixedness and therefore shrinks the sphere as shown in Fig. 2.11c. This occurs for instance in long, unstabilized fibers suffering from temperature- or stress-induced random polarization rotations. If the eigenstates are unaltered while the phase information is partially lost, we speak

about pure dephasing as sketched in Fig. 2.11d. This is a prominent process for atomic Zeeman qubits, whose phase is very sensitive to magnetic field fluctuations while populations transfer between both states is not likely to occur. In Fig. 2.11e we simulate polarization-dependent loss of 50 % for L-polarized light and reconstruct χ with the algorithm for non-trace-preserving processes. This process does not shrink, displace or rotate the sphere; it is still mapped to itself since the output states are fully polarized. We expect that $|R\rangle$ and $|L\rangle$ are unaltered while the superposition states are "pulled" towards $|R\rangle$. This is confirmed by Fig. 2.11e: the sphere is distorted and the superposition states are not located at their original position anymore. In contrast, if we apply the algorithm for trace-preserving processes, we get a wrong estimation as illustrated in Fig. 2.11f. We find that the superposition states are shifted towards $|R\rangle$, but far less than they should. Moreover the sphere is shrunken indicating depolarization of $|L\rangle$ and a "population" transfer from $|L\rangle$ to $|R\rangle$, which we certainly do not expect.

2.2.5 Bell test experiments

An alternative experimental method to verify maximally entangled Bell-states are Bell tests, which we briefly introduce below. Their origin goes back to 1935 when Einstein, Podolsky and Rosen asked the question if the physical reality described by quantum mechanics can be complete [207] (the so-called EPR paradox). They found that the measurement of non-commuting observables of a joint quantum state consisting of two particles is inconsistent with the principles of realism and locality. As they assumed any physical theory must obey these principles, they concluded that QM cannot be complete as of yet. Subsequently, it was suggested to introduce local hidden variables (LHV) to modify quantum mechanics. If those variables are known, results of measurements on two-particle states could be predetermined and quantum mechanics can be formulated as a local-realistic theory (LRT). However, in 1964 John Bell deduced statistical bounds on measurement results of two-particle states for theories governed by LHV, which do not hold for quantum mechanics [208]. He formulated his famous inequality that needs to be fulfilled for LHV-theories but is violated by quantum mechanics. In the following we show how to experimentally test this inequality.
A typical Bell test experiment is sketched in Fig. 2.12. An EPR-source generates pairs of spatially separated qubits in a maximally entangled Bell state, which are sent to the observers Alice and Bob. Each observer performs projective measurements in one out of two - in the ideal case randomly selected - basis settings $a \in \{\alpha, \alpha'\}$ on Alice's side and $b \in \{\beta, \beta'\}$ on Bob's side. Note that in the example of entangled photons all settings are typically located in the plane containing the linear polarizations of the Poincaré-sphere (H,V,D,A) with $\alpha, ..., \beta'$ being the angles with respect to one of the basis states. The projective measurements delivers the respective outcomes $x, y \in \{0, 1\}$ corresponding to the two orthogonal projectors per basis setting. We repeat those trials for a large number of Bell states and record the number of detected coincidences $N_{\mathrm{a,b}}^{\mathrm{x,y}}$ in the respective basis setting a, b, which are either correlated $N_{\mathrm{a,b}}^{0,0}/N_{\mathrm{a,b}}^{1,1}$ or anti-correlated

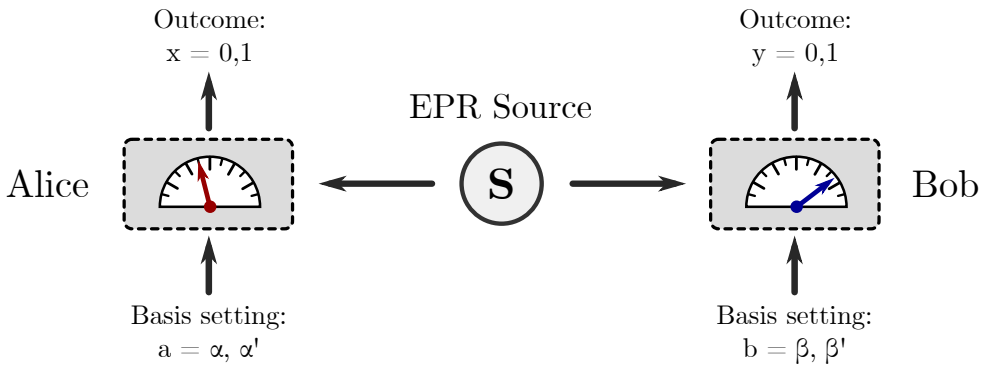

Figure 2.12. Principle of Bell test experiments. An EPR source generates two qubits in a maximally entangled Bell state, which are distributed to Alice and Bob. Both perform projective measurements randomly in one out of two particular basis settings $a = \alpha, \alpha'$ and $b = \beta, \beta'$, respectively. Correlations of the measurement outcomes in all combinations of bases a and b yield the Bell parameter S.

$N^{0,1}_{\mathrm{a,b}}/N^{1,0}_{\mathrm{a,b}}$. Subsequently, we calculate correlators $\langle\sigma_{\mathrm{a}}\sigma_{\mathrm{b}}\rangle$ defined as

$$\langle\sigma_{\mathrm{a}}\sigma_{\mathrm{b}}\rangle = \frac{N^{0,0}_{\mathrm{a,b}} - N^{0,1}_{\mathrm{a,b}} - N^{1,0}_{\mathrm{a,b}} + N^{1,1}_{\mathrm{a,b}}}{N^{0,0}_{\mathrm{a,b}} + N^{0,1}_{\mathrm{a,b}} + N^{1,0}_{\mathrm{a,b}} + N^{1,1}_{\mathrm{a,b}}}. \tag{2.67}$$

We find that the correlator equals $+1$ if the measurement outcomes are correlated and -1 in case of anti-correlations. The Bell inequality in an experiment-friendly form has been proposed by Clauser, Horne, Shimony and Holt in [209] and is therefore known a CHSH-inequality

$$S = \left|\langle\sigma_\alpha\sigma_\beta\rangle + \langle\sigma_\alpha\sigma_{\beta'}\rangle\right| + \left|\langle\sigma_{\alpha'}\sigma_\beta\rangle - \langle\sigma_{\alpha'}\sigma_{\beta'}\rangle\right| \leq 2 \tag{2.68}$$

with S being the so-called Bell parameter. According to Bell's theorem, this inequality has to be fulfilled, i.e. S must not exceed a value of 2 in case of a LRT. However, if we consider the correlators as quantum mechanical expectation values of the measurement operator $\sigma_\alpha\sigma_\beta$, and take one of the four Bell states, we find in some particular basis settings (e.g. $\alpha = 0°$, $\alpha' = 90°$, $\beta = -45°$, $\beta' = 45°$ in the case of Ψ^- Bell-states) the following correlator values: $\langle\sigma_{0°}\sigma_{-45°}\rangle = \langle\sigma_{0°}\sigma_{45°}\rangle = \langle\sigma_{90°}\sigma_{-45°}\rangle = 1/\sqrt{2}$ and $\langle\sigma_{90°}\sigma_{45°}\rangle = -1/\sqrt{2}$. Hence, we calculate $S = 2\sqrt{2}$ and therefore a violation of Bell's inequality. Note that $2\sqrt{2}$ is the maximum value of S, a further reason why Bell states are considered as maximally entangled.

The first experimental Bell test violating Bell's inequality has been performed by Freedman and Clauser [210] with photons from an atomic cascade in Calcium. From then on a large number of Bell tests were conceived in different physical systems, among them SPDC sources [211–216], trapped ions [217, 218] and atoms [112] or NV centers in diamond [68]. The main purpose of those experiments was the closure of a series of loopholes, which would allow for violations of Bell's inequality with LRTs due to experimental imperfections or communication between Alice and Bob; for an overview on this topic see [219]. Apart from the fundamental aspect of Bell test experiments, they

provide a quite beneficial alternative to QST to verify entangled Bell states since they feature an important advantage: they neither rely on a series of assumptions (e.g. the Hilbert space dimension) made in QST nor on maximum-likelihood estimation yielding merely the most-likely state. In contrast, a Bell parameter surpassing the value of two – directly deduced from experimental raw data – unambiguously verifies the respective Bell state. Interestingly, this paves the way to certify entangled states, or even the devices in quantum networks and computers, e.g. EPR-sources, converters, measurement setups, detectors or quantum gates, with a minimum number of assumptions. This technique is known as device-independent certification [220, 221].

2.3 Integrating QFC devices into quantum networks: Challenges, requirements and figures of merit

In this section we take a closer look on the question whether QFC could be a useful technique as telecom interface for quantum network links or even small-scale quantum networks consisting of more than two QNNs. To this end, we have to be able to scale up the number of devices without considerably decreasing the performance of the network links and without increasing the complexity and error-proneness, which might render the respective experiments impossible. We identified a "wish list" of requirements and figures of merit itemized in Tab. 2.1 to assess QFCDs with respect to their potential to be scaled-up for quantum network experiments and applications. We divide them into five categories: **(I)** The first category incorporates the well-established conversion metrics. The external device efficiency (EDI) is defined as the "fiber-to-fiber" efficiency of the complete QFCD, i.e. the ratio between converted photons leaving the output fiber and input photons entering the launch fiber. Hence, it takes into account the conversion efficiency within the WG and all passive optical losses (e.g. coupling efficiencies, transmission of optical elements and filters, etc.). CIB and process fidelity have been explained already in Sect. 2.1.2 and 2.2.4. The presence of those metrics in the wish list is obvious: the efficiency affects the entanglement generation rate between QNNs while background and process fidelity determine the quality of the entanglement. **(II)** In the second category we summarize the pump laser properties. Due to energy and momentum conservation the frequency and phase of the pump laser is imprinted on the converted photon. However, many quantum network links rely on quantum interference of indistinguishable photons (e.g. [112]), phase-sensitive single-photon interference (e.g. [69]) or absorption/reflection of photons by QNNs (e.g. [65]). This requires the pump lasers of all QFCDs to be frequency-stable (if necessary even phase-locked) below the characteristic linewidth of the QNNs (depending on the system this may vary between several GHz and a few kHz). Furthermore, the output power of the pump laser should be stable to avoid efficiency fluctuations or drifts. With currently achievable experimental parameters, the overall entanglement generation rate in quantum networks is expected to be several orders of magnitude lower compared to classical communication networks, i.e. quantum network experiments will certainly take quite some time. Hence, the performance of the pump laser should be reliable enough to allow for a continuous operation of the network without considerable maintenance downtimes ("24/7-operation"). Ideally,

we would have a turn-key system available, which can be operated without any expert knowledge on the laser itself. **(III)** A further important requirement is the integration in existing QNNs. At least in the near future, it will not be unusual that QFCDs are not constructed at the site of the nodes. Moreover, the nodes may be operated within an existing network infrastructure that the QFCDs must be adapted to. Therefore, the devices should be compact and fully transportable standalone systems that neither interfere with the operation of the QNNs nor require any specific infrastructure.

Table 2.1. Requirements and figures of merit to scale-up QFCDs for quantum networks

Category	**Figure of merit/Requirement**
(I) Conversion metrics	High external device efficiency Low conversion-induced background High process fidelity of qubit conversion
(II) Pump laser properties	High frequency and power stability Reliable 24/7-operation Turn-key system
(III) Integration in existing QNNs	Compact and transportable system Stand-alone system and operation
(IV) Miniaturized devices	Integration into 19-inch racks Integration on a single chip
(V) Advanced functionalities	Bi-directional operation (SHG and DFG) Photon bandwidth manipulation Conversion to multiple frequency channels Dispersion cancellation

(IV) The next step in this direction is the miniaturization of QFCDs enabling reduced space requirements and fast relocation of the devices. At first we may think about integrating all components, i.e. lasers, electronics and optical setups, into standardized 19-inch racks, which are well-established in classical telecom infrastructure. The ultimate goal in miniaturization is the on-chip integration. While this has already been achieved for polarization-dependent frequency QFCDs [159,222,223], it is much more sophisticated for PPQFC. **(V)** Eventually, we can imagine some advanced functionalities, partly going beyond the capabilities of the devices presented in this thesis. One aspect is bi-directional operation, i.e. the device acts simultaneously as up- and down-converter with equal performance. This might be interesting for network links relying on emission and absorption of photons [65]. Photon bandwidth compression and stretching by means of dispersion engineering [224] or chirped pump pulses has great potential to connect dissimilar quantum systems featuring different linewidths of their optical transitions (e.g. semiconductor quantum dots and atomic systems). Furthermore, by utilizing several pump lasers with different wavelengths, conversion in different frequency channels

is possible. This may find application in multiplexing or routing in quantum networks. Broadband photons typically suffer from dispersion in optical fibers resulting in distortion of the spectral and temporal wavepacket [225]. By using chirped pump pulses, we can compensate for this and therefore cancel out dispersive effects. Note that this list is for sure not complete; there might be many more ideas to develop QFC further towards a useful tool in quantum networks.

Chapter 3

Polarization-preserving quantum frequency conversion of $^{40}Ca^{+}$-resonant photons to the telecom bands

Contributions: The experiments in this chapter have been performed at Saarland University under the joint supervision of Prof. Christoph Becher and Prof. Jürgen Eschner.
The QFCD to the telecom O-band in its polarization-dependent version was originally constructed by Andreas Lenhard. The polarization-preserving QFC was designed, constructed and operated by M.B. with advice from Stephan Kucera (S.K.), Benjamin Kambs (B.K.) and Jonas Becker. The interferometer path length stabilization was implemented by M.B. with help from Sebastian Rühle as part of his bachelor thesis. All measurements and simulations in Sect. 3.1 were performed and evaluated by M.B. The group of J. Eschner represented by S.K. and Jan Arenskötter (J.A.) contributed to all experiments in this chapter by providing laser light at 854 nm as well as hard- and software for polarization control and measurement.
The polarization-preserving QFC to the telecom C-band was designed by M.B. Construction and characterization were conceived by M.B. and Tobias Bauer (T.B.) as part of his master thesis. The simulation program for the trichroic waveguide coupling was developed by M.B. and extensively modified and improved by T.B. with help from B.K.
The experiment in Sect. 3.3 was conceived by M.B., T.B., J.A., and S.K. The entangled photon-pair source was developed and operated by S.K. and J.A. while the QFC was operated by M.B. and T.B. All data were analyzed by M.B. and T.B.

Part of the results from Sect. 3.1 are published in Nat. Commun. **9**, 1998 (2018).

The development of polarization-preserving quantum frequency conversion devices (PPQFCDs) constitutes one of the core elements of the experimental work in this thesis. In this chapter we present two PPQFCDs being designed to connect 854 nm, the wavelength of the dipole transition $4^2P_{3/2} \Leftrightarrow 3^2D_{5/2}$ in trapped $^{40}Ca^{+}$-ions, to the telecom O- and C-band. The first converter addressing the O-band at 1310 nm (henceforth referred to as "O-band converter") is a modification of an existing polarization-dependent device [146, 169] and can be seen as the prototype version for our PPQFC. This means we develop alignment procedures and characterization techniques, and we outline the critical components to achieve the best possible performance based on this converter. A detailed description of the setup and a comprehensive characterization of the latter can be found in Sect. 3.1. Note that all experiments in Chap. 4 and 5, in which PPQFC is combined with a trapped-ion QNN to demonstrate building blocks for quantum networks, employ this converter. The target wavelength of 1310 nm, which is less favorable than 1550 nm in terms of absorption losses in fibers, is historically justified: in the scope of an earlier experiment it was planned to measure two-photon interference between converted photons from trapped ions and silicon-vacancy centers in diamond. The latter have a transition wavelength of 737 nm, which allows for low-background QFC solely to the O-band. Another argument for the O-band might be the coexistence of quantum and classical signals in a fiber network, e.g. for QKD in a metropolitan area, since the DWDM channels of the classical communication are mainly located in the C-band [226, 227].
Without the restriction to the O-band we designed a new generation of converters to translate 854 nm to the telecom C-band at 1550 nm (henceforth referred to as "C-band converter"). This converter is considerably improved with respect to all relevant figures of merit, which is outlined in Sect. 3.2 together with the setup and characterization of the device. In Sect. 3.3 we test the C-band converter with nonclassical light, more specifically polarization-entangled photon pairs emitted by an SPDC source. We will demonstrate the preservation of entanglement after PPQFC even if the converted photons are transmitted through up to 40 km of optical fibers.

3.1 Polarization-preserving QFC from 854 nm to the telecom O-band

We start with the frequency converter translating 854 nm to the telecom O-band at 1310 nm by means of the DFG process 1/854 nm - 1/2456 nm = 1/1310 nm. As discussed in Sect. 2.1.3, there are six different schemes for PPQFC available, each with certain advantages and disadvantages. However, it has been shown that only the single-crystal Mach-Zehnder configuration is feasible for our specific wavelength combination for several technical reasons: all two-crystal schemes can be disregarded since only one WG chip was available at the beginning of the project. The double-pass configuration requires polarization-independent guiding and efficient recoupling of both polarization components of all three fields simultaneously. Several tests with light at 854 nm revealed that the WG supports both polarizations, but the intensity distribution of the two orthogonally-polarized spatial modes are quite dissimilar; most likely

caused by a non-square WG cross section. This renders simultaneous recoupling of both modes almost impossible. The Sagnac configuration requires a PBS, which operates at 854 nm, 1310 nm and 2456 nm. Such a PBS is quite difficult to manufacture, since the polarization-splitting layer has to be designed to possess similar Brewster angles for three widely separated wavelengths. Moreover, light at 2456 nm is considerably absorbed by the glass substrate and the reflecting layer [228]. Apart from this, all schemes except the SCMZC need twice the pump power at 2456 nm (about 2 W in total). Since the pump laser system delivers only 1 W, conversion efficiencies would be reduced approximately by a factor 2/3. Based on these findings, we chose the SCMZC for this particular wavelength combination.

3.1.1 Implementation of PPQFC in a single-crystal Mach-Zehnder configuration

In this section we present a detailed description of the experimental setup and the main components as well as their characterization. Fig. 3.1 illustrates a schematic representation of the complete setup.

Nonlinear waveguide

The heart of the converter is a zinc-doped periodically-poled lithium niobate (Zn:PPLN) ridge waveguide chip designed for the DFG-process 1/854 nm - 1/2456 nm = 1/1310 nm (*NTT Electronics*). The 40 mm long chip consists of 12 ridge WGs with lateral dimensions of 9 µm × 16 µm. They are arranged in six groups with different poling periods ranging from 22.60 µm to 22.85 µm in steps of 50 nm. The two WGs in each group differ slightly in their width. Both end facets are polished and possess anti-reflective (AR) coatings for all three wavelengths to minimize reflection losses. To achieve phase-matching, the WG temperature can be tuned and actively stabilized by means of a Peltier element. Precise positioning of the chip with respect to the coupling lenses is possible with a 5-axis translation stage. This particular chip was already utilized in the polarization-dependent version of this converter constructed by A. Lenhard; hence temperature tuning properties, spectra of down-converted photons, spatial mode profiles and further details regarding the nonlinear material can be found in his PhD thesis [169]. Note that throughout this work we always employed the second WG in the third group ($\Lambda = 22.70\,\mu m$) at an operating temperature of $T = 31\,^{\circ}C$.

Pump laser at 2456 nm

Efficient down-conversion to the O-band - both for single photons and for classical light - relies on the performance of the continuous-wave (cw) pump laser at 2456 nm, which has to meet certain requirements:

(I) An output power of at least 1 W to achieve maximum conversion efficiency.

(II) A spatial single-mode operation to guarantee efficient coupling to the fundamental WG mode.

(III) A narrow linewidth on the time-scale of the single photon wavepacket to avoid altering its linewidth or temporal shape. A kHz linewidth on microsecond time-scales would be desirable.

While the requirements can be easily fulfilled in the visible (VIS) or short-wave part of the near-infrared spectral region where diode and solid-state lasers are well-established, it is more challenging at 2456 nm. At the beginning of the 854 nm-conversion project the only solution was an optical parametric oscillator, a device that has been used already in former QFC experiments in our group [134, 137] (nowadays Cr^{2+}:ZnSe/S-based solid-state lasers are commercially available and implemented in recent QFCDs in our group [148, 156, 225]). Here we employ a home-built OPO delivering 1 W of single-mode, single-frequency output power at 2456 nm. The OPO is pumped by a diode laser at 1081 nm (DL Pro, *Toptica Photonics*) amplified with an ytterbium-doped fiber amplifier (*LEA Photonics*) with 15 W maximum output power. The OPO consists of a 40 mm long PPLN crystal inside a signal-resonant bow-tie ring cavity. Tuning of the idler wavelength from 2310 nm to 2870 nm is achieved by changing the poling period, the crystal temperature or the cavity length via a piezo actuator. The tuning range allows for covering the whole telecom O-band from 1260 nm to 1360 nm with the converted light. Note that the OPO system described in [169] has been completely disassembled after a total failure of the ytterbium-doped fiber amplifier. Afterwards we revised the optical and mechanical design of the OPO. The latest version of the setup and its optical properties are presented in Appendix B.

Frequency converter setup

As mentioned in Sect. 2.1.3, the idea to overcome the polarization selectivity of the DFG-process using a single-crystal Mach-Zehnder configuration is a polarization interferometer, which is illustrated in Fig. 3.1 and works as follows: arbitrarily polarized input light at 854 nm is coupled out of a SM fiber and split into H- and V-polarized components by a PBS. Subsequently, a HWP rotates the not convertible H-polarized light by 90° to V. Both beams are coupled via dichroic mirrors (*Layertec*), featuring high reflectivity (HR) for 854 nm and high transmission (HT) for 1310 nm and 2456 nm, into the same WG from opposite directions. To focus the free-space beam to the fundamental WG mode, we employ aspheric lenses (AL) made of zinc selenide with a focal length of 11 mm and a broadband AR-coating for all three wavelengths on both sides (*II-VI Infrared*). Zinc selenide is the material of choice in this case because of lower absorption losses at 2456 nm ($< 1\,\%$ per lens) compared to standard glass.
The pump field is guided in free-space from the OPO to the converter. In fact, a single-mode (SM) fiber to clean-up the spatial mode would be desirable, but mid-IR fibers are expensive, lossy (≈ 0.2 dB/m) and require expensive optics for in-/outcoupling. The beam passes a combination of an HWP and a rutile polarizer for power control and to align the polarization to V. To achieve best possible coupling to the fundamental mode, we employ a magnifying telescope made of two AR-coated spherical calcium fluoride (CaF_2) lenses. A 1600 nm longpass filter acts as clean-up filter to remove background at the single-photon level around the target wavelength. Since we intend to

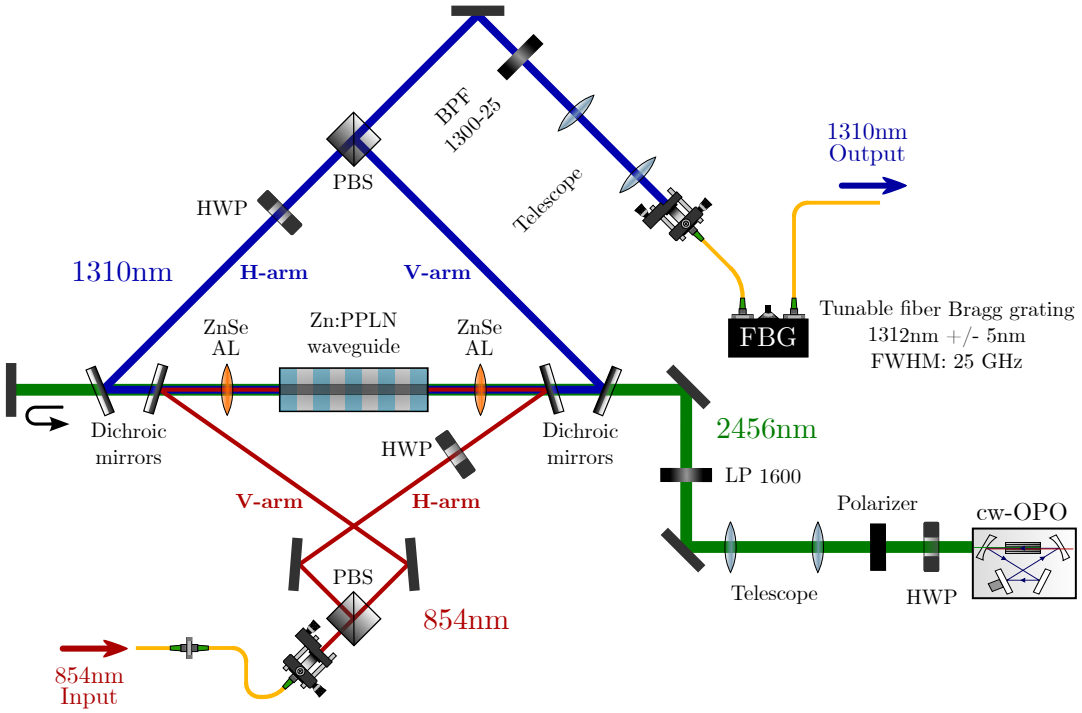

Figure 3.1. Setup of the Mach-Zehnder-type PPQFC. Schematic illustration of the setup for polarization-preserving quantum frequency conversion from 854 nm to the telecom O-band at 1310 nm in a single-crystal Mach-Zehnder configuration. All essential components are shown. Further details on the setup are given in the main text. The optical setup of the continuous-wave optical parametric oscillator (cw-OPO) can be found in Appendix B. Abbreviations: HWP: half-wave plate, PBS: polarizing beamsplitter, LP: longpass filter, ZnSe AL: zinc selenide aspheric lens, Zn:PPLN: zinc-doped periodically-poled lithium niobate, BPF: bandpass filter.

convert 854 nm light in the WG in both directions, the pump field needs to be aligned in double-pass configuration. To this end, the transmitted pump field is collimated, backreflected by a silver mirror, and recoupled to the same WG.
Both converted components are separated using dichroic mirrors (HR for 1310 nm and HT for 2456 nm) from the pump and superimposed on a second PBS after reversing the prior rotation from H to V with another HWP. Coupling into a SM fiber (SMF-28e+) is realized with an AR-coated aspheric lens ($f = 8$ mm) and a magnifying telescope for optimized mode-matching. Furthermore, we have two spectral filters for the converted light in the output arm, a free-space bandpass filter and a tunable fiber Bragg grating. We will discuss spectral filtering and CIB later in this section.

An obstacle limiting the device efficiency in nearly all existing QFCDs is the simultaneous coupling of multiple beams with different wavelengths to the WG fundamental mode. This is hindered by chromatic dispersion in the aspheric WG-coupling lenses resulting in wavelength-dependent focal lengths; e.g. for our ZnSe lenses we get $f_{854} = 10.423$ mm, $f_{1310} = 10.816$ mm and $f_{2456} = 11.014$ mm. Hence, we cannot achieve simultaneous

optimal coupling relying on collimated beams. In fact only one beam can be collimated while all others must be converging or diverging. In Sect. 3.2.2 we will present an advanced method to solve this problem, which requires precise knowledge of the initial beam parameters, though. Since a beam profiler working at wavelengths $>1700\,\mathrm{nm}$ was not available, the beam parameters of the pump beam could not be measured. Instead, we apply a brute-force method to align the QFC:

(I) We start by coupling 854 nm light in the H-arm to the WG. The advantage is that 854 nm can be conveniently visualized with infrared sensor cards; hence WG coupling is easily established from scratch. By monitoring the transmitted power and mode profiles, we optimize the lateral WG and AL positions to eliminate astigmatism.

(II) Next we couple the 2.4 µm beam to the WG exploiting the 854 nm light, which is already coupled, as guide beam. This step is the most challenging one because liquid-crystal sensor cards for 2.4 µm respond only slowly and weakly, and need a long time to recover. Besides, they do not visualize 854 nm, hence good overlap of both beams over long distances (several meters) is essential at this point. We found a coupling efficiency of only 60 % in the first try indicating that a telescope for beam shaping is necessary. Since the beam parameters were unknown, combinations of five standard spherical lenses (SL) with different focal lengths were tested. The best coupling efficiency of 89 % is achieved employing a magnifying telescope with focal lengths $f_1 = 75\,\mathrm{mm}$ and $f_2 = 100\,\mathrm{mm}$ of the lenses and a distance of 173 mm between them. Note that the distances between the WG and ALs are determined by the optimum for 2.4 µm and subsequently fixed. This has proven successful since 2.4 µm is by far the most inconvenient field in terms of beam characterization, beam shaping and handling.

(III) In the next step we align the pump in double-pass configuration by recoupling the transmitted beam into the same WG. To establish recoupling and to optimize its efficiency, a pellicle beamsplitter has proven quite helpful. It can be inserted into the incident beam to monitor the recoupled power without causing aberrations or beam displacement. From this we estimate a recoupling efficiency of approximately 96 %.

(IV) With the pump beam aligned we optimize the 854 nm coupling to the WG. Unfortunately, the distances between ALs and WG are unknown, i.e. we cannot calculate the best beam parameters by means of matrix optics. On top of this, the beam parameters of incident and transmitted pump beam are dissimilar since the WG acts as spatial mode filter. Thus, the respective distances between the two ALs and the WG are slightly different. The consequence is an asymmetry in the setup certainly being a disadvantage of the SCMZC. We know that both pump beams are almost collimated, i.e. the distance between ALs and WG is roughly f_{2456}. Thus, high coupling efficiencies for 854 nm require non-collimated beams. To achieve optimal coupling, we tested a series of ALs for fiber-outcoupling available from Thorlabs (ranging from $f = 4.5\,\mathrm{mm}$ to $f = 15.3\,\mathrm{mm}$). For each lens

we varied the distances between AL and fiber facet as well as between the WG-coupling AL and the fiber-coupling AL to generate a non-collimated beam with the correct divergence and a focal point at the correct position. With the best combination consisting of an AL with $f = 13.86\,\text{mm}$ (C560TME-B, *Thorlabs*) and a distance between both lenses of 745 mm, we achieve coupling efficiencies of 79.7 % (78.2 %) for the H(V)-arm. The limiting factor is most-likely the non-perfect overlap between the Gaussian input mode and the elliptical mode of the WG. A further improvement might be possible with telescopes made of cylindrical lenses, which is in our setup complicated due to space limitations in the 854 nm beam path.

(V) Finally, we repeat the same alignment procedure for the converted light. The best solution would be to measure all beam parameters with a beam profiler and calculate the best combination of lenses and distances. However, the beam profiler was broken and under repair at that time. It turned out to be the simplest solution to use another magnifying telescope ($f_1 = 35\,\text{mm}$ and $f_2 = 100\,\text{mm}$, $d_{\text{SL-SL}}$: 201 mm) in order to collimate the beam. Subsequently, the converted light is coupled into a telecom fiber using an AL with $f = 8\,\text{mm}$ (A240TM-C, *Thorlabs*). We measure fiber-coupling efficiencies of 82.0 % (77.8 %) for the H(V)-arm, again limited by the elliptical WG mode as well as the asymmetry of the setup.

External device efficiency

An important figure of merit of QFCDs is the conversion efficiency, whereby two measures are well-established: the external device efficiency (EDI) η_{dev} already mentioned in Sect. 2.3 and the internal conversion efficiency η_{int}. The latter gives the probability that an input photon is converted to a target photon within the nonlinear WG. Hence, it gives an idea of the spatial mode overlap between pump and input field as well as transmission losses in the WG. We mentioned in Sect. 2.1.1 that we are only interested in photon-to-photon conversion efficiencies, i.e. if we compare macroscopic intensities of classical light measured with calibrated power meters, we need to take the wavelength ratio into account. Accordingly, the EDI, which includes all optical losses and non-perfect efficiencies in the setup, is defined as

$$\eta_{\text{dev}} = \frac{P^{1310}_{\text{output fiber}}}{P^{854}_{\text{input fiber}}} \cdot \frac{\lambda_{1310}}{\lambda_{854}}. \tag{3.1}$$

Fig. 3.2a shows the external device efficiencies of both interferometer arms $\eta_{\text{dev,H}}$ and $\eta_{\text{dev,V}}$ in dependence on the pump power P at 2456 nm. The data points can be fitted quite well by the theoretical curve (Eq. 2.13)

$$\eta_{\text{dev}}(P) = \eta_{\text{dev,max}} \cdot \sin^2\left(\sqrt{\eta_{\text{nor}} P}\, L\right). \tag{3.2}$$

In a perfectly symmetric setup with respect to forward and backward conversion, we would expect the two curves to overlap. Unfortunately, the setup is not fully symmetric:

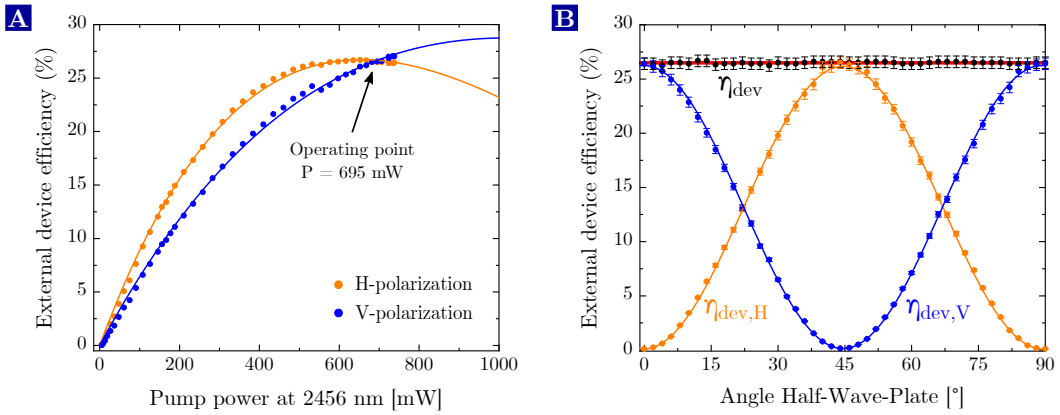

Figure 3.2. External device efficiency. **(A)** Measurement of the external device efficiencies $\eta_{\mathrm{dev,H}}(\eta_{\mathrm{dev,V}})$ with H(V)-polarized 854 nm input light at different pump powers P (measured behind the rutile polarizer). The data are fitted according to Eq. 2.13. The converter operates at the intersection point ($P = 695\,\mathrm{mW}$) where $\eta_{\mathrm{dev,H}}$ and $\eta_{\mathrm{dev,V}}$ equal 26.5 %. **(B)** The external device efficiencies measured for different linear input polarizations with a fixed pump power of 695 mW. As expected the device efficiency η_{dev} is - within the error bars - independent of the input polarization, while $\eta_{\mathrm{dev,H}}(\eta_{\mathrm{dev,V}})$, which are obtained by blocking the opposite interferometer arm, obey $\sin^2(\cos^2)$-functions.

due to absorption losses in the lenses and dichroic mirrors behind the WG, the backward-propagating pump power is lower. Thus, the curve of the V-polarized arm (blue data points) is shifted to higher pump powers. Nevertheless, we identify an operating point at the intersection of both curves, which ensures equal EDIs of 26.5 % for H- and V-polarized light. Its absolute value is determined by a series of single efficiencies and transmissions, which we individually measured with classical light to identify the major sources of loss. We separately investigate both polarization components since most single efficiencies and transmissions are dissimilar due to the asymmetric setup. All individual efficiencies/transmissions of both arms are listed in Tab. 3.1. For H-polarized light the EDI is given by

$$\eta_{\mathrm{dev,H}} = \eta_{\mathrm{int,H}} \cdot \eta_{\mathrm{wg,H}} \cdot T_{\mathrm{dichroic,H}} \cdot T_{\mathrm{bpf}} \cdot T_{\mathrm{optics,H}} \cdot \eta_{\mathrm{fiber,H}} \cdot T_{\mathrm{fbg}} \cdot f_{\mathrm{asym}} = 26.5(2)\,\%. \quad (3.3)$$

For the internal efficiency $\eta_{\mathrm{int,H}}$ we find 96.6(5) %. Note that such a measurement is typically prone to errors since it is estimated from the efficiency measured behind the AL and accordingly necessitates to precisely determine the transmissions of the ALs. However, if we compare $\eta_{\mathrm{int,H}}$ with the signal depletion of 97.4 %, which is an upper bound of $\eta_{\mathrm{int,H}}$, the measured efficiency seems to be realistic within the error bars. The WG and fiber coupling efficiencies already mentioned above are represented by $\eta_{\mathrm{wg,H}}$ and $\eta_{\mathrm{fiber,H}}$. $T_{\mathrm{dichroic,H}}$ denotes the joint transmission and reflection losses of the three dichroic mirrors (1x reflection of 854 nm, 1x transmission of 1310 nm and 1x reflection of 1310 nm). The rather poor transmission of 81.6 % is explained by non-standard angles of incidence (AOI), for which the dielectric coatings are not optimized (all coatings are designed for 45° AOI). Further transmission losses are introduced by the bandpass-filter with $T_{\mathrm{bpf}} = 97.1\,\%$ and the fiber Bragg grating with $T_{\mathrm{fbg}} = 69.5\,\%$. All

Table 3.1. Individual efficiencies and transmissions of the H- and V-arm of the O-band converter.

Efficiency/transmission	Abbreviation	H-arm	V-arm
Internal conversion efficiency	η_{int}	96.6(5) %	89.6(5) %
Waveguide coupling efficiency	η_{wg}	79.7 %	78.2 %
Dichroic mirror transmission	T_{dichroic}	81.6 %	86.6 %
Bandpass filter transmission	T_{bpf}	97.1 %	
Optical elements transmission	T_{optics}	82.5 %	83.6 %
Fiber coupling efficiency	η_{fiber}	79.7 %	77.8 %
Fiber Bragg grating transmission	T_{fbg}	69.5 %	
Asymmetry-correction factor	f_{asym}	92.4 %	–

transmission losses in the remaining optical elements (fiber coupling lenses, ZnSe-lenses, polarizing beamsplitters, telescope lenses, etc.) are combined in $T_{\text{optics,H}}$. Although each element has a fairly high transmission ($> 98\,\%$), the large number of elements results in a significant contribution of $T_{\text{optics,H}} = 82.5\,\%$. Eventually, the H-arm features a slightly higher device efficiency due to the asymmetric setup. To ensure an equal conversion efficiency for both polarization components, we deliberately decrease the efficiency with the second HWP. We account for this with an asymmetry-correction factor $f_{\text{asym}} = 92.4\,\%$. Note that another possibility would be to increase the pump power, however, we observed an unstable operation of the OPO at higher powers.
The external conversion efficiency of the V-polarized arm is calculated in an analogous manner, yielding

$$\eta_{\text{dev,V}} = \eta_{\text{int,V}} \cdot \eta_{\text{wg,V}} \cdot T_{\text{dichroic,V}} \cdot T_{\text{bpf}} \cdot T_{\text{optics,V}} \cdot \eta_{\text{fiber,V}} \cdot T_{\text{fbg}} = 26.6(2)\,\%. \quad (3.4)$$

Comparing the numbers of both arms (see Tab. 3.1), dissimilar T_{dichroic} and a decreased internal efficiency of the V-arm catches the eye, while all other efficiencies and transmissions only reveal slight variations. The decrease of $\eta_{\text{int,V}}$ is caused by a reduced amount of pump power in the backward-propagating direction being directly apparent in Fig. 3.2a: at the operating point the blue curve has not yet reached the maximally attainable efficiency.

As a first test towards polarization-preserving operation we will prove that the EDI is independent of the input polarization. To this end, we operate the converter at 695 mW pump power to ensure equal efficiencies for H- and V-polarization. Next we choose a linear input polarization and rotate it in the HVDA-plane of the Poincaré-sphere (the equatorial plane in Fig. 2.8a) using a HWP. Fig. 3.2b illustrates the EDI (black data points) as well as the individual device efficiencies per arm (orange and blue data points) for different HWP angles (the 90°- rotation of the HWP corresponds to a 360°- rotation in the HVDA-plane). As desired η_{dev} is independent of the input polarization within the error bars, which is confirmed by a fit with a constant function

(red solid line). In contrast, the efficiencies per arm, which we obtain by blocking the opposite arm, obey $\sin^2/\cos^2$-functions (orange/blue solid lines) as predicted by Malus' law. Note that this measurement does not prove polarization-preserving operation, yet. It does not contain any information about the phase relation between H and V, hence we cannot make any assumption whether the converter preserves superpositions of H and V.

Conversion-induced background

A figure of merit at least as important as the EDI is the amount of CIB. Fortunately, our wavelength combination is quite beneficial in terms of background due to three aspects: first, we operate in the long-wavelength pumping regime (cf. Sect. 2.1.2). Second, the 2.4 µm pump field is spectrally separated by $-3560\,\mathrm{cm}^{-1}$ from 1310 nm. Although ASR background has been observed in lithium niobate at least until $-1600\,\mathrm{cm}^{-1}$, no further peaks appear beyond $-1600\,\mathrm{cm}^{-1}$. Since the ASR rate exponentially decreases with the energy difference (Sect. 2.1.2), we claim that ASR background is negligible around 1310 nm. Third, we are able to separate the strong pump field itself quite easily from the converted light by means of standard bandpass filters due to the large spectral distance and its location in the long-wave part of the NIR. The background spectrum between 900 nm and 1700 nm of this particular WG has been investigated already by A. Lenhard in his PhD thesis. He identified a plethora of peaks, which are attributed to nonlinear optical processes, e.g. SHG of the pump or cascaded processes (for details see Sect. 2.1.2 and [169]). Fortunately, no peaks appeared within a 20 nm window around 1300 nm. Nevertheless, we still observe a considerable amount of background in this region, which points towards a broadband background floor. The origin was never clarified, but one possible explanation is SR and/or SPDC background stemming from the frequency-doubled pump. To eliminate the majority of background sources, we utilize a multi-stage narrowband filter system consisting of the following parts:

(I) A 1600 nm longpass filter (*Edmund Optics*) to clean-up the pump light generated by the OPO. This is necessary to remove leaking OPO pump light at 1086 nm creating SR and SPDC background as well as light around the target wavelength generated in the OPO by undesired nonlinear processes.

(II) A broadband interference bandpass filter with a bandwidth of 25 nm (BPF, central wavelength: 1300 nm, *Edmund Optics*) in the output arm.

(III) A narrowband tunable fiber Bragg grating with a bandwidth of 25 GHz (FBG, central wavelength tunable from 1307–1317 nm, *Advanced Optics Solutions GmbH*).

The filter system enabled an unconditional background count rate of 7.98 cps measured at 695 mW of pump power without 854 nm input light. Note that detector dark-counts were separately measured and subtracted. If we take the detection efficiency of 70 % into account, we obtain a generated background count rate of 11.4 cps. We will see that it is sufficiently low for all experiments involving trapped-ion QNNs in Chap. 4 and 5. Note that "unconditional" implies in this context that we do not apply any time-gating

or -filtering, but we consider this value as a time-averaged count rate of detection events randomly distributed in time.

3.1.2 Path length stabilization

Polarization-preserving operation requires that not only the relative amplitude of arbitrary superpositions of H and V remains unaltered, but also their relative phase. This implies that the two individual pathways of the converter must be interferometrically stable on a sub-wavelength scale. To this end, we implement an active path length stabilization employing a PID loop: we send classical light generated by a frequency-stabilized laser through the interferometer, measure the acquired relative phase, and apply the feedback signal to a piezo actuator connected to one of the mirrors. A frequency-stabilized laser is advisable for this task, since we did not make special effort to balance the path length of the interferometer arms. Hence, frequency changes of the stabilization laser will shift the whole interference pattern to slightly different path length differences. For instance, an unbalance of 5 cm and a frequency change of 100 MHz leads to a 15 nm shift of the path length difference for a 854 nm laser, which already causes an error of roughly 2 % in the path length difference.
Before we take a closer look at the technical details, we need to understand how to obtain an interference signal, which we use as PID error signal. Although we routinely call our QFCD an interferometer, first-order interference is not observed behind the second PBS. While a standard interferometer features non-polarizing beam splitters, we have polarizing beam splitters and, accordingly, orthogonally polarized light in the arms, which does not reveal interference. Nevertheless, with some slight modifications we obtain an interference-like signal[1]. To calculate the signal, we employ Jones calculus: we start with diagonally polarized input light of power P; the corresponding Jones vector is $\vec{J}_{\text{inp}} = {}^1/\sqrt{2}\,(a,a)^T$ with $|\vec{J}_{\text{inp}}|^2 = |a|^2 = P$. The interferometer introduces a time-dependent phase shift $\phi(t) = \frac{2\pi}{\lambda}\Delta s(t)$ between H and V due to fluctuations of the path length difference $\Delta s(t)$. We calculate the Jones vector behind the second PBS with the Jones matrix M_{Phase} to

$$\vec{J}_{\text{PBS}} = M_{\text{Phase}} \cdot \vec{J}_{\text{inp}} = \frac{1}{\sqrt{2}} \begin{pmatrix} a \\ a e^{i\phi(t)} \end{pmatrix} \quad \text{with} \quad M_{\text{Phase}} = \begin{pmatrix} 1 & 0 \\ 0 & e^{i\phi(t)} \end{pmatrix}. \tag{3.5}$$

The trick to obtain an interference-like signal is to insert a quarter-wave plate (QWP) behind the PBS, aligned at 45° with respect to the horizontal plane (alternatively a HWP aligned at 22.5°), followed by another PBS. The QWP acts as follows:

$$\vec{J}_{\text{QWP}} = M_{\text{QWP,45}} \cdot \vec{J}_{\text{PBS}} = \frac{1}{\sqrt{2}} \begin{pmatrix} 1 & -i \\ -i & 1 \end{pmatrix} \cdot \vec{J}_{\text{PBS}} = \frac{1}{2} e^{i\frac{\phi(t)}{2}} \begin{pmatrix} a e^{-i\frac{\phi(t)}{2}} + a e^{i\frac{\phi(t)}{2} - i\frac{\pi}{2}} \\ a e^{-i\frac{\phi(t)}{2} - i\frac{\pi}{2}} + a e^{i\frac{\phi(t)}{2}} \end{pmatrix} \tag{3.6}$$

[1] A more precise denomination for our setup would be "polarization interferometer" to avoid confusion with "normal" interferometers. However, for the sake of simplicity we just call it interferometer since the polarization interference and the normal interference signals have the same shape and properties.

The last PBS splits H- and V-components of $\vec{J}_{\mathrm{QWP}}$; if we measure the output power P_{H} and P_{V} in both ports we get

$$P_{\mathrm{H}} = \left|\frac{1}{2}e^{i\frac{\phi(t)}{2}}\left(ae^{-i\frac{\phi(t)}{2}} + ae^{i\frac{\phi(t)}{2}-i\frac{\pi}{2}}\right)\right|^2 = \frac{1}{2}P\left(1+\sin(\phi(t))\right) \quad \text{with} \quad P = |a|^2,$$
$$P_{\mathrm{V}} = \left|\frac{1}{2}e^{i\frac{\phi(t)}{2}}\left(ae^{-i\frac{\phi(t)}{2}-i\frac{\pi}{2}} + ae^{i\frac{\phi(t)}{2}}\right)\right|^2 = \frac{1}{2}P\left(1-\sin(\phi(t))\right). \tag{3.7}$$

This is exactly what we want, namely an output signal which depends on the path length difference. However, P_{H} and P_{V} are still sensitive to the overall power of the stabilization laser and therefore prone to errors. A power insensitive measure is the contrast

$$C = \frac{P_{\mathrm{H}} - P_{\mathrm{V}}}{P_{\mathrm{H}} + P_{\mathrm{V}}} = \sin(\phi(t)) = \sin\left(\frac{2\pi}{\lambda}\Delta s(t)\right), \tag{3.8}$$

which solely depends on the path length difference. Note that Eq. 3.8 is only valid if both photodetectors feature balanced efficiencies and no offset voltages (e.g. caused by stray light). In case of different efficiencies $\eta_{\mathrm{pd1/2}}$ and offset voltages $v_{\mathrm{off1/2}}$, P is replaced by $\eta_{\mathrm{pd1/2}}P + v_{\mathrm{off1/2}}$ and the contrast is computed to

$$C = \frac{P\left(\Delta\eta + \bar{\eta}\sin(\phi(t))\right) + \Delta v + \bar{v}\sin(\phi(t))}{P\left(\bar{\eta} + \Delta\eta\sin(\phi(t))\right) + \bar{v} + \Delta v\sin(\phi(t))} \tag{3.9}$$

with $\Delta\eta = \frac{\eta_{\mathrm{pd1}}-\eta_{\mathrm{pd2}}}{2}$, $\bar{\eta} = \frac{\eta_{\mathrm{pd1}}+\eta_{\mathrm{pd2}}}{2}$, $\Delta v = \frac{v_{\mathrm{off1}}-v_{\mathrm{off2}}}{2}$ and $\bar{v} = \frac{v_{\mathrm{off1}}+v_{\mathrm{off2}}}{2}$. We find a contrast with a reduced visibility, which is sensitive to fluctuations of the offset voltage and not independent of the power anymore. Thus, special effort should be made in the experiment to avoid those effects by means of stray light shielding, hard- or software based offset subtraction and gain balancing using neutral density filters and variable-gain photodiodes.

To meet the first requirement of the active stabilization, a frequency-stabilized laser, we rely on lasers from the ion trapping group. The idea is to utilize a laser which is not converted, but transmitted through the conversion setup. The light is supplied via a second SM800 fiber connecting the converter and the ion lab, i.e. available wavelengths are 850 nm, 729 nm and 866 nm. We performed tests with these lasers by coupling them into the interferometer via the second input port of the first PBS. Although the second part of the interferometer is optimized for 1310 nm, we got enough leakage to measure interference-like signals at the second output port of the second PBS. While the 850 nm laser was still converted with an efficiency of nearly 10^{-7} resulting in background at the single-photon level, and the 729 nm laser was reflected by the AR-coatings of the WG, the 866 nm laser worked out and revealed a proper interference signal.

However, we became aware of the main obstacle of this scheme while performing quantum process tomography with converted light: we observed drifts of the phase of the converted light on an hour time-scale. We identified frequency drifts of the pump laser as the main issue, since the phase of light generated via difference frequency generation is determined by the phase of input and pump light. If we change the

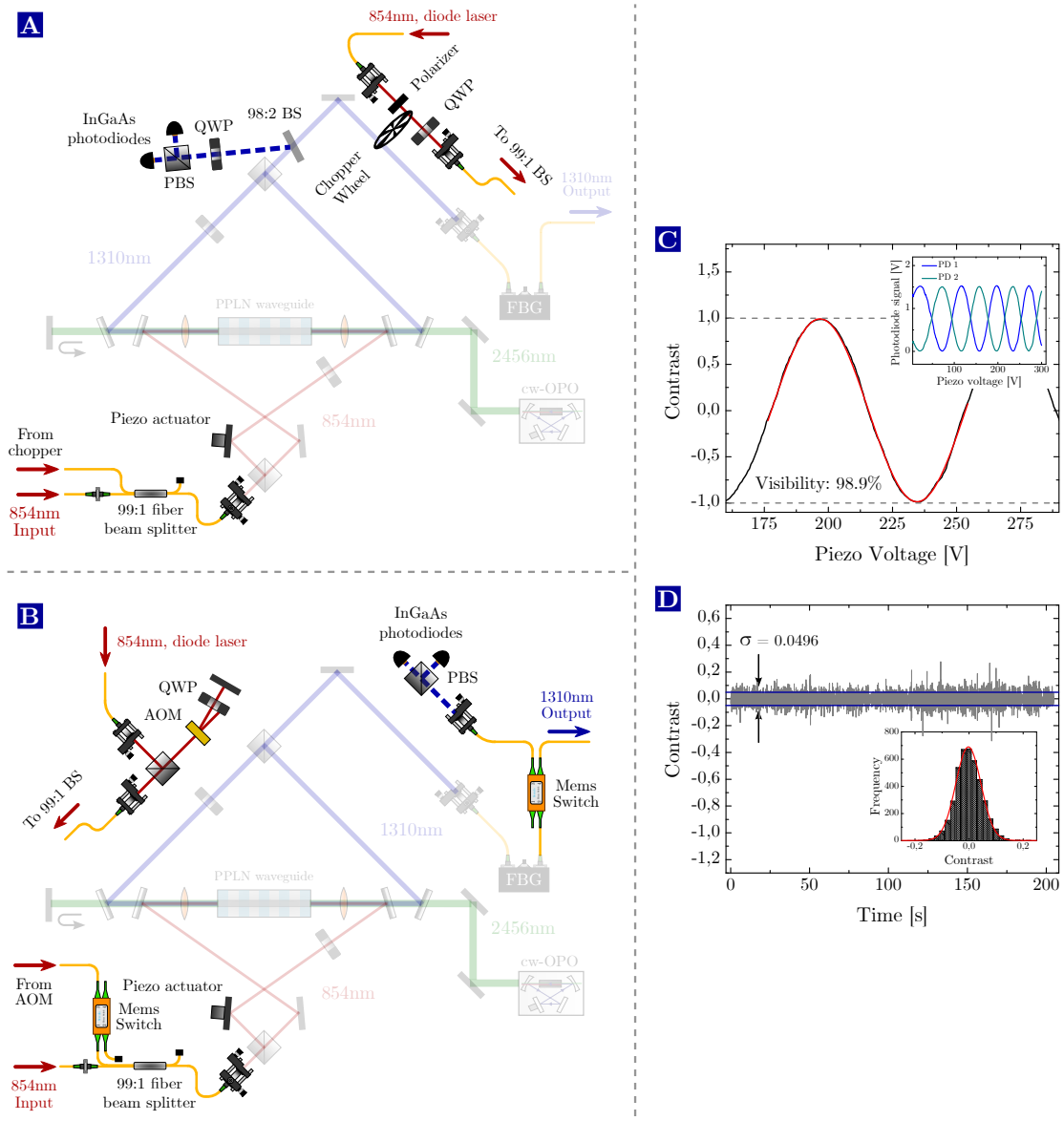

Figure 3.3. Path-length stabilization of the interferometer. **(A)**/**(B)** Schematic representations of the setups for active path length stabilization of the SCMZC. The setup in **(A)** has been utilized for all experiments in this chapter as well as the ion-telecom-photon entanglement in Chap. 4. The setup in **(B)** is a modified version to allow for synchronization to an external trigger, which is required for the atom-photon state transfer in Chap. 5. Details on the setups are explained in the main text. **(C)** The contrast at different piezo actuator voltages. A fit to the data reveals a visibility of 98.9 %. Inset: the raw signals of the two photodiodes, which are used to calculate the contrast. **(D)** displays the performance of the active stabilization. If the stabilization is switched on, the contrast obeys a Gaussian distribution around the setpoint (see inset) with a standard deviation of $\sigma = 0.0496$.

pump laser frequency, we also change the relative phase difference between the forward- and backward-propagating pump light in the WG since the backward-propagating light passes an additional 60 cm long free-space distance (in principle a similar effect as that for an unstabilized laser mentioned above). Thus, we imprint different phases on the converted light in the two arms even if the interferometer itself is stabilized. As an estimation: a π phase shift requires a 250 MHz frequency shift, which is definitely realistic for an unstabilized OPO.
To solve this issue, we can either stabilize the OPO frequency to a few MHz, or we use the 854 nm laser for stabilization since 854 nm will be down-converted and therefore acquires the correct phase shift. The first option is technically fairly difficult to realize, but the second option complicates the setup, too. To protect the single-photon detectors against the macroscopic intensities of the stabilization laser, we rely on a triggered scheme employing a chopper wheel as sketched in Fig. 3.3a. The 854 nm laser emerges from a SM fiber and passes through a homebuilt chopper wheel (manufactured from a blackened hard drive disk, rotation speed 10 Hz), which blocks single-photon path and laser path in an alternating way with a duty cycle of 87.5 % (10 %: laser path open, 2.5 %: both paths blocked). Polarizer and QWP guarantee a correct input polarization in the DARL-plane. The laser is coupled into the interferometer by a 99:1 fiber beam splitter with 99 % transmission for the single photons and 1 % for the laser. 2 % of the light is separated behind the second PBS with a bulk optic 98:2 beam splitter to measure the path length difference by means of a QWP, a PBS and two indium gallium arsenide (InGaAs) photodiodes (PDA10CS, *Thorlabs*). The analog output signals are acquired by a NI DAQ card (USB-6002, *National Instruments*), which also generates the analog PID output signal. The latter is amplified to 0-300 V with an high-voltage amplifier and applied to a ring piezo actuator (*Piezomechanik*) connected to one of the WG coupling mirrors in the 854 nm path. Data processing including the PID controller is implemented in Labview. Furthermore, data acquisition and PID calculation have to be synchronized with the chopper wheel; to this end an Arduino reads out the position sensor of the chopper wheel and sends a timed trigger pulse to the DAQ card.
Fig. 3.3c shows the contrast while the piezo actuator is tuned. A sinusoidal fit to the curve confirms the expected course and reveals a visibility of 98.9 %. The deviation from 100 % is most probably caused by slightly different detection efficiencies and a non-perfect input polarization, however, this is sufficient for our purpose. The photodiode output signals are displayed in the inset. As expected both signals follow $\sin^2$-functions and reveal a π phase shift with respect to each other. As locking point we choose the zero-crossing where the slope has its highest value. A time trace of the contrast over 200 s with active stabilization is depicted in Fig. 3.3d. We observe a Gaussian-distributed contrast around the locking point with a standard deviation of $\sigma_{\text{stab}} = 0.0496$. This translates - together with the measured visibility - to a phase uncertainty of $\pi \cdot 0.016$. In Sect. 3.1.4 we will thoroughly investigate how phase fluctuations impact the performance of QFCDs.
During the experiments with our trapped-ion QNN (Chap. 5), a further issue arose: stabilization laser light at 854 nm is reflected from the WG facet and coupled back into the single-photon input channel. This has proven critical in the atom-to-photon state

transfer since the light is resonant with the ion's respective dipole transition and therefore disturbs the protocol. A way out is to synchronize the stabilization to the sequence, i.e. during the stabilization cycle we perform laser cooling of the ion being unaffected by resonant 854 nm light. To this end, we need devices which we can switch on purpose, hence, we replaced the chopper wheel by an acousto-optic modulator (AOM) and two microelectromechanical (MEMS) switches as sketched in Fig. 3.3b. In detail, the 854 nm input path contains an AOM in double-pass configuration cascaded with a MEMS switch to suppress any leakage in the "off"-state. In the output arm, another MEMS switch guides the light either to the single-photon detectors or to the InGaAs photodetectors. A single MEMS switch (specified suppression >60dB) has proven to be sufficient to reduce the number of detected photons to <10. Note that the QWP in front of the PBS and photodiodes is not necessary since the required rotation is realized in the fiber. The performance of this stabilization scheme is the same as that of the chopper-based scheme.

3.1.3 Single-photon detectors for telecom wavelengths

In this section we briefly introduce our single-photon detectors for telecom wavelengths. All experiments in this thesis are performed with commercial superconducting nanowire single-photon detectors (SNSPD). The operating principle of our SNDPDs is as follows: the detector chip consists of a thin layer of niobium nitride (NbN) arranged as a meandering nanowire. A telecom fiber (SMF-28) is aligned right above the nanowires so that the whole fiber output can be absorbed by the meander structure. The nanowire chip is housed in a closed-cycle cryostat operating at 2.5 K in order to reach superconductivity. Now, a constant electrical bias current slightly below the critical current is applied to the wires. As soon as a single photon is absorbed by the meandering nanowires, the superconductivity quenches locally - leading to a so-called "hotspot" - which gives rise to a resistive region. This redirects the current to an amplifier connected in parallel (the amplifier has a much lower input impedance than the resistive region) and creates a voltage pulse serving as detection signal. Some advantages of SNSPDs compared to InGaAs avalanche photodiodes are the fast recovery time <10 ns after a detection event because of the small heat input, and the low timing jitter of ≈ 70 ps (record values are even below 10 ps [229, 230]). Moreover, the photon absorption process can be quite efficient and well-protected from the environment resulting in high system detection efficiencies (SDE) $>90\,\%$ and ultra-low dark-count rates (DCR) down to <1 cps [231]. Of course these advantages come at the cost of a larger technical overhead due to the cryogenic system. Further technical details on SNSPDs can be found in [232, 233].
Our current system (EOS, *Single Quantum*) hosts four detector chips within the cryostat, two of them specified with 75 % SDE at 1310 nm and a DCR of 300 cps, and two chips with 25 % SDE at 1310 nm and a DCR of 300 cps. However, SDE and DCR are tunable via the bias current applied to the nanowires, which is illustrated in Fig. 3.4: it displays the relative detection efficiencies (RDE) and DCR of the two highly efficient detector chips at 1310 nm (Fig. 3.4a & b) and 1550 nm (Fig. 3.4c & d) at different bias currents. Since we are not able to reliably measure absolute detection efficiencies, we only measure RDE, i.e. we send an arbitrary photon flux to the detector and re-

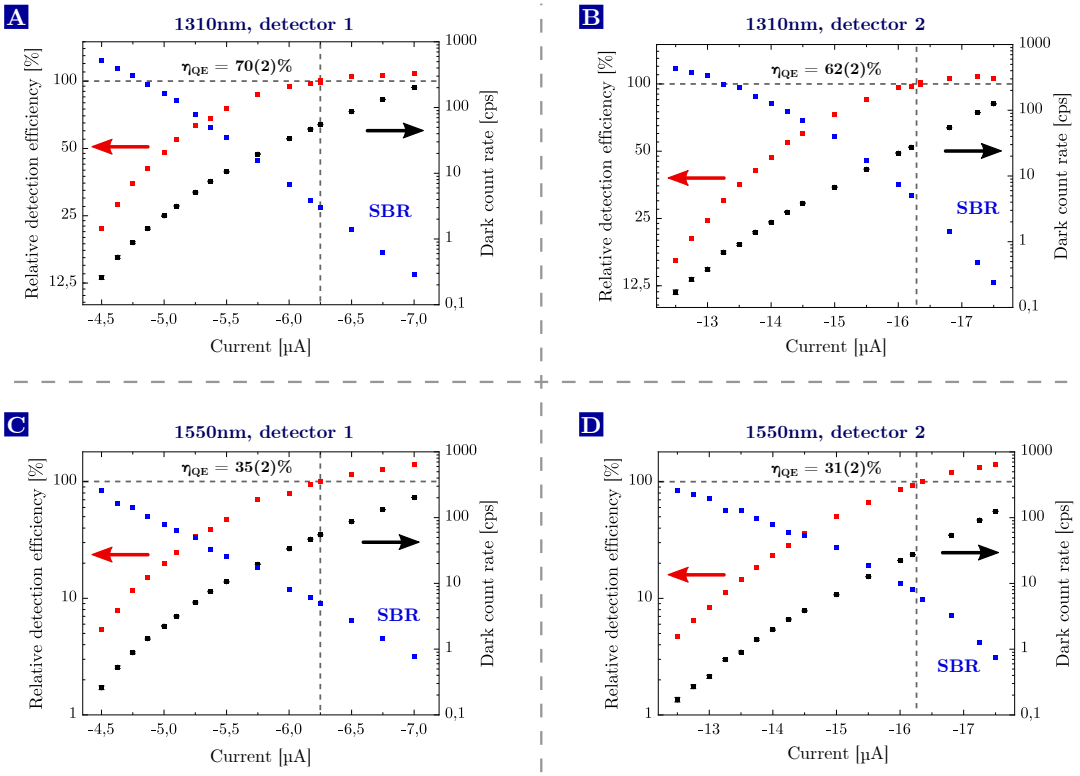

Figure 3.4. Properties of the SNSPDs for telecom photon detection. **(A)/(B)** Logarithmic plots of the relative detection efficiency at 1310 nm (RDE, red data points), dark-count rate (DCR, black data points) and SBR (blue data points) of the two highly-efficient detector chips at different bias currents. The SBR has no absolute scale (this depends on the brightness of the photon source), but it is solely the quotient of RDE and DCR to illustrate the theoretical case for a background-free single-photon input, e.g. from a trapped ion. The increase with lower bias currents is caused by a different scaling of RDE and DCR. **(C)/(D)** The same measurements at 1550 nm.

fer the detected count rate to the rate at one particular bias current, which we define as 100 %. At 1310 nm the absolute efficiency at this point is extracted from the data sheet. The values at 1550 nm are not specified, but an estimation from the manufacturer was provided. This estimation is consistent with observations made throughout several experiments performed in our group (either in this work or in [225]) by comparing measured and expected single-photon count rates. We find in Fig. 3.4, that RDE and DCR go down with lower bias currents, indeed, but their scaling differs. While the RDE at 1310 nm is reduced by one order of magnitude, the DCR is reduced by three orders. Thus, the signal-to-background ratio of the detector, which is proportional to the ratio between RDE and DCR, increases with decreasing bias currents (blue dots in Fig. 3.4). Note that the SBR has no absolute scaling, which would depend on the brightness of the single-photon source. We can interpret the blue dots as theoretical case of a photon input without constant background floor, e.g. a perfect single-photon source without QFC. In fact, this effect features an advantage: in case of dark-count

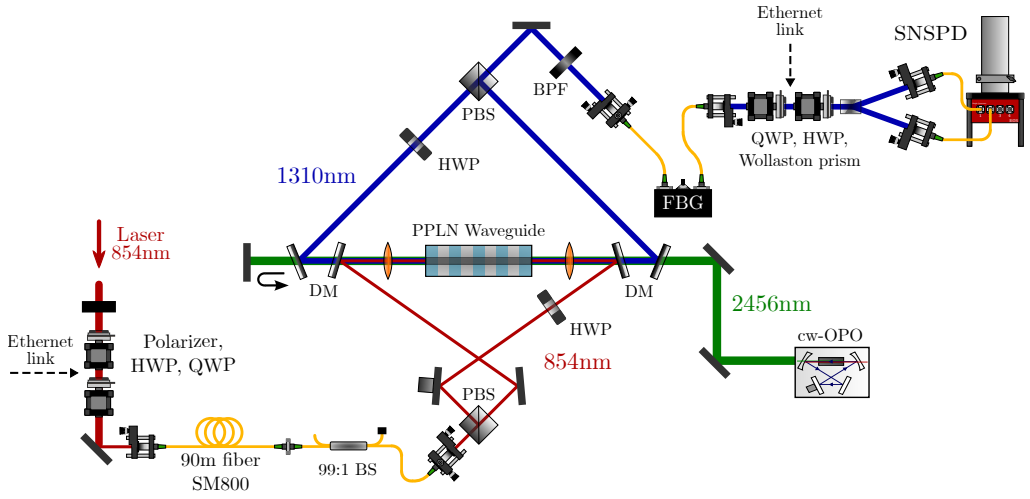

Figure 3.5. Setup for quantum process tomography. **(A)** Schematic experimental setup to perform quantum process tomography. Note that most components associated with the path length stabilization were omitted for the sake of simplicity.

sensitive measurements, the SBR can be considerably increased if we renounce the high detection efficiency and accept an increased measurement time. Unfortunately, the effect is much weaker (but still present) at 1550 nm because the detectors are optimized for 1310 nm and the photon energy, which is proportional to the heat input on the detector, is smaller at longer wavelengths.

3.1.4 Conversion of arbitrarily polarized light

To complete the O-band converter characterization, we demonstrate polarization-preserving conversion of arbitrarily polarized light by means of quantum process tomography, which we already introduced in Sect. 2.2.4. The schematic setup is depicted in 3.5: we generate input polarization states at 854 nm with a combination of polarizer, HWP and QWP. This combination allows for generation and projection of arbitrary polarization states since we are able to rotate any possible state on the Poincaré-sphere onto a certain linear polarization with rotatable HWP and QWP (in this order from the perspective of the polarizer). The waveplates are mounted on stepper motors (ST4118, *Nanotec*) and controlled by an Arduino with an angular resolution of 0.1125°. By sending commands to the Arduino via its serial interface or via an ethernet link, we can remotely change the waveplate angles. In particular the ethernet link has proven useful to control several motors in different labs from one PC. The 854 nm light is guided through a 90 m long fiber link connecting the ion and converter lab. Although the fiber passes through maintenance areas and entrance halls of the building that lack any air-conditioning, it has a remarkable stability with respect to unitary polarization rotations. This has been investigated in more detail in [169]. Behind the converter follows a free-space setup for projective measurements of the polarization state. Similar to the state preparation unit it consists of two ethernet-controlled zero-order waveplates, but

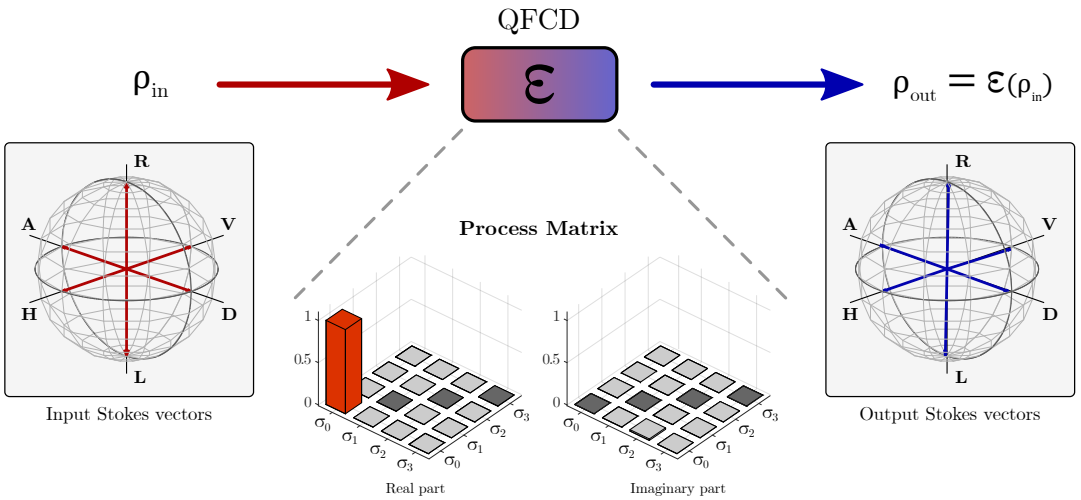

Figure 3.6. Principle and results of quantum process tomography. For quantum process tomography, a huge number of input states ρ_{in} at 854 nm in six different polarizations H, V, D, A, R & L (see Poincaré-sphere on the left) is prepared. For each input state, we measure the Bloch vector of the converted state by means of single-qubit tomography (Poincaré-sphere on the right). Subsequent maximum-likelihood estimation yields the process matrix. The red bar represents the identity operation, which is the only non-zero entry in case of an ideal process. Its value is denoted as process fidelity, yielding $\mathcal{F}_{pro} = 99.75(6)\,\%$.

employs a Wollaston prism (WP10-C, *Thorlabs*) instead of a polarizer. The latter is well-suited for projective measurements since both orthogonally polarized output beams possess a suppression of 10^{-5} for the complementary polarization (for comparison: typical values for PBS are 10^{-3} of the transmitted and 10^{-2} of the reflected beam). We couple both beams to AR-coated SM fibers connected to the SNSPDs. The SDE of the SNSPDs is polarization dependent, it can be reduced by up to 50 % for the wrong input polarization. Hence, we use homebuilt manual fiber polarization controllers to optimize for maximum SDE. Note that it is advisable that all waveplates in all labs are oriented in the same direction with respect to the optical axis, and have the same direction of rotation. Otherwise complex basis exchanges occur, which are potentially non-unitary and typically hard to debug.

Before we perform QPT, we need to correct for all unitary polarization rotations caused by the SM fibers and the QFCD, whose interferometer phase is not necessarily stabilized at the setpoint where the input phase is exactly preserved. To this end, we first measure the rotation matrix of the whole setup M_{rot} and multiply it to the Stokes vectors of the respective measurement bases, i.e. we perform QPT in a rotated measurement basis, which exactly compensates the unitary rotation of the setup. The rotations matrix is determined with classical light by sending 36 different polarization states equally distributed over the Poincaré-sphere through the setup and measuring the Stokes vector of each output state. A subsequent singular value decomposition yields the rotation matrix (details can be found in the appendix of [204]). QPT starts with the preparation of a huge number of photonic input states ρ_{in} at 854 nm in the six basis states ($|H\rangle$,

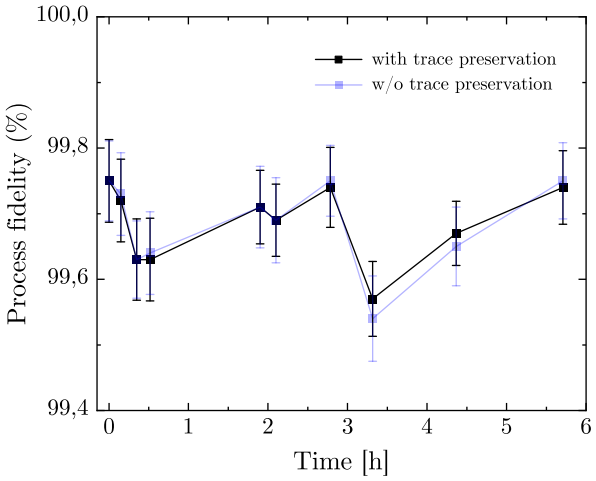

Figure 3.7. Long-term stability of the process fidelity. Measurement of the process fidelity over 6 hours, a typical time scale for experiments with trapped ions. The fidelities are reconstructed with and without trace-preservation to identify polarization-dependent loss.

$|V\rangle$, $|D\rangle$, $|A\rangle$, $|R\rangle$ & $|L\rangle$). The Stokes vectors of the input states are displayed as red arrows in the left Poincaré-sphere in Fig. 3.6. We attenuate the laser until the SNSPDs display count rates well above the DCR and measure the Stokes vector of the respective converted output states by means of single-qubit tomography. The reconstructed vectors are shown as blue arrows in the right Poincaré-sphere in Fig. 3.6. We find that the output Stokes vectors are only slightly distorted from the input vectors, which already suggests preservation of the polarization state with high fidelity. To quantify this, we reconstruct the process matrix, which is shown in Fig. 3.6. As desired the χ_{00}-entry corresponding to the identity operation (marked as red bar) is dominant while all other entries are close to zero. We know from Sect. 2.2.2 that the value of the χ_{00}-entry is identified as process fidelity; we find $\mathcal{F}_{\text{pro}} = 99.75(6)\,\%$, which verifies polarization-preserving operation with high fidelity. The error bars are deduced from Monte Carlo simulations assuming Poissonian statistics of the detected counts.

The experiments with trapped ions typically involve integration times of several hours, i.e. it is important to know if the process fidelity is sufficiently long-term stable. To this end, we record the process fidelity over a period of six hours. The result is shown in Fig. 3.7: we identify slight fluctuations of the fidelity between 99.75 % and 99.55 %, being most probably caused by polarization drifts in the 90 m long fiber or power fluctuations of the input light. Nevertheless, the fidelity does not drop below 99.5 % and returns to its original values, hence we cannot identify long-term drifts that progressively degrade $\mathcal{F}_{\text{pro}}$. For our reconstruction we assume equal conversion efficiencies of both polarization components, which implies a trace preserving process. It is conceivable, however, that for instance power fluctuations of the OPO or drifts in the coupling efficiency in one arm lead to polarization-dependent loss (PDL), which might cause errors in the reconstruction process. To quantify the impact of PDL, we also reconstruct the process matrix without the constraints for trace preservation. In Fig. 3.7 we only find slight

differences between both reconstruction methods, and those are in particular smaller than the error bars. Thus, we conclude that PDL is not the dominant error source in this case.

Robustness against phase and efficiency-ratio fluctuations

In this section we clarify the question whether the measured values of the process fidelity are limited by the QFCD itself or by external factors such as polarization drifts in the 90 m long fiber, the angular resolution of the waveplates, or the precision of our technique to compensate unitary rotations. Within the QFCD, we identify phase fluctuations stemming from the non-perfect active path length stabilization and drifts of the conversion efficiencies of both arms relative to each other as two possible error sources. The latter is interpreted as PDL or efficiency mismatch and is quantified by the ratio of the conversion efficiencies of H and V $\gamma_{\mathrm{eff}} = \eta_{\mathrm{dev,V}}/\eta_{\mathrm{dev,H}}$. To quantify their impact, we perform a series of simulations with their results displayed in Fig. 3.8. The general idea is to simulate process matrices for a QFCD being affected by the error sources mentioned above, and calculate with those matrices converted output states in case of a maximally entangled input state. From the output state we deduce purity and fidelity in order to assess the influence of the error sources. In detail, the simulation is carried out as follows:

(I) We assume a huge number of photons at the input wavelength sent through the converter. Each photon is initially in a maximally entangled Bell-state with another particle, e.g. a second photon or a trapped atom. Purity and Bell-state fidelity of the initial state ρ_{in} are accordingly 100 %.

(II) The first step is to simulate process matrices for unitary phase rotations and unequal conversion efficiencies of H and V. To this end, we proceed in a similar way as in QPT: we choose the six basis states $|H\rangle$, $|V\rangle$, $|D\rangle$, $|A\rangle$, $|R\rangle$ & $|L\rangle$ as input states and we mimic the action of the frequency converter by multiplying a Mueller matrix to the respective Stokes vectors in order to obtain the "converted" output states

$$\vec{S}_{\mathrm{out}}^{(1\ldots6)} = M_{\mathrm{PhRot/EffRat}} \cdot \vec{S}_{\mathrm{in}}^{(1\ldots6)}. \tag{3.10}$$

The Mueller matrices for unitary phase rotations around the x-axis ϕ_{x} and efficiency ratios γ_{eff} take the following form:

$$M_{\mathrm{PhRot,\,x}}(\phi_{\mathrm{x}}) = \begin{pmatrix} 1 & 0 & 0 & 0 \\ 0 & \cos(\phi_{\mathrm{x}}) & \sin(\phi_{\mathrm{x}}) & 0 \\ 0 & -\sin(\phi_{\mathrm{x}}) & \cos(\phi_{\mathrm{x}}) & 0 \\ 0 & 0 & 0 & 1 \end{pmatrix} \tag{3.11}$$

and

$$M_{\mathrm{EffRat}}(\gamma_{\mathrm{eff}}) = \eta_{\mathrm{dev,H}} \cdot \begin{pmatrix} 1/2\,(1+\gamma_{\mathrm{eff}}) & 1/2\,(1-\gamma_{\mathrm{eff}}) & 0 & 0 \\ 1/2\,(1-\gamma_{\mathrm{eff}}) & 1/2\,(1+\gamma_{\mathrm{eff}}) & 0 & 0 \\ 0 & 0 & \sqrt{\gamma_{\mathrm{eff}}} & 0 \\ 0 & 0 & 0 & \sqrt{\gamma_{\mathrm{eff}}} \end{pmatrix} \tag{3.12}$$

Note that the output Stokes vectors in case of efficiency ratios unequal to one have to be normalized to the overall intensity by dividing them through the first entry S_0

$$\vec{S}_{\text{out}}^{(1\ldots6)} = \vec{S}_{\text{out}}^{(1\ldots6)} / S_{0,\text{out}}^{(1\ldots6)}, \tag{3.13}$$

which mimics the post-selection process in a real experiment.

(III) Next, we reconstruct the process matrix χ with the six input and calculated output states by means of maximum-likelihood estimation. Unitary phase rotations are trace-preserving while efficiency mismatches are reconstructed without the constraints for trace preservation. Note that, although the output Stokes vectors are calculated and free of experimental imperfections, linear inversion as described in [205] fails in the case of non-trace-preserving process matrices.

(IV) Eventually, we calculate the density matrix of the converted output state ρ_{out} with the simulated process matrix χ according to Eq. 2.41. From ρ_{out} we compute the Bell-state fidelity $\mathcal{F}_{\text{out}} = \text{Tr}\left(\rho_{\text{out}} |\Psi\rangle \langle\Psi|_{\text{Bell}}\right)$ and the purity $\mathcal{P}_{\text{out}} = \text{Tr}\left(\rho_{\text{out}}^2\right)$, which are displayed in Fig. 3.8a-d on the y-axis. Note that in this particular case the Bell-state fidelity equals the process fidelity. Of course we cannot generalize this for arbitrary input states. For instance, the polarization state $|H\rangle$ is insensitive to PDL or phase drifts and therefore $\mathcal{F}_{\text{out}}$ remains unaltered although $\mathcal{F}_{\text{pro}}$ is smaller than one. We will see in Chap. 4 that a non-perfect process fidelity degraded by PDL might even improve the Bell state fidelity.

We start with the simulation of time-independent phase rotations; the results are depicted in Fig. 3.8a. As expected, the fidelity is 100 % for zero phase rotations and drops to zero for a π phase rotation. On the contrary, the purity remains constant since time-independent unitary operations do not degrade the purity. The absolute values of few exemplary process matrices are shown to illustrate how process matrices of unitary rotations look like. These results are not really surprising and could be easily obtained without an elaborate simulation, however, it verifies that our method delivers correct results. A more interesting case is represented in Fig. 3.8b. Now we assume that the interferometer phase fluctuates over time, being modeled by a Gaussian distribution with standard deviation $\Delta\phi_{\text{x}}$ and a mean value of zero. We obtain the output state by means of Monte Carlo simulations: we repeat steps **(II)** – **(IV)** 5000 times for each standard deviation $\Delta\phi_{\text{x}}$. In each step, the phase rotation ϕ_{x} is a random number deduced from the Gaussian distribution. The final density matrix entries from which fidelity and purity are calculated are the mean values of all 5000 individual entries. We find in Fig. 3.8b that the purity decreases for increasing phase uncertainty, too. The reason is that random phase fluctuations over time introduce mixedness and accordingly reduce the purity. The extreme case would be a random phase resulting in a statistical mixture with $\mathcal{P} = 1/4$. However, we find that fidelity and purity are rather robust against phase fluctuations. If we consider the standard deviation of the active path length stabilization of $\sigma_{\text{stab}} = \pi \cdot 0.016$ (cf. Sect. 3.1.2), we get $\mathcal{F}_{\text{phase}} = 99.94\,\%$ and $\mathcal{P}_{\text{phase}} = 99.88\,\%$, which is still remarkably high.

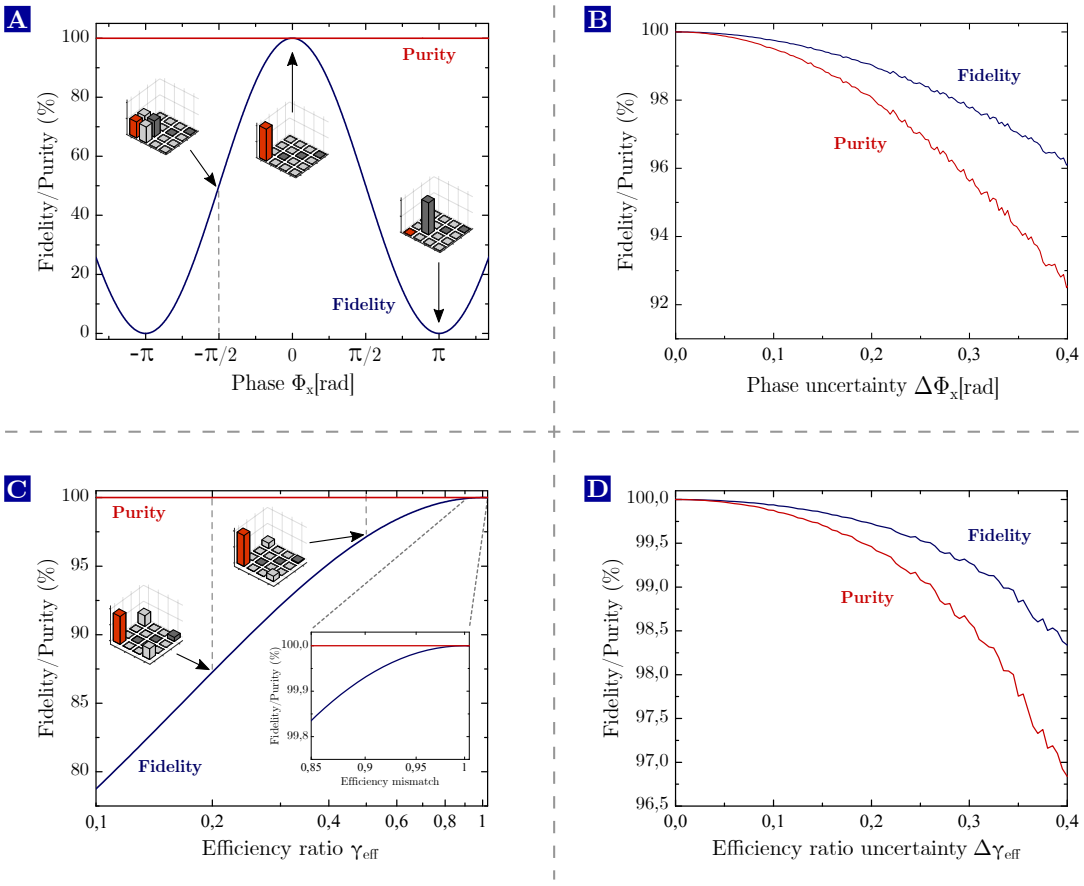

Figure 3.8. Robustness of fidelity and purity against phase and efficiency-ratio fluctuations. Simulations to quantify the impact of fluctuations of the interferometer phase ϕ_x and the ratio of conversion efficiencies of H and V $\gamma_{eff} = \eta_{dev,V}/\eta_{dev,H}$ on the fidelity and purity of entangled states. In all figures we assume that we send a photon through a QFCD, which is maximally entangled with another particle, i.e. initial purity and Bell-state fidelity are 100 %. Fidelity and purity on the y-axis accordingly denote those of the converted states calculated from the simulated process matrices. In this particular case the output fidelity is identical to the process fidelity. **(A)** shows fidelity and purity in dependence on constant phase differences along with a few exemplary process matrices. As expected, the fidelity equals zero for π phase shifts, while the purity is unaffected by constant phase differences since unitary operations do not decrease the purity. **(B)** Monte Carlo simulation of fidelity and purity assuming Gaussian-distributed phase fluctuations with a standard deviation $\Delta\phi$. Now the purity is also reduced because random phase fluctuations introduce mixedness. **(C)** The same situation as in **(A)** but for different efficiency ratios. **(D)** Monte Carlo simulation of fidelity and purity assuming Gaussian-distributed efficiency-ratio fluctuations with a standard deviation $\Delta\gamma_{eff}$.

We repeat similar simulations for different efficiency ratios starting again with the time-independent case. We observe in Fig. 3.8c that the purity remains constant as expected, while the fidelity drops for increasing γ_{eff}. To verify our results, we multiply γ_{eff} to the

light-matter Bell-state $|\Psi\rangle = \frac{1}{\sqrt{2}}(|H,\uparrow\rangle - |V,\downarrow\rangle)$ in the following way:

$$|\Psi\rangle_{\text{eff}} = \frac{1}{\sqrt{1+\gamma_{\text{eff}}^2}}(|H,\uparrow\rangle - \gamma_{\text{eff}} \cdot |V,\downarrow\rangle)\,. \tag{3.14}$$

If we calculate the Bell-state fidelity of this state, we get the same results as the simulation. The inset of Fig. 3.8c shows a magnification of the upper part for small γ_{eff}. Again we find a high robustness of the fidelity; $\mathcal{F}$ is still above 99.8 % for an efficiency ratio of 0.85. A worst-case number for the O-band converter observed in the experiments is a drop to 0.9 during one day caused by drifts of the OPO output power or the fiber/WG coupling efficiencies. This corresponds to a fidelity of $\mathcal{F}_{\text{eff}} = 99.93\,\%$. Finally, the dependence of fidelity/purity on Gaussian-distributed fluctuations of γ_{eff} (see Fig. 3.8d) is obtained by Monte Carlo simulation. Due to OPO output power fluctuations we estimate a standard deviation of $\Delta\gamma_{\text{eff}} = 0.02$ corresponding to a fidelity of $\mathcal{F} = 99.997\,\%$, i.e. the impact of this effect is negligible.
To conclude, we simulated that the O-band converter degrades the fidelity in the worst-case to $\mathcal{F} = \mathcal{F}_{\text{phase}} \times \mathcal{F}_{\text{eff}} = 0.9994 \times 0.9993 = 0.9987$, which is still higher than the absolute values and the long-term drifts of the measured process fidelities. Thus, we believe that the non-perfect initial fidelity is probably limited by the polarization compensation scheme: due to short integration times this scheme might be prone to laser power fluctuations. The loss of fidelity on long time-scales ($\approx$ hours) is caused most probably by polarization drifts in the fiber connecting the labs. However, those issues have not been investigated in more detail within this thesis.

3.2 Polarization-preserving QFC from 854 nm to the telecom C-band

We have seen that it is possible to achieve high-fidelity polarization-preserving operation of a QFCD with high efficiency and low background. We will prove that this is sufficient to serve as telecom interface for trapped-ion QNNs in Chap. 4 and 5, where we employ the O-band converter to demonstrate ion-telecom-photon entanglement and an atom-to-telecom-photon state transfer. However, if we assess the O-band converter with respect to our scaling criteria presented in Chap. 2.3, we identify some drawbacks. The first drawback is the cw-OPO at 2.4 µm: the wavelength is rather inconvenient in terms of handling and availability of SM fibers. Furthermore, the whole OPO system is anything but a turnkey system since we cannot adjust output power and wavelength in a convenient and reliable way. After switching off and on, both are different than before and typically cannot be restored to their original values. On top of this, the OPO is not protected from backreflected pump-light by means of an optical isolator, as none have been available at this wavelength. As a consequence mode-hops frequently occur, which frustrates frequency- and power-stable operation. In combination with a downtime of almost 50 % over the course of this thesis (mainly caused by several failures of the Yb-doped fiber amplifier) 24/7-operation is illusory. Note that the OPO could be replaced by a commercially available Cr^{2+}:ZnSe/S solid-state laser, which has proven itself in

24/7-operation [156]. However, also these lasers showed to be extremely sensitive to backreflections and not more stable in terms of frequency and output power than our OPO [225]. Another drawback of the O-band converter is the space requirement. OPO and converter require a complete optical table and the possibilities for miniaturization (e.g. to fit into a 19-inch rack) are fairly limited, thus, transportability is complicated to facilitate. For the integration in existing experiments a standalone system would be desirable. To this end, one wants to get rid of the path length stabilization, which causes issues such as leakage of stabilization light into the single-photon input channel or synchronization overhead.
Thus, we started in 2018 the construction of a new QFCD translating 854 nm to the telecom C-band via the DFG-process 1/854 nm - 1/1904 nm = 1/1550 nm. This particular wavelength combination has been already implemented by Krutyanskiy et al. in [164], from which we essentially adopted the choice of the pump laser and spectral filters. However, we employ a different configuration and improved the device in terms of device efficiency and background. The C-band converter features two key advantages: on the one hand, coherent light at 1904 nm is conveniently generated by a commercially available thulium-doped fiber laser system with sufficiently high power and good spectral properties. On the other hand, the device enables construction in an intrinsically phase-stable and symmetric Sagnac configuration, i.e. the experimental overhead is substantially reduced bringing standalone and miniaturized devices within reach.

3.2.1 Experimental setup

Sagnac interferometer

The schematic drawing of the setup is shown in Fig. 3.9. The core part is the Sagnac interferometer consisting of the WG chip, aspheric coupling lenses, HWP, four mirrors and a PBS. The latter is custom-made (*B. Halle Nachfl.*) in order to act as PBS for all three wavelengths and to minimize losses by means of broadband AR-coatings. Caused by a manufacturing-process related uncertainty of the thickness of the reflective layer, the optimal reflection angle with respect to extinction ratio is not necessarily 90° (corresponding to 0° AOI) [228]. We measured the appropriate extinction ratios $\gamma_{ex,t} = T_H/T_V$ ($\gamma_{ex,r} = R_V/R_H$) of the transmitted (reflected) output port for all three wavelengths in dependence on the AOI. We find an optimum at 0° (by chance) where all γ_{ex} are > 200 except for $\gamma_{ex,r,854} = 175$ and $\gamma_{ex,r,1904} = 73$. In fact, the non-perfect extinction ratios do not degrade the process fidelity but only the conversion efficiency. If we assume for instance $\gamma_{ex,r,854} = 100$, the reflected port contains 1 % of the "wrong" polarization component. However, this fraction is not repolarized by the PBS but possesses still its original polarization [228]. Hence, the polarization selectivity of the DFG-process inhibits frequency conversion, which reduces the efficiency but avoids undesired polarization mixing.
All mirrors in the Sagnac interferometer are silver-coated mirrors being reflective over a broad wavelength range as well as less angular sensitive and expensive than custom-made dielectric mirrors; of course at the cost of slightly reduced reflectivities. It follows an achromatic HWP (700-2500 nm, *B. Halle Nachfl.*) in the H-arm and two WG coupling

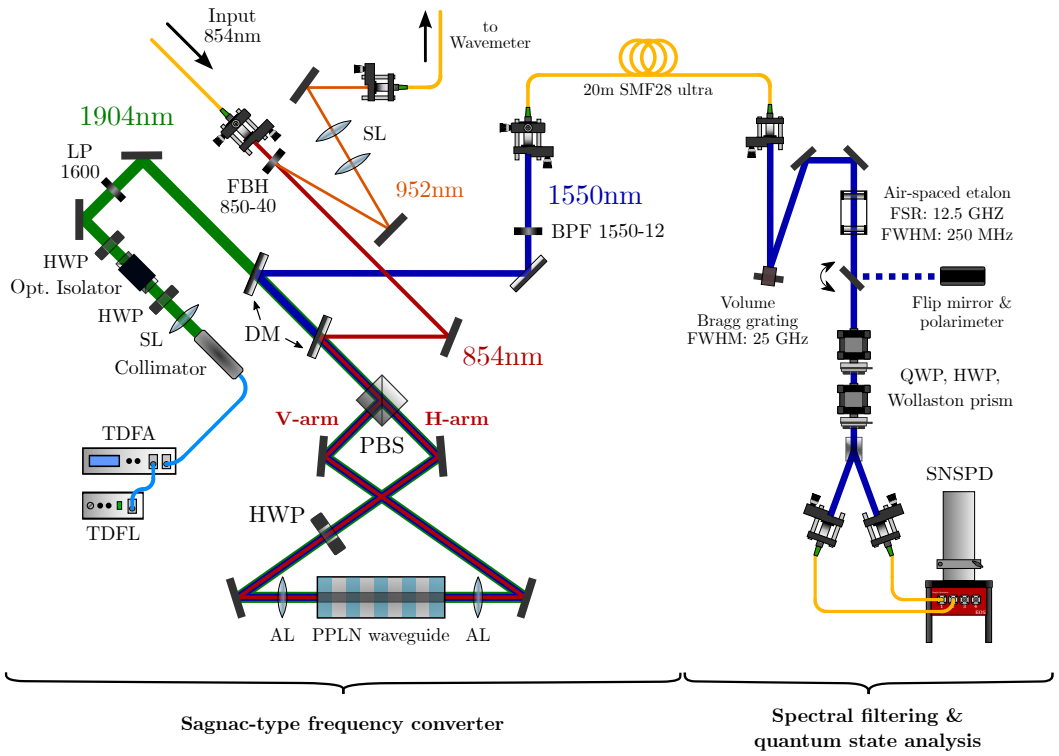

Figure 3.9. Setup of the Sagnac-type PPQFC for $^{40}Ca^{+}$-ion wavelengths. Schematic representation of the setup for PPQFC from 854 nm to the telecom C-band at 1550 nm in a Sagnac configuration. New abbreviations: TDFL: thulium-doped fiber laser, TDFA: thulium-doped fiber amplifier.

ALs made of glass with focal length $f = 11$ mm and custom AR-coatings for all involved wavelengths (*Layertec*). The Zn:PPLN ridge WG chip is quite similar to that used in the O-band converter, i.e. a 40 mm long crystal with 12 WG in six groups with poling periods $\Lambda = 22.4\,\mu\text{m}$ ... $22.65\,\mu\text{m}$ with a pitch of 50 nm. An essential difference is the lateral dimension of $12.9\,\mu\text{m} \times 14\,\mu\text{m}$ for the first and $12.9\,\mu\text{m} \times 13\,\mu\text{m}$ for the second WG in each group. The advantage is an almost non-elliptical fundamental WG mode, which renders possible high coupling efficiencies of the incident beams (details are presented in the next section). Besides, the mechanical design of the WG and AL holder is simplified. Both ALs are mounted on XYZ translation stages (MDE122, *Elliot Martock*). For the WG holder the X and Z axis degrees of freedom, which have proven to be unnecessary, are omitted. A detailed characterization of this particular chip in terms of temperature tuning properties and SPDC spectra as well as pictures of the mechanical design can be found in the master thesis of T. Bauer [234]. The experiments in this thesis are performed with the first WG of the sixth group ($\Lambda = 22.65\,\mu\text{m}$) featuring the lowest phasematching temperature of $T = 19\,^{\circ}\text{C}$. The 854 nm input and 1550 nm converted light are both coupled from SM fibers (SM780-HP and SMF28 Ultra) via dichroic mirrors into the Sagnac interferometer and subsequently to the WG.

Pump laser and frequency stabilization

The pump light at 1904 nm is generated by a thulium-doped fiber laser (TDFL, model AP-SF, *AdValue Photonics*) and amplified up to 2 W by a thulium-doped fiber amplifier (TDFA, model AP-AMP1, *AdValue Photonics*). The TDFL offers temperature tuning of the output wavelength from 1903.8656 nm to 1904.1657 nm, which corresponds to target wavelengths between 1549.9352 nm and 1550.1341 nm (exact input wavelength: 854.44333 nm). Fast frequency tuning by 400 MHz is enabled via a piezo actuator with a bandwidth of 1 kHz. The laser linewidth is < 50 kHz in 100 µs according to manufacturer's data. The collimated output beam first passes a spherical lens for mode-matching to the WG. A subsequent HWP and an optical isolator are necessary for power adjustment and to prevent damage of the amplifier due to backreflections. The latter is critical since the Sagnac configuration in principle acts as a mirror, i.e. almost the total power is backreflected to the amplifier. Another HWP is employed to change the pump laser polarization, which determines the ratio of pump powers in the H- and V-arm $\gamma_{\mathrm{pump}} = P_{\mathrm{H}}/P_{\mathrm{V}}$ and helps to equalize the conversion efficiencies in both arms. To cut off background around the target wavelength generated in the amplifier or the fibers, we use a 1600 nm longpass filter (*Edmund Optics*).
In the next section we will explain the necessity of spectral filtering down to 250 MHz FWHM. Hence, the laser frequency has to be stable up to few MHz in order to avoid degradation or fluctuations of the EDI. Unfortunately, we observed drifts up to 50 MHz over a few hours estimated from the power transmitted through the filter. To minimize the drift, we actively stabilize the frequency of the laser using a wavelength meter (Wavemeter (WM), WS6-200, *High Finesse*). Although the absolute accuracy of the WM is merely specified to 200 MHz, we measured a much better accuracy below 10 MHz utilizing a reference laser at 780 nm, being absolutely stabilized by doppler-free spectroscopy of an atomic Rubidium vapor. We believe that the significantly better performance is caused by the stable environment in our lab (mainly temperature and humidity) and by thorough fixation of the WM and the SM fiber connected to it in order to avoid polarization drifts and spatial aberrations to the interferometer inside the WM. Unfortunately, our WM only detects light between 330 nm and 1750 nm, i.e. we cannot detect the pump light directly. We take advantage of the - in principle undesired - weakly phasematched SHG in the WG, which delivers roughly 200 nW of 952 nm light. The SHG light is separated from the 854 nm input light using a bandpass filter (FBH850-40, *Thorlabs*), collimated and beam-shaped with two spherical lenses, coupled to a SM fiber, and guided to the WM. Due to the limited SHG power, the PID update rate is merely 2 Hz, which is sufficient, however, to compensate for long-term drifts. The PID loop is implemented in Labview and feedback is applied to the TDFL's piezo actuator using a DAQ card for analog output signal generation.

Spectral filtering and quantum state analysis

Just like for the O-band converter, we need to apply spectral filtering to reduce the amount of CIB. In fact, the C-band wavelength combination is a little less advantageous in terms of background: the spectral separation between pump and target wavelength

is $-1200\,\mathrm{cm}^{-1}$, i.e. ASR background is still present (see Sect. 2.1.2). For our particular wavelength combination, ASR has been identified as the main background source by Krutyanskiy el al. via temperature-dependent measurements confirming the expected Boltzmann distribution [164]. In order to reduce ASR background to less than 100 cps, narrowband spectral filtering down to 250 MHz is required. This is realized by a combination of an interference bandpass filter with FWHM = 12 nm (FBH1550-12, *Thorlabs*), a reflective volume Bragg grating (VBG, *Optigrate*) with FWHM = 25GHz, and an air-spaced plane-plane etalon with a free spectral range of FSR = 12.5 GHZ and FWHM = 250 MHz (*SLS Optics*). Note that the FSR of the etalon matches the FWHM of the VBG to suppress neighboring etalon modes. In principle, even a larger etalon FSR or a smaller VBG FWHM is desirable, however, large efficiencies of both components are merely possible with the given values. A calculation using the theoretical spectra of both filters indicates that the background transmitted through all neighboring modes together contributes to $\approx 30\,\%$ of the total background. At this point the question may arise why we use VBGs instead of FBGs being well-established at telecom wavelengths. The reason is the transmission loss: while VBGs show reflectivities around 97 %, FBG filter systems are much worse with transmissions between 60-70 %. This is not caused by the FBG itself as its reflectivity is typically $> 95\,\%$, but by the fiber optic circulator built-in the filter system.

As shown in Fig. 3.9, the bandpass filter is inserted in the Sagnac setup in front of the fiber coupler, while VBG and etalon are "outsourced" to the state projection setup. In fact, VBG and etalon are very sensitive to beam divergence and feature the best reflection/transmission only for well-collimated beams. Since we do not have collimated beams in the Sagnac setup but in the projection setup, the best position is there.

In the experiment we observed drifts of the resonance frequency of the etalon, which we attribute to its dependence on air pressure and air temperature. Both measures affect the refractive index of air and, thus, the FSR of the etalon. Note that the etalon temperature itself has a negligible effect since the spacers are made of low-thermal expansion glass (ULE glass, *Corning*). With our parameters $\lambda = 1550\,\mathrm{nm}$ and $L_{\mathrm{etalon}} = 12\,\mathrm{mm}$ we are able to estimate the resonance frequency shift with respect to the frequency of the converted light via

$$\Delta\nu_{\mathrm{res}} = \nu_{\mathrm{conv}} - \left\lfloor \frac{\nu_{\mathrm{conv}}}{\nu_{\mathrm{fsr}}} \right\rceil \cdot \nu_{\mathrm{fsr}} \quad \text{with} \quad \nu_{\mathrm{fsr}} = \frac{c}{2L \cdot n\,(p_{\mathrm{air}}, T_{\mathrm{air}})} \tag{3.15}$$

to 51.3 MHz/hPa and 182 MHz/°C. The temperature- and pressure-dependent refractive indices are extracted from NIST's "refractive index of air calculator" based on the Ciddor equations [235]. While the temperature dependence is less critical since our labs are temperature-stabilized to within $\approx 0.2\,^{\circ}\mathrm{C}$, the pressure dependence is a serious problem: air pressure drifts of 10 hPa are not unusual in case of weather changes, i.e. the resonance frequency is shifted by twice the linewidth. To remove both effects, we insert the etalon into an evacuated vacuum t-piece with AR-coated windows on both end ports and a valve to connect a vacuum pump at the third port. The leakage rate is estimated to be $10^{-8}\,\mathrm{m^3Pa/s}$, i.e. the increase in pressure is about 10 hPa/month. After evacuation, we did not observe anymore significant drifts of the transmitted intensity

related to air pressure over a period of 9 hours. Further details on the design of the vacuum chamber as well as characterization measurements can be found in [234].
Behind the spectral filters follows the setup to perform quantum state analysis, which is identical to that of the O-band converter. A motorized flip mirror guides the light to a polarimeter (*Thorlabs*) to measure the rotation matrix of the whole setup with classical light.

3.2.2 Trichroic waveguide coupling

The challenge to achieve simultaneous optimal coupling of all three fields to the fundamental WG mode (denoted as trichroic coupling) has been discussed already in Sect. 3.1.1: due to chromatic dispersion of the aspheric WG coupling lenses (AL_{wg}), best possible coupling cannot be reached with incident collimated beams, even if they possess different beam diameters. In fact, only one beam could be collimated if the distance between WG facet and AL_{wg} matches the respective focal length. Here, we devise an optimization routine to achieve best possible trichroic coupling employing a comparable simple optical setup with minimal demand for optical components (e.g. lenses or telescopes). Note that we commonly speak about trichroic WG coupling although the converted field is generated in the WG and coupled to a fiber, actually. However, the scheme is fully bi-directional, i.e. we can arbitrarily swap fiber and WG coupling if we merely deal with fundamental modes. In our routine we allow all fields to be non-collimated, which offers an advantage: the incident beams rarely possess the correct diameter since standard AL from Thorlabs' stock are not available with arbitrary focal lengths, i.e. we would need to change the diameter of the collimated beam with telescopes, which are obsolete in our scheme. The idea of the routine is illustrated in Fig. 3.10a and consists of the following steps:

(I) We first calculate the electric fields $E_{wg}(x, y)$ and intensities $S_{wg}(x, y)$ of the fundamental WG modes for each wavelength according to equations 2.14 and 2.18 with the WG height and width from the datasheet. Graphical representations of S_{wg} are shown in the first row in Fig. 3.10b.

(II) In the second step we optimize the coupling of the converted field by maximizing the spatial mode overlap η_{mode} between the incident beam and the fundamental WG mode. The spatial mode overlap is defined as the normalized overlap integral of E_{wg} and the E-field of the incident beam at the WG facet E_{in} according to

$$\eta_{mode} = \frac{\left|\int E_{in}^{*}(x, y, \vec{p})\, E_{wg}(x, y)\, dA\right|^2}{\left|\int E_{in}^{*}(x, y, \vec{p})\, E_{in}(x, y, \vec{p})\, dA\right|^2 \cdot \left|\int E_{wg}^{*}(x, y)\, E_{wg}(x, y)\, dA\right|^2}. \quad (3.16)$$

We know that a non-collimated beam, characterized by a certain divergence and distance between AL_{wg} and the focal point, is required to maximize η_{mode}. The idea is to generate such a beam merely with a fibercoupler placed at the correct distance $d_{al,1550}$ to the AL_{wg}, and, to match the correct divergence, with an appropriate fiber coupling lens AL_{1550} with the distance $d_{fib,1550}$ to the fiber facet. This setting is illustrated in Fig. 3.10a together with the 1550 nm beam waist $\omega(z)$

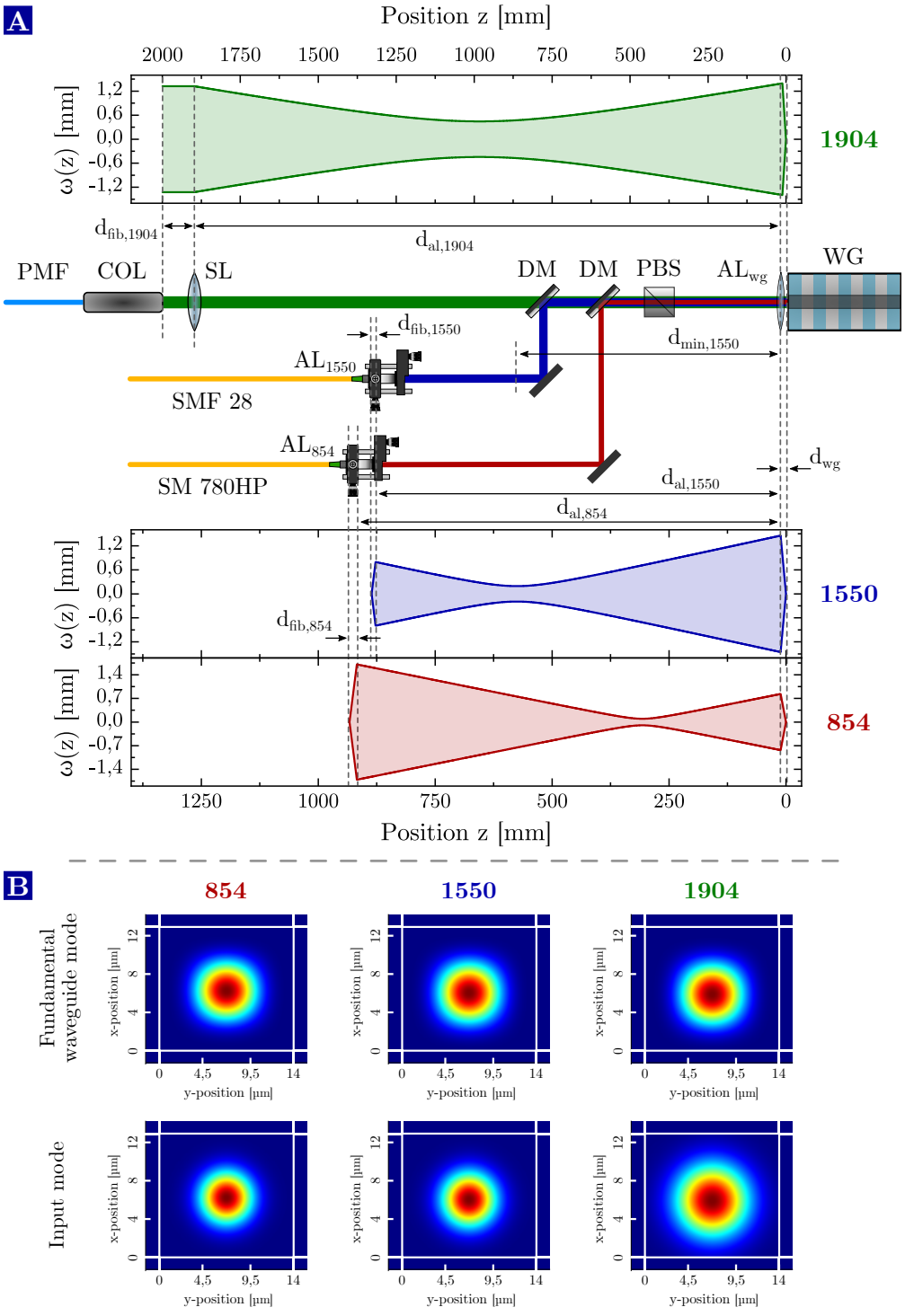

Figure 3.10. Optimization of the trichroic waveguide coupling. **(A)** General idea and simulation results for optimal coupling of all three fields to the fundamental WG mode. A detailed description is presented in the main text. **(B)** The calculated fundamental WG modes and the simulated modes of all incident beams at the WG facet.

depending on the position z along the optical axis. The E-field at the WG facet is fully determined by the mode-field diameter (MFD) of the fiber and the above mentioned parameters, i.e. $E_{\text{in}} = E_{\text{in}}(\vec{p})$ with $\vec{p}$ being a set of parameters $\vec{p} = (d_{\text{fib,1550}}, f_{\text{al,1550}}, d_{\text{al,1550}}, d_{\text{wg}})$. Note that the MFD and $f_{\text{al,wg,1550}}$ are fixed and do not appear in $\vec{p}$. For the optimization, we first calculate E_{in} by means of ray transfer optics method, subsequently the spatial mode overlap η_{mode} and, finally, we numerically minimize $1 - \eta_{\text{mode}}$ by varying the parameters $d_{\text{fib,1550}}$, $d_{\text{al,1550}}$ and d_{wg} within certain constraints. The constraints are for instance for $d_{\text{al,1550}}$ given by a maximum value of 3 m to avoid huge optical path lengths and a minimum value of $d_{\text{min,1550}} = 600$ mm due to the length of the interferometer plus further space limitations. The parameter $f_{\text{al,1550}}$ is not completely "free", but fixed to certain values given by all standard aspheric lenses available from Thorlabs' stock. We repeat this procedure for each available $f_{\text{al,1550}}$ and select in the end the combination with the best spatial overlap. Note that we can perform this step also with the input or pump field, however, the converted wavelength is in between the other wavelengths and therefore a good starting point.

(III) In the third step we repeat the same procedure for the 854 nm beam with the slight difference that the distance d_{wg} between WG facet and AL_{wg} is now a fixed parameter.

(IV) Finally, we perform the optimization for the pump light. The TDFA output is not a fiber-to-free-space port but a collimator, though. So we add a plano-convex spherical lens (made of CaF_2) in order to obtain a non-collimated beam. (see Fig. 3.10a)

The whole optimization routine is implemented in Matlab and features a user-friendly graphical user interface (details can be found in [234]). Fig. 3.10a displays the results of the optimization along with all relevant optical components and distances. The three graphs show the final beam waists of the fields in dependence on the position z along the optical axis. It is clearly visible that none of the beams is collimated but has a focal point somewhere in the setup. All parameters are listed in Tab. 3.2. We find very high spatial mode overlaps of 99.5 % (99.3 %) for input (converted) field and a slightly reduced overlap of 93.5 % for the pump light. We confirm this by the intensity distribution of the calculated fundamental WG modes $S_{\text{wg}}(x, y)$ and incident beam free-space mode at the WG facet $S_{\text{in}}(x, y)$ illustrated in Fig. 3.10b. While the 854 nm and 1550 nm modes match quite well to each other, a slight discrepancy can be identified for 1904 nm. Non-perfect coupling efficiencies of the pump light are acceptable since we are able to partially compensate those with higher laser powers. Note that the routine has been further improved in the meantime: we do not fix d_{wg} after step **(III)** anymore, but we conduct the whole optimization routine for a large number of different d_{wg} and select the best combination afterwards. Thereby we pushed the mode overlap for 1904 nm to 96.0 %.

To confirm the simulation results by measurements, we constructed the Sagnac configuration according to the calculated lenses and distances. The first step is to align

Table 3.2. Results of the trichroic WG coupling optimization routine. The highest spatial mode overlaps η_{mode} are simulated for the given combinations of aspheric/spherical lenses and distances. Note that Thorlabs specifies the focal lengths of their lenses at design wavelengths of 780 nm or 633 nm. Due to chromatic dispersion the focal lengths in the table differ from their specified values.

WL [nm]	Lens, f [mm]	d_{fib} [mm]	d_{al} [mm]	d_{wg} [mm]	η_{mode}
854	A260-B, 15.34	15.733	906	–	99.5 %
1550	A240-C, 8.174	8.388	866	11.5268	99.3 %
1904	LA5835-D, 1021	–	1888	–	93.5 %

the whole interferometer with 854 nm light. The strategy is to align one interferometer arm in terms of high transmission through the WG and a mode profile close to the fundamental WG mode, simultaneously. Next, the second AL behind the WG is precisely aligned with respect to the WG to minimize astigmatism and to avoid non-perpendicular AOI leading to chromatic dispersion. The same procedure is repeated the other way round. Once both arms are aligned, one can slightly vary the position of the fibercoupler to gain the last few percent of coupling efficiency. The achieved coupling efficiencies η_{wg} are listed in Tab. 3.3: we measure 96.2 % (97.1 %) for the H(V)-arm at a distance of 890 mm. If we keep in mind that η_{wg} also incorporates attenuation loss in the WG, reflection losses of the AR-coatings on the end facets, imperfections of the WG geometry and aberrations of the molded aspheric lenses, the measured efficiencies are in good agreement with the simulated overlap. The 2 % deviation of the distance $d_{\text{al,854}}$ is most probably caused by uncertainties in the fiber MFD. To prove that we mainly couple to the fundamental mode, we measured the spatial intensity distribution of the transmitted beam, which has been collimated with the AL_{wg}, with a beam profiler. The result is shown in Fig. 3.11a: we merely identify the fundamental mode and no significant higher-order contributions. The respective x- and y- cross-sections are fitted with Gaussian distributions revealing only slight deviations from the ideal course in the wings. If we take a closer look at the widths $\sigma_{\text{x}} = 286(5)\,\mu\text{m}$ and $\sigma_{\text{y}} = 309(5)\,\mu\text{m}$ extracted from the fits, we find almost equal values indicating an highly symmetric Gaussian profile. In fact, the larger width in y-direction is even expected since the mode confinement in y is lower because of the substrate. Besides, the near-Gaussian spatial mode profiles and high coupling efficiencies are a clear evidence for the excellent

Table 3.3. Comparison between measured and simulated results.

WL [nm]	η_{mode} simu.	$\eta_{\text{wg,H}}$ meas.	$\eta_{\text{wg,V}}$ meas.	d_{al} simu.	d_{al} meas.
854	99.5 %	96.2 %	97.1 %	906 mm	890 mm
1550	99.3 %	96.9 % ($\eta_{\text{fib,H}}$)	96.9 % ($\eta_{\text{fib,V}}$)	866 mm	850 mm
1904	93.5 %	89.4 %	88.9 %	1888 mm	1940 mm

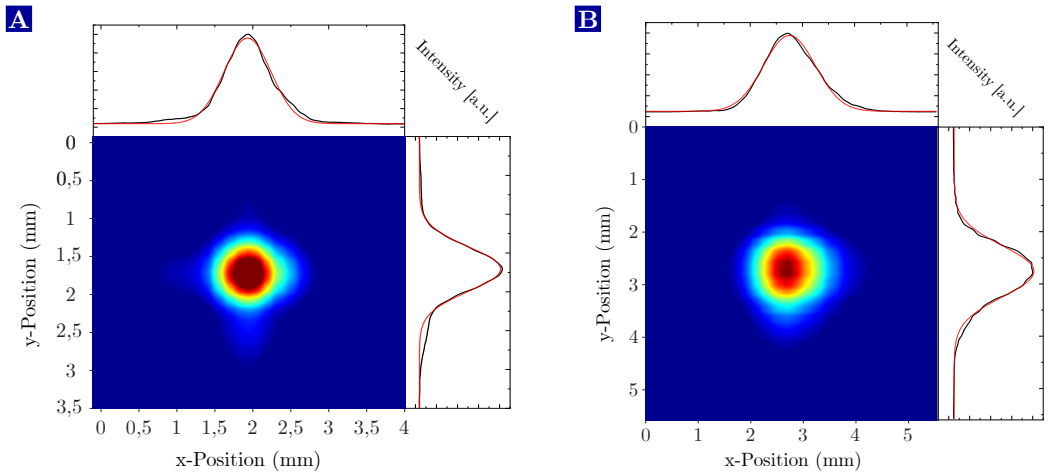

Figure 3.11. Output modes of the 854 nm and 1550 nm fields. The spatial mode profiles of the transmitted input field at 854 nm without pump field **(A)** and the converted field at 1550 nm **(B)** behind the WG. Each beam has been collimated with the ALs and measured with a beam profiler. We find no higher-order modes but only the fundamental WG mode indicating proper mode-matching of the incident beams. The small charts illustrate the x and y cross-sections through the mode. Gaussian fits to the data reveal near-Gaussian WG mode profiles being consistent with the simulations.

quality of our WGs, certainly a key requirement to achieve those results.
Subsequently after the 854 nm alignment, the pump light is coupled to the WG and frequency conversion is established. During the alignment, special attention needs to be paid to chromatic dispersion within the Sagnac interferometer. If the three-color beam does not impinge perfectly perpendicular onto an optical component, the three beams suffer from displacement or even divergence with respect to each other caused by dissimilar refraction angles. This is definitely the case for the WG and ALs since the WG facets are not cut perfectly perpendicular with respect to the optical axis. Thus, the 854 nm beam for instance might be coupled perfectly from both sides to the WG, while it is not possible to simultaneously achieve this for 1904 nm without misaligning one arm. We compensate for this chromatic dispersion by deliberately misaligning one AL_{wg} in the x-y plane in order to introduce additional chromatic dispersion counteracting the original one.
For pump and converted light we observe similar results as for 854 nm, i.e. the coupling efficiencies are a few percent below the calculated mode overlap at an optimum distance slightly different from the simulated value. The reasons are the same as mentioned above. Note that the efficiencies for the 1550 nm light are fiber-coupling efficiencies; the WG coupling efficiencies are expected to be very similar due to the bi-directionality, though. We also measured the spatial mode profile of the generated 1550 nm light behind the WG (see Fig. 3.11b). Just as for the 854 nm beam, only the fundamental mode, obeying a symmetric Gaussian distribution, is apparent. All in all, we conclude that all experimental results agree quite well with the simulated data from our optimization routine. An additional benefit of the routine is the minimal demand for optical

components, which avoids losses and simplifies miniaturization of QFCDs.

3.2.3 Performance of the device

In this last section, we investigate the performance of the PPQFCD, i.e. external device efficiency, CIB and process fidelity. The EDI is again determined by a series of individual efficiencies and transmissions, which are listed in Tab. 3.4 for the H- and V-arm. $T_{\mathrm{optics,854}}$ accounts for transmission losses in the 854 nm path mainly caused by the silver mirrors, PBS and HWP. The ALs for WG coupling have a transmission of $T_{\mathrm{al,854}}$ = 93 % at 854 nm, which is surprisingly low since all lenses are AR-coated; there is no explanation so far. At 1550 nm we find a significantly higher transmission of $T_{\mathrm{al,1550}}$ = 98.1 %. In total we have three of those in the setup: one for WG coupling and two for fiber in- and outcoupling. The spectral filters account for a joint transmission of T_{filter} = 88.3 % with the individual transmissions T_{bpf} = 96 %, T_{vbg} = 98.5 and T_{etalon} = 93.4 %. The fiber coupling efficiency is divided in two parts: the incoupling efficiency η_{fiber} = 96.9 % and the transmission of the output facet T_{fibfac} = 96.5 % , which is limited by Fresnel reflections amounting to 3.5 %. The input facet is AR-coated and does not suffer from reflection losses. The internal efficiency η_{int} and transmission losses in the 1550 nm path $T_{\mathrm{optics,1550}}$ are pretty hard to measure in a Sagnac configuration, hence we are only able to measure the device efficiency and calculate back the product $\eta_{\mathrm{int}} \cdot T_{\mathrm{optics,1550}}$. We measure 93.3 % (88.0 %) for the H(V)-arm. We believe that the difference is mainly caused by the HWP since its transmission and rotation angle is quite sensitive to its position, the wavelength, and the angle with respect to the optical axis. Since we optimized this for 854 nm, it might be not ideal for 1550 nm. Nevertheless, if we divide the higher value (93.3 %) by the reflectivity of two silver mirrors at 1550 nm (98.5 % per mirror) and the PBS transmission ($T \approx$ 98 %) we obtain internal efficiencies around 97 %, similar to the O-band converter. We end up at external device efficiencies of 60.1 % (57.2 %) for the H(V)-arm, which are to our knowledge the highest values reported so far for a QFCD. An interesting remark at this point: if we take a closer look at Tab. 3.4, we find that it is neither straightforward nor simple to further increase the EDI to let's say > 70 %. We can go up to 66 % (from 57.2 %) by replacing all silver mirrors by custom dielectric mirrors, which improves $T_{\mathrm{optics,854}}$ and $T_{\mathrm{optics,1550}}$, and by employing a custom fiber with AR-coatings on both end facets. All other numbers are already very close to the maximum, i.e. they cannot be further improved (e.g. WG or fiber couplings) or an improvement requires highly customized or post-selected devices to gain the last few percent, which might be possible for the spectral filters, aspheric lenses, PBS and HWP. Hence, even an increase of η_{dev} to 75 - 80 % would require extraordinary financial efforts. Further extensions towards unity device efficiency seem to be unrealistic for fabrication of small series devices.
The pump-power dependent device efficiencies are shown in Fig. 3.12. We find a much better overlap of both curves compared to the O-band converter due to the higher symmetry of the Sagnac configuration. A further advantage of the Sagnac configuration is that we are able to to conveniently equalize $\eta_{\mathrm{dev,H}}$ and $\eta_{\mathrm{dev,V}}$ by changing the ratio between the pump power in each arm $\gamma_{\mathrm{pump}} = P_{\mathrm{H}}/P_{\mathrm{V}}$ by means of the pump laser polarization. Operating points of P_{H} = 485 mW and P_{V} = 625 mW ensure $\eta_{\mathrm{dev,H}}$ =

Table 3.4. Individual efficiencies and transmissions of the H- and V-arm of the C-band converter.

Efficiency/transmission	Abbreviation	H-arm	V-arm
Opt. elements transmission, 854 nm	$T_{\text{optics,854}}$	92.3 %	
AL transmission, 854 nm	$T_{\text{al,854}}$	93.0 %	
Waveguide coupling efficiency	η_{wg}	96.2 %	97.1 %
AL transmission, 1550 nm (3x)	$(T_{\text{al,1550}})^3$	94.4 %	
Bandpass filter transmission	T_{bpf}	96.0 %	
Fiber in/out-coupling efficiency	$\eta_{\text{fiber}} \cdot T_{\text{fibfac}}$	93.5 %	
Volume Bragg grating transmission	T_{vbg}	98.5 %	
Etalon transmission	T_{etalon}	93.4 %	
Int. eff. and opt. el. trans. (est.)	$\eta_{\text{int}} \cdot T_{\text{optics,1550}}$	93.3 %	88.0 %
External device efficiency	η_{dev}	60.1 %	57.2 %

$\eta_{\text{dev,V}} = 57.2\,\%$.
Next, we investigate the background: we already mentioned in Sect. 3.2.1 that ASR is the dominant background source in this DFG-process. Fig. 3.12b displays the generated and detected CIB count-rates ($R_{\text{cib, gen/det}}$) at different total pump powers $P_{\text{tot}} = P_{\text{H}} + P_{\text{V}}$. We measured $R_{\text{cib, det}}$ with the detection setup shown in Fig. 3.9 including the projection setup using two SNSPDs. We operate SNSPD 1 (2) at a bias current of -6.25 µA (-16.7 µA) corresponding to 35(3) % (31(3) %) SDE and a measured DCR of 60.5(3) cps (54.0(3) cps). All measured CIB count-rates are dark-count subtracted and time-averaged over 15 min to get sufficiently low Poissonian error bars. The orange and blue data points in Fig. 3.12b represent $R_{\text{cib, det}}$ of each SNSPD while the green data points denote the sum of both. The reason for different CIB count-rates of both SNSPDs is mainly the dissimilar SDEs. The most interesting number is $R_{\text{cib, gen}}$ (black data points). To this end, we divide $R_{\text{cib, det}}$ by the SDE and the transmission of the projection setup of $\eta_{\text{pro}} = 88\,\%$. The considerably larger error bars (larger than $1/\eta_{\text{pro}}\eta_{\text{sde}}$) are caused by the additional uncertainty of the SDEs. At the operating point $P_{\text{tot}} = 1110\,\text{mW}$ we find $R_{\text{cib, gen}} = 24(3)\,\text{cps}$, which compares well with the O-band converter ($R_{\text{cib, gen}} = 11.4\,\text{cps}$) taking into account the more than twice as high EDI. In principle, we expect for ASR background a linear dependence on the pump power following the literature [134]. However, because DFG and SFG obey the same phasematching condition, ASR background around 1550 nm is up-converted to 854 nm subsequently after it is generated in the WG. Since the spectral-filter bandwidth is small compared to the acceptance bandwidth of the DFG-process ($\approx 80\,\text{GHz}$), phasematching is ensured for the entire detectable ASR background. This results in a reduction of the ASR background at 1550 nm of almost a factor of 2 at the operating point where the internal conversion efficiency has its maximum. The effect has been already observed

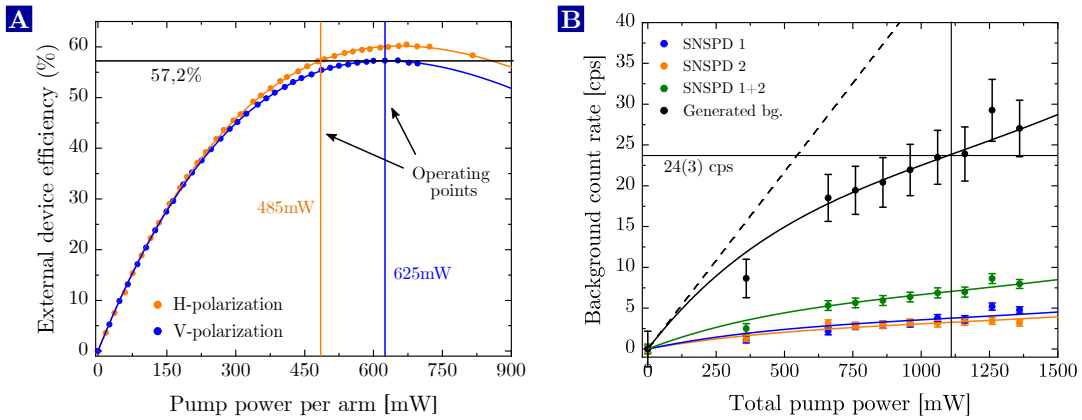

Figure 3.12. External device efficiency and conversion-induced background. **(A)** Measurement of the external device efficiencies $\eta_{\mathrm{dev,H}}$ and $\eta_{\mathrm{dev,V}}$ in dependence on the pump powers per arm P_{H} and P_{V}. Due to different device efficiencies of both arms the curves do not overlap. However, the arms are pumped with different powers since we are able to change the ratio $\gamma_{\mathrm{pump}} = P_{\mathrm{H}}/P_{\mathrm{V}}$ by adjusting the pump laser polarization. At $P_{\mathrm{H}} = 485\,\mathrm{mW}$ and $P_{\mathrm{V}} = 625\,\mathrm{mW}$ we achieve $\eta_{\mathrm{dev,H}} = \eta_{\mathrm{dev,V}} = 57.2\,\%$. **(B)** The detected and generated CIB count-rates ($R_{\mathrm{cib,\,det/gen}}$) in dependence on the total pump power $P_{\mathrm{tot}} = P_{\mathrm{H}} + P_{\mathrm{V}}$. $R_{\mathrm{cib,\,gen}}$ excludes the SNSPD detection efficiency and transmission losses in the projection setup. At the operating point (1110 mW) we measure $R_{\mathrm{cib,\,gen}} = 24.2\,\mathrm{cps}$ caused by ASR scattering. In principle, we expect a linear dependence on the pump power (black dashed line) for ASR background, however, up-conversion of the ASR flattens the curves. The solid lines are fits with the respective model presented in the main text.

by Maring et al. [142, 236] and modeled as

$$\begin{aligned} R_{\mathrm{cib}}(P) &= \int_0^L \alpha_{\mathrm{asr}} P \left(1 - \eta_{\mathrm{int}}^{\mathrm{max}} \cdot \sin^2\left((L-x)\sqrt{\eta_{\mathrm{nor}} P}\right)\right) dx \\ &= \alpha_{\mathrm{asr}} P L \left(1 - 1/2\,\eta_{\mathrm{int}}^{\mathrm{max}} + \frac{1/2\,\eta_{\mathrm{int}}^{\mathrm{max}}}{L\sqrt{\eta_{\mathrm{nor}} P}} \sin\left(L\sqrt{\eta_{\mathrm{nor}} P}\right) \cos\left(L\sqrt{\eta_{\mathrm{nor}} P}\right)\right) \end{aligned} \tag{3.17}$$

comprising a linear term $\alpha_{\mathrm{asr}} PL$ related to ASR background and a nonlinear term related to up-conversion of ASR background. Fits to the data with this model (solid lines in Fig. 3.12b) indicate good agreement. Note that α_{asr} is the only free parameter while η_{nor} is extracted from the pump-power dependent device efficiency, $L = 40\,\mathrm{mm}$, and $\eta_{\mathrm{int}}^{\mathrm{max}}$ is assumed to be 95 %. For comparison, the dashed black line shows the expected linear course disregarding up-conversion to 854 nm.

If we compare our CIB rate with that measured by Krutyanskiy et al. [164] ($R_{\mathrm{cib,\,gen}} = 58\,\mathrm{cps}$) we find an unexpected discrepancy (the majority of the components such as WGs, pump laser, spectral filters are identical). Taking into account their EDI of 30 %, we expect for our device $R_{\mathrm{cib,\,gen}} = 110\,\mathrm{cps}$ assuming that the background suffers in the same way from the lower efficiency. One reason for the discrepancy are the different phasematching temperatures (19 °C vs. 38 °C), corresponding to a factor 1.43 in the

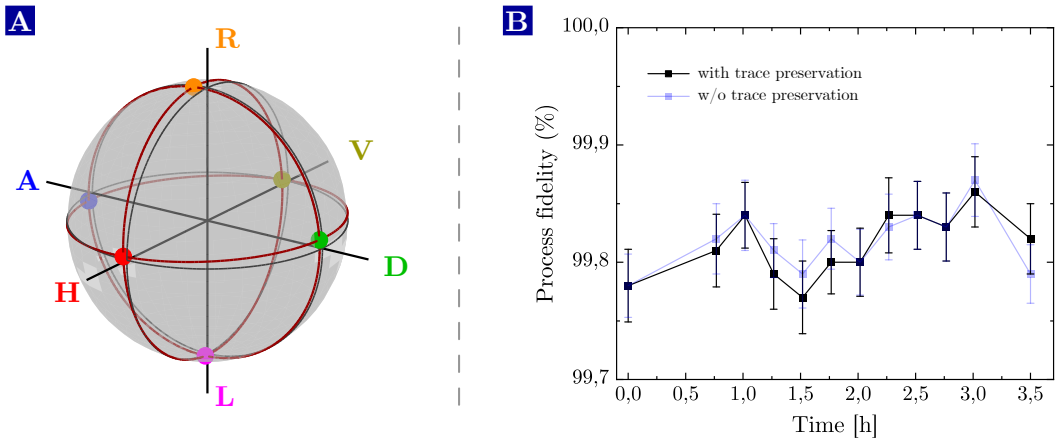

Figure 3.13. Process fidelity and long-term stability. **(A)** Bloch-sphere representation of the process matrix measured via QPT. **(B)** The process fidelity over 3.5 hours. We observe an excellent long-term stability without any significant drops of the process fidelity. Note that this includes the 90 m long fiber connecting the converter and ion lab.

ASR background, i.e. we expect $R_{\text{cib, gen}} \approx 77$ cps. In fact, the remaining difference stems from the dissimilar configurations. In their CaCG, the whole pump power is transmitted through both WGs, so let's say $2N$ background photons are created. In the Sagnac configuration we pump both arms with about half P_{tot}, hence $N/2$ photons per arm and N photons behind the PBS. Since we found the ASR background behind the WG to be almost unpolarized, roughly one half of the background takes the second output port of the PBS, so we end up at $N/2$. With the additional factor four we expect about 20 cps, close to our generated CIB rate.

To finish the characterization of the C-band converter, we prove polarization-preserving operation by means of quantum process tomography. Fig. 3.13a illustrates the Bloch sphere representation of the measured process matrix with $\mathcal{F}_{\text{pro}} = 99.81(3)\,\%$. As expected we find only slight deviations from the ideal sphere caused by a rotation around the x-axis. The long-term stability of the process fidelity is shown in Fig. 3.13b. We observe an excellent long-term stability, most probably due to less polarization drifts in the 90 m long fiber connecting the labs. The better overall process fidelity compared to the O-band converter is attributed to the absence of the phase stabilization, a higher power stability of the pump laser and the improved polarization rotation measurement utilizing a polarimeter.

3.3 QFC of polarization-entangled photons from a SPDC source

Until now we characterized our PPQFCDs merely with coherent light, either at macroscopic intensities or at the single-photon level. The next step is to convert nonclassical light and demonstrate the preservation of quantum correlations after PPQFC. To this end, we employ a photon-pair source based on cavity-enhanced SPDC, which has

been constructed and operated by J. Eschner's group. The source emits narrowband, nearly-degenerate polarization-entangled photon pairs at 854 nm with one photon being resonant with the $4^2P_{3/2} \Leftrightarrow 3^2D_{5/2}$ transition in $^{40}Ca^+$-ions and the second photon being 480 MHz detuned. We briefly introduce the source in Sect. 3.3.1 and subsequently explain the complete experiment consisting of source and converter. In Sect. 3.3.2 we demonstrate preservation of polarization entanglement during PPQFC with high fidelity, even if the telecom photons are transmitted through kilometer-scale fibers with lengths of 20 km and 40 km.

3.3.1 Narrowband entangled photon pair source at 854 m

The source is based on SPDC in a type-II[2] periodically-poled KTP (PPKTP) crystal designed to create frequency-degenerate photons at 854 nm. The SPDC process requires pump light at 427 nm generated by cavity-enhanced SHG of a frequency-stabilized diode laser. The main purpose of the source is to deliver entangled photon pairs for heralded absorption experiments with trapped Ca^+-ions [131], i.e. the photons have to match the linewidth of the atomic transition $\Delta\omega = 2\pi \cdot 22.5\,\text{MHz}$. Since the SPDC spectrum is rather broadband ($\approx 150\,\text{GHz}$ depending on the crystal length), it is possible to either apply strong spectral filtering, which considerably reduces the pair rate, or to insert the nonlinear crystal into an optical resonator. The latter results in a comb-like spectrum where the spectral density is reordered into narrowband teeth and is therefore favorable in terms of ion-resonant pair rate.

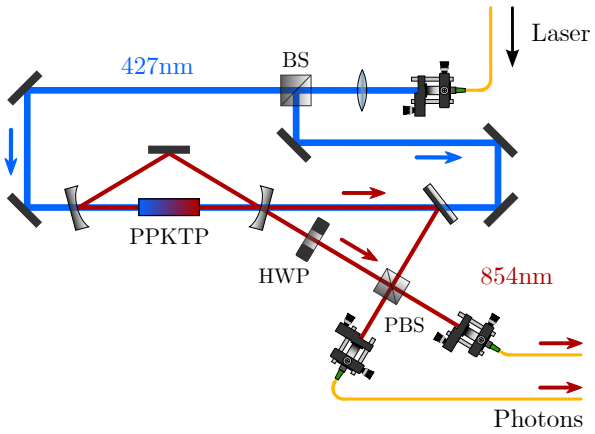

Figure 3.14. Narrowband entangled photon-pair source. Simplified schematic representation of the cavity-enhanced SPDD-source delivering narrowband polarization-entangled photon pairs at 854 nm (adapted from [204]). Setup and functionality will be explained in the main text. A much more detailed scheme can be found in [237].

The scheme of the source is shown in Fig. 3.14: the crystal is surrounded by a 14.7 cm long 3-mirror ring cavity with two HR-mirrors and one partially reflecting outcoupling-mirror ($R_H = 95.8\,\%$, $R_V = 96.7\,\%$). The cavity length is actively stabilized to be reso-

[2]Type-II phasematching means that a vertically-polarized pump photon creates two orthogonally polarized (H and V) down-converted photons.

nant with the $P_{3/2} \Leftrightarrow D_{5/2}$ transition. Due to birefringence, the orthogonally-polarized modes are not degenerate, but separated by 480 MHz, and they possess different finesses (H: 119, V: 145) and accordingly different linewidths of 15.4 MHz (H) and 12.8 MHz (V). This is a problem since absorption of both polarizations from the ion is frustrated, and dissimilar linewidths render the photons partially distinguishable and therefore decrease the entanglement fidelity. To overcome those issues, the source is arranged in a stabilized Mach-Zehnder interferometer. The 427 nm light is split in two parts and pumps the crystal from two sides. The clockwise and counter-clockwise propagating photons leave the cavity at the outcoupling mirror under different angles and are superimposed at a PBS, i.e. each output beam has contributions from both input ports with orthogonal polarizations. Due to an HWP inserted in one output arm, the two contributions from each input port stem from the same polarization modes within the cavity and are indistinguishable in terms of linewidth and absolute frequency. Note that Sagnac configurations are widely used for this purpose in the literature [238, 239], which cannot be realized in our source for technical reasons.
In its current configuration, the source generates entangled photon-pairs with an ion-resonant pair rate of 5×10^4 $^{\text{pairs}}/_{\text{s·mW}}$ and a Bell-state fidelity around 98 %. Theoretical background, further technical details and a complete characterization of a previous (slightly different) version of the source can be found in S. Kucera's PhD thesis [204] and J. Arenskötter's master thesis [237].

3.3.2 Experiment and results

The experimental setup for PPQFC of entangled photons is sketched in Fig. 3.15. We define the signal photons generated by the SPDC source as those resonant with the ion's optical transition while the idler arm contains the detuned photons. The source described in Sect. 3.3.1 is not yet in single-mode operation, i.e. it emits photons in multiple longitudinal cavity modes. Since the narrowband spectral filters of the PPQFC transmit only one longitudinal mode, the signal and idler count rates would be highly asymmetric. In this case the majority of the photons is not correlated with each other and contributes to uncorrelated background coincidences known as accidental background. In fact, accidental background is always present in cw-pumped SPDC sources due to coincidences between photons from consecutively emitted pairs with a time difference smaller than the width of the coincidence peak. However, the accidental background is lower if the second arm is filtered, too (for details see [204]). To achieve this, the signal photons first pass a filter lens (FSR: 50 GHz, FWHM: 100 MHz) to get rid of all adjacent cavity modes. The filter lenses are monolithic Fabry-Pérot cavities (FPI) made out of plano-convex glass lenses with HR-coatings on both end facets [240, 241]. The main advantage compared to air-spaced FPIs is a comparable simple stabilization of its resonance frequency; it only requires a temperature stabilization of the whole lens. Subsequently, we project and detect the signal photons with silicon avalanche photodiodes (APD, *Excelitas Technologies*). The idler photons are frequency-converted in three different schemes a), b) and c) corresponding to different fiber lengths. In scheme a) we demonstrate preservation of entanglement during QFC. To this end, the idler photons are guided to the PPQFC via the 90 m long fiber connecting the labs and

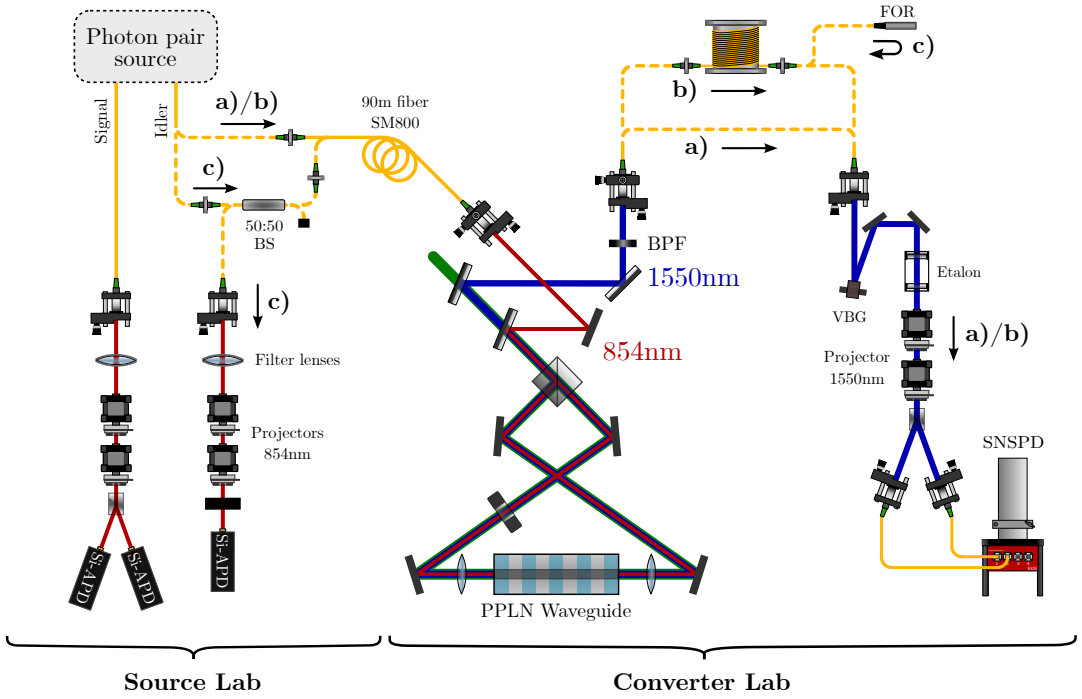

Figure 3.15. Setup for conversion of entangled SPDC-photons. The setup to demonstrate preservation of polarization entanglement during QFC using photon pairs from a SPDC source. The signal photon is projected and detected with silicon APDs in the source lab, while the idler photon is guided to the QFC lab. The labels a), b) and c) denote different measurement schemes: In a) and b) we immediately send the photons to the PPQFC and project/detect them at 1550 nm with the SNSPDs. In b) we additionally insert a 20 km long fiber between converter and projector. In c) we demonstrate entanglement over 40 km of fiber in the following way: first, the photons pass a 50:50 fiber beam splitter. One half of the photons is down-converted to 1550 nm, transmitted through 20 km of fiber and backreflected employing a fiber optic retroreflector. They pass again the 20 km fiber and are up-converted to 854 nm. The doubly-converted photons are projected and detected with a projection setup connected to the second input port of the beam splitter.

projected/detected at 1550 nm with the SNSPDs. The PPQFC setup and polarization compensation method are identical to those presented in Sect. 3.2.1. Additional spectral filtering to remove adjacent cavity modes is not required at 1550 nm since narrowband filtering is already implemented to suppress CIB. The SNSPD output pulses are sent through BNC cables installed in parallel to the fiber to the source lab and recorded by a 2-channel time-tagging electronics (Picoharp 300, *PicoQuant*). Scheme b) intends to prove preservation of entanglement over more than 20 km of fiber. To this end, we insert a 20 km long spooled telecom fiber between the PPQFC and the projection setup. The fiber spool is within a closed polystyrene box and temperature-stabilized to 0.1 °C to suppress temperature-induced polarization rotations. Using classical light, we measure a transmission of 42 % including both fiber-fiber connectors, which matches well to the expected attenuation of 0.18 dB/km in the used fiber. In c) we extend the fiber length to 40 km and additionally demonstrate bi-directional operation of the PPQFCD. In this

scheme, the idler photons are split with a 50:50 BS. One half is lost, while the second half is down-converted, transmitted through the 20 km-fiber and reflected employing a fiber optic retroreflector (P1-SMF28ER-P01-1, *Thorlabs*). Thus, the photons pass again the fiber and are subsequently back-converted to 854 nm. We confirmed by transmission measurements with classical light as well as the photon count rates that the PPQFCD possesses the same EDI in both directions, which underlines the advantage of the Sagnac configuration. The second input port of the BS guides the photons to a further projection setup for 854 nm. The filter lens suppresses adjacent modes as well as up-converted ASR background. Note that a fiber optic circulator might be preferable to avoid loosing 75 % of the photons, however, we cope with this loss due to the high brightness of the source.

Results

We verify entanglement via quantum state tomography. Correlation of the signal and idler detection events reveals the signal-idler cross correlation with the typical bunching peak related to the nonclassical temporal correlation (see Sect. 2.2.3 or [204]). We obtain the number of coincidences per basis setting C by summing up all coincidences in a 50 ns window around the peak center corresponding to almost 100 % of the peak area. From those numbers we reconstruct the density matrix by means of maximum-likelihood estimation as described in Sect. 2.2.3. Before we present the results, we take a closer look at the SBR. As mentioned above, cw-pumped SPDC sources are always affected by accidental coincidences. The number of signal coincidences S is proportional to the pair rate R_{pair} and the probabilities $\eta_{\mathrm{s,i}}$ to detect signal and idler photons according to

$$S \propto \eta_{\mathrm{s}}\eta_{\mathrm{i}}R_{\mathrm{pair}}. \tag{3.18}$$

On the contrary, the background is determined by the product of the detected signal and idler count rates $R_{\mathrm{det,s,i}}$, which depend on the pair rate as well as detector dark-counts and CIB:

$$B \propto R_{\mathrm{det,s}}R_{\mathrm{det,i}} \quad \text{with} \quad R_{\mathrm{det,s,i}} = \eta_{\mathrm{s,i}}R_{\mathrm{pair}} + R_{\mathrm{dcr,s,i}} + R_{\mathrm{cib,s,i}}. \tag{3.19}$$

In our experiments $\eta_{\mathrm{s,i}}R_{\mathrm{pair}}$ is much larger than $R_{\mathrm{dcr,s,i}}$ and $R_{\mathrm{cib,s,i}}$, i.e. accidental coincidences is the dominant background source while detector dark-counts and CIB are negligible. Thus, we assume $B \propto \eta_{\mathrm{s}}\eta_{\mathrm{i}}R_{\mathrm{pair}}^2$ and get

$$\mathrm{SBR} = \frac{S}{B} \propto \frac{1}{R_{\mathrm{pair}}}. \tag{3.20}$$

We find that the SBR does not depend on $\eta_{\mathrm{s,i}}$ since losses in one channel decrease signal and accidental coincidences in the same way. Hence, QFC does not alter the SBR as long as R_{dcr} and R_{cib} are much lower than the signal count rates $\eta_{\mathrm{s,i}}R_{\mathrm{pair}}$. For our measurements we calculate the SBR as explained in Sect. 2.2.3 and quantify its influence on Bell-state fidelity and purity according to Eq. 2.56. Besides, we reconstruct density matrices from background-subtracted raw data. Since the background is very sensitive to

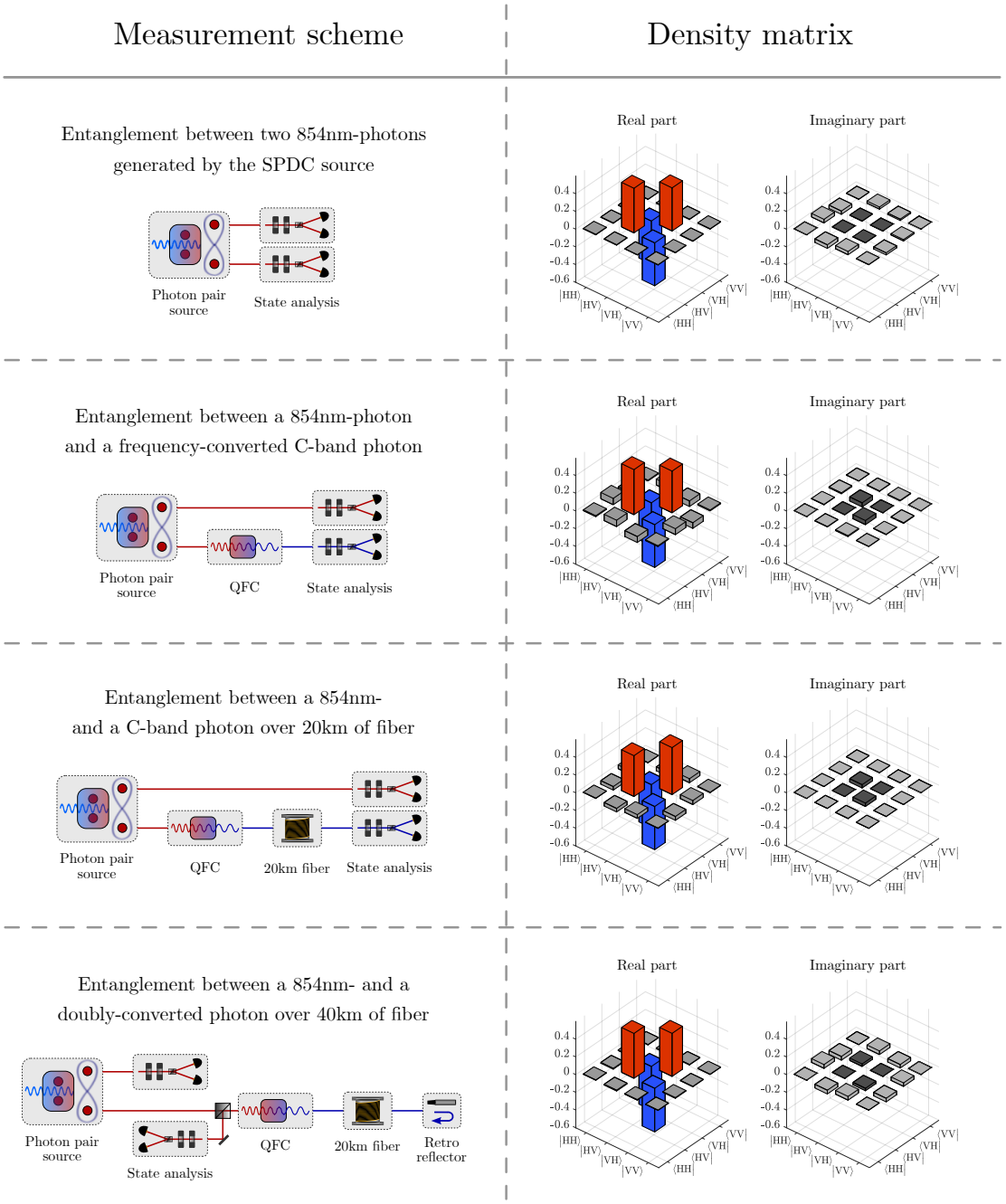

Figure 3.16. Preservation of photon-photon entanglement during PPQFC. The measured density matrices for different measurement schemes, which are illustrated by the drawings in the left column. As expected we find Ψ^- Bell-states. All density matrices are reconstructed from background-subtracted data. The matrices without background subtraction (BGS) can be found in Appendix C.

count rate fluctuations and may differ between the measurements, background subtraction (BGS) is a valuable tool to verify the functionality of our PPQFCD by comparing fidelities and purities before and after QFC.
The density matrices reconstructed from background-subtracted data of all measurement schemes are illustrated in Fig. 3.16, while the respective Bell-state fidelities, purities and SBRs are listed in Tab. 3.5. All density matrices without BGS can be found in Appendix C. We first take a look at the performance of the source without PPQFC represented by the first density matrix in Fig. 3.16. Ideally, we expect the Ψ^- Bell-state $1/\sqrt{2}\,(|HV\rangle - |VH\rangle)$ with four non-zero density matrix entries: two diagonal elements with equal heights of 0.5 denoting the "population" terms $\{|HV\rangle\langle HV|, |VH\rangle\langle VH|\}$ (red bars) and two off-diagonal elements with equal heights of -0.5 identifying the coherences $\{-|HV\rangle\langle VH|, -|VH\rangle\langle HV|\}$ (blue bars). The density matrix clearly indicates a Ψ^--state with a high fidelity of 98.0(1) % and a purity of 96.9(2) %. If we calculate the maximum achievable fidelity limited by the purity according to Eq. 2.39, we find $\mathcal{F}_{\max} = 98.4\,\%$, hence the fidelity is mainly limited by the purity and not by unitary rotations of the state. Fidelity and purity without BGS are calculated as 76.9(3) % and 61.9(4) %, respectively. The fidelities are still well above the classical threshold of 50 %, but significantly lower in comparison with the background-corrected values. Unfortunately, the SPDC source was in a non-perfect condition when the measurements were conceived since it suffered from regular failures and uncertainties of the cavity lock resulting in pair rate fluctuations. Moreover, the SBR was low because of non-perfect optical alignment of the output beams. With Eq. 2.56 and 2.58 we are able to calculate the expected fidelity and purity with the measured SBR of 2.26; we get 99.9 % and 101.08 % for fidelity and purity, respectively, and hence slightly overestimate both measures. We attribute this to the pair rate fluctuations resulting in different SBRs for each basis setting. In this situation the ansatz of a maximally mixed contribution from the background assumed for Eq. 2.56 and 2.58 is not valid anymore. Besides, fluctuating pair rates result in non-physical density matrices, i.e. the MLE might find a density matrix, which is the most-likely one, but not well-supported by the experimental data.
Next, we measure entanglement between a photon at 854 nm and a frequency-converted photon at 1550 nm (scheme a)) as shown in Fig. 3.15. The respective density matrix reveals a background-corrected fidelity of 97.29(03) % and a purity of 98.9(1) %, which

Table 3.5. Bell-state fidelities, purities and SBR of entangled photons from a SPDC source in the four different measurement schemes.

Scheme	Fidelity with Ψ^- Bell-state		Purity		SBR
	w/ BG sub.	w/o BG sub.	w/ BG sub.	w/o BG sub.	
854 - 854	98.0(1) %	76.9(3) %	96.9(2) %	61.9(4) %	2.26
854 - 1550	97.29(3) %	78.7(1) %	98.9(1) %	65.9(1) %	1.86
854 - 1550, 20 km	98.33(3) %	74.0(1) %	98.7(1) %	58.2(1) %	2.15
854 - 854, 40 km	98.9(1) %	75.8(3) %	99.4(1) %	61.8(4) %	2.02

proves the preservation of polarization entanglement during PPQFC. Interestingly, the purity is higher than before, while the fidelity is worse. The decrease in fidelity is due to unitary rotations, which is visible in the density matrix due to the presence of undesired entries. The origin is most probable non-perfect compensation of the polarization rotation between source and converter lab. Nevertheless, we infer from the high purity that PPQFC does not introduce significant depolarization. If we consider fidelity and purity without BGS, we find slightly higher values compared to the source without QFC although the SBR is decreased to 1.86. In fact we do not have an explanation for this result, but it is most likely related to pair-rate fluctuations or the slightly different spectral filter setup.
In the third measurement we add the 20 km fiber into the telecom path (scheme b)) yielding fidelities and purities very similar to those without the fiber. This time the purity is slightly reduced whereas the fidelity is higher. Unfortunately, the pair-rate fluctuations of the source do not allow for precise conclusions on the influence of the converter or the fiber since all values are not fully consistent. Moreover, it is difficult to give reliable error bars since the assumptions of Poissonian-distributed detection events is not fulfilled, i.e. the error bars in Tab. 3.5 are expected to be too small. Nevertheless, fidelities and purities clearly prove entanglement even without BGS. Besides, all values are rather similar, hence a significant degradation due to the converter cannot be identified.
Surprisingly, the best results are obtained in the most complex measurement demonstrating two-step QFC and photon-photon entanglement over 40 km of fiber. We find a fidelity of 98.9(1) % and remarkably high purity of 99.4(1) %. In the absence of unitary rotations the purity would enable a maximum fidelity of even 99.7 %. Those results are quite promising since neither the 40 km fiber, being prone to temperature-induced polarization rotations, nor the double-pass through the converter degrades the purity. An explanation for the higher purity might be that we measured scheme c) at comparable long integration times (several hours instead of a few minutes), hence fluctuating pair rates are potentially averaged out. Moreover, the cavity-lock of the source has been improved before this measurement resulting in a more stable operation. Note that during the preparation of this thesis, the source has been further improved in terms of stability and SBR enabling raw fidelities larger than 90 %, too. We conclude that PPQFC enables entanglement distribution over large kilometer-scale fiber distances with high fidelity. As a comparison: while the transmission through the 40 km fiber is 17.5% at 1550 nm, it is 10^{-14} at 854 nm completely preventing a measurement of entanglement.

3.4 Summary and discussion

In this chapter we presented two PPQFCDs translating photons at 854 nm resonant with the $4^2P_{3/2} \Leftrightarrow 3^2D_{5/2}$ transition in trapped $^{40}Ca^+$-ions to the telecom O-band and C-band at 1310 nm and 1550 nm, respectively. We employ difference-frequency generation in nonlinear WGs made of lithium niobate stimulated by strong classical cw pump lasers at 2456 nm and 1904 nm, respectively. The O-band converter is constructed in a single-crystal Mach-Zehnder configuration to overcome the polarization

dependence of the DFG-process. We simultaneously achieved for both polarization components an EDI of 26.5 %, which compares well with values from polarization-dependent [82, 137, 141, 142, 148] and polarization-preserving [164, 166] QFCDs in the literature. Furthermore, we proved that the efficiency of 26.5 % is independent of the input polarization, a prerequisite for polarization-preserving operation. An unconditional CIB count rate of 11.4 cps was observed, which is to our knowledge the lowest CIB of a QFCD reported so far in the literature. Next, we introduced the schemes to actively stabilize the interferometer path-length difference as well as our superconducting-nanowire single-photon detectors for telecom wavelengths. Both are required to prove polarization-preserving operation by means of quantum process tomography. A maximum process fidelity of 99.75(6) % and a sufficiently good long-term stability with $\mathcal{F}_{\mathrm{pro}} > 99.5\,\%$ over six hours has been observed. To quantify the influence of the converter on $\mathcal{F}_{\mathrm{pro}}$ we performed Monte-Carlo simulations revealing that neither interferometer phase fluctuations nor efficiency mismatches between the polarization components considerably decrease $\mathcal{F}$ in our case.

In the second part we presented the setup and complete characterization of the C-band converter being a clearly improved version of the O-band converter. To ensure polarization preservation, an intrinsically phase-stable Sagnac configuration is employed. In order to boost the EDI, we developed an optimization routine to improve the coupling of input, target and pump field to the fundamental WG mode by maximizing the overlap integral between WG mode and incident beam. With this method we achieved coupling efficiencies larger than 96 % for 854 nm and 1550 nm. Relying on optimized optical components, the EDI is 57.2 % for both polarization components being to our knowledge the highest device efficiency achieved so far for a QFCD. At the same time, the converter features process fidelities around 99.8 % stable over several hours and low background of 24(3) generated cps, which is almost identical to the O-band converter taking the dissimilar device efficiencies into account.

As a first field test, we converted nonclassical light, namely narrowband polarization-entangled photons at 854 nm emitted by an SPDC source, to 1550 nm and demonstrated preservation of polarization entanglement during PPQFC. We briefly introduced the source generating photon pairs in a Ψ^{-} Bell-state with a raw fidelity of 76.9(3) % and a background-subtracted fidelity of 98.0(1) %, as well as the joint setup consisting of source and PPQFCD. First, we demonstrated polarization entanglement between a photon at 854 nm and a telecom photon with a raw (background-subtracted) fidelity of 78.7 % (97.3 %). The background mainly stems from accidental coincidences generated by the source while the contribution of the converter is negligible. Second we extended the range between the photons by inserting 20 km of fiber into the telecom channel. We still observed entanglement with high fidelity of 74.0(1) % (raw) and 98.33(03) % (bg-sub.). Finally, we increased the fiber length to 40 km by means of a double-pass through the fiber and the PPQFCD yielding entanglement between a 854 nm-photon and a doubly-converted 854 nm-photon with fidelities of 75.8(3) % (raw) and 98.9(1) % (bg-sub.). The latter verifies that PPQFC enables entanglement distribution over large fiber distances of more than 40 km and on top a completely bi-directional operation of the PPQFCD.

Table 3.6. Requirements and figures of merit to scale-up QFCDs for quantum networks: Performance of the O- and C-band converter.

Figure of merit/Requirement	O-band converter	C-band converter
High external device efficiency	✔	✔
Low conversion-induced background	✔	✔
High process fidelity of qubit conversion	✔	✔
High frequency and power stability (pump)	✘	✔✘
Reliable 24/7-operation (pump)	✘	✔
Turn-key pump laser system	✘	✔
Compact and transportable system	✘	✘
Stand-alone system and operation	✘	✔
Integration into 19-inch racks	✘	✘
Integration on a single chip	✘	✘
Bi-directional operation (SHG and DFG)	✘	✔
Photon bandwidth manipulation	✘	✘
Conversion to multiple frequency channels	✘	✘
Dispersion cancellation	✘	✘

We finish this chapter by assessing both converters with respect to our criteria for QFCDs in quantum networks introduced in Sect. 2.3. Tab. 3.6 displays the complete list featuring check marks and x-marks indicating if they are fulfilled by the respective QFCD. Starting with the conversion metrics, both devices feature high process fidelities around 99.8 %, which is higher than the best atom-photon entanglement fidelities reported for QNNs so far [59, 89], hence high process fidelity is fulfilled. A similar argument holds for the CIB, which is in the same range as dark-count rates of state-of-the-art superconducting detectors for telecom wavelengths. We will find in the next chapter that the amount of background limits the SBR of single photons emitted by QNNs to nearly 300. To asses the EDI it is helpful to investigate at which fiber distance QFC starts to become beneficial, i.e. at which distance the attenuation losses at the original wavelength are higher than the device efficiency and the losses at the target wavelength. Assuming attenuation coefficients of 3.5 dB/km at 854 nm, 0.3 dB/km at 1310 nm and 0.18 dB/km at 1550 nm, we calculate 1.8 km and 730 m for the O-band and C-band converter, respectively. Both values are below typical distances between QNNs expected for inter-city quantum networks of > 10 km [82, 242]. Regarding the pump laser properties, the integration in existing experiments, and efforts towards miniaturization, we already pointed out at the beginning of Sect. 3.2 that the O-band converter does not fulfill any of those requirements mainly due to the OPO-based pump laser (this may change if the already mentioned Cr^{2+}:ZnSe/S lasers are available with an improved performance with respect to frequency and power stability). On the contrary, the TDFL/TDFA-system at 1904 nm pumping the C-band converter is a convenient turn-key system designed for

24/7-operation. Its output power is stable within a few percent and its frequency is actively stabilized. However, we added a x-mark on this requirement since in quantum networks a much better frequency stability ($\approx$ kHz) and potentially even a phase-lock might be necessary, which requires a much more sophisticated stabilization scheme. Due to the absence of an active stabilization, the C-band converter can be operated completely independent as a stand-alone system. Up to now, no efforts towards miniaturization were made; the converter still requires about one third of an optical table. Ongoing promising work on an improved optical/mechanical setup intends to integrate the whole system including spectral filters and state projection into a 19-inch rack. All advanced functionalities except the already mentioned bi-directional operation of the C-band converter are out of reach with the current devices, but could be implemented in future devices since we currently do not see any fundamental obstacles.

Chapter 4

High-fidelity entanglement between a trapped ion and a telecom photon via quantum frequency conversion

Contributions: The experiments in this chapter have been performed at Saarland University in the labs of Prof. Christoph Becher and Prof. Jürgen Eschner, who jointly supervised the experiments. Matthias Bock (M.B.) and Pascal Eich (P.E.) conceived the experiments and analyzed the data with support from Stephan Kucera (S.K.). The QFCD was operated by M.B. whereas the ion trap was operated by P.E. The ion-photon entanglement sequence has been developed and implemented by P.E., Matthias Kreis and S.K. with advice from Philipp Müller. The software tools to extract the histogramized ion-photon state correlations from the raw data were developed by S.K. while the MLE-based quantum state reconstruction has been implemented by M.B.

The main results in this chapter are published in Nat. Commun. **9**, 1998 (2018) and in the PhD thesis of Pascal Eich [243].

In this chapter we present a complete device generating entangled states between a Zeeman qubit in a trapped $^{40}Ca^{+}$-ion and the polarization state of a telecom photon as an elementary building block for quantum networks. To this end, we combine a trapped-ion QNN with our PPQFCD connecting 854 nm to the telecom O-band at 1310 nm. We characterize the device with respect to entanglement generation rates and SBR, and verify light-matter entanglement at 854 nm and 1310 nm, i.e. before and after PPQFC, via QST. The chapter is organized as follows: in Sect. 4.1.1 we first introduce our trapped-ion QNN and briefly explain how we trap and manipulate $^{40}Ca^{+}$-ions. Next, we present the experimental sequence and results of entanglement generation between a single ion and the polarization state of an emitted photon at 854 nm (Sect. 4.1.2). Finally, we describe the complete device combining the trapped-ion QNN with PPQFC

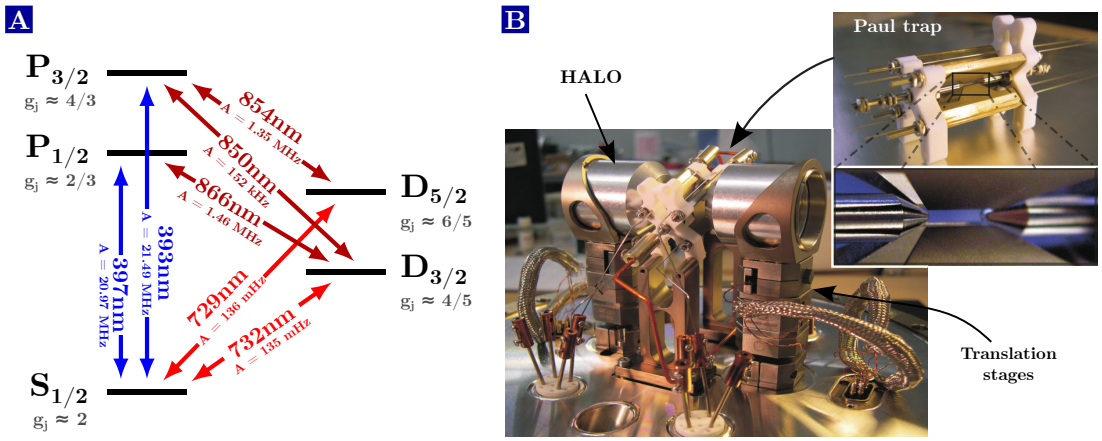

Figure 4.1. Ion trap and $^{40}Ca^{+}$-ion level scheme. **(A)** The level scheme of $^{40}Ca^{+}$-ions with all relevant levels and optical transitions. The transitions at 393/397 nm and 850/854/866 nm are dipole-allowed while those at 729/732 nm are quadrupole transitions. g_j denote the Landé-factors and A the Einstein coefficients. **(B)** Picture of the ion trap setup outside the vacuum chamber. Ions are stored in a linear Paul trap made of blade-shaped electrodes. Photon collection from the ion is realized with high-aperture laser objectives (HALOs) mounted on piezo translation stages. Both figures were created by S. Kucera [204]

and demonstrate the preservation of light-matter entanglement during PPQFC with high fidelity (Sect. 4.2).

4.1 Quantum node based on single trapped $^{40}Ca^{+}$-ions

In this thesis, we utilize $^{40}Ca^{+}$-ions, a well-studied ion species for QIP, whose level scheme including the Landé-factors g_j and all relevant optical transitions with their respective Einstein coefficients A, is shown in Fig. 4.1a. The ion has a long-lived ground state ($S_{1/2}$) and two short-lived excited states $P_{3/2}$ and $P_{1/2}$ with a lifetime of about 7 ns. Ground and excited states are connected via optical dipole transitions at 393 nm and 397 nm, which are utilized for Doppler cooling, fluorescence-based state-readout, and as excitation path for light-matter entanglement generation. Moreover, Ca^{+}-ions possess two metastable states $D_{3/2}$ and $D_{5/2}$ with a lifetime of roughly 1.17 s. All states have several Zeeman sublevels; for the sake of clarity they are not shown in Fig. 4.1a. The D-states are connected to the ground state via quadrupole transitions at 729 nm and 732 nm and to the P-states via dipole transitions at 850 nm, 854 nm and 866 nm. While the transition at 854 nm is our photonic interface, coherent manipulation of the ion for high-fidelity state readout or the preparation of atomic qubits makes use of the quadrupole transition at 729 nm.

4.1.1 Trapping and coherent manipulation of single ions

In this section we briefly introduce the ion trap and the tools to perform coherent manipulation and atomic-state analysis. The setup has been developed by the Eschner

group over many years, hence a much more detailed description can be found in the PhD theses of P. Eich [243], S. Kucera [204], C. Kurz [244], and J. Huwer [245].
We store ions in a linear Paul trap depicted in the inset of Fig. 4.1b. The trap consists of four blade-shaped stainless-steel electrodes mounted on marcor holders. Two opposite electrodes are grounded whereas a radio frequency (RF) voltage with $\nu \approx 25.9\,\mathrm{MHz}$ is applied to the two remaining electrodes to generate the oscillating potential for the radial confinement of the ions. The axial confinement is ensured by a constant voltage applied to two end-tip electrodes. The radial and axial trap frequencies are determined by the trap geometry and the amplitudes of the RF and static voltages, and given as $\omega_{\mathrm{rad}} \approx 2\pi \cdot 3.7\,\mathrm{MHz}$ and $\omega_{\mathrm{ax}} = 2\pi \cdot 1.166\,\mathrm{MHz}$, respectively. To load the trap with single ions, neutral Ca-atoms are dispensed by an resistive-heater oven and ionized in two steps using a narrowband frequency-doubled laser at 422.67 nm and a broad UV-LED emitting around 380 nm [246].
Photon collection from the ion employs two high-aperture laser objectives (HALOs) as shown in Fig. 4.1b. The Paul trap is located in the middle between the two HALOs, the axis through the HALOs is defined as 0°-axis. To ensure optical access under 90°, the trap is mounted at an angle of 22.5° with respect to the 90°-axis (an alternative are holes in the end-tip electrodes). Both HALOs are mounted on xyz-translation stages for precise positioning with respect to the ion. The HALOs allow for diffraction limited imaging and are AR-coated for all transition wavelengths. They have a numerical aperture (NA) of 0.4 corresponding to an opening angle of about 47.2° and a covered solid angle of $\Omega = 4\pi \cdot 4.17\,\%$. During the experiments in this thesis, one HALO is aligned to achieve best coupling of emitted 854 nm-photons into a SM fiber, whereas the second HALO is optimized for collection of fluorescence light at 397 nm.
We can apply magnetic fields in all three directions by means of three coil pairs mounted to the flanges outside the vacuum chamber. We perform all experiments with a magnetic field of 2.8 Gauss along the axis through the HALOs, which defines the quantization axis (z-axis) of the ion. The coil pairs on the x- and y-axis are used to compensate for the earth magnetic field as well as further stray fields originating e.g. from magnetic mirror mounts or electrical devices. A well-known source of decoherence of atomic Zeeman qubits with different magnetic quantum numbers m is magnetic field noise (in all three directions). For instance, time-dependent z-fields change the energy difference between the qubit states and accordingly influence the temporal evolution of the qubit phase. Although the evolution is coherent, it may differ for each prepared superposition state, which effectively destroys the phase coherence (so-called shot-to-shot dephasing) and typically limits the T_2-time of the ground-state Zeeman qubit to a few hundreds of microseconds. Prominent frequency components in the noise are the 50 Hz power-line frequency and its higher harmonics. The components at 50 Hz and 150 Hz are compensated by an active feed-forward control loop lifting the coherence time of the ground-state qubit to $T_2 \approx 800\,\mu\mathrm{s}$. Note that the constant magnetic field in z-direction acts as a guiding field, i.e. field noise in x- or y-direction, whose amplitude is typically much weaker than the constant z-field, is strongly suppressed since they have only a tiny influence on length and direction of the total field vector. Hence, the dominant contribution originates from field noise in z-direction.

Cooling and coherent manipulation

For cooling and coherent manipulation on the optical dipole and quadrupole transitions, frequency-stabilized external cavity diode-lasers (ECDLs) are utilized. The following lasers are used during the experiments in this thesis:

(I) **397 nm:** Laser light at 397 nm is generated by a frequency-doubled, amplified diode laser at 794 nm. We employ this laser for Doppler cooling and fluorescence-based state readout.

(II) **866 nm:** The laser at 866 nm is required as repumper of the metastable $D_{3/2}$-state, which gets populated during Doppler cooling and fluorescence readout with 397 nm.

(III) **393 nm:** Light at 393 nm is utilized to excite the ion on the $S_{1/2} \Leftrightarrow P_{3/2}$ transition for the generation of single photons at 854 nm (cf. Chap. 5).

(IV) **854 nm:** We use the 854 nm laser as repumper of the $D_{5/2}$-state and to excite the ion on the $D_{5/2} \Leftrightarrow P_{3/2}$ transition for single-photon generation at 854 nm. Moreover, this laser is frequency-doubled to 427 nm serving as pump laser for the SPDC source employed in Chap. 3.

(V) **729 nm:** Coherent manipulation on the $S_{1/2} \Leftrightarrow D_{5/2}$ transition for optical pumping, state preparation and Zeeman-selective state readout is performed with the 729 nm laser (Rabi frequency up to $\Omega \approx 2\pi \cdot 250\,\mathrm{kHz}$).

All lasers interacting with dipole transitions have to possess linewidths much below the natural linewidths in the order of a few MHz, and a sufficient long-term stability to enable experiments over several days. We achieve this by locking the laser frequency with the so-called transfer-lock scheme [247]. The scheme is based on a master laser, which is frequency-stabilized to an absolute reference. In our case this is a diode laser at 852 nm locked to a hyperfine transition of the Caesium D2-line by means of Doppler-free saturation spectroscopy of an atomic vapor. The stability of this laser is transferred to all other lasers using a series of optical cavities, whose lengths are locked to the 852 nm laser via the Pound-Drever-Hall (PDH) technique. The cavities are doubly-resonant for 852 nm and the wavelength of the slave laser we intend to stabilize (e.g. 854 nm), i.e. if we lock the slave laser frequency to a cavity resonance (again via the PDH-technique), the absolute frequency stability of the master laser is effectively transferred to the slave laser. Typical values of the achieved stability are in the order of a few hundreds of kHz. Note that we employ the scheme in Chap. 6 in a very similar configuration to stabilize the pump laser of the QFCDs for 780 nm, hence a more detailed description is given there. Coherent manipulation on a quadrupole transition has significantly higher demands on the spectral properties of the laser: the linewidth as well as the long-term stability should be in the Hz-regime. Thus, the 729 nm laser is locked to a high-finesse ultra-low expansion (ULE) cavity (Finesse $\approx$480000, linewidth $\approx$4 kHz). The temperature-stabilized cavity is placed within an evacuated chamber and mounted on an active vibration-isolation platform resulting in a low drift rate of 80 mHz/s. Note

that it would be an arbitrary coincidence if the longitudinal cavity modes are exactly located at the respective optical transitions, i.e. we use AOMs to tune the lasers to the correct frequency.
Coherent manipulation on the magnetic dipole transition $S_{1/2}, m = -1/2 \Leftrightarrow S_{1/2}, m = +1/2$ with a frequency of roughly $2\pi \cdot 7.8\,\mathrm{MHz}$ is achieved with a RF-field generated by a coil below the vacuum chamber (Rabi frequency $\Omega \approx 2\pi \cdot 100\,\mathrm{kHz}$).

The experiment is controlled on a sub-microsecond time-scale by a PXI-based commercially available system ("Hydra", *Signadyne, now: Keysight Technologies*), which is synchronized to an external atomic clock. The system features a series of arbitrary waveform generators (AWG) to control amplitude, frequency and phase of the lasers via AOMs, a 8-channel time-to-digital converter (TDC) with 320 ps resolution to record detection events from the APDs or SNSPDs, and 64 digital input/output channels, e.g. for amplitude control of the lasers or trigger signals to synchronize external devices to the sequence. Fast experimental sequences of laser/RF-pulses and state-readout cycles are programmed using flow-charts and directly executed on the PXI cards. Different sequences (e.g. the main experiment sequence or intermediate spectroscopy sequences) are initialized by an attached PC using Matlab scripts. For the measurements including QFC, the output pulses from the SNSPDs as well as trigger pulses for the interferometer path length stabilization are transmitted between the telecom lab and the control unit via 90 m long BNC cables laid alongside the optical fibers. In fact, the cable length is already critical since electronic pulses are considerably attenuated. Thus, the input threshold of TDC has to be lowered almost to the minimum to record the SNSPD pulses. In future experiments involving even longer distances, optical communication systems will have to be implemented to replace BNC cables.

4.1.2 Ion-photon entanglement at 854 nm

Entanglement generation scheme and experimental setup

In this section we proceed with the generation and verification of entanglement between two Zeeman states of the $D_{5/2}$-manifold and the polarization of a spontaneously emitted photon at 854 nm. The principle idea of the entanglement generation scheme is sketched in Fig. 4.2a. We start in the $S_{1/2}$ ground-state and excite the ion to the short-lived $P_{3/2}$-state with a π-polarized laser at 393 nm perpendicular to the quantization axis. Spontaneous decay to the $D_{5/2}$-state leads to entanglement between the Zeeman states $|\downarrow\rangle = \left|D_{5/2}, m = -3/2\right\rangle$ and $|\uparrow\rangle = \left|D_{5/2}, m = +1/2\right\rangle$, and the polarization states $|\sigma^+\rangle$ and $|\sigma^-\rangle$ of the emitted 854 nm-photon. For photon collection along the quantization axis – determined by the static magnetic field – $|\sigma^+\rangle$ and $|\sigma^-\rangle$ correspond to $|R\rangle$ and $|L\rangle$, respectively. Since the two transitions have different Clebsch-Gordan coefficients (CGC) of $\sqrt{6/15}$ for σ^+ and $\sqrt{3/15}$ for σ^-, the decay probabilities differ by a factor two. Thus, the theoretically expected ion-photon entangled state is not a Bell-state, but the

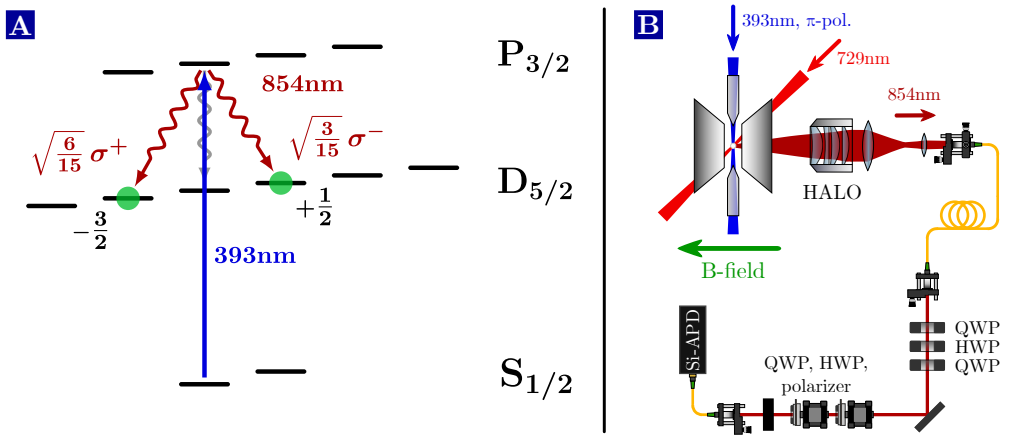

Figure 4.2. Setup and level scheme for ion-photon entanglement generation. **(A)** Ion-photon entanglement at 854 nm is generated via spontaneous decay from the $P_{3/2}$- to the $D_{5/2}$-state after excitation with a π-polarized laser at 393 nm perpendicular to the quantization axis. Since the emitted photons are collected along the quantization axis, π-polarized photons (gray arrow) are suppressed. **(B)** Schematic setup of the trapped-ion QNN. A detailed explanation of the setup is given in the main text.

asymmetric state

$$|\Psi\rangle_{\text{asym}} = \sqrt{\frac{2}{3}}\,|\sigma^+,\downarrow\rangle + \sqrt{\frac{1}{3}}\,|\sigma^-,\uparrow\rangle$$
$$= \sqrt{\frac{2}{3}}\,|R,\downarrow\rangle + \sqrt{\frac{1}{3}}\,|L,\uparrow\rangle\,. \tag{4.1}$$

The experimental setup is shown in Fig. 4.2b. We collect the emitted photons at 854 nm with one of the HALOs. The photons pass a demagnifying telescope and are coupled to a SM fiber with an efficiency of 39 %. Behind the fiber, a combination of QWP, HWP and QWP is used to compensate for unitary rotations induced by the fiber and optical elements in the beam path (e.g. HALO, viewport, dichroic mirrors,...). To perform tomography of the polarization state, we use the known setup consisting of motorized half- and quarter-wave plates, polarizer and a silicon APD (SPCM-AQR-14, *Perkin Elmer*) with 30 % SDE and a DCR of 117.7 cps.

We mentioned earlier that the HALO covers a solid angle of $4\pi \cdot 4.17\,\%$, hence we may naively assume a collection efficiency of 4.17 %. However, we have to account for different spatial dipole emission patterns of π- and σ-transitions as well as destructive interference effects due to the SM fiber coupling. A detailed description of this can be found in the PhD-thesis of P. Eich [243], here we sketch briefly the main results. We define the ion reference frame with the quantization axis as z-axis and the x-axis in the optical table plane. An observer at the location (θ, φ) with the azimuthal angle θ with respect to the z-axis and the polar angle φ defined in the x-y plane detects emitted photons with a certain polarization. The latter is defined in its own reference frame with the z-axis being parallel to the $\vec{k}$-vector of the photon. We obtain for the

position-dependent, normalized amplitudes for π- and σ-polarized emission

$$\vec{A}_{\pi} = -\sqrt{\frac{3}{8\pi}}\sin(\theta)\,\vec{e}_{H,ph} \quad \text{and} \quad \vec{A}_{\sigma^{+/-}} = \sqrt{\frac{3}{8\pi}}\,\frac{e^{i\varphi}}{2}\,(\cos(\theta)\,\vec{e}_{H,ph} \pm i\,\vec{e}_{V,ph}) \quad (4.2)$$

with the unit vectors $\vec{e}_{H,ph}$ and $\vec{e}_{V,ph}$ for H- and V-polarized light, which correspond to the unit vectors in the ion reference frame in θ- and φ-direction, respectively. We find that the π-emission pattern is doughnut-like shaped with maximal intensities perpendicular to the z-axis, in which the atomic dipole oscillates, and minimal intensities along the z-axis. In contrast, σ-emission has its maximum along the quantization axis. For $\theta = 0°$, σ^{+} and σ^{-} correspond to R- and L-polarized light, respectively. To calculate the free-space collection efficiencies η_{fs}, we integrate the spatial emission patterns over the opening angle (47.2°) of the HALO for symmetric collection along the quantization axis, yielding

$$\eta_{\text{fs}}^{\pi} = \int_{\theta=0}^{47.2°/2}\int_{\varphi=0}^{2\pi}\left|\vec{A}_{\pi}(\theta,\varphi)\right|^2 \sin(\theta)\,\mathrm{d}\theta\,\mathrm{d}\varphi \approx 0.51\,\%$$

$$\eta_{\text{fs}}^{\sigma^{+/-}} = \int_{\theta=0}^{47.2°/2}\int_{\varphi=0}^{2\pi}\left|\vec{A}_{\sigma^{+/-}}(\theta,\varphi)\right|^2 \sin(\theta)\,\mathrm{d}\theta\,\mathrm{d}\varphi \approx 6.02\,\%. \quad (4.3)$$

Hence, we collect 0.51 % and 6.02 % of the total emitted intensity in 4π for π- and σ-transitions, respectively. For the calculation of the fiber-coupling efficiency we have to consider the complex electric fields $\vec{E}_{\pi/\sigma^{+/-}} \propto ie^{ikr} \cdot \vec{A}_{\pi/\sigma^{+/-}}$, which includes the phase information and gives rise to interference effects at the fiber facet. Calculating the overlap between the electric fields and the fiber mode indicates that σ-polarized photons can be coupled with maximal 40 % efficiency to the fiber, whereas π-polarized photons are completely suppressed due to destructive interference [243]. The latter can be intuitively understood from the rotational symmetry of $\vec{A}_{\pi}$ with respect to φ, i.e. the contributions from φ and $\varphi + \pi$ cancel each other. In our case, we take advantage of this since a contribution from the π-transition results in a reduction of the Bell-state fidelity of the ion-photon state. Taking into account the CGCs for σ- and π-decay (σ^{+}:$\sqrt{6/15}$, σ^{-}:$\sqrt{3/15}$, π:$\sqrt{6/15}$), the final collection probability for σ-emission is $0.6 \times 6.02\,\% \approx 3.61\,\%$. The measured coupling efficiency to the SM fiber is 39 %, which is consistent with the calculated overlap and results in a total collection efficiency $\eta_{\text{coll}} \approx 1.4\,\%$.

Actually, the scheme to create ion-photon entanglement introduced above is simplified a lot and necessitates a more detailed treatment. The first issue arises from the unfavorable branching ratio between the 854 nm- and 393 nm-transitions. Considering the Einstein coefficients $A_{393} = 21.49\,\text{MHz}$, $A_{854} = 1.35\,\text{MHz}$ and $A_{850} = 152\,\text{kHz}$ (see Fig. 4.1a) we find that the ion decays with a probability of about 93.4 % via the 393 nm-transition and only with 5.9 % via the desired 854 nm-transition. Thus, for excitation with a resonant and sufficiently short (shorter than the $P_{3/2}$-state lifetime of 7 ns) π-pulse at 393 nm, the entanglement generation rate at 854 nm would be quite low. The best possibility to solve this issue are cavity-mediated Raman transitions where the

branching ratio is manipulated in favor of the 854 nm-transition by means of cavity QED techniques [59]. However, this approach is technically sophisticated and requires many years of development. Thus, we generate single photons not by π-pulse excitation, but via spontaneous Raman-scattering employing "quasi-cw" excitation with a 3 µs long off-resonant 393 nm-pulse. The efficiency to generate a photon at 854 nm within the 3 µs is close to 100 % for a sufficiently high laser power, since we re-excite the ion after each decay to the ground state until it decays to the metastable $D_{5/2}$-state where it cannot be excited anymore. The dynamics of this process is quantified by simulations, which can be found in P. Eich's PhD thesis [243]. The scheme is beneficial in terms of generation efficiency, but it suffers from two disadvantages: first, the time-bandwidth product of the emitted photons is not at the Fourier-limit anymore, since the photons end up in a temporally mixed state. The wavepacket is at least a factor 17 longer than expected from the natural linewidth[1]. The second issue is the creation of a statistical mixture of two ion-photon entangled states as illustrated in Fig. 4.3b. If the ion decays back to $|S_{1/2}, m = +1/2\rangle$ under emission of a σ^--photon at 393 nm, it is re-excited to $|P_{3/2}, m = +1/2\rangle$, which results in the generation of an entangled state with a different atomic qubit. The emitted photons related to this qubit cannot be distinguished from the desired photons and lower the fidelity of the desired entangled state. To solve this problem, we detect the population in the "wrong" atomic-qubit states via fluorescence readout and discard those events in the QST. A detailed description of this method is presented in the following section.

Experimental sequence

The experimental sequence is illustrated in Fig. 4.3a. It starts with 8.25 µs of Doppler cooling on the $S_{1/2} \Leftrightarrow P_{1/2}$ transition including repumping of population from the $D_{5/2}$- and $D_{3/2}$-manifold with laser light at 854 nm and 866 nm, respectively. The comparable short cooling time is sufficient since the scheme does not rely on resonant excitation pulses, which typically heat up the ion. After cooling, the ion is in a mixture between the two ground-state Zeeman levels. Note that optical pumping to one of the Zeeman-states is possible, but not helpful. The states get mixed anyway due to the above mentioned back-decay during the excitation cycle. It follows a 3.05 µs long π-polarized excitation pulse at 393 nm to excite the ion to $P_{3/2}$. Spontaneous Raman-scattering of a single 854 nm-photon creates a mixture of the two ion-photon entangled states

$$|\Psi\rangle_{\text{asym}} = \sqrt{\frac{2}{3}}\,|R,\downarrow\rangle + \sqrt{\frac{1}{3}}\,|L,\uparrow\rangle \qquad \text{and} \tag{4.4}$$

$$|\Psi\rangle_{\text{unde}} = \sqrt{\frac{1}{3}}\,\big|R, D_{5/2}\, m = -1/2\big\rangle + \sqrt{\frac{2}{3}}\,\big|L, D_{5/2}\, m = +3/2\big\rangle \tag{4.5}$$

[1] In fact, this is almost uncritical for ion-photon entanglement apart from a larger amount of uncorrelated background due to the longer wavepacket. However, the effect significantly reduces the visibility of Hong-Ou-Mandel interference of photons from independent trapped ions and accordingly the success rate of photonic Bell-state measurements, which is associated with the generation rate of remote ion-ion entanglement.

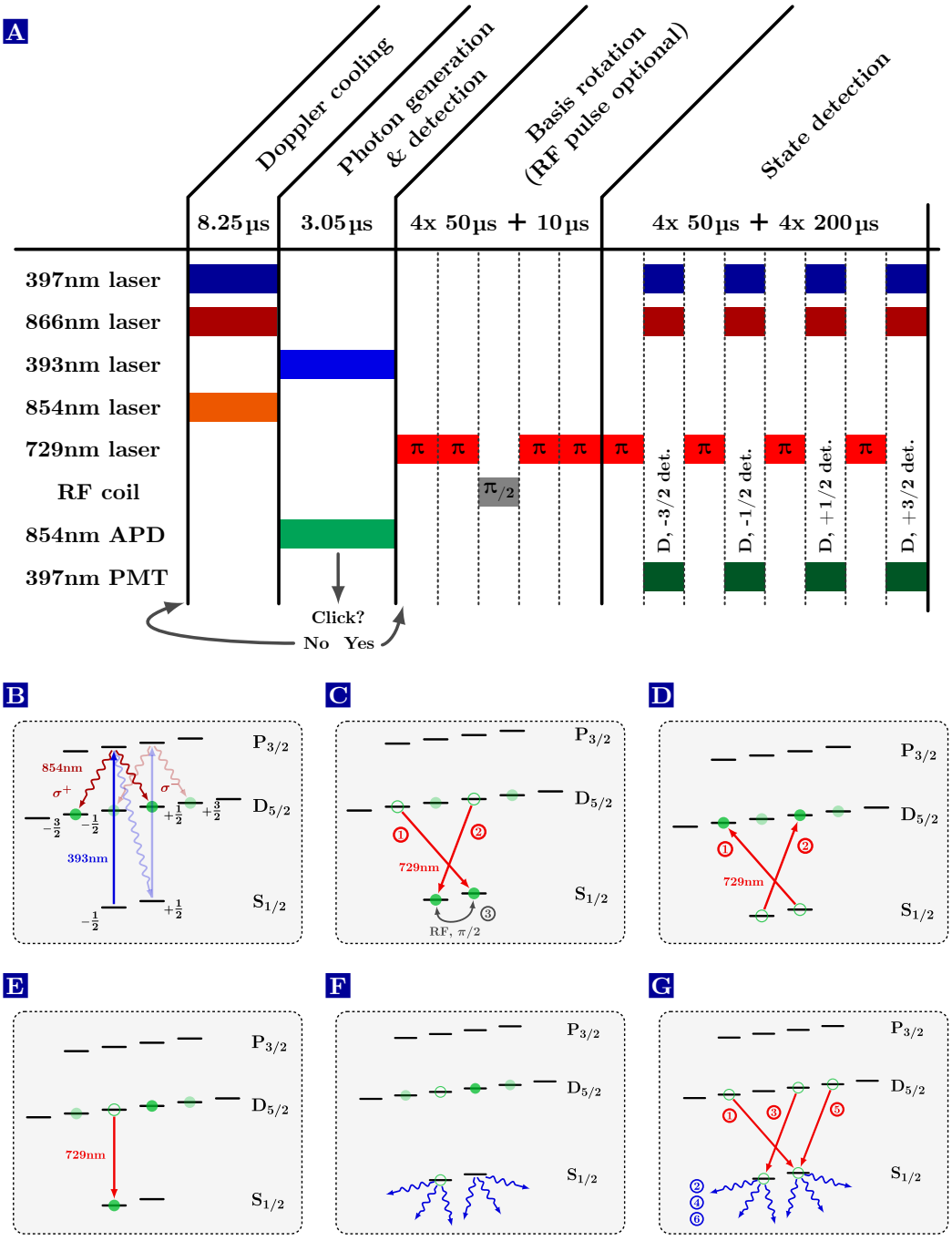

Figure 4.3. Experimental sequence for ion-photon entanglement generation. **(A)** Timeline of the experimental sequence showing all lasers and detectors. Doppler cooling and photon generation are repeated until a photon is detected by the APD, which triggers the atomic-state readout. **(B)** Spontaneous decay via the 393 nm-transition to $|S_{1/2}, m = +1/2\rangle$, subsequent excitation to $|P_{3/2}, m = +1/2\rangle$ and decay via the 854 nm-transition leads to a mixture of two entangled states. **(C)** – **(G)** Pulse sequences of the fluorescence-based atomic-state readout. The $\pi/2$-pulse on the RF-transition is optional and only applied for σ_x/σ_y-measurements.

with $|\Psi\rangle_{\text{unde}}$ being the undesired second entangled state. In addition, there is a small probability of 0.66 % for a decay from $P_{3/2}$ to the $D_{3/2}$-manifold upon emission of a photon at 850 nm. These photons are also collected and detected, i.e. we have to detect population in $D_{3/2}$ and discard these events during the atomic-state readout to avoid a decrease in fidelity.
The atomic-state analysis is performed conditioned on the detection of a photon within the 3.05 µs time window. In case of no detection event the sequence restarts with Doppler cooling. Note that this represents the post-selection process mentioned in Sect. 2.2.2: for the evaluation we only consider the cycles in which the photonic qubit is detected. The readout sequence starts with a coherent transfer of the atomic qubit to the ground-state Zeeman qubit by two 50 µs long π-pulses at 729 nm (Fig. 4.3c). Projective measurements in the superposition bases ($\sigma_{\text{x/y}}$) require an additional basis rotation. To this end, we apply a 10 µs long $\pi/2$-pulse on the RF-transition with a fixed phase to rotate orthogonal superposition states to the respective eigenstates, i.e. the phase of the superposition state is translated to population of the eigenstates according to

$$\sqrt{1/2}|m = -1/2 + m = +1/2\rangle \quad \rightarrow \quad |m = +1/2\rangle \tag{4.6}$$

$$\sqrt{1/2}|m = -1/2 - m = +1/2\rangle \quad \rightarrow \quad |m = -1/2\rangle. \tag{4.7}$$

Subsequently, the population is shelved back to $D_{5/2}$ by two pulses at 729 nm (Fig. 4.3d). In case of a σ_{z}-measurement the population transfer is still performed and the RF pulse is replaced by a 10 µs waiting time to obtain the same time delays. Next, we read out the atomic state by means of fluorescence detection, which correspond to the atomic σ_{z}-measurement (see Fig. 4.3e/f/g). We first transfer the population from $|D_{5/2}, m = -1/2\rangle$ (one of the undesired qubit states) to the ground state and switch on the cooling lasers at 397 nm and 866 nm. Scattered photons at 397 nm are collected with the second HALO, coupled to a multi-mode fiber, and detected with a photomultiplier tube (PMT). If the detected counts integrated over 200 µs surpass a certain threshold, we record a "bright"-event, i.e. a positive measurement outcome of the respective projector. In this particular case, we want to detect and eliminate the undesired state, hence we omit bright-events for the QST. The reason, that we start with one of the undesired states, is to eliminate in the same step detection events from erroneously emitted photons at 850 nm. The emission of 850 nm-photons and decay to $D_{3/2}$ results in a bright-event since the $D_{3/2}$-states are part of the cooling cycle. Finally, we read out the two qubit states $|\downarrow\rangle$ and $|\uparrow\rangle$ as well as the second undesired state by further π-pulses at 729 nm followed by fluorescence detection. The whole sequence without atomic-state analysis takes 11.3 µs (8.25 µs for Doppler cooling and 3.05 µs for photon generation), yielding a maximum achievable repetition rate of nearly 88.5 kHz. In the experiment the rate will be lower due to the state analysis conditioned on the detection of a photon; the exact value depends on the number of detected photons.

Photon wavepackets and generation rates

Prior to the characterization of the entangled state via QST, we take a closer look to the photon wavepacket as well as entanglement generation rates and SBR. Fig. 4.4a shows the measured wavepacket obtained via time-correlated single photon counting (TCSPC) employing the sequence trigger as start and detection events of the APD as stop trigger. We find the expected one-sided exponential decay with a time constant (1/e-width) of 240(2) ns extracted from a fit to the data (red solid line). Hence, the length of the wavepacket exceeds the excited state lifetime of 7 ns by a factor 34. The lower limit would be a factor 17 determined by the branching ratio between 393 nm and 854 nm-transitions, which prevents the generation of Fourier-limited photons in quasi-cw excitation. The difference between the two factors stems from a limited laser power at 393 nm, which does not allow for driving the transition in saturation [243].
Note that we did not measure the wavepacket separately, but added up all individual measurements from the QST in different basis settings. Thus, the displayed numbers actually correspond to coincidences between the sequence trigger and photon detection events conditioned on bright-events from the desired atomic qubit in the atomic-state readout (i.e. detected photons stemming from a decay to the second atomic qubit or the $D_{3/2}$-state under emission of a 850 nm-photon are already discarded).
To maximize the SBR in the evaluation, we apply time-filtering of the detected coincidences. We take into account all coincidences within a 300 ns long time window displayed in Fig. 4.4a. The window incorporates 69.6 % of the coincidences of the whole wavepacket and is a good trade-off between SBR, which decreases with larger time windows, and the amount of signal coincidences. First, we deduce the entanglement generation rate $\gamma_{\mathrm{gen}}^{854}$ from the time-filtered number of coincidences. To this end, we only consider signal coincidences excluding background stemming from APD dark-counts (the subtraction is performed as described in Sect. 2.2.3). With 114200 coincidences in 4132 s we obtain for the detected rate

$$\gamma_{\mathrm{det}}^{854} = \frac{114200}{4132\,\mathrm{s}} = 27.6\,\mathrm{Hz}. \tag{4.8}$$

The entanglement generation rate is calculated by dividing the detected rate by the efficiency of the projection and detection setup, yielding

$$\gamma_{\mathrm{gen}}^{854} = \frac{27.6\,\mathrm{Hz}}{T_{\mathrm{pol,trans}} \cdot f_{\mathrm{pol,ab}} \cdot \eta_{\mathrm{fiber}} \cdot \eta_{\mathrm{apd}}} = 256\,\mathrm{Hz} \tag{4.9}$$

with the transmission of the polarizer $T_{\mathrm{pol,trans}} = 78\,\%$, the quantum efficiency of the APD $\eta_{\mathrm{apd}} = 30\,\%$, and the coupling efficiency to the fiber between projector and APD $\eta_{\mathrm{fiber}} = 92\,\%$. The factor $f_{\mathrm{pol,ab}} = 50\,\%$ takes into account that the polarizer absorbs photons orthogonally-polarized to its orientation, i.e. on average one half of the photons is absorbed. As a check for consistency, we measured all individual efficiencies and transmissions between ion trap and detectors to estimate the theoretically expected rate. With a repetition rate of $\gamma_{\mathrm{rep}}^{854} \approx 58\,\mathrm{kHz}$ we calculate

$$\gamma_{\mathrm{gen,\,theo}}^{854} = \gamma_{\mathrm{rep}}^{854} \cdot \eta_{\mathrm{coll}} \cdot f_{\mathrm{mix}} \cdot f_{850} \cdot f_{\mathrm{window}} \approx 254\,\mathrm{Hz}. \tag{4.10}$$

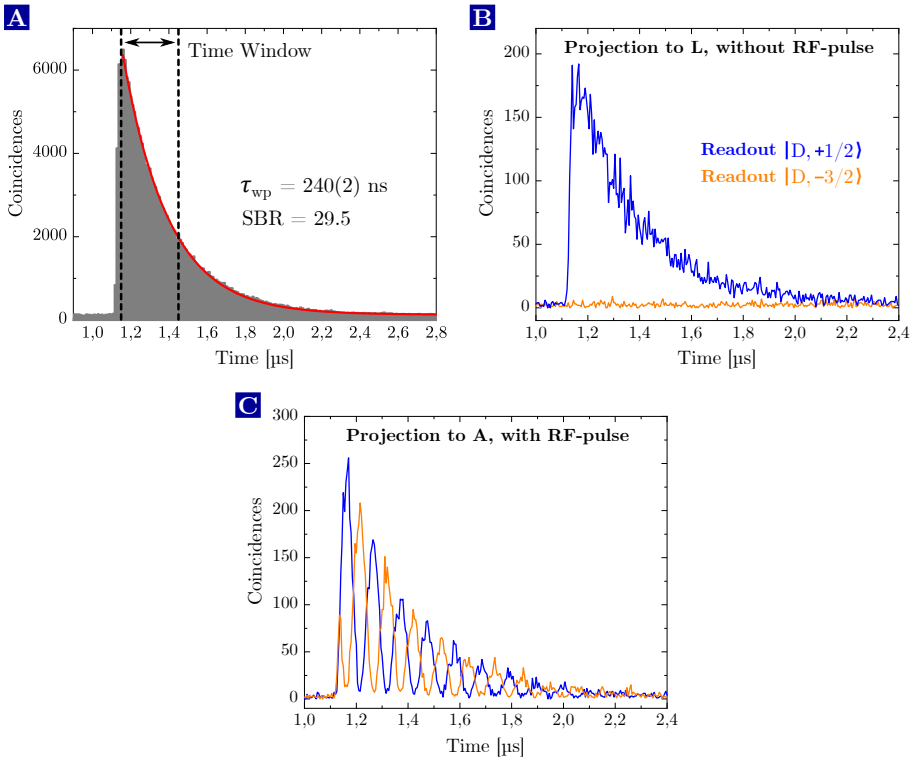

Figure 4.4. Photon wavepackets at 854 nm **(A)** Time-correlated coincidences between the sequence trigger and detected photons conditioned on bright-events from the atomic-state readout. An exponential fit gives a time constant of 240(2) ns. QST takes into account coincidences within the displayed 300 ns long time interval corresponding to 69.6 % of the whole wavepacket. **(B)** Time-correlated coincidences for joint σ_z-measurements of both qubits. **(C)** The same is in **(B)** but now both qubits are projected to superposition bases. The oscillations represent the Larmor precession of the atomic qubit, whose period is much shorter than the length of the photon. We can consider this as a read-out in a rotating basis, i.e. one setting is sufficient to extract all atomic σ_x/σ_y-measurements.

being in very good agreement with the measured rate. The individual terms denote the collection efficiency from the ion $\eta_{\text{coll}} = 1.4\,\%$, and the fraction of the coincidences within the 300 ns time-window $f_{\text{window}} = 69.6\,\%$. Since the entanglement generation scheme creates a statistical mixture of two entangled states with different Zeeman qubits in the $D_{5/2}$-manifold, half of the photons arises from a decay to the second qubit, which we take into account with $f_{\text{mix}} = 50\,\%$. Moreover, decay to the $D_{3/2}$-state and emission of a photon at 850 nm further reduces the efficiency for 854 nm-photon generation. With the Einstein coefficients of the two transitions $A_{854} = 1.35\,\text{MHz}$ and $A_{850} = 0.152\,\text{MHz}$, respectively, we get for the correction factor $f_{850} = A_{854}/\left(A_{854} + A_{850}\right) = 89.9\,\%$.
We calculate a SBR of 29.5, determined by the number of signal coincidences (114200 in 4132 s) divided by the number of background coincidences $B_{854} = 3868$ within the 300 ns window. In contrast to the experiments with the SPDC source, the background is solely determined by APD dark-counts. We confirm this by calculating the theoretically

expected background from the measured DCR of the APD ($R_{\mathrm{dcr,\,apd}} = 117.7\,\mathrm{cps}$). We find

$$B^{854}_{\mathrm{theo}} = R_{\mathrm{dcr,\,apd}} \cdot 300\,\mathrm{ns} \cdot \gamma^{854}_{\mathrm{rep}} \cdot f_{\mathrm{mix}} \cdot f_{850} \cdot 4132\,s = 3803 \tag{4.11}$$

being in good agreement with the measured number. We mentioned in Sect. 2.1.2 that in the case of triggered single-photon sources with time-gating the probability to detect a dark count within the time window – given by $R_{\mathrm{dcr,\,apd}} \cdot 300\,\mathrm{ns}$ – is the relevant measure. This is the reason why we achieve a SBR much larger than one although $R_{\mathrm{dcr,\,apd}} > \gamma^{854}_{\mathrm{det}}$.

Ion-photon entanglement

Leading to the characterization of ion-photon entanglement, four exemplary photon wavepackets of different basis settings are illustrated in Fig. 4.4b & c. For a σ_z- measurement of both qubits (without the optional RF-pulse in the state analysis) we only expect coincidences for joint projections onto $|R\rangle$ and $|D, -3/2\rangle$ or $|L\rangle$ and $|D, +1/2\rangle$. This is clearly visible in Fig. 4.4b for a projection to $|L\rangle$ in terms of a large contrast in coincidences conditioned on bright-events from the two atomic states. A different outcome appears in Fig. 4.4c: it displays the wavepackets for a readout of both qubits in superposition bases (with RF-pulse). If we consider the entangled state given in Eq. 4.1, we do not expect – in a fixed basis setting – oscillations in time, but a similar result as in Fig. 4.4b. However, the atomic qubit is formed by Zeeman states with an energy splitting proportional to the static magnetic field applied along the quantization axis. Hence, if we prepare a superposition state, its relative phase oscillates in time with the Larmor frequency $\omega_{\mathrm{L}} = \Delta E/\hbar = g\mu_{\mathrm{B}}\Delta m B/\hbar$, which is in the order of a few MHz. Accordingly, the entangled state becomes time-dependent

$$|\Psi\rangle_{\mathrm{asym}}(t) = \sqrt{\frac{2}{3}}\,|R,\downarrow\rangle + \sqrt{\frac{1}{3}}\,e^{\phi_0 + i\omega_{\mathrm{L}}(t - t_{\mathrm{emit}})}\,|L,\uparrow\rangle \tag{4.12}$$

with t_{emit} being the emission time of the photon. This time is relevant since the relative phase starts to oscillate only after the entangled state is created via the emission of a photon. In the experimental sequence the atomic-state readout is initialized at a fixed time t_{readout} with respect to the sequence trigger at $t = 0$, which is independent of t_{emit}. Thus, the probabilities to find the photon for instance in $|H\rangle$ and the atomic qubit in one of the states $|+\rangle_{\mathrm{x}}$ or $|-\rangle_{\mathrm{x}}$ at time t_{readout} are

$$\begin{aligned} p_{H,+}(t_{\mathrm{readout}}) &= |\langle H, +_{\mathrm{x}}\,|\,\Psi_{\mathrm{asym}}\rangle|^2 = \frac{1}{4} + \frac{\sqrt{2}}{6}\cos(\phi_0 + \omega_{\mathrm{L}}\Delta t) \\ p_{H,-}(t_{\mathrm{readout}}) &= |\langle H, -_{\mathrm{x}}\,|\,\Psi_{\mathrm{asym}}\rangle|^2 = \frac{1}{4} - \frac{\sqrt{2}}{6}\cos(\phi_0 + \omega_{\mathrm{L}}\Delta t) \end{aligned} \tag{4.13}$$

with $\Delta t = t_{\mathrm{readout}} - t_{\mathrm{emit}}$. We find that the probabilities oscillate with the Larmor frequency in dependence on the emission time, which explains the findings in Fig. 4.4c. The non-perfect visibility stems from the dissimilar CGC; if we assume a Bell state,

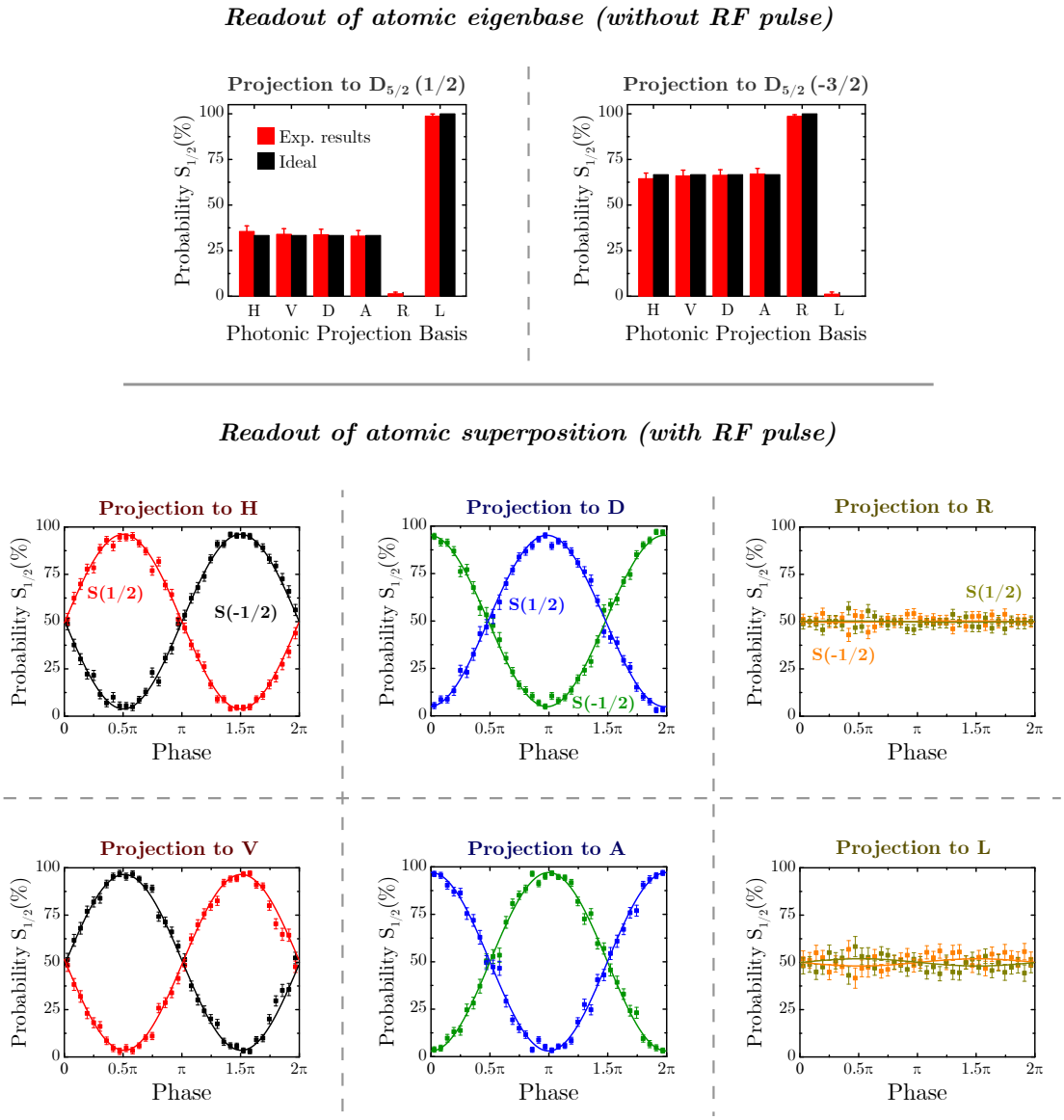

Figure 4.5. Conditioned probabilities of the atomic ground-state read-out. The background-corrected probabilities to find the ion in one of the ground states $|S_{1/2}, m = \pm 1/2\rangle$ conditioned on the detection of a photon in a certain basis setting. In the upper part the ion is measured in the eigenbasis (without the $\pi/2$-pulse on the RF transition). As expected, we find a large contrast in the respective photonic eigenbases $|R\rangle/|L\rangle$, whereas the probabilities for the photonic superposition bases are around 33 % and 66 %, which is related to the different Clebsch-Gordan coefficients (CGC). In the lower part we read-out in the atomic superposition basis. Due to Larmor precession of the atomic qubit, we effectively read-out in multiple bases. Their number is determined by the number of bins in which we sort the coincidences with respect to their Larmor phase (in this case 36). The graphs show balanced probabilities for projection to $|R\rangle/|L\rangle$ and the typical parity oscillations for $|H\rangle/|V\rangle$ and $|D\rangle/|A\rangle$.

the probabilities are given as $p_{H,+} = 1/2 \cos^2(\phi_0 + \omega_L \Delta t/2)$. We can interpret this effect either as a time-dependent entangled state, or as a time-independent state measured in a rotating readout basis. This means the oscillations can be considered as parity oscillations commonly observed for entangled states. As shown in Fig. 4.4c, we resolve many oscillation periods since the photon wavepacket is much longer than the Larmor period of around 100 ns. We use this to our advantage because a single measurement contains all outcomes in σ_x- and σ_y-direction. A projective measurement of the photon to one of the other linear polarization states reveals a similar outcome. As an example, the probabilities for projection to $|D\rangle$ are given by

$$p_{D,+/-}(t_{\text{readout}}) = \frac{1}{4} \pm \frac{\sqrt{2}}{6} \sin(\phi_0 + \omega_L \Delta t), \tag{4.14}$$

i.e. the oscillating coincidences are phase-shifted by $\pi/2$ with respect to $|H\rangle$. Accordingly, the phase shifts are π and $3\pi/2$ for projection to $|V\rangle$ and $|A\rangle$, respectively. Note that the capability to resolve the oscillations relies on a sufficiently good time resolution of the single-photon detectors and can be considered as an erasure of the which-path information caused by the energy difference of the two optical transitions.
An overview of the results from all basis settings is presented in Fig. 4.5. To obtain those graphs, the coincidences within the time window are sorted with respect to their Larmor phase into histograms of 36 bins. A free parameter is the initial phase ϕ_0, which depends on the travel time of the photon, and determines the phase of the final entangled state. It is chosen to maximize the fidelity with the desired state $|\Psi\rangle_{\text{asym}}$. Note that we plotted the conditioned probabilities instead of the number of coincidences. The probabilities are calculated via Bayesian inference, which is explained in detail in [204]. We employ it merely to get a suitable graphical representation of the parity oscillations, though[2]. The MLE algorithm to reconstruct the density matrices instead utilizes the raw coincidences and the respective relative frequencies. The upper part of Fig. 4.5 displays the probabilities – averaged over all 36 bins – to find the ion in one of the eigenstates for different photonic projectors. The large contrast between the probabilities of $|R\rangle$ and $|L\rangle$ is clearly visible and in good agreement with the theoretical values (black bars), whereas the linear polarizations yield probabilities around 33 % and 66 % for $|\uparrow\rangle$ and $|\downarrow\rangle$, respectively. The difference of a factor two represents the asymmetric CGCs. In the lower part the probabilities for a projection to the atomic superposition bases are depicted. The four graphs on the left represent a projection to linear polarization states, which reveal parity oscillations featuring the respective phase shifts of $\pi/2$, π and $3\pi/2$. In contrast, a projection to $|R\rangle$ and $|L\rangle$ yields equal probabilities for all possible atomic superpositions, hence, no oscillations appear in this case.

The reconstructed density matrices with and without BGS are illustrated in Fig. 4.6a and Fig. 4.6b, respectively. The asymmetric CGCs are clearly visible in the different heights diagonal elements (red bars). Nevertheless, we can already infer by eye a high purity of the entangled state because undesired contributions, which are represented by

[2] If we plot the coincidences in the same way, the fringes are distorted and cannot be fitted with sinusoidal functions due to the exponential decay of the photon wavepacket.

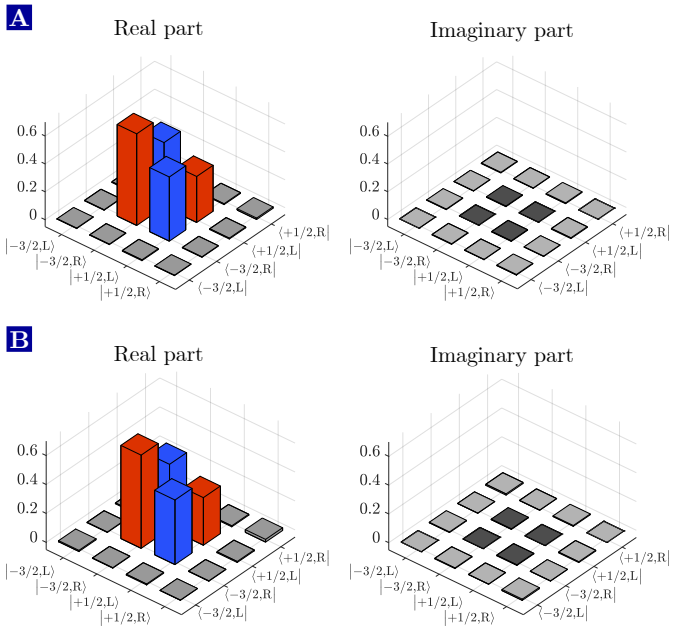

Figure 4.6. Density matrices of ion-NIR-photon entangled states. Real and imaginary part of the reconstructed density matrices of the entangled state between ion and 854 nm-photon **(A)** with and **(B)** without background subtraction. The different heights of the diagonal elements (red bars) are related to the dissimilar CGC of the σ^+- and the σ^--transitions. The fidelities with the expected state (Bell state) are 98.2(2) % (95.4(2) %) and 96.1(2) % (93.4(2) %) with and without BGS, respectively.

the gray bars, are small compared to the red and blue bars. To characterize the functionality of the sequence, we first evaluate the reconstructed state including BGS. We achieve a fidelity with the expected (asymmetric) state of $\mathcal{F}_{\text{asym}} = 98.2(2)\,\%$ and a purity of $\mathcal{P} = 96.5(3)\,\%$. The maximum fidelity for the given purity according to Eq. 2.39 is $\mathcal{F}_{\max}(\mathcal{P}) = 98.2(3)\,\%$, which verifies that the fidelity is solely limited by decoherence and not by unitary rotations of the state. Decoherence is caused by polarization-dependent loss in the optical elements between ion trap and projector, the limited coherence time of the atomic qubit, and non-perfect π-pulses on the quadrupole transition degrading the fidelity of the atomic-state readout. Furthermore, we calculate the fidelity with the Ψ^+ Bell-state. The Bell-state fidelity of the ideal asymmetric state is given as

$$\mathcal{F}_{\text{Bell, max}} = \left\langle \Psi^+ \right| \rho_{\text{asym}} \left| \Psi^+ \right\rangle = \frac{1}{2}\left(\frac{2}{3} + \frac{1}{3} + \frac{2\sqrt{2}}{3}\right) = 97.14\,\%. \tag{4.15}$$

Interestingly, the fidelity is still quite high despite the large asymmetry. The reconstructed ion-photon state has a Bell-state fidelity of $\mathcal{F}_{\text{Bell}} = 95.4(2)\,\%$ being consistent with $\mathcal{F}_{\text{asym}} \times 0.9714$.

In a realistic quantum repeater scenario the numbers without BGS are the relevant measures. In this case we deduce a purity of $\mathcal{P} = 92.4(4)\,\%$ and fidelities of $\mathcal{F}_{\text{asym}} = 96.1(2)\,\%$ and $\mathcal{F}_{\text{Bell}} = 93.4(2)\,\%$. The fidelities are again in good agreement with the

maximum achievable fidelity limited by the purity (cf. Tab. 4.1). As a cross-check we compute the background-free fidelity from the SBR of 29.5 according to Eq. 2.56. The value $\mathcal{F}_{\mathrm{bgf}}(\mathcal{F}_{\mathrm{asym}}) = 98.5(2)\,\%$ is slightly higher than the fidelity obtained via BGS. This is expected because the BGS method is designed to underestimate fidelities in case of non-perfect counting statistics (see Sect. 2.2.3), resulting in a reduction of the "best possible" value on the order of its standard deviation.
We conclude that – even without BGS – all fidelities are many standard deviations above the classical threshold of 50 %, as well as above the threshold of 70.7 % necessary to violate Bell's inequality. All fidelities and purities are again summarized in Tab. 4.1.

Table 4.1. Reconstructed fidelities and purities at 854 nm.

Reconstruction	$\mathcal{F}_{\mathrm{asym}}$ [%]	$\mathcal{F}_{\mathrm{Bell}}$ [%]	$\mathcal{P}$ [%]	$\mathcal{F}_{\mathrm{max}}(\mathcal{P})$ [%]	$\mathcal{F}_{\mathrm{bgf}}$ ($\mathcal{F}_{\mathrm{asym}}$) [%]
w/ bg subt.	98.2(2)	95.4(2)	96.5(3)	98.2(3)	–
w/o bg subt.	96.1(2)	93.4(2)	92.4(4)	96.0(4)	98.5(2)

4.2 Preservation of ion-photon entanglement during QFC

With the trapped-ion QNN as source of light-matter entanglement and the O-band converter presented in the Sect. 3.1 we have all ingredients to implement a complete device generating entanglement between a matter qubit and a telecom photon. The combined setup is illustrated in Fig. 4.7a: we employ a flip mirror in the ion lab to couple the emitted photons to the 90 m long fiber connecting ion and converter lab. The PPQFCD is operated in the same configuration as during the process tomography in Sect. 3.1.4. The whole experiment is controlled from the ion lab: the waveplate angles are set via the ethernet link by the control PC, and detection events from the SNSPDs are sent to the ion lab via 90 m long BNC cables and recorded by the Hydra.
First, we take a look at the converted photon wavepackets. Fig. 4.7b displays the total time-correlated coincidences from all basis settings together with the 300 ns-window in analogy to 854 nm. An exponential fit reveals a time constant of 258(2) ns, which is slightly higher compared to 240(2) ns without QFC. The temporal profile of photons generated via spontaneous Raman-scattering strongly depends on power and detuning of the 393 nm laser. During the experiment the laser was not actively stabilized, but tuned by hand each 10 minutes by monitoring the temporal profile of scattered 393 nm-photons. Hence, frequency drifts of the 393 nm laser are the most probable explanation for the different time constants. The additional delay caused by the fiber and BNC cables between the labs shifted the photon towards the end of the 3 µs long photon generation and detection period, which explains the abrupt cut-off. In Fig. 4.7c & d exemplary photon wavepackets for individual basis settings are shown. We obtain similar results as in the unconverted case, i.e. a large contrast between the coincidences if both qubits are projected to the eigenbases, and an oscillatory behavior with a high visibility for

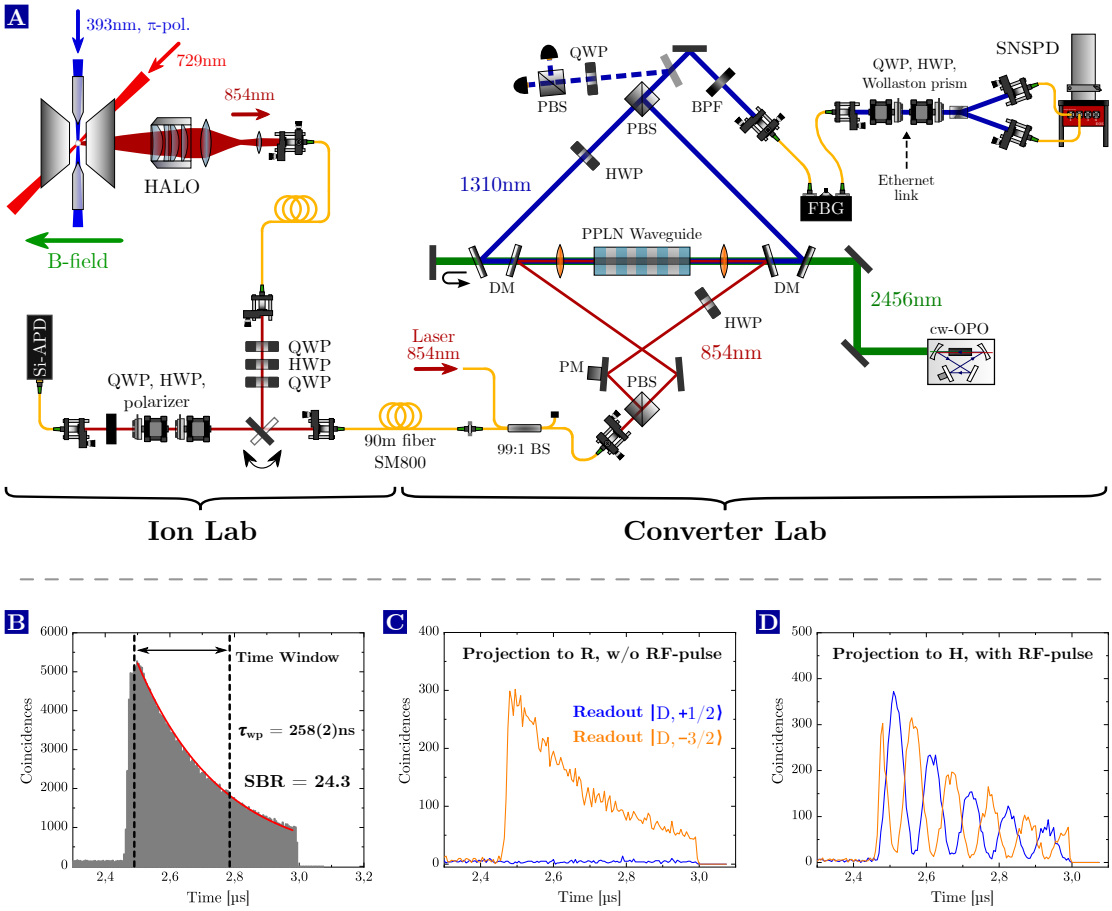

Figure 4.7. Setup for ion-telecom-photon entanglement and photon wavepackets. **(A)** Schematic representation of the joint setup combing the trapped-ion QNN and the O-band converter to generate entanglement between a trapped ion and a telecom photon. **(B)** The time-correlated coincidences summed up from all measurement bases. The time constant of the wavepacket is slightly increased to 258(2) ns (before QFC: 240(2) ns); most probably due to power- or frequency drifts of the 393 nm laser. The SBR after QFC is 24.3 calculated from the time-filtered coincidences in a 300 ns long time interval. **(C)** and **(D)** Time-correlated coincidences for projective measurements of both qubits in the **(C)** eigenbases and **(D)** superposition bases analogous to those presented in Fig. 4.4 for 854 nm.

projection to superposition bases.

With the time-filtered number of coincidences from the total photon wavepacket in Fig. 4.7a we compute entanglement generation rate and SBR in an analogous way as in Sect 4.1.2. We obtain for the detected rate

$$\gamma_{\mathrm{det}}^{1310} = \frac{193120\,\mathrm{events}}{7779\,\mathrm{s}} = 24.8\,\mathrm{Hz}. \tag{4.16}$$

Note that we employ two SNSPDs to simultaneously detect both orthogonal polarization components instead of a single APD at 854 nm. To compare the detected rates before and after conversion we have to account for this factor 2. We get $\gamma_{\mathrm{det}}^{1310}/2 \cdot \gamma_{\mathrm{det}}^{854} = 45\,\%$,

which is significantly higher than the EDI of $\eta_{\text{dev}} = 26.5\,\%$ and caused by the higher quantum efficiencies of the SNSPDs. The entanglement generation rate at 1310 nm is calculated to

$$\gamma_{\text{gen}}^{1310} = \frac{24.8\,\text{Hz}}{T_{\text{proj}} \cdot \frac{\eta_{\text{snspd1}}+\eta_{\text{snspd2}}}{2}} = 43.5\,\text{Hz} \tag{4.17}$$

with the transmission of the projection setup $T_{\text{proj}} = 86.5\,\%$ and the quantum efficiencies of the SNSPDs $\eta_{\text{snspd1}} = 70(2)\,\%$ and $\eta_{\text{snspd2}} = 62(2)\,\%$. To check for consistency, we calculate the theoretically expected rate from the individual transmissions and efficiencies in the telecom setup measured with classical light. We get for the overall transmission of the converter

$$T_{1310} = T_{\text{fiber}} \cdot \eta_{\text{dev}} \cdot \eta_{\text{stab}} = 17.6\,\% \tag{4.18}$$

with $\eta_{\text{stab}} = 87.5\,\%$ being the duty cycle of the path-length stabilization and $T_{\text{fiber}} = 75.8\,\%$ the transmission of the fiber between the labs, which includes fiber coupling, attenuation loss, and the fiber-fiber connector to the converter. With a sequence repetition rate of $\gamma_{\text{rep}}^{1310} \approx 61.7\,\text{kHz}$ (the rate is slightly increased compared to $\gamma_{\text{rep}}^{854}$ because the atomic-state analysis is performed less often due to the lower detected event rate) the expected generation rate is

$$\gamma_{\text{gen, theo}}^{1310} = \gamma_{\text{gen, theo}}^{854} \cdot \gamma_{\text{rep}}^{1310}/\gamma_{\text{rep}}^{854} \cdot T_{1310} \approx 47\,\text{Hz} \tag{4.19}$$

being consistent with the measured number.
With the number of background events $B_{1310} = 7953$ we calculate a SBR of the time-filtered coincidences of 24.3. Interestingly, the SBR is – compared to the case without QFC – only slightly decreased although the detected rates at 1310 nm and 854 nm differ by a factor 0.45. However, at the same time the background is reduced by roughly a factor of two, which partially compensates the losses.
At telecom wavelengths the background has two contributions: a major part (on average 93.5 %) stems from detector dark-counts and a minor part (on average 6.5 %) from the CIB of 11.4 cps. Hence, we obtain for the total background count-rate at 1310 nm

$$\begin{aligned} R_{\text{dcr}}^{1310} &= R_{\text{dcr, snspd1}} + \frac{R_{\text{dcr, conv}}}{2} \cdot \eta_{\text{snspd1}} + R_{\text{dcr, snspd2}} + \frac{R_{\text{dcr, conv}}}{2} \cdot \eta_{\text{snspd2}} \\ &= 58.7\,\text{cps} + \frac{11.4\,\text{cps}}{2} \cdot 0.7 + 56.4\,\text{cps} + \frac{11.4\,\text{cps}}{2} \cdot 0.62 = 122.6\,\text{cps} \end{aligned} \tag{4.20}$$

and accordingly for the theoretically expected total background

$$B_{\text{theo}}^{1310} = R_{\text{dcr}}^{1310} \cdot 300\,\text{ns} \cdot \gamma_{\text{rep}}^{1310} \cdot f_{\text{mix}} \cdot f_{850} \cdot 7779\,s = 7935, \tag{4.21}$$

which is again in good agreement with the measured value.

To characterize the full quantum interface, we measured the density matrices of the ion-photon state after frequency conversion. From background-subtracted data we reconstruct the density matrix in Fig. 4.8a yielding fidelities of $\mathcal{F}_{\text{asym}} = 97.6(1)\,\%$ and

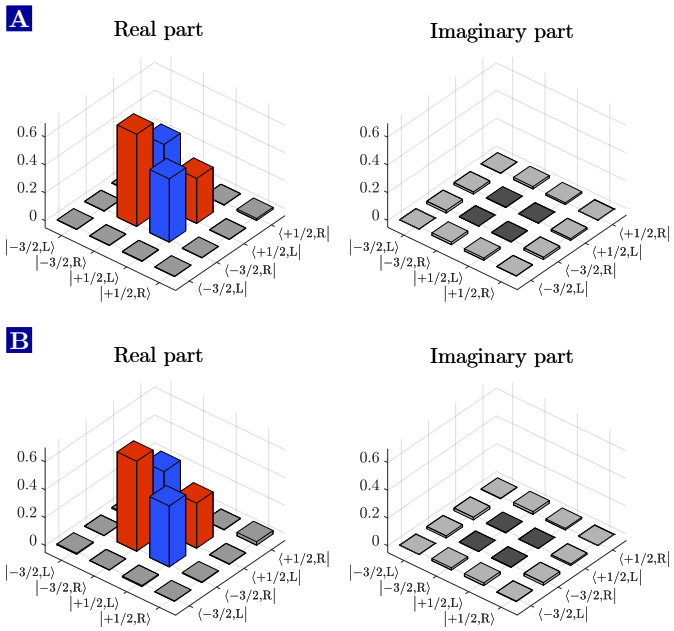

Figure 4.8. Density matrices of the ion-photon state after PPQFC. The reconstructed density matrices **(A)** with and **(B)** without BGS. The fidelities with the expected state (Bell state) are 97.6(1) % (94.6(2) %) and 95.0(2) % (92.1(2) %) with and without BGS, respectively.

$\mathcal{F}_{\text{Bell}} = 94.6(1)\,\%$, and a purity of $\mathcal{P} = 95.6(3)\,\%$. The result clearly verifies entanglement between the atomic qubit and a telecom photon. Compared to the unconverted ion-photon state, $\mathcal{F}_{\text{asym}}$ is decreased by 0.6 %. We mainly attribute this to the non-perfect process fidelity (max. contribution $\approx 0.35\,\%$) and to slow polarization drifts of the fiber connecting the labs.
If no BGS is applied, we reconstruct the density matrix in Fig. 4.8b with $\mathcal{F}_{\text{asym}} = 95.0(2)\,\%$, $\mathcal{P} = 90.5(3)\,\%$, and $\mathcal{F}_{\text{Bell}} = 92.1(2)\,\%$. Note that the fidelities are still well above the classical threshold of 50 %. We already mentioned that 6.5 % of the background stems from CIB and 93.5 % from detector dark-counts. Hence, we expect only a tiny influence of CIB on the fidelity since the SBR would be 374 in the absence of detector dark-counts. To verify this, we mimic the case of background-free detectors and subtract only 93.5 % of the total background. We obtain $\mathcal{F}_{\text{asym}} = 97.4(1)\,\%$, $\mathcal{P} = 95.2(3)\,\%$, and $\mathcal{F}_{\text{Bell}} = 94.4(1)\,\%$, i.e. the fidelities are merely reduced by 0.2 %, which confirms our expectation. All fidelities and purities are summarized in the first part of Tab. 4.2. Similar to the measurement without QFC, the maximum fidelities for the given purities $\mathcal{F}_{\text{max}}(\mathcal{P})$ as well as the background-free fidelities $\mathcal{F}_{\text{bgf}}$ ($\mathcal{F}_{\text{asym}}$) show perfect agreement with the respective reconstructed fidelities.

An interesting feature of the PPQFCD is that it renders possible the generation of maximally entangled states. To this end, we utilize the converter to introduce polarization-dependent loss of 50 % for the σ^+-polarized photons to compensate for the dissimilar

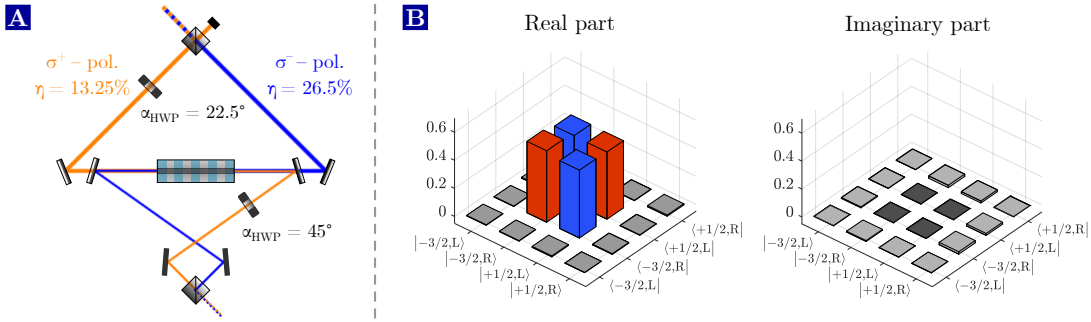

Figure 4.9. Generation of ion-photon Bell-states by polarization-dependent loss. **(A)** The scheme to compensate for the different Clebsch-Gordan coefficients by introducing polarization-dependent loss in the PPQFCD. The EDI for σ^+-polarized photons – corresponding to the transition with the larger CGC – is decreased by a factor two. To this end, the second HWP is set to 22.5°, so half of the photons leave the PBS via the second output port. **(B)** The reconstructed density matrix with BGS. The asymmetry in the heights of the diagonal elements has disappeared and we obtain fidelities of 97.8(1) % (w/ bg-sub.) and 93.4(2) % (w/o bg-sub.) with the Ψ^+ Bell-state.

CGCs. The idea is sketched in Fig. 4.9a: we align the polarization of the 854 nm-photons so that the orthogonal polarization-states in the interferometer arms are exactly σ^+ and σ^-. Next, the EDI of the σ^+-arm is decreased by a factor two by setting the second HWP to 22.5°. As a result, 50 % of the photons leave the PBS at the second output port and are absorbed by a beam block. Thus, we balance the CGCs at the expense of one third of the photons; accordingly generation rates and SBR have to be multiplied by 2/3. The measured density matrix with BGS is displayed in Fig. 4.9b. The asymmetry in the diagonal elements has disappeared, and we obtain $\mathcal{F}_{\text{Bell}} = 97.8(1)\,\%$ and $\mathcal{P} = 95.8(3)\,\%$ (without BGS: $\mathcal{F}_{\text{Bell}} = 93.4(2)\,\%$, $\mathcal{P} = 87.7(3)\,\%$; all other numbers are listed in the second part of Tab. 4.2). The density matrix verifies that we have created

Table 4.2. Reconstructed fidelities and purities at 1310 nm.

Reconstruction	$\mathcal{F}_{\text{asym}}$ [%]	$\mathcal{F}_{\text{Bell}}$ [%]	$\mathcal{P}$ [%]	$\mathcal{F}_{\text{max}}(\mathcal{P})$ [%]	$\mathcal{F}_{\text{bgf}}$ ($\mathcal{F}_{\text{asym}}$) [%]
Raw state after PPQFC $\left(\lvert\Psi\rangle_{\text{asym}}\right)$					
w/ bg subt.	97.6(1)	94.6(1)	95.6(3)	97.7(3)	–
w/ snspd bg subt.	97.4(1)	94.4(1)	95.2(3)	97.5(3)	97.6(1)
w/o bg subt.	95.0(2)	92.1(2)	90.5(3)	95.0(3)	97.9(2)
Bell-state generation via CGC compensation					
w/ bg subt.	–	97.8(1)	95.8(3)	97.9(3)	–
w/ snspd bg subt.	–	97.6(1)	95.5(2)	97.7(2)	97.9(1)
w/o bg subt.	–	93.4(2)	87.7(3)	93.4(3)	97.9(2)

a Bell state between ion and telecom photon with high fidelity. Interestingly, in this measurement run the fidelity is only reduced by 0.4 % in comparison with the unconverted value and, thus, also in accordance with the process fidelity, which we attribute to a better polarization stability of the 90 m long fiber.

4.3 Summary and discussion

In this chapter, we presented a complete device generating light-matter entanglement between a trapped-ion QNN and a telecom photon. We started with an overview of our trapped-ion node followed by the experimental sequence to generate entanglement between two Zeeman sublevels of the $D_{5/2}$-manifold and the polarization of a spontaneously emitted photon at 854 nm. We achieve an entanglement generation rate of 256 Hz, which is roughly one to two orders of magnitude lower than state-of-the-art cavity [90] or free-space trapped-ion QNN [61, 89]. The higher rates of the other free-space nodes are explained by a higher NA of the objective for photon collection (NA = 0.6), faster experimental sequences employing ultrafast laser pulses and optimized laser cooling/state preparation, and by utilizing different optical transitions in other ion species for photon generation. Note that similar results can be expected in our setup with an improved sequence and by emitting single photons at 393 nm instead of 854 nm. However, it is quite challenging to convert single photons from 393 nm to telecom wavelengths with high efficiency and low background [144, 248, 249].
Light-matter entanglement is verified by QST of the joint ion-photon state yielding fidelities with the theoretically expected state – which is not a Bell state but slightly asymmetric due to different CGCs of the optical transitions – of 98.2(2) % and 96.1(2) % with and without subtraction of background stemming from detector dark-counts, respectively. The numbers are in good agreement with other trapped-ion QNNs, but among the highest fidelities for light-matter entanglement compared to neutral-atom or solid-state QNNs. Further improvements to lift the fidelity towards 100 % are state-of-the-art commercially-available SNSPDs with negligible DCRs (< 1 cps) and efficiencies > 80 % at 854 nm, an improved atomic coherence e.g. by reducing magnetic field noise with a µ-metal shielding [94], or a 729 nm laser with better spectral properties to improve the fidelity of the atomic-state readout.
In the next step we connected the trapped-ion QNN with the O-band converter to demonstrate ion-telecom-photon entanglement. We achieved an entanglement generation rate of 43.5 Hz in perfect agreement with the transmission and efficiencies at telecom wavelengths. Significant improvements are possible by utilizing the C-band converter with more than twice the device efficiency, or improved fiber-fiber connectors (e.g. E2000 connectors, see Chap. 6). The SBR was measured to be 24.3 limited by detector dark-counts and CIB. Interestingly, converter background is only responsible for 6.5 % of the background, hence a SBR of 374 would be possible with ideal single-photon detectors. It is worth to note that this number does not decrease with increasing fiber lengths since the background is just as attenuated as the signal. Thus, a reduction of detector dark-counts is a major prerequisite to achieve reasonable SBRs over fiber distances of several tens of kilometers. An increase to 200 is already possible with our

detectors by operating them at lower bias currents (see Sect. 3.1.3). Besides that, recent progress in the development of NbTiN-based SNSPDs with milli-Hertz DCRs is very promising in this direction [250]. A further increase of the SBR to >1000 requires spectral filters with smaller bandwidths. Commercial fiber Bragg gratings offer bandwidths down to 1 GHz without a significant decrease in transmission (*Advanced optical solutions GmbH*), which is well above the photon bandwidth of 23 MHz, but reduces the background roughly by a factor 25.
Finally we verified that PPQFC preserves ion-photon entanglement via QST of the converted ion-photon state yielding purity-limited fidelities of 97.6(1) % with BGS, 97.4(1) % with subtraction of the detector part of the background and 95.0(2) % without BGS. A comparison of fidelities before and after PPQFC reveals a decrease of 0.8 % (0.2 % stemming from converter background, 0.6 % due to $\mathcal{F}_{\text{pro}}$ and drifts in the fibers). Further improvements of the fidelity are possible with an active polarization stabilization of the complete photonic channel. Nevertheless, we can claim the PPQFC has only a slight influence on purity and fidelity and therefore represents a promising device for quantum network applications. As a nice feature, we demonstrated the generation of ion-photon Bell states by utilizing the PPQFC to compensate for the asymmetric CGCs via PDL. We achieved Bell-state fidelities of 97.8(1) % (w/ bg subt.) and 93.4(2) (w/o bg subt.), which are among the highest fidelities for entanglement between telecom light and matter reported so far. In particular, these values bring ion-ion entanglement with fidelities in the order of 90 % within reach, being clearly above the threshold to realize a loophole-free Bell test [112], self-testing of quantum network links [221] or fully device-independent QKD [251].

Chapter 5

Direct quantum state transfer from a trapped ion onto a telecom photon

Contributions: The experiments in this chapter have been performed at Saarland University in the labs of Prof. Christoph Becher and Prof. Jürgen Eschner, who jointly supervised the experiments. Stephan Kucera (S.K.) and Matthias Bock (M.B.) conceived the experiment; while M.B. operated the QFCD, S.K. was in charge of the ion trap. The experiment was originally initiated by Pascal Eich (P.E.), who designed the experimental sequence and performed first tests with help from Matthias Kreis, S.K. and M.B. The data was analyzed by M.B. and S.K. The software tools to extract the histograms from the raw data were developed by S.K. and modified by P.E., whereas the maximum-likelihood estimation for state and process reconstruction was implemented by M.B.

After demonstration of ion-telecom-photon entanglement, we realize a different quantum network protocol, namely a state transfer from a trapped ion onto a telecom photon. Analogous to atom-photon entanglement, quantum state transfer enables entanglement distribution and quantum communication between remote QNNs as proposed in [252]. The original proposal relies on atoms strongly coupled to optical cavities, which enables efficient emission (absorption) of photons from the first (second) QNN. Experiments towards this goal employ neutral atoms [65, 253], ions [254] or superconducting qubits [255–257]. However, we can also imagine alternative approaches without optical cavities. They rely for instance on heralded absorption in order to eliminate the influence of low absorption probabilities on the process fidelity [131, 258], or ensemble-based absorptive quantum memories with efficiencies comparable to cavity QED systems [158,259,260]. In this chapter, we demonstrate one part of a state transfer between two QNNs: the direct transfer of an initial atomic qubit onto the polarization state of a telecom photon. We first introduce the protocol and sequence in the trapped-ion QNN. Subsequently, we present the results both at 854 nm and after PPQFC at 1310 nm.

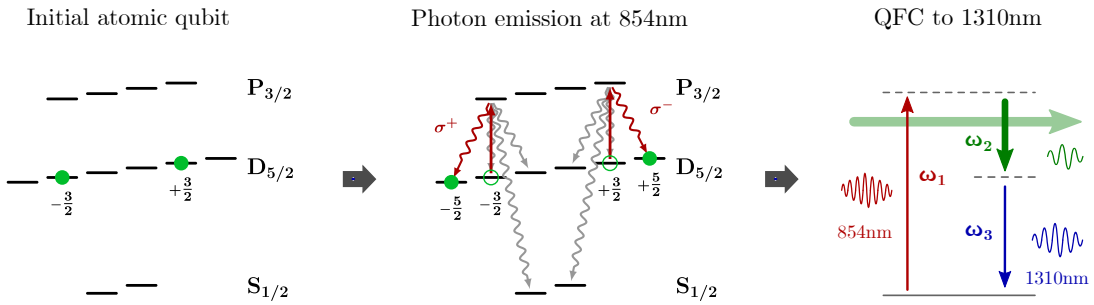

Figure 5.1. Scheme of the atom-to-telecom-photon quantum state transfer. The scheme starts with the preparation of an initial atomic qubit formed by the two Zeeman sublevels $|D_{5/2}, m = \pm 3/2\rangle$. Excitation with a π-polarized laser at 854 nm and spontaneous decay to the $|D_{5/2}, m = \pm 5/2\rangle$ states creates an ion-photon entangled state, whose amplitudes and phase are determined by the initially prepared state. The gray arrows denote undesired decay paths. PPQFC of the emitted photon to the telecom O-band and a projective measurement of the atomic state in the superposition basis projects the initial qubit onto the telecom photon.

5.1 Protocol and experimental sequence

The idea of the protocol is sketched in Fig. 5.1. We start at time t_0 by preparing an initial atomic qubit in the $D_{5/2}$-manifold spanned by the states $|-3/2\rangle = \left|D_{5/2}, m = -3/2\right\rangle$ and $|+3/2\rangle = \left|D_{5/2}, m = +3/2\right\rangle$ of the form

$$|\Psi\rangle_{\text{init}} = \frac{1}{\sqrt{\alpha^2 + \beta^2}} \left(\alpha|-3/2\rangle + e^{i\left(\phi_0 + \omega^{\text{L}}_{3/2}(t-t_0)\right)} \beta|+3/2\rangle \right) \tag{5.1}$$

with full control over the coefficients α and β, and the initial phase ϕ_0. Due to the energy splitting between $|-3/2\rangle$ and $|+3/2\rangle$, the phase of the superposition state oscillates with the respective Larmor frequency $\omega^{\text{L}}_{3/2}$. Subsequently, the initial state is excited to the $P_{3/2}$-manifold with a π-polarized laser at 854 nm. The ion decays with a probability of 3.9 % to the states $|\pm 5/2\rangle = \left|D_{5/2}, m = \pm 5/2\right\rangle$ under emission of a single photon at 854 nm. The probability of 3.9 % is determined by the branching ratios and CGCs with respect to other decay paths (gray arrows in Fig. 5.1), which we explain in more detail later in this section. After emission, the ion ends up in the intermediate state

$$|\Psi\rangle_{\text{inter}} = \frac{1}{\sqrt{\alpha^2 + \beta^2}} \left(\alpha|-5/2, R\rangle + e^{i\left(\phi_0 + \omega^{\text{L}}_{3/2}(t_{\text{emit}}-t_0) + \omega^{\text{L}}_{5/2}(t-t_{\text{emit}})\right)} \beta|+5/2, L\rangle \right), \tag{5.2}$$

which is an entangled ion-photon state. Its relative amplitudes and phase are determined by the coefficients of the initial state. To map the initial state onto the photon polarization, the ion is projected – at a fixed time t_{proj} – to one of the superposition states $|-5/2\rangle \pm |5/2\rangle$ in order to erase the information about the initial qubit from the ion sub-system. Hence, we obtain for the final photon state

$$|\Psi\rangle_{\text{photon}} = \frac{1}{\sqrt{2}} \left(\langle -5/2| \pm \langle 5/2|\right) |\Psi\rangle_{\text{inter}}$$
$$\propto \frac{1}{\sqrt{\alpha^2+\beta^2}} \left(\alpha|R\rangle \pm e^{i\left(\phi_0+\phi'+t_{\text{emit}}\left(\omega^{\text{L}}_{3/2}-\omega^{\text{L}}_{5/2}\right)\right)}\beta|L\rangle\right) \tag{5.3}$$

with $\phi' = \omega^{\text{L}}_{3/2} t_0 + \omega^{\text{L}}_{5/2} t_{\text{proj}}$. In comparison to $|\Psi\rangle_{\text{init}}$ the Larmor precession introduces an additional constant phase shift ϕ' between $|R\rangle$ and $|L\rangle$ and a phase shift depending on the emission time of the photon (similar as for ion-photon entanglement in the previous chapter). The protocol is finalized by PPQFC of the emitted photon to the telecom O-band. Note that we call the protocol a direct state transfer in contrast to a teleportation-based scheme, which relies on an entangled photon-pair source and heralded absorption [261].

The experimental sequence is sketched in Fig. 5.2. It starts with 10 µs of Doppler cooling (including the 854 nm laser to repump the $D_{5/2}$-manifold) followed by 50 µs of optical pumping to $|S_{1/2}, m = -1/2\rangle$. The most apparent optical pumping scheme would be purely σ-polarized light at 397 nm to polarization-selectively depopulate the state $|S_{1/2}, m = -1/2\rangle$. However, since we collect fluorescence light at 397 nm along the quantization axis, we cannot send laser light along this axis without destroying the PMTs. For this reason, optical pumping is performed by frequency-selective depopulation of the state $|S_{1/2}, m = +1/2\rangle$ via the quadrupole transition (see Fig. 5.2a). Subsequent repumping of $|D_{5/2}, m = -3/2\rangle$ with the 854 nm laser results either in a decay to the desired state $|S_{1/2}, m = -1/2\rangle$ being decoupled from the 729 nm laser, or to $|S_{1/2}, m = +1/2\rangle$, which starts the pump cycle anew.
In the next step the initial atomic qubit is prepared (Fig. 5.2c). To this end, we apply a 5 µs long $\pi/2$-pulse with phase ϕ_{RF} on the RF-transition in the ground-state followed by two π-pulses at 729 nm (each 8 µs long) to transfer the population from the $S_{1/2}$-states to $|-3/2\rangle$ and $|+3/2\rangle$, respectively. While the initial phase ϕ_0 of the atomic qubit is determined by the phase of the RF-pulse, the coefficients α and β can be controlled by varying the length of the RF-pulse between 0 and π.
Photon generation using a π-polarized laser at 854 nm and photon detection is scheduled in a subsequent 2.5 µs window. The projective measurement of the ion to $|-5/2\rangle \pm |5/2\rangle$ is conditioned on a detection click of the APD (854 nm) or SNSPD (1310 nm); in case of no click the sequence is restarted. Fig. 5.2d illustrates the photon generation with the desired decay path to the outer $D_{5/2}$-states marked as red arrows. Due to the respective branching ratio and CGCs, this decay only occurs with a probability of 3.9 %. In the majority of the attempts the ion decays to the $S_{1/2}$-states under emission of a photon at 393 nm (93.5 %), the remaining $D_{5/2}$-states (1.95 %), or the $D_{3/2}$-manifold under emission of a 850 nm-photon (0.66 %, not shown in Fig. 5.2d). Some of these undesired decay paths are uncritical, whereas others alter the process fidelity. Hence, we have to distinguish and discard those from desired events. The decay path to the inner Zeeman states ($|-1/2\rangle$ and $|+1/2\rangle$) is most uncritical: although we may detect the emitted 854 nm-photon or get a dark count, the successive state projection is selective for the outer Zeeman states. If there is no population in these states, we only obtain

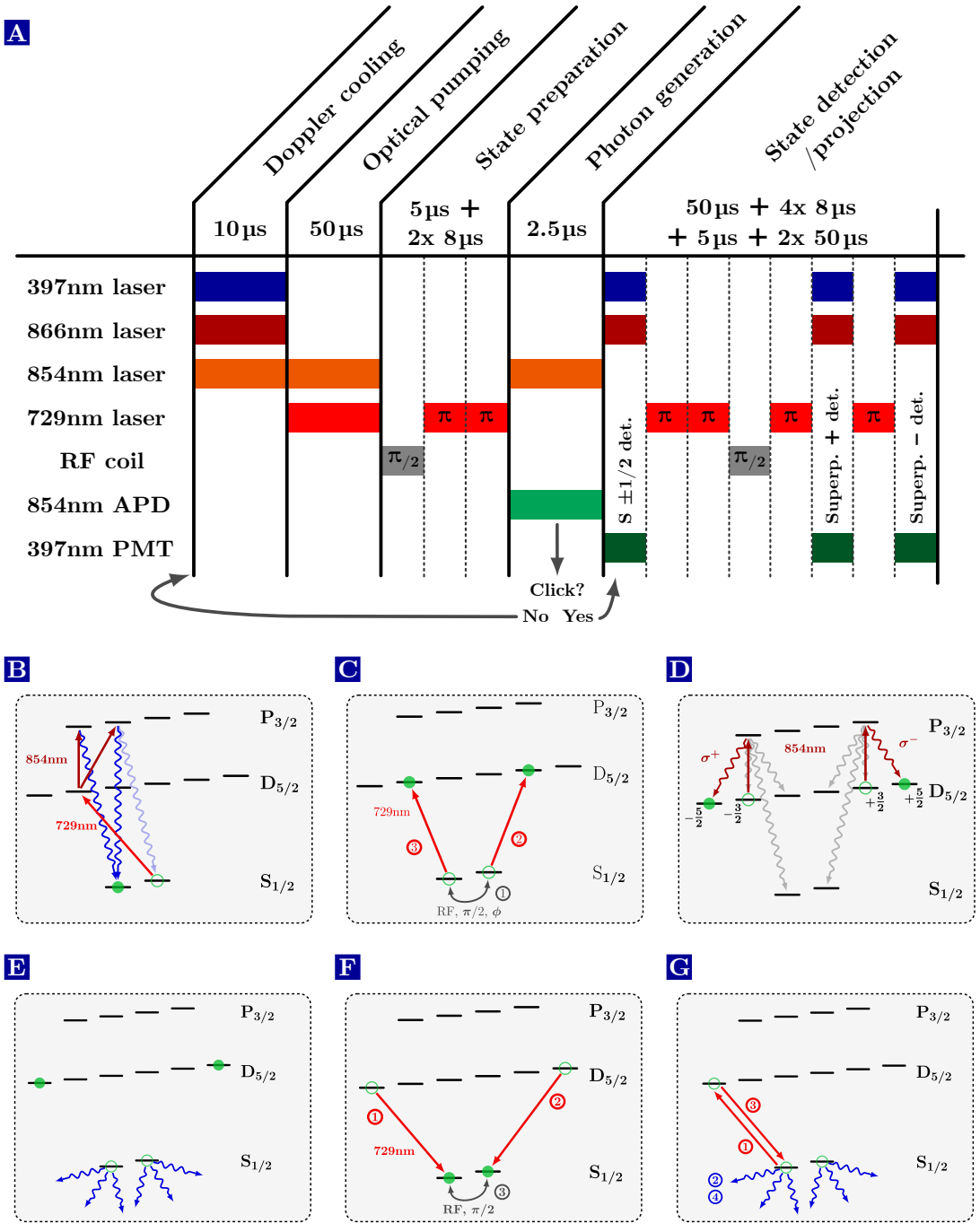

Figure 5.2. Experimental sequence of the atom-photon state transfer. **(A)** Timeline of the experimental sequence showing all lasers and detectors. The first four steps are repeated until a photon is detected by the APD, which serves as trigger for the atomic-state detection. **(B)** Optical pumping to $|S_{1/2}, m = -1/2\rangle$. **(C)** Preparation of the initial atomic qubit. **(D)** Excitation with a π-polarized laser at 854 nm and all possible decay paths. The desired decay to $|D_{5/2}, m = \pm 5/2\rangle$ is marked with red arrows. **(E)** – **(G)** Fluorescence-based atomic-state readout in the superposition basis.

dark-events and the detected photon is discarded[1]. The decay path back to the initial-qubit states results in a statistical mixture of the states because of the incoherent nature of the spontaneous Raman process. If the ion is subsequently re-excited and decays to the outer Zeeman states, the final photonic state is a mixed state, too. This effect is unavoidable and lowers the process fidelity, which we will discuss at a later point (further details and simulations can be found in the PhD thesis of P. Eich [243]). The remaining decay path to $S_{1/2}$ is critical, too. Although the emitted photon at 393 nm is not detected by the APD, a dark count in the time window can initialize the state projection. Since the $S_{1/2}$-states are part of the cooling cycle, population in these states induces a false bright-event from the fluorescence readout. We take this into account by means of an additional fluorescence-readout step of 50 µs length to eliminate the ground-state population before the actual state projection (Fig. 5.2e). Note that the decay path to $D_{3/2}$ is also eliminated in this step since population in $D_{3/2}$ is repumped by the 866 nm laser, which also results in a bright-event.
The state projection to $|-5/2\rangle \pm |5/2\rangle$ works in a similar way as in the ion-photon entanglement experiment: the population from the outer Zeeman states is frequency-selectively transferred to the $S_{1/2}$-states by two π-pulses on the quadrupole transition. A $\pi/2$-pulse on the RF transition rotates the "+" and "–" superposition states to $|S_{1/2}, m = +1/2\rangle$ and $|S_{1/2}, m = -1/2\rangle$, respectively (Fig. 5.2f). Finally, we successively detect both superpositions via fluorescence readout; during the first readout step (+ detection) the population of the "–" superposition is shelved to $D_{5/2}$ employing π-pulses at 729 nm (Fig. 5.2g).

To perform the experiment, we employ the same setup as for the ion-photon entanglement (cf. Fig. 4.7a) except two differences: we replaced the projection setup at 854 nm by the Wollaston-based setup with two APDs (see Fig. 3.15), and we use the modified phase-stabilization scheme explained in Sect. 3.1.2. As mentioned, back-reflected stabilization light at 854 nm disturbs the initial-qubit preparation by repumping population from the $D_{5/2}$-manifold to the ground state. To solve this issue, we synchronized the stabilization to the sequence, i.e. we introduced each 50 ms an extra time window of 5 ms to execute the stabilization. During this time the actual sequence is interrupted and replaced by laser cooling.

5.2 Results

The performance of the state transfer is characterized by quantum process tomography. To this end, we conduct three experimental runs: two runs in which we prepare the initial atomic qubit in the eigenstates $|-3/2\rangle$ and $|+3/2\rangle$, and one run starting from a balanced superposition state with $\alpha = \beta = 1/\sqrt{2}$ and $\phi_{\mathrm{RF}} = 0$. One superposition state is enough for QPT as its Larmor precession guarantees that we can can extract multiple input states (in this case 12, being determined by the number of histogram bins). In each

[1] In fact this is not 100% correct since a decay from $D_{5/2}$ to $S_{1/2}$ leads to a false bright-event. However, the duration of the state projection (< 200 µs) is well below the lifetime of the $D_{5/2}$-state (1.17 s), hence this contribution is negligible.

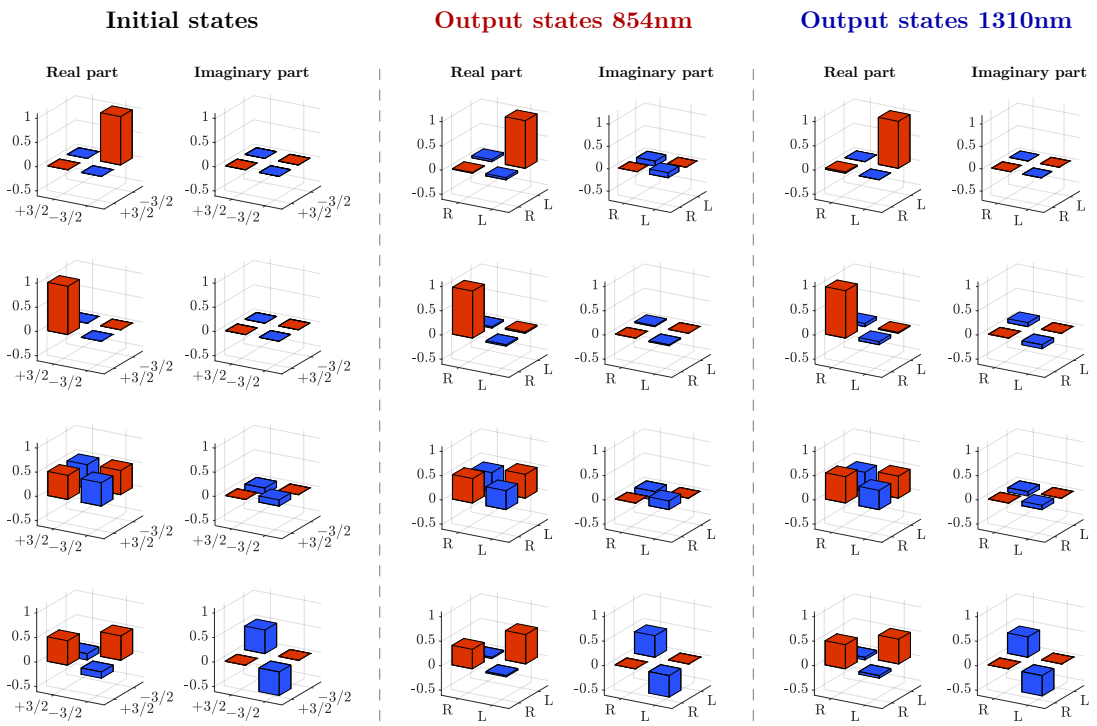

Figure 5.3. Single-qubit density matrices of input and output states. Density matrices of four different initial atomic states and the respective photonic output states at 854 nm and 1310 nm. The first and second rows show the eigenstates, whereas the third and fourth row display two exemplary (out of 12) superposition states. The initial-qubit matrices represent the theoretically expected states, while the photonic density matrices are measured by quantum state tomography.

run we perform full single-qubit tomography of the emitted photonic polarization qubit. The whole data evaluation is similar to Chap. 4 employing the process reconstruction algorithms presented in Sect. 2.2.

We start with the SBR and success probability of the protocol, which we extract from the whole data set of the QPT. We post-select events in a 350 ns long time window, which includes 86 % of the photon wavepacket. At 854 nm we collected 30286 signal and 612 background events in 29362 s yielding a SBR of 49.5. The higher SBR in comparison to the previous chapter (SBR: 29.5) is caused by a lower DCR of the second APD in the projection setup. Taking into account the sequence repetition rate of 7.66 kHz, we calculate a success probability, i.e. the probability to detect a photon per excitation try, of 1.35 $\times 10^{-4}$. We find a good agreement with the theoretical value of 1.28 $\times 10^{-4}$ determined by the collection efficiency ($\eta_{\text{coll}} \approx 1.4\,\%$), the efficiency of the desired decay path to the outer Zeeman states ($\eta_{\text{dec}} = 3.9\,\%$), the fraction of the photon wavepacket within the time window ($f_{\text{window}} = 86\,\%$), the transmission of the projection setup plus some fiber-fiber connectors ($T_{\text{proj}} \approx 85\,\%$), and the mean efficiency of the APDs ($\eta_{\text{apd}} = 32\,\%$). After PPQFC we measured 12135 signal and 326 background events in 33345 s, hence the SBR is 37.2. The discrepancy to 24.3 in the ion-photon entanglement

experiment is explained by a lower bias current of the first SNSPD in order to balance the SDEs of both SNSPDs to 62 %. At this current, the DCR is almost reduced to one half of the previous value. The success probability in this measurement is 4.5 $\times 10^{-5}$, which agrees well with the expected value of

$$p_{\text{theo}}^{1310} = \eta_{\text{coll}} \cdot \eta_{\text{dec}} \cdot f_{\text{window}} \cdot T_{\text{fiber}} \cdot \eta_{\text{dev}} \cdot T_{\text{tomo}} \cdot \eta_{\text{snspd}} = 5.1 \times 10^{-5}. \tag{5.4}$$

The small deviation is most probably caused by an additional fiber-fiber connector, whose transmission was not independently measured.
A selection of reconstructed single-qubit density matrices of the emitted photons at 854 nm and 1310 nm is illustrated in Fig. 5.3. The first column contains four initial atomic states: the two eigenstates $|-3/2\rangle$ and $|+3/2\rangle$ as well as two representative balanced superposition states with different phases. Note that these density matrices correspond to the theoretically expected states. We resigned to measure them since it has been already shown that atomic states can be prepared with high fidelity [244]. The second and third column show the measured photonic output states at 854 nm and 1310 nm. From the single-qubit matrices we extract the average fidelity according to Eq. 2.43, i.e. we calculate the mean value of the overlap fidelities of the two eigenstates and four superposition states equally distributed on the equatorial plane of the Bloch sphere. The results are listed in Tab. 5.1: without BGS we obtain at 854 nm average fidelities of 95.7(10) % (95.1(10) %) for projection of the ion to the + (–) superposition state and at 1310 nm values of 93.6(17) % (94.4(16) %), which verifies that the protocol works with high fidelity.

Table 5.1. Average and process fidelities of the atom-to-photon quantum state transfer before and after PPQFC

Measurement	$\mathcal{F}_{\text{avg}}$ [%]	$\mathcal{F}_{\text{pro}}$ [%] w/o bg subt.	$\mathcal{F}_{\text{pro}}$ [%] w/ bg subt.	$\mathcal{F}_{\text{pro}}(\mathcal{F}_{\text{avg}})$ [%] calculated
854 nm, Superposition +	95.7(10)	94.2(5)	95.1(6)	93.6(15)
854 nm, Superposition –	95.1(10)	93.2(7)	94.0(8)	92.7(15)
1310 nm, Superposition +	93.6(17)	91.2(13)	92.6(13)	90.4(26)
1310 nm, Superposition –	94.4(16)	91.1(12)	92.3(11)	91.6(24)

Besides the average fidelity, we reconstruct the process matrix and specify the process fidelity. The process matrices of the + superposition at 854 nm and 1310 nm including their Bloch sphere representation are plotted in Fig. 5.4. We find high process fidelities of 94.2(5) % (854 nm) and 91.2(13) % (1310 nm) confirming a successful state transfer onto the photon polarization state (the values for the – superposition are in a similar range and can be found in Tab. 5.1).
The imperfection in fidelity is caused by a series of error sources. **(I)** one source is the finite SBR; to quantify its influence we reconstruct the density matrices using background-corrected data. We obtain $\mathcal{F}_{\text{pro}} = 95.1(6)$ % at 854 nm and $\mathcal{F}_{\text{pro}} = 92.6(13)$ % at

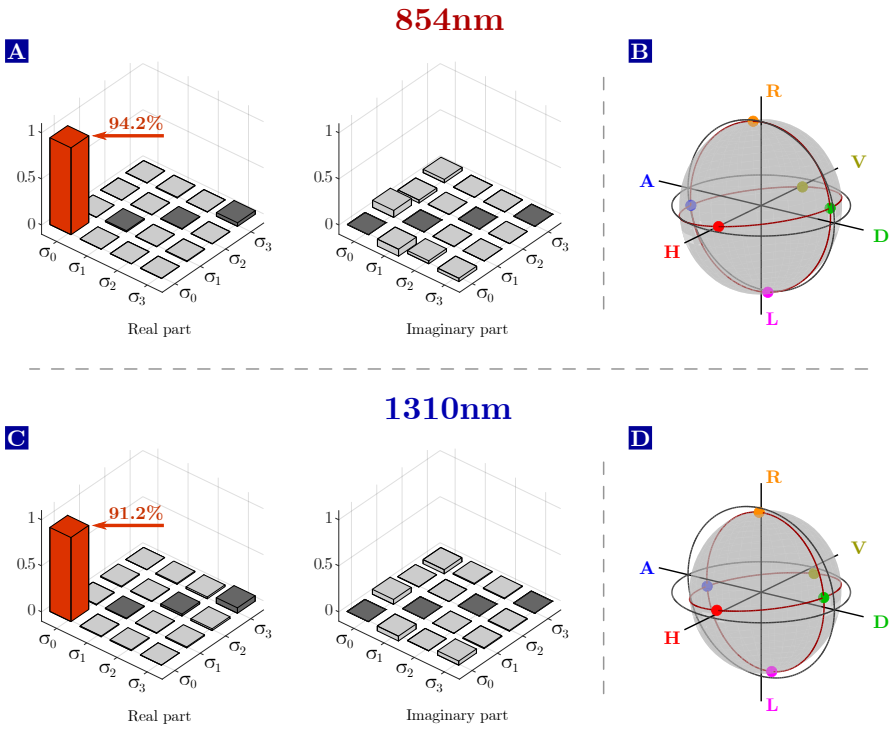

Figure 5.4. Quantum process tomography of the state transfer. **(A)** Real and imaginary part of the reconstructed process matrix at 854 nm. The process fidelity is 94.2(5) %. **(B)** The Bloch sphere representation of the process matrix. **(C)** and **(D)** Process matrix and Bloch sphere representation at 1310 nm. The process fidelity is decreased to 91(13) %, most probably due to polarization drifts between ion trap and projection setup.

1310 nm, i.e. fidelity losses of 0.9 % and 1.4 %, which are - within the error bars - in good agreement with the measured SBRs. **(II)** The back-decay to the initial state accounts for a decrease of 0.6 % for the time-filtering window of 350 ns. We estimate this from a simulation based on a rate-equation model, which can be found in the PhD thesis of P. Eich [243]. **(III)** Another source of infidelity is the coherence time of the atomic superposition-states. The main contribution of the coherence time stems from the waiting time in the outer Zeeman states, which are most sensitive to magnetic field fluctuations due to the large Δm. With the coherence time of the state $|-5/2\rangle + |5/2\rangle$ of 178 µs [204] and the waiting time of roughly 68 µs we calculate a reduction in process fidelity of 3.5 %. **(IV)** The remaining 0.8 % (at 854 nm) are most probably attributed to PDL in the optical elements between trap and detector, a limited phase resolution due to the comparably rough binning of 8.8 ns (12 bins per Larmor oscillation with period 105 ns), a non-perfect fidelity of the atomic state readout, and a unitary rotation, which is identified in the Bloch sphere representations in Fig. 5.4b/d and has not been well-compensated during the experiment. **(V)** The loss of fidelity at 1310 nm is much higher than expected from the process fidelity of the PPQFCD. Since the duration of the experiment was almost three days, we believe that the main issue are slow polarization drifts in the fiber connecting the labs. In future experiments with integration

times of several days, it is advisable to implement an automatized stabilization scheme of the polarization rotation (c.f. [112]).
Finally, as a cross-check between average and process fidelities, we calculate the expected process fidelity from $\mathcal{F}_{\text{avg}}$ according to Eq. 2.44. The results are listed in the last column in Tab. 5.1. Within the error bars the expected fidelities are in good agreement with the reconstructed ones without BGS.

To conclude, we successfully implemented a direct atom-to-photon state transfer from an initial atomic-qubit formed by two Zeeman states of the $D_{5/2}$-manifold onto the polarization state of a spontaneously emitted photon at 854 nm. Using PPQFC we extended the protocol to telecom wavelengths towards a state transfer between remote QNNs. We characterized the protocol via QPT and found process fidelities of 94.2(5) % and 91.2(13) % at 854 nm and 1310 nm, respectively. Furthermore, we calculated average fidelities of 95.7(10) % (854 nm) and 93.6(17) % (1310 nm), which are in good agreement with the process fidelities and cross-validate our reconstruction methods. All fidelities compare well with other implementations of the scheme with trapped atoms or ions [65, 254]. The success probability to detect a photon per excitation trial is 1.35 $\times 10^{-4}$ at 854 nm and 5.1×10^{-5} 1310 nm and mainly limited by the collection efficiency (1.4 %), the intrinsic efficiency of the protocol (3.9 %) and the external device efficiency of the QFC (26.5 %). In terms of success probability we cannot compete with the cavity-assisted experiments with trapped atoms or superconducting qubits [255–257] enabling values above 10 % (an exception is the trapped-ion experiment [254] with a comparable success probability; although the cavity enables higher efficiencies, strong time-filtering was necessary to minimize infidelities due to back-decay to the initial state, which was encoded in the ground-state Zeeman qubit). The protocol can be improved in the future in two directions: on the one hand we can lift the process fidelity by a higher atomic coherence time, an active stabilization of the polarization rotation in all SM fibers, and the elimination of PDL in the optics around the trap. On the other hand, higher success probabilities are possible with an optical cavity, which offers a larger collection efficiency as well as a larger intrinsic efficiency of the protocol by changing the branching ratio in favor of the 854 nm transition.

Chapter 6

PPQFC system for an elementary Rubidium-atom based quantum network link

Contributions: The experiments in this chapter have been performed at Saarland University in the lab of Prof. Christoph Becher (C.B.), who supervised the experiments.
The project idea was devised by Matthias Bock (M.B.), C.B., Wenjamin Rosenfeld (W.R., LMU Munich) and Prof. Harald Weinfurter (H.W., LMU Munich). The complete PPQFC system has been designed, constructed and operated by M.B. with advice on technical and/or physical aspects from Benjamin Kambs, Stephan Kucera, Matthias Kreis (all Saarland university), W.R., Kai Redeker, Robert Garthoff (R.G.) and Tim van Leent (T.v.L., all LMU Munich). Tobias Bauer (Saarland university) contributed to the frequency stabilization of the master lasers as part of his bachelor thesis. Matthias Kreis provided electronic circuit schemes and software for the cavity locking electronics. The classical polarization analysis on the BSM platform has been implemented by R.G. and T.v.L. All experimental results in this chapter were measured and analyzed by M.B.

Part of the results from this chapter are published in Phys. Rev. Lett. **124**, 010510 (2020).

In this chapter we present the design, construction and characterization of a PPQFC system devised as telecom interface for extending an elementary quantum network link in the city-center of Munich [112,221]. The network link is based on two remote traps for single ^{87}Rb-atoms, each capable of creating entanglement between an atomic Zeeman-qubit and the polarization state of a single photon at 780 nm. The traps are connected by a 700 m long fiber link in order to generate atom-atom entanglement via entanglement swapping employing a photonic BSM. To extend the network link to larger fiber lengths

– and eventually to larger physical distances – we designed a transportable system consisting of two PPQFCDs to convert single photons at 780 nm to the telecom S-band at 1522 nm, and a photonic BSM for telecom wavelengths.
The chapter is organized as follows: in Sect. 6.1 we sketch the idea of the final experiment – atom-atom-entanglement over km long fibers – and deduce a series of design criteria for the QFC system. Afterwards we present the setup and characterization of the three parts of the QFC system, namely the master laser system, the PPQFCD, and the BSM for telecom wavelengths, in Sect. 6.2 and 6.3, respectively. The section on the PPQFCD furthermore includes a characterization of the nonlinear WGs, an investigation of Raman background, which is the critical source of background in this DFG-process, and the implementation of a narrowband spectral filter system with a bandwidth as low as 27.3 MHz to sufficiently suppress Raman background.

6.1 Design criteria of the QFC system

A sketch of the experiment to establish atom-atom entanglement over kilometer-scale fibers is shown in Fig. 6.1a. Single ^{87}Rb-atoms are trapped in two distinct optical dipole traps (ODT) located at two remote laboratories in the city-center of Munich (see Fig. 6.1c). The labs – labeled as "Lab 1" and "Lab 2" – are separated by 398 m and connected via a 700 m long fiber link. Note that the distances were chosen on purpose to close the locality loophole in a recently performed loophole-free Bell test [112]. Each atom trap is designed and optimized for light-matter entanglement generation according to the scheme in Fig. 6.1b. An atomic Zeeman qubit formed by the states $|\downarrow\rangle = |S_{1/2}, F = 1, m_\mathrm{F} = -1\rangle$ and $|\uparrow\rangle = |S_{1/2}, F = 1, m_\mathrm{F} = +1\rangle$ is entangled with the polarization of a single photon at 780 nm via resonant excitation followed by spontaneous emission in free-space. The photons from both traps are fiber-coupled and guided to PPQFCDs located in the two labs in close proximity to the traps. Each of the converted photons is then forwarded through telecom fibers with a length of up to 10 km, which in the first step are realized by fiber spools, in addition to the fiber link between the labs. A central BSM consisting of a 50:50 fiber BS, two PBS and four single-photon detectors, which is adapted from an equivalent setup for 780 nm [64], renders possible projective measurements of the photons to Ψ^- and Ψ^+ Bell-states, and heralds the creation of atom-atom entanglement. Fig. 6.1c shows a map with the two labs in Munich: each lab is additionally equipped with QRNG required for a loophole-free Bell test or device-independent protocols. The BSM for 780 nm is located in lab 1 as well.

The complexity of the experiment sets higher demands on the QFC system compared to the trapped-ion experiments, which we already discussed in Sect. 2.3. Recalling the categories of figures of merit to scale-up QFCDs listed in Tab. 2.1, we realize that pump laser properties as well as the integration into existing QNNs become relevant in addition to the conversion metrics. To fulfill the requirements related to these categories, we first have to choose a suitable wavelength combination of the DFG-process. We decided for a pump laser at 1600 nm, i.e. single photons at 780 nm are converted to the telecom S-band at 1522 nm, being a trade-off between the following criteria:

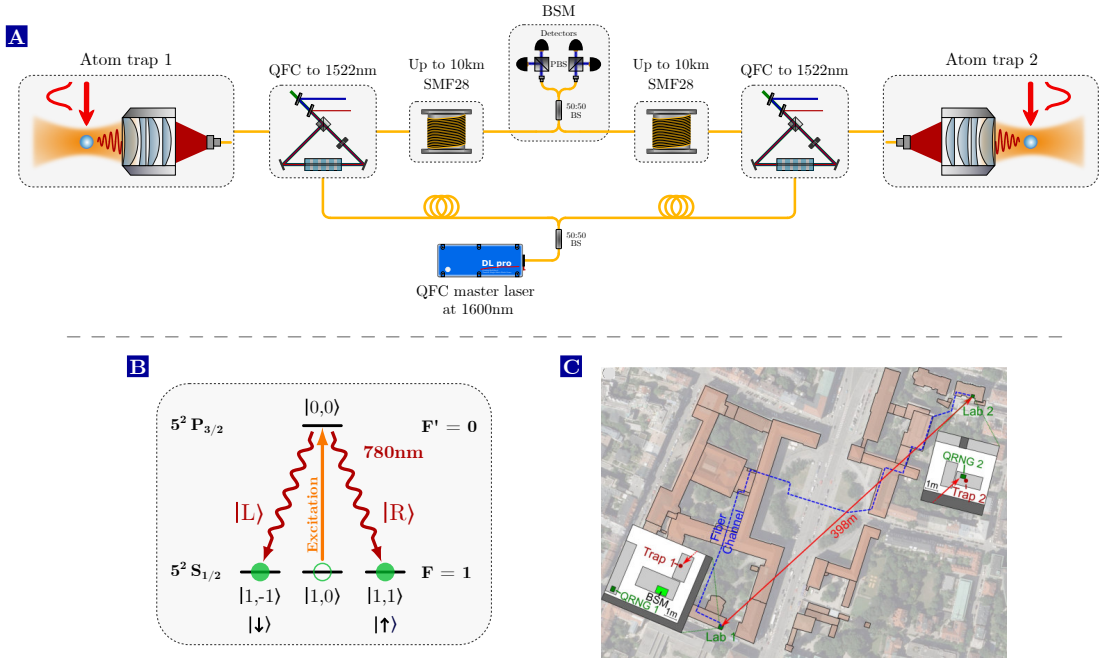

Figure 6.1. Atom-atom entanglement over kilometer-scale fibers. **(A)** The scheme to entangle two single trapped ^{87}Rb-atoms in remote traps over several kilometers of fiber. The single atoms in both traps emit photons at 780 nm, which are entangled with internal electronic states and frequency-converted to the telecom S-band at 1522 nm. The converted photons are transmitted through fibers with lengths of several kilometers, interfere in a fiber-BS at a central BSM, and are detected to swap atom-photon to atom-atom entanglement. Both PPQFCDs are pumped by a single master laser at 1600 nm, which guarantees frequency indistinguishability of the converted photons, a requirement for the quantum interference at the BSM. **(B)** The scheme for entanglement generation between two Zeeman sublevels of the $S_{1/2}, F = 1$ ground-state of a ^{87}Rb-atom and the polarization state of a spontaneously emitted photon at 780 nm. **(C)** Overview of the elementary quantum network link in the city center of Munich (figure taken from [112]). It consists of two atom traps in different buildings, which are separated by 398 m (air distance) and 700 m of fiber. The BSM is located in lab 1.

(I) The target wavelength should be as close as possible to the telecom C-band around 1550 nm where attenuation in optical fibers is minimal.

(II) To achieve a sufficiently low amount of CIB, the QFC should operate in the long-wavelength pumping regime. Moreover, the frequency difference between pump and target wavelength should be as large as possible to minimize ASR background around the target wavelength.

(III) The BSM relies on quantum interference of the photons from both traps. To allow for a large interference visibility, the frequency-converted photons must be indistinguishable with respect to their central wavelength as well as their spectral and temporal shape. The demand on the shape requires a single-frequency pump laser with a linewidth substantially smaller than the photon linewidth of

5.1 MHz. To obtain identical central wavelengths of independently converted photons, two alternative configurations are obvious: (I) a single master laser, which is distributed to the QFCDs located at each node, (II) separate pump lasers for each converter whose frequencies are absolutely stabilized with a precision much below the photon linewidth.

(IV) The pump lasers have to deliver 2 W of single-frequency output light in order to achieve high internal conversion efficiencies approaching 100%. Moreover, the lasers must satisfy the properties listed Tab. 2.1 (high power stability, reliable 24/7-operation, turn-key system). The latter is specified in particular as complexity (and potentially also the measurement periods) increases along with an increasing number of nodes, hence requirements on the reliability of all components also increase.

Pump lasers with wavelengths ranging from 1565 nm to 2050 nm can be used to convert 780 nm to the telecom bands if restricted to the long-wavelength pumping regime. To meet the requirements on spectral properties, output power and long-term stability, a MOPA configuration (Master Oscillator Power Amplifier) comprised of a narrowband, tunable seed laser (e.g. single-frequency diode or fiber lasers) and a fiber amplifier is a suitable candidate. This cuts the wavelength range into two windows; one from 1565 nm to 1605 nm covered by Erbium-doped fiber amplifiers (EDFA) [152, 166] and one from 1900 nm to 2050 nm where Thulium-doped fiber lasers (TDFL/TDFA) are available [82]. While the wavelength combinations with TDFLs offer superior background properties in the QFC, Erbium-based systems are far more developed and allow for target wavelengths in or close to the C-band. Thus, we chose 1600 nm as pump wavelength, which corresponds to the largest possible frequency separation between pump and target wavelength (1522 nm) within the Erbium gain spectrum. In fact, polarization-dependent and polarization-preserving QFCDs based on this particular wavelength combination have already been implemented by the Imoto group (Osaka University) to convert nonclassical light from SPDC sources [147, 150] and atomic ensembles [154, 166]. Another advantage is that 1600 nm can be conveniently transmitted with low losses through optical fibers, i.e. even if the nodes are separated by several kilometers, a single master laser in combination with EDFAs is sufficient to supply all QFC devices. Hence, spectral indistinguishability of the frequency-converted photons is guaranteed.
To account for a comparatively easy integration into existing quantum optics experiments, the QFC system consists of a series of mobile standalone platforms. Each platform has a top layer with the optical setups, which are placed on honeycomb breadboards and covered by black hardboards for laser safety and stability reasons. The breadboards are mounted on a substructure made of item profiles with one or multiple layers occupied with control electronics. To reduce mechanical vibrations, all platforms are decoupled from the environment with sorbothane isolators. Number and size of the isolators are optimized with respect to low cut-on frequencies (around 30 - 50 Hz) for a given weight of the platform.
In total, the system consists of four platforms, namely a master laser system to provide frequency-stabilized light at 780 nm and 1600 nm for the DFG-process (I), two PPQFC

devices to equip both nodes in the network link with a telecom interface (II & III), and a platform to perform a BSM at telecom wavelengths (IV). In the following sections we present these platforms in more detail. A selection of photographs of the individual platforms can be found in Appendix D.

6.2 Master laser system

The operation of the QFC system requires two lasers: one at 780 nm serving for alignment and benchmarking of the QFCDs, and one at the pump wavelength (1600 nm) to drive the DFG-process. We will find out later in this section, that narrowband spectral filtering of the frequency-converted photons down to 27 MHz is necessary to reduce ASR background; i.e. both lasers should be frequency-stabilized to an absolute long-term stability in the sub-MHz regime. Hence, the master laser platform contains - in addition to the lasers - optical and electronic components to realize the frequency stabilization as well as optical components to distribute both lasers to the other platforms, which is illustrated in Fig. 6.2a. In the following, we briefly explain the individual components and laser locking scheme; a detailed description can be found in the Bachelor thesis of T. Bauer [262].
Both lasers are tunable, single-frequency diode lasers (DL pro, *Toptica Photonics*). The 780 nm laser is utilized – in addition to the alignment of the QFCDs – to provide an absolute frequency reference to lock the 1600 nm laser via the transfer-lock scheme. The reason is that the 780 nm laser can be conveniently stabilized via spectroscopy of an atomic Rb-vapor, whereas narrow optical transitions (< 1 MHz) for spectroscopy are not easily available around 1600 nm. The wavelength of the 780 nm laser is stabilized to 780.23314 nm, corresponding to the ^{87}Rb hyperfine transition $5^2S_{1/2}, F = 1 \leftrightarrow 5^2P_{3/2}, F' = 0$, by Doppler-free saturation spectroscopy using an commercial vapor cell (Cosy, *TEM Messtechnik*). Note that this is the transition on which the single photons for light-matter entanglement generation are emitted (cf. Fig. 6.1b). In Fig. 6.2b we find the ^{87}Rb Doppler-free spectroscopy signal (red curve) with the allowed hyperfine transitions between the lower ground-state $S_{1/2}, F = 1$ and the excited states $P_{3/2}, F' = 0, 1, 2$. The unlabeled peaks are the crossover-resonances commonly appearing in Doppler-free spectroscopy. The combination of the positions of each peak obtained via a multi-peak Lorentzian fit and the literature values of the hyperfine splitting (from [263]) gives rise to the frequency scale on the x-axis. The gray dashed line indicates the transition $S_{1/2}, F = 1 \leftrightarrow P_{3/2}, F' = 0$ on which the laser is locked. To achieve a top-of-fringe lock, we employ a lock-in technique: a sinusoidal modulation of the diode current with a frequency of 200 kHz induces sidebands onto the laser. A subsequent demodulation of the spectroscopy signal with the modulation frequency gives rise to a dispersive error signal, which is equivalent to the derivative, and features a linear slope with a zero-crossing at the peak position (blue curve in Fig. 6.2b). Since we lock to one of the weakest hyperfine transitions, we need a rather high amount of laser power to get a proper error signal. Thus, the transitions are considerably power-broadened by a factor 4-5 compared to the natural linewidth. In the locked mode we estimate an absolute stability of ≈ 800 kHz rms from a long-term measurement of the error signal.

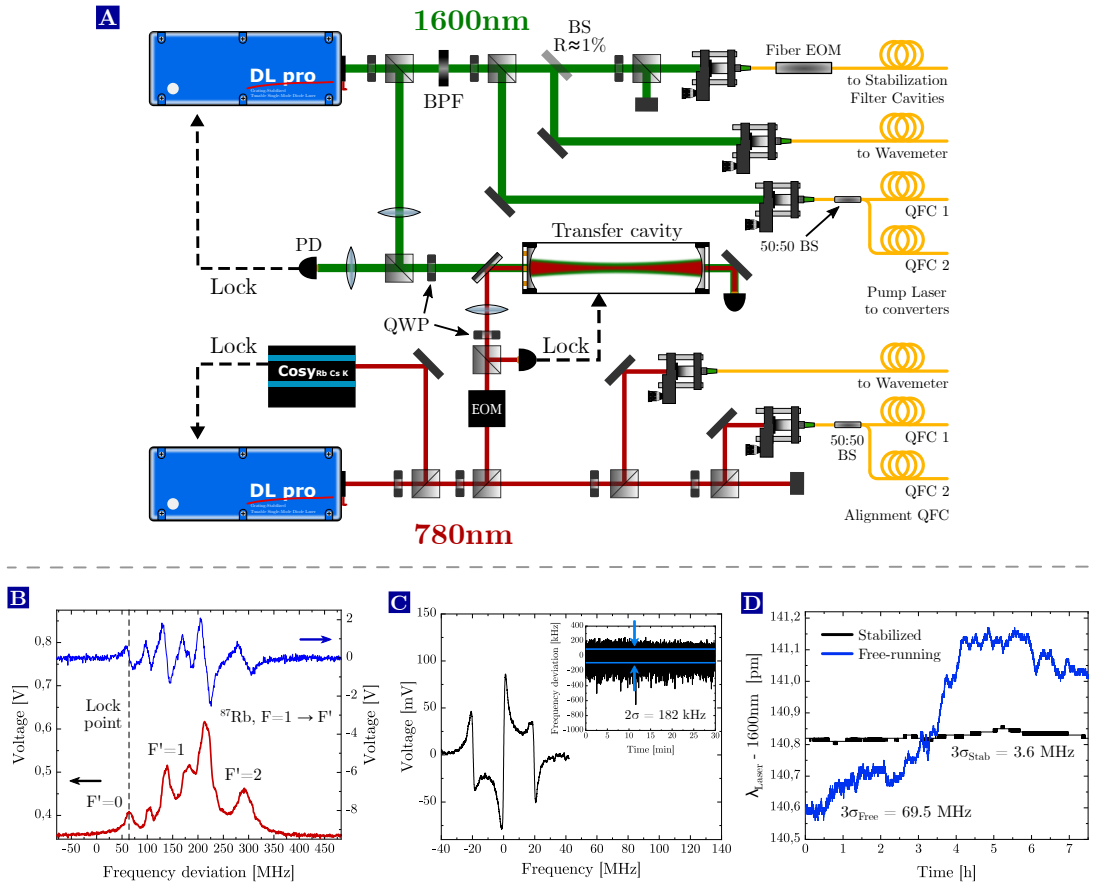

Figure 6.2. Master laser system. **(A)** Schematic illustration of the optical setup of the master laser system showing all essential components. All cube beam-splitters and unlabeled wave plates are PBS and HWPs, respectively. **(B)** ^{87}Rb Doppler-free spectroscopy signal (red curve) and dispersive error signal (blue curve) with three hyperfine transitions from $F = 1$ to $F' = 0, 1, 2$ and three crossover resonances. The laser frequency is locked to the transition $F = 1 \leftrightarrow F' = 0$. **(C)** The PDH error signal of the 780 nm laser if the cavity length is scanned. Based on the time trace of the error signal, the linewidth of the cavity, and the gradient of the PDH signal, we estimate a frequency uncertainty of the cavity resonance of $\sigma = 91$ kHz relative to the 780 nm laser. A similar calculation for the 1600 nm laser (graphs not shown) yields a frequency uncertainty of 75 kHz relative to the cavity. **(D)** Wavelength of the 1600 nm laser over several hours in the free-running and locked mode measured with a wavemeter. Since the accuracy of the wavemeter is only specified to 200 MHz, we can merely make qualitative conclusions on the stability implying that the measured uncertainties cannot be considered reliable.

The confocal transfer cavity for the stabilization of the 1600 nm laser is doubly resonant for 780 nm and 1600 nm, has a free spectral range of 500 MHz ($L = 150$ mm), and theoretical finesses of roughly 280 at 780 nm (measured: 243) and 310 at 1600 nm (measured: 266). Its design is similar to that in [247], i.e. the main part is a length-adjustable lens tube. One of the mirrors is glued on a homebuilt mount with an external thread to

screw it into one of the ends of the tube. The second mirror is not firmly connected to the mount screwed into the tube, but detached by a rubber O-ring. Three piezo actuators are used to press the mirror against the O-ring, which enables fine tuning of the cavity length. Coarse tuning of the length is facilitated by an active temperature stabilization of the lens tube using heating wires. If the cavity is not evacuated, its optical path length depends on the refractive index of air. In turn, this leads to slightly differing optical path lengths at both wavelengths due to chromatic dispersion. This becomes critical if fluctuations of the air pressure or temperature change the refractive indices. In this case we obtain a relative change between the effective lengths at 780 nm and 1600 nm resulting in frequency shifts of the 1600 nm laser even if the cavity length is locked [264]. To minimize the influence of air pressure and temperature, the whole cavity is placed within an evacuated chamber. The lock of the cavity length to the 780 nm laser is realized via the PDH technique: 130 µW of 780 nm light pass an EOM (*Qubig*), which modulates sidebands at 19.4 MHz onto the laser, a PBS, QWP and a spherical lens with $f = 350$ mm to achieve optimal mode-matching to the cavity. The combination of PBS and QWP separates the beam reflected by the cavity from the incident beam and forwards it to a photodiode. Commercial electronics (*Qubig*) demodulate the photodiode signal with the modulation frequency yielding the PDH signal displayed in Fig. 6.2c. A homebuilt electronics system (a revised version of that presented in [264]) then uses the PDH signal to lock the cavity length by applying fast feedback to the piezo actuators and slow feedback to the temperature. To assess the performance of the lock, we extract the uncertainty of the resonance frequency with respect to the 780 nm laser from a comparison of the PDH signal recorded in the locked state over 30 min with the PDH signal obtained by scanning the cavity length (inset of Fig. 6.2c). We find an uncertainty of $\sigma = 91$ kHz, which is well below the absolute stability of the 780 nm laser. The 1600 nm laser is locked to the cavity via the PDH technique, too. The optical setup is similar to that of the 780 nm light; in this path the cavity coupling-lens has a focal length of 500 mm. The generation of the PDH signal and the locking is performed by the digital control electronics of the DL pro. Instead of using an EOM, the sidebands are created via a modulation of the diode current with 12.5 MHz. A similar evaluation of the error signal yields a frequency uncertainty with respect to the cavity of $\sigma = 76$ kHz.

A disadvantage of the transfer-lock scheme is that we achieve absolute accuracy only within one FSR since we cannot distinguish between different longitudinal modes of the cavity. Hence, an additional absolute reference at 1600 nm is required. To distinguish between two neighboring cavity modes with the 1600 nm laser is comparatively uncritical since the absolute accuracy of the measurement device solely needs to be better than the FSR divided by two, i.e. 250 MHz. This is fulfilled by our wavelength meter (WS6-200, *High Finesse*), which has a specified accuracy of 200 MHz. Note that the actual accuracy in the stable environment of our labs is significantly better (< 10 MHz, Sect. 3.2.1). However, the situation becomes more complex if we lock the cavity length to the 780 nm laser on a different longitudinal mode. The cavity is resonant if the laser frequency equals multiples of the free spectral range, i.e. $\nu_{780} = n \cdot \mathrm{FSR}$ and $\nu_{1600} = m \cdot \mathrm{FSR}$ with the mode numbers n and m. Due to a limited accuracy of the

temperature stabilization, it may happen that we lock the cavity length to the next but one mode resonant to the 780 nm laser, i.e. we get $n' = n+2$ with $\nu_{780} = n' \cdot \text{FSR'}$. The frequency shift that occurs for the mode $m' = m+1$ of the 1600 nm laser due to the change of the cavity length is given as

$$\begin{aligned}\Delta\nu_{1600} &= (m+1)\cdot \text{FSR'} - m \cdot \text{FSR} = (m+1)\cdot \text{FSR} \cdot \frac{n}{n+2} - m \cdot \text{FSR} \\ &= \frac{n-2m}{n+2} \cdot \text{FSR}. \end{aligned} \tag{6.1}$$

We find that if the mode numbers and accordingly the frequencies of the two lasers differ by a factor two, the frequency shift equals zero. Since ν_{780} is quite close to $2\cdot\nu_{1600}$ in our case, we only obtain a small frequency shift of 17 MHz. Thus, an absolute accuracy of at least 8.5 MHz is necessary to verify that the cavity is locked to the correct longitudinal mode resonant to the 780 nm laser. To ensure this precision with the wavemeter, we calibrate it with the 780 nm laser about 2-3 times per week in order to compensate for long-term drifts of the absolute accuracy caused by environmental effects (e.g. temperature, humidity, air pressure,...).
We stabilize the laser to 1600.1419 nm, which corresponds to a wavelength of the converted light of 1522.7106 nm. With the absolute stability of the 780 nm laser and the relative frequency uncertainties of the transfer-lock, we estimate a stability of nearly 1 MHz. Unfortunately, we do not have the possibility to measure the long-term stability with a precision below 1 MHz. To get a rough idea and to obtain an upper bound of the stability, we record the wavelength of the 1600 nm laser over several hours in the free-running as well as the locked mode with the wavemeter. The result is shown in Fig. 6.2d: it is clearly visible, that the free-running laser reveals a much larger drift of its wavelength ($3\sigma_{\text{free}} = 69.5$ MHz) compared to the uncertainty of the locked laser. However, the exact numbers are not reliable and should be merely considered as a qualitative statement.
As shown in Fig. 6.2a, the light of both lasers, which is not sent to the Cosy cell, transfer cavity or wavemeter, is coupled to SM fibers and guided to the other platforms for different purposes. For both lasers we have 50:50 beam splitters to distribute alignment and pump light to the two PPQFCDs. In addition we employ the 1600 nm laser to lock the length of two 27.3 MHz-broad cavities, which are part of the spectral filtering stage, and located on the BSM platform. Further details on this will be explained in Sect. 6.3.3.

6.3 Polarization-preserving QFC for the Rubidium D2-line

We proceed with the description of the PPQFCDs, which are constructed in Sagnac configuration for the same reasons as mentioned in Sect. 3.2 for the C-band converter for 854 nm. Both devices are designed and set up to be identical; moreover all components were simultaneously ordered and are from the same batch. We will see that merely slightly different WG properties cause discrepancies of the device efficiency and CIB in

the range of a few percent. Since many issues are similar to the C-band converter for 854 nm (e.g. alignment, properties of optical components,...), we here only present those aspects which were omitted in the previous chapters, or are unique to this wavelength combination.

6.3.1 Nonlinear waveguide chips

The two PPLN waveguide chips are almost identical to those for 854 nm: both chips are 40 mm long and contain six WGs with three poling periods (18.15 µm, 18.20 µm and 18.25 µm) and two different lateral geometries of 7.8 µm × 9.4 µm and 7.8 µm × 9.8 µm. We already mentioned that we are able to tune and stabilize the WG temperature in order to achieve best possible phasematching for a given wavelength combination. To identify suitable WGs and their operating point, we couple a few mW of optical power at the input wavelength to the WGs and measure SPDC spectra at different temperatures with an optical spectrum analyzer (OSA, model AQ6370B, *Yokogawa*). A representative spectrum of the signal field of each chip is shown in Fig. 6.3a & b (black trace). The idler field is at wavelengths > 1700 nm and therefore outside the sensitivity range of the OSA. A suitable WG is characterized by a spectrum, which shows good agreement with the theoretically expected sinc^2-function determined by the phasematching condition. A sinc^2-behavior is clearly visible in Fig. 6.3a & b, however, we also identify asymmetries. In general, symmetric spectra are not expected since the phase mismatch $\Delta k'$ does not scale linear with the wavelength. This is confirmed by simulations (red trace), which calculate the phase mismatch taking wavelength combination, temperature-dependent refractive indices, WG dispersion, and WG geometry into account (the simulations were performed by B. Kambs, Saarland university; for details see [225]). The deviations of the measured spectrum may result from imperfections in the WG geometry or random duty-cycle errors of the QPM grating [265]. Nevertheless, those deviations are small and we infer a high quality of the WGs. The maximum efficiency of the DFG-process is attainable at the top of the sinc^2-curve, hence, we record the peak wavelength at different temperatures to identify an ideal operating point. The results are shown in Fig. 6.3b & c: we see that all WGs enable frequency conversion to the whole S-band, the C-band until 1550 nm, and partly even to the E-band down to 1360 nm. A similar simulation as above again yields theoretical curves (solid lines) in good agreement with the data points.
Both converters are operated with the G3WG2 (the WGs whose spectra are shown in Fig. 6.3a & b) at temperatures of 44.4 °C (lab 1) and 52.1 °C (lab 2), respectively. Since none of the WGs possess spectra with huge deviations from the sinc^2-curve, we selected the third group due to the lowest phase matching temperatures (mainly for convenience, we do not significantly benefit in terms of CIB in this temperature range as mentioned in Sect. 2.1.2). Moreover, the second WG of this group enables larger coupling efficiencies for input and pump field on both chips. Note that the 780 nm laser was not yet locked to the correct wavelength during the measurements, but only roughly set to the correct value with the OSA, which explains slight deviations between the final optimal temperatures and those in Fig. 6.3b & c.

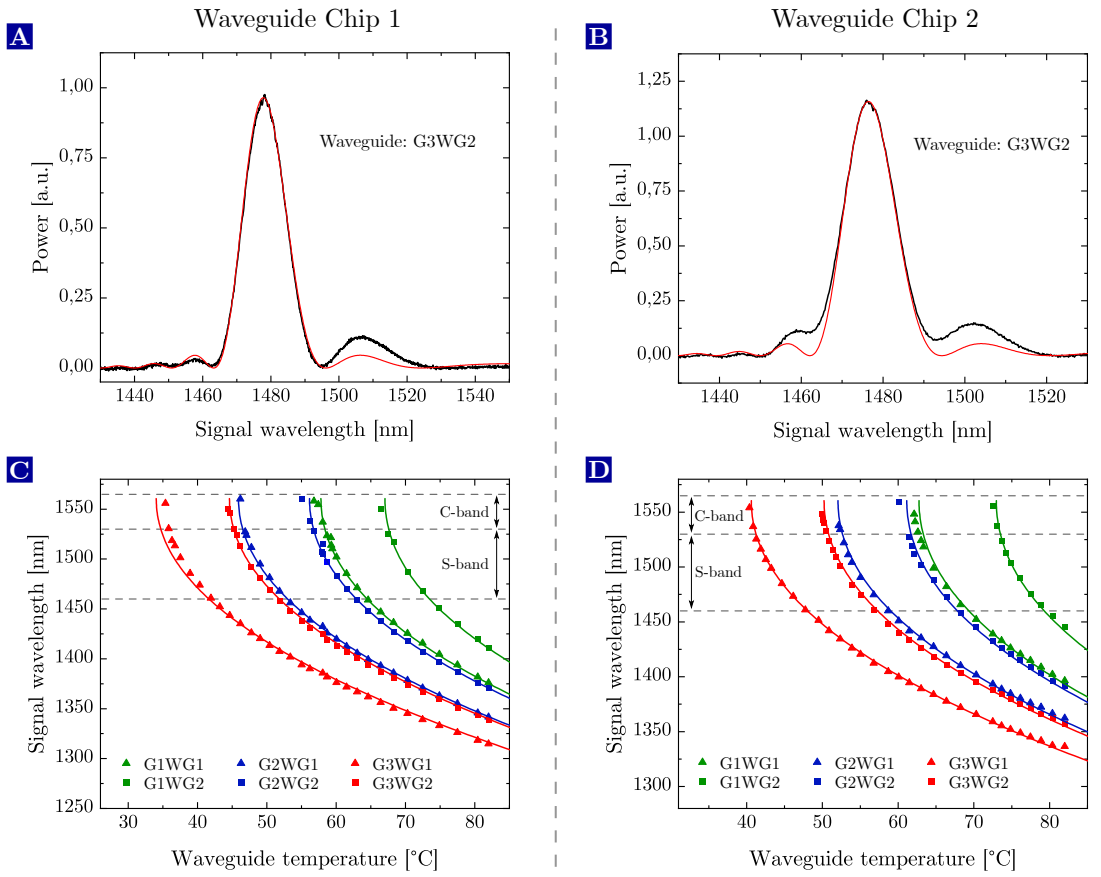

Figure 6.3. Temperature-tuning curves and spectra of the waveguides. **(A)/(B)** SPDC spectra of the second WGs in the third group, which are employed in all following experiments. The black points are measurement data, the red solid lines are simulations (performed by B. Kambs, [225]). **(C)/(D)** The center wavelengths of the spectra of all six WGs on each chip at different temperatures for a pump wavelength around 780.23 nm. The solid lines are again simulations.

6.3.2 Investigation of Raman background

CIB is here – in contrast to the Ca^+-converters – a major issue and significantly limits the performance of the QFC system. The reason is the comparable small spectral separation between pump and target field of 9.526 THz ($-317.8\,cm^{-1}$) resulting in a large amount of ASR background (cf. Sect. 2.1.2). We quantify this by a measurement of the ASR spectrum of the converter with the OSA. In order to obtain a realistic estimation of the amount of scattered photons, we meet the following crucial points: **(I)** The pump laser is set to the final pump wavelength of 1600.14 nm. **(II)** The WG is already aligned in Sagnac configuration; all fields are coupled in both directions and the pump powers per arm are set to maximum conversion efficiency. **(III)** The only spectral filter is a shortpass filter (edge at 1538 nm, corresponds to $-252\,cm^{-1}$) to suppress the pump laser. Fig. 6.4a displays the spectrum from $-700\,cm^{-1}$ to $-252\,cm^{-1}$, i.e. in the range between

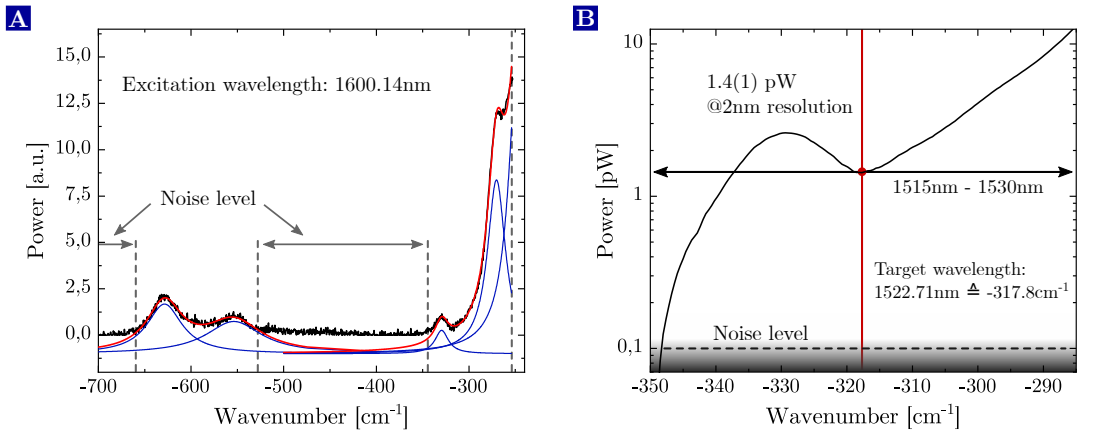

Figure 6.4. Investigation of Raman background. **(A)** The anti-Stokes Raman spectrum measured behind the converter with an excitation wavelength of 1600.14 nm. In the areas marked by gray dashed lines the noise level of the optical spectrum analyzer is approached; there Raman scattering is still present, but roughly one order of magnitude below the noise level [134]. The gray dashed line close to the right margin indicates the onset of the SPF to suppress the pump laser. The blue and red solid lines are multi-peak Lorentzian fits. **(B)** The ASR spectrum measured with a large integration time around the target wavelength of the QFC process, which is marked by the red vertical line.

1439 nm and 1538 nm. A multi-peak structure is clearly visible; Lorentzian fits (blue and red solid lines) reveal center positions of −631, −554, −329, −270 and −246 cm^{-1} (the last value of −246 cm^{-1} is outside the measurement range; its position is extracted from [173]). Similar center positions were measured in ASR spectra [134,135,173,184] or the respective SR spectra [173,266]. A comparison of the measurements reveals that not all peaks appear in each measurement, moreover their relative intensities significantly vary. For instance the peak at −631 cm^{-1} is not present in [134] but very pronounced in [135]. As mentioned in Sect. 2.1.2, these findings could be related to different excitation wavelengths. Note that additional peaks are expected to appear between −350 and −530 cm^{-1} as well as beyond −660 cm^{-1}, however, their intensity is below the noise level of the OSA. The spectrometer equipped with a LN_2-cooled InGaAs CCD-camera, which has a much lower noise level and was employed to measure the spectra in [173], was demounted and not available for the present measurements.

A more quantitative prediction of ASR background around the target wavelength is derived from Fig. 6.4b. It displays the ASR background between 1515 nm and 1530 nm measured in the highest sensitivity mode of the OSA, i.e. the noise level is reduced to 0.1 pW by means of long integration times, a small spectral resolution of 2 nm, and an internal chopper. By design, the target wavelength 1522.71 nm is in a local minimum between the peaks at −329 and −270 cm^{-1}. The power on the y-axis is defined as power per resolution, i.e. we find a power density of [1.4(1) pW]/2 nm = 0.70(5) pW/nm at the target wavelength. This corresponds to $R_{\mathrm{cib,\,gen}}$ = 41.4 photons/MHz bandwidth assuming that the background is equally distributed in the 2 nm-window. If we compare this to 0.1 photons/MHz of generated background in the C-band converter (filter band-

width: 250 MHz), and keep in mind that collection efficiencies and temporal lengths of the photons emitted by trapped ions and atoms are in a similar order of magnitude, it is obvious that narrowband filtering down to the small MHz-regime is required to achieve acceptable SBRs.

6.3.3 Narrowband spectral filtering system

In order to find an optimal filter bandwidth, we have to consider the spectral density of the background, the linewidth of the photon as well as the technical realizability of the filter system. The first two issues are addressed in Fig. 6.5a: it displays the theoretically expected background count-rate (black solid line) and the transmission of a spontaneously emitted photon with a linewidth of 5.1 MHz (blue solid line) at different filter bandwidths. The detected background count-rate is calculated as

$$R_{\mathrm{bcr}} = R_{\mathrm{dcr,\ snspd1}} + R_{\mathrm{dcr,\ snspd2}} + \Delta\nu_{\mathrm{fil}} \cdot 41.4\,\mathrm{cps/MHz} \cdot \frac{\eta_{\mathrm{snspd1}} + \eta_{\mathrm{snspd2}}}{2}. \qquad (6.2)$$

It is composed of the SNSPD dark-counts and the generated converter background, which is multiplied by the average SDE. We use the values associated with the bias currents at which the SNSPDs are operated in the following experiments, namely SDEs of 36 % and 32 %, and DCRs of 63 cps and 53 cps, respectively. At large filter bandwidths R_{bcr} is dominated by ASR background being approximately linear dependent on $\Delta\nu_{\mathrm{fil}}$ up to roughly 50 GHz, whereas a saturation effect caused by the constant detector DCR appears at small filter bandwidths. While a small filter bandwidth is appealing to suppress ASR background, it also affects the transmission of the emitted photons: if the filter bandwidth approaches the photon linewidth, we start to absorb part of the photons. To calculate the photon transmission, we assume the filter transmission to be a Lorentzian function with FWHM = $\Delta\nu_{\mathrm{fil}}$, which is valid in our case as we will see later in this chapter. The filter function is multiplied with a Lorentzian-shaped photon with FWHM = 5.1 MHz yielding the shape of the transmitted photon. Finally, the area of the transmitted photon is divided by that of the original photon. The result is shown in Fig. 6.5a: if the filter bandwidth equals the photon linewidth, the transmission is reduced to 50 %, however, surprisingly the effect is already significant for filter bandwidths much broader compared to the photon. For instance even at $\Delta\nu_{\mathrm{fil}}$ = 100 MHz the transmission is merely 94.3 %. This can be understood by the fact that Lorentzian functions only slowly decay compared to Gaussian functions. Therefore, a considerable part of their total area resides outside the transmission window of the filter leading to strong absorption. A good measure to identify a suitable operating point is the SBR of the filter given as the ratio between T_{pho} and R_{bcr} (red solid line in Fig. 6.5a). An absolute scale is not provided since this depends on the photon source. However, we are mainly interested in its trend, which reveals a maximum around 7 MHz. Thus, a good trade-off is a filter bandwidth around 30 MHz: it is only a factor 1.5 below the maximal possible SBR, it still allows for a photon transmission $> 80\,\%$, i.e. we do not degrade the entanglement generation rate much, it does not considerably alter the temporal shape of the photon wavepacket, and it is possible to construct such a filter with high overall transmission as we will see below. Note that the red and blue

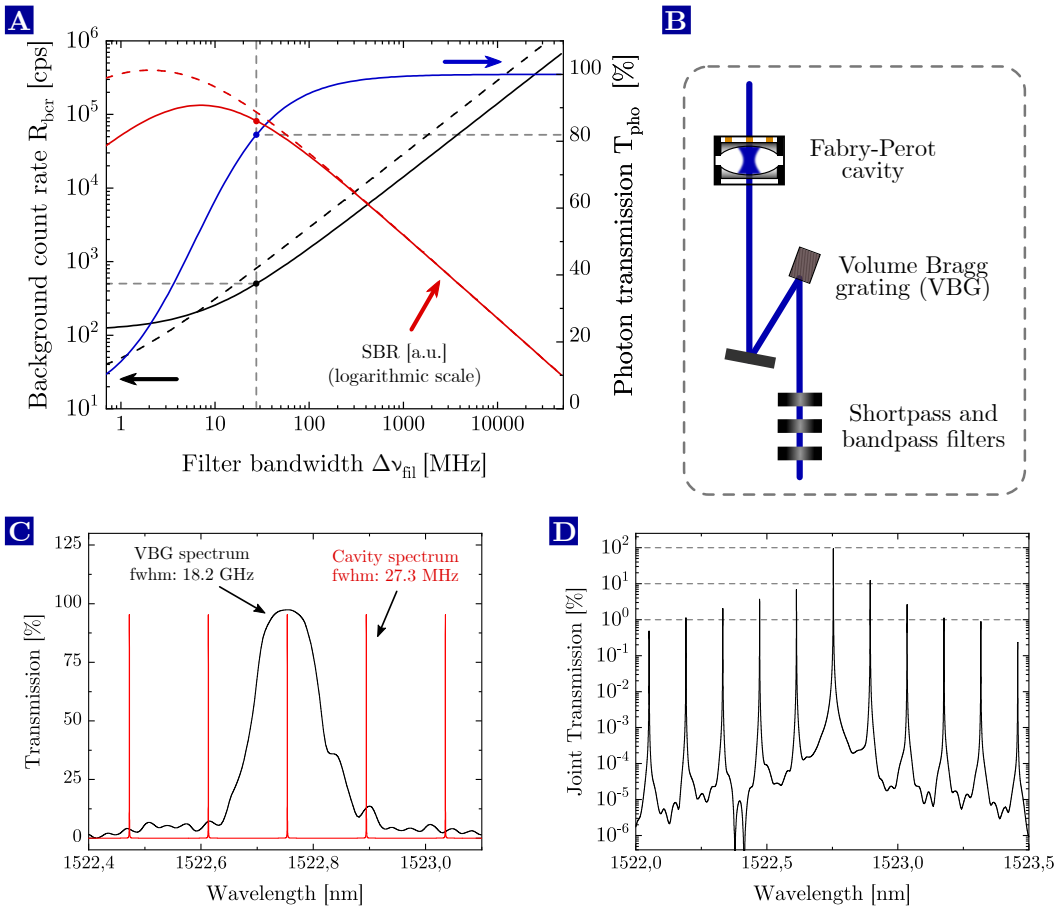

Figure 6.5. Narrowband spectral filtering stage. **(A)** Transmission probability of an emitted and converted photon with a linewidth of 5.1 MHz (blue line), background count-rate (black line) and theoretical scaling of the SBR (red line) at different filter bandwidths. The background count-rate is composed of CIB and detector dark-counts. The red and black dashed lines are calculated for improved SNSPDs (details see main text). The final filter bandwidth of 27.3 MHz is indicated by the vertical gray dashed lines. **(B)** Scheme of the spectral filtering stage consisting of cavity, VBG and interference filters. **(C)** Theoretical transmission spectrum of the cavity (red line) and measured reflection spectrum of the VBG (black line) around the target wavelength. **(D)** Joint transmission spectrum of the cavity and VBG.

dashed lines are for improved SNSPDs with state-of-the-art performance with a SDE of 70 % and a DCR per detector of 10 cps. In this case even more narrowband filtering is beneficial in terms of SBR since the influence of the DCR is further reduced.
We implement narrowband filtering with a broadband suppression in a similar way as in the C-band converter (cf. Sect. 3.2.1). As shown in Fig. 6.5b we combine short- and bandpass filters with a VBG and an air-spaced FPI. The broadband interference filters, in detail one BPF (Center wavelength: 1535 nm, FWHM: 30 nm, *Omega optical*) and two shortpass filters (1560 nm cut-off) are mainly intended to remove residual pump laser and ASR induced by the pump laser originating from the WG and fibers. The

narrowband part should possess a single transmission window and a suppression as high as possible outside this window. To this end, we combine a VBG (*Optigrate*) with a FWHM of 25 GHz and a FPI acting as filter cavity (FC) with a FSR of 18.2 GHz and a linewidth of 27.3 MHz (a detailed description and characterization of the FPI will be given below). The respective reflection/transmission spectra of VBG and FPI are sketched in Fig. 6.5c. The VBG spectrum has been measured by the manufacturer whereas the FPI spectrum is calculated. The FSR of the FPI is chosen such that the first two neighboring longitudinal modes are outside the central reflection peak of the VBG to minimize leakage through these modes. Although a higher FSR might be desirable to further suppress leakage, the finesse of the FPI is limited to about 660 given by the mirror coatings, i.e. a larger FSR would result in a larger FWHM of the modes. To quantify the leakage, the joint transmission spectrum of VBG and FPI is shown in Fig. 6.5d. An integration over all neighboring peaks yields that they contribute 25.2 % to the overall transmission. Note that small deviations from this number may result from undesired transverse cavity modes, however, the first and second order mode are already suppressed with $>1{:}500$ with respect to the fundamental mode. Thus, their contribution is negligible.
The operating point of the filter system is marked as gray dashed lines in Fig. 6.5a, revealing a photon transmission of 81.8 % and an expected CIB count-rate of $R_{\mathrm{cib,\,gen}} = 1130\,\mathrm{cps}$ ($R_{\mathrm{bcr}} = 500\,\mathrm{cps}$). If we include leakage through neighboring modes, we obtain a value of $R_{\mathrm{cib,\,gen}} = 1510\,\mathrm{cps}$ ($R_{\mathrm{bcr}} = 630\,\mathrm{cps}$).

Narrowband filter cavity

The filter cavity is formed by the same mirrors as the transfer cavity, which are triply-resonant for 780 nm, 1522 nm and 1600 nm. They have a radius of curvature of 150 mm and a reflectivity of 99.53 % at 1522 nm, which corresponds to a theoretical finesse of 670. To achieve a FSR in the order of 18 GHz, the cavity should posses a length of about 8.3 mm, i.e. it is not confocal anymore but still clearly in the stability regime. The design is quite similar to the transfer cavity, which relies on a length-adjustable lens tube as spacer between the mirrors. The lens tube features two advantages: first, the cavity mirrors are surrounded by the lens tube rendering the cavity rather insensitive to airflow and acoustic waves. Second, the adjustable tube allows for convenient coarse tuning of the the cavity length. This is useful to set the length to the desired FSR, which cannot be done precise enough during the assembly of the cavity. The whole cavity is clamped to a mirror mount for precise alignment with respect to the incident beam. The mount is placed on a separate optical breadboard, which is isolated from the main board with sorbothane feets to protect the cavity from mechanical vibrations. The optical setup of the cavity is shown in Fig. 6.6a. The converted light exits a SM fiber and is coupled to the cavity mode with a spherical lens. The optimal spatial mode-matching is calculated using the same method as for the WG coupling yielding the focal lengths and distances between the SL and AL in front of the fiber. We obtain a combination of an AL with $f_{\mathrm{AL}} = 11\,\mathrm{mm}$ and an SL with $f_{\mathrm{SL}} = 250\,\mathrm{mm}$ resulting in a measured cavity transmission of 96.5 % in resonance at 1522 nm. This number is most probably limited by a tilt or a non-perfect centering of the mirrors as well as losses in the coatings, for which the

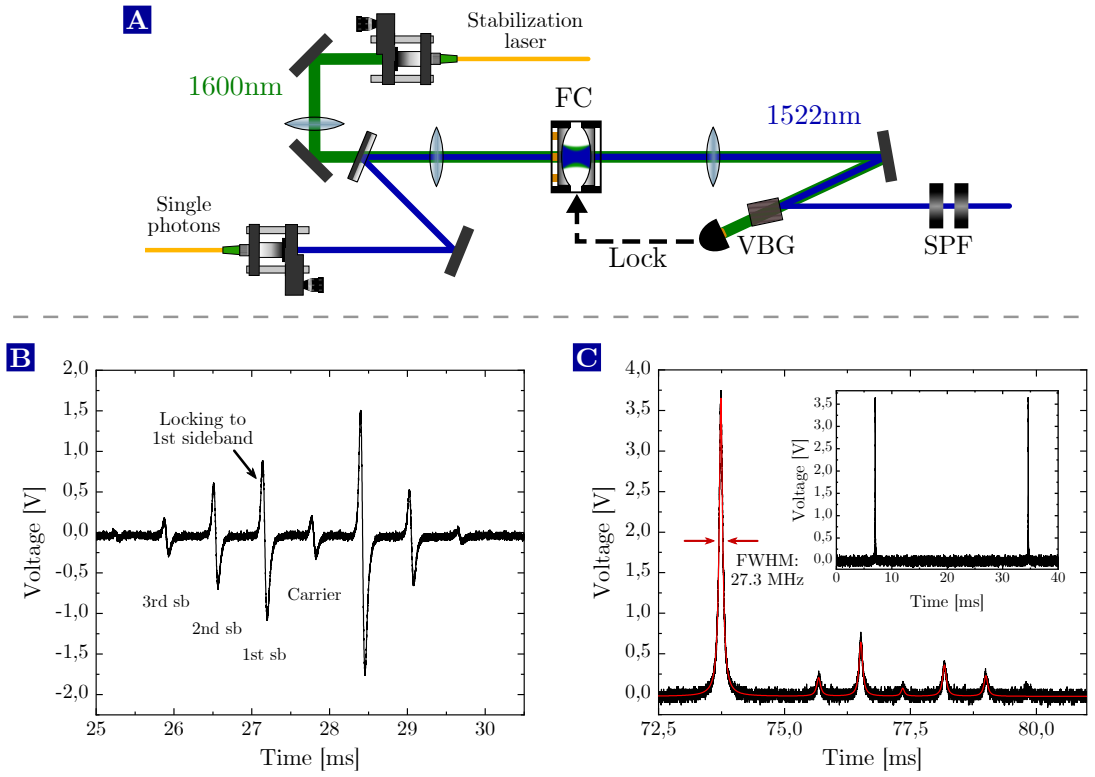

Figure 6.6. Characterization of the filter cavities. **(A)** Scheme of the filter cavity setup. The cavity length is locked employing the 1600 nm laser, which is also transmitted through the cavity and separated from the converted light by the VBG. **(B)** Dispersive error signal of the cavity length stabilization. The lock point is the first EOM sideband, whose frequency distance to the carrier is optimized for maximal transmission of the converted light. **(C)** Transmission signal for a cavity length scan: it shows the longitudinal modes of the converted light (large peak) and the carrier and EOM sidebands of the stabilization laser. Using the EOM driving frequency as reference, we obtain a linewidth of 27.3 MHz. Inset: Length scan over two longitudinal modes. No transverse modes are visible; a closer investigation reveals a suppression of $>1{:}500$.

mirrors have not been optimized.

To maintain maximum transmission of the emitted photons, the cavity length has to be actively stabilized since it is not designed as a ULE cavity. To this end, we employ the frequency-stabilized 1600 nm laser. The cavity length is stabilized on the transmitted 1600 nm light; here we take advantage of the sidebands already modulated onto the laser to implement a laser-power-insensitive lock-in scheme. The sideband frequency of 12.5 MHz is chosen on purpose as trade-off, being **(I)** much larger than the transfer cavity linewidth of 1.7 MHz resulting in a suitable PDH signal, and **(II)** smaller than the FC linewidth (27.3 MHz) to get a suitable lock-in signal. At the master laser platform (see Fig. 6.2a) the 1600 nm laser first passes a bandpass filter (center wavelength: 1600 nm, FWHM: 50 nm, *Edmund optics*) to remove amplified spontaneous emission (ASE) at 1522 nm, which is otherwise transmitted through the cavity and results in additional background counts. Next, it is coupled to a fiber-based electro-optical modu-

lator with a bandwidth of 10 GHz (MPZ-LN-10, *iXblue*). The EOM is required because it is quite unlikely to find a FSR being a divisor of the pump and target frequency with a precision of < 1 MHz (much smaller than the FC linewidth). A numerical calculation yields only two FSRs in a range between 12 and 35 GHz located at roughly 12.9 and 19.3 GHz[1]. Moreover, a double resonance cannot be reached by tuning the pump laser since the frequency of the converted light is inevitably shifted by the same value in opposite direction due to the DFG-process. To solve this issue, we use the EOM, which is powered by a home-build driver whose output frequency can be tuned between 150 MHz to 350 MHz by a voltage-controlled oscillator (for details see master thesis of T. Bauer [234]). Now, the cavity is not locked to the carrier, but to one of the first- or second-order sidebands. In this situation, we need to solely find a cavity length featuring resonance frequencies at 1522 nm and 1600 nm with a separation covered by the tuning range of the driver. This provides enough flexibility to find a suitable cavity length within roughly 100 different FSRs. The 1600 nm light is guided with a fiber from the master laser platform to the filter setup, overlapped with the converted light on a DM and coupled to the cavity using a spherical lens with $f = 300$ nm (see Fig. 6.6a). The transmitted laser is split from the converted light by the VBG and detected with an InGaAs photodiode. The electrical signal is demodulated with the modulation frequency of 12.5 MHz employing home-built electronics, yielding a dispersive error signal for the PID lock as shown in Fig. 6.6b. The lock itself is performed by a commercially-available digital locking electronics (Laselock, *TEM Messtechnik*). Behind the VBG, two SPF are inserted to fully suppress the stabilization light as well as remaining pump light from the converter.

A characterization measurement of the cavity is shown in Fig. 6.6c. The inset shows two longitudinal modes measured with the converted light. A zoom into the baseline (not shown in the figure) reveals two remaining transverse modes with a suppression of >1:500 with respect to the longitudinal modes, which verifies proper spatial mode-matching of the incident beam. The cavity length is calculated according to $L_{\mathrm{cav}} = R_{\mathrm{curv}}\,(1 - \cos(\pi d_{\text{lo-tr}}/d_{\text{lo-lo}}))$ (see [267]) with the radius of curvature R_{curv} and the distances between the longitudinal and first transverse mode $d_{\text{lo-tr}}$ and two longitudinal modes $d_{\text{lo-lo}}$. We obtain a cavity length of 8.24 mm corresponding to a FSR of 18.2 GHz. The linewidth is derived from a Lorentzian fit of the longitudinal mode to 27.3 MHz (Fig. 6.6c). The frequency scale is provided by the transmitted 1600 nm laser since the distance between sidebands and carrier is determined by the modulation frequency of 270.28 MHz. From FSR and linewidth we compute a finesse of 666 in good agreement with the theoretical value of 670.

The transmission of the whole filter system as shown in Fig. 6.6a is measured to be 90.7 %, determined by the transmission of the filter cavity (96.5 %), spherical lenses (2×98.8 %), shortpass filters (2×99.4 %) and the diffraction efficiency of the VBG (97.4 %).

[1] Although 19.3 GHz is close to the desired FSR of 18 GHz, it is quite challenging to find the correct longitudinal mode.

6.3.4 Sagnac-type PPQFCD and Bell-state measurement

Experimental setups

The optical setup of the PPQFCDs is shown in Fig. 6.7a. The input light at 780 nm is coupled out of a SM fiber (780HP) with an aspheric lens (f = 8 mm), overlapped with the pump laser on a DM, and coupled to the Sagnac interferometer. The latter consists of similar optical/optomechanical components as in the C-band converter (see Sect. 3.2.1), i.e. a custom-made PBS for all three wavelengths, an achromatic HWP (both from *B. Halle Nachfl.*), two AR-coated aspheric lenses (f = 11 mm) and the PPLN waveguide. Instead of four silver mirrors, we utilize only two in order to minimize losses due to their non-perfect reflectivity. However, this configuration is much more challenging to align and therefore not recommended[2].
The pump light is generated by an EDFA (CEFA-L-PB-HP-PM-33, *Keopsys*), which amplifies the weak seed laser guided via a SM fiber from the master laser system to the QFC device. A fiber polarizer ensures that only correctly linear-polarized light is fed into the EDFA. The amplified light with a power around 1.2 W is coupled out of a polarization-maintaining fiber with an aspheric lens (f = 11 mm) and spectrally filtered by a stack of three bandpass filters (center wavelength: 1600 nm, FWHM: 50 nm, *Edmund optics*) to eliminate ASE at the target wavelength. A subsequent PBS cleans-up the pump-light polarization, which is polluted with light not guided in the correct axis of the PM fiber. The overall power is controlled by a HWP and PBS; another HWP is employed to set the pump-laser polarization and, accordingly, the relative power in the interferometer arms. The converted light is separated by another DM and subsequently coupled to a SM telecom fiber with an AR-coated end facet. The majority of the spectral filtering system is outsourced to the BSM platform for technical reasons: first, mode-matching to the filter cavity is simplified due to a clean spatial mode exiting the SM fiber between the PPQFC and the BSM platform. Second, we can place both filter setups associated with the two converters in close proximity to each other on the BSM board, hence, we need to distribute the stabilization laser only to the BSM board. Moreover, the technical overhead for stabilization is reduced since we profit from a series of synergies in the electronics. Only the bandpass filter is placed on the QFC platform to avoid erroneous detection of remaining pump light by the power meter during alignment.
We optimized the trichroic WG coupling with the same method as described in Sect. 3.2.2. Unfortunately, the simulated aspheric lenses and distances between the lenses did not provide the desired results, but 10-15 % lower coupling efficiencies. The reason for this large discrepancy was never clarified, the most probable explanation are deviations in the WG dimensions with respect to the values provided by the manufacturer. Thus, a suitable combination of ALs and distances was identified with the iterative method applied for the O-band converter (see Sect. 3.1.1). In detail, we achieve WG-coupling efficiencies of 90 % at 780 nm with $f_{al,\,780}$ = 8 mm and $d_{al,\,780}$ = 844 mm, 87 % at 1600 nm with $f_{al,\,1600}$ = 11 mm and $d_{al,\,1600}$ = 1250 mm, and a fiber-coupling efficiency of the converted light of 91 % with $f_{al,\,1522}$ = 8 mm and $d_{al,\,1522}$ = 875 mm. Interestingly, these

[2] In fact, the C-band converter was constructed after the Rb-converters. Hence, the four-mirror configuration has been chosen from the experience of aligning the Rb-converters.

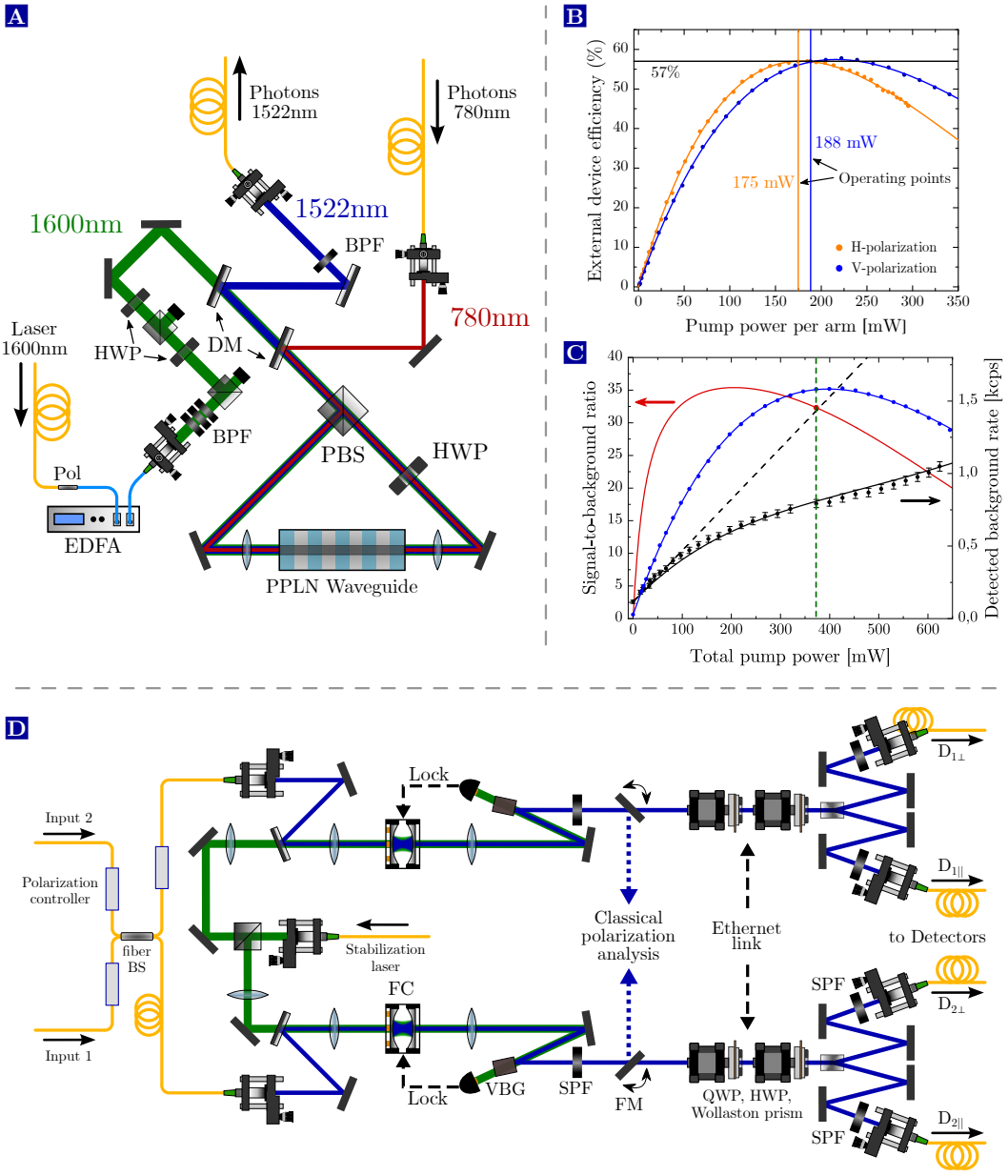

Figure 6.7. Setup and performance of the PPQFCDs and BSM. **(A)** Schematic representation of the setup for polarization-preserving quantum frequency conversion from 780 nm to the telecom S-band at 1522 nm in a Sagnac configuration. **(B)** The external device efficiencies $\eta_{\mathrm{dev,H}}$ and $\eta_{\mathrm{dev,V}}$ of the converter in lab 1 at different pump powers per arm. To compensate for small asymmetries in the setup, the arms are pumped with different powers. We achieve equal device efficiencies of $\eta_{\mathrm{dev,H}} = \eta_{\mathrm{dev,V}} = 57\,\%$. **(B)** Detected background count-rates (black dots), total device efficiency (blue dots) and theoretically expected SBR (red line) in dependence on the total pump power. The black and blue solid lines are fits to the data with the appropriate model (main text). The green vertical line indicates the operating point of the converter during the experiment. **(D)** Optical setup of the platform containing the BSM and the spectral filtering stage.

parameters are far away from the simulated ones ($f_{al,\,780} = 15.3\,\mathrm{mm}$, $f_{al,\,1522} = 15.3\,\mathrm{mm}$, $f_{al,\,1600} = 18.8\,\mathrm{mm}$), however, we believe that multiple sets of parameters enable comparably good results; the simulation solely selects the best combination.

The final platform containing the BSM and the main part of the spectral filters is sketched in Fig. 6.7d. It is located in a third laboratory nearby the atom lab 1 and connected to both atom labs via SM fibers. Both fibers are connected to the input fibers of the BSM via fiber-fiber connectors. Note that we do not employ FC/APC connectors – which are commonly used in most academia labs – but E2000-connectors (*Diamond SA*), instead. Apart from a much more convenient handling in terms of dirt and damage protection, the connectors feature a mechanical design which allows for an excellent reproducibility of efficient fiber-to-fiber coupling. Moreover, the fiber cores are actively centered with respect to the cladding in order to minimize transmission losses due to non-overlapping cores to below 0.1 dB. Additionally, we can easily insert km long spooled fibers in different lengths, each equipped with E2000-connectors, between input fibers and BSM. The input part consists of a non-polarizing 50:50 fiber-BS with three polarization controllers (PCD-M02, *General Photonics*) in the two input and one of the output ports. The latter allow for voltage-controlled manipulation of the polarization state on the whole Poincaré-sphere and are required for the automatized polarization compensation. To achieve a large visibility of the HOM interference, the BS should possess a low PDL and a splitting ratio as close as possible to 50:50. To this end, we ordered several BS from different companies and selected the best splitter. In the worst combination of input and output ports, it features a PDL of 0.05 dB, a splitting ratio of 49.7:50.3 and an excess loss of 0.16 dB. These values are sufficiently good to allow for HOM visibilities larger than 99.9 % [268]. Both beams exit the fibers and pass the spectral filters as described in Sect. 6.3.3. The stabilization laser at 1600 nm is distributed to both filter cavities employing a non-polarizing beam splitter. Behind the filter system two motorized flip mirrors switch the beam to the classical polarization analysis, which is part of the automatized polarization compensation and implemented utilizing PBS, non-polarizing BS and photodetectors. The setup is very similar to the polarization analysis at 780 nm; a detailed description of its setup as well as the design of the complete polarization compensation can be found in [269]. Subsequently, the light passes the projection setups being implemented in a similar way as in the previous chapters. All four beams are coupled to AR-coated fibers and guided to the detectors. The last SPF is inserted directly in front of the fiber-coupler to avoid leakage of stray light into the fibers. The projection setup has an overall transmission of 92.2 %, determined by the transmission through the waveplates and prism (97.8 %) and the fiber coupling (94.3 %).

Performance of the PPQFCDs

On the PPQFC platform we achieve an external conversion efficiency of 62.8 %. It is determined by the coupling of the input light to the WG (90 %), internal efficiency (96.2 %), and SM fiber in- and out-coupling (91 % × 96.5 % = 87.8 %). As for the 854 nm-converters, the passive losses in all optical components (mainly PBS, HWP, as-

pheric lenses, silver mirrors and bandpass filter) sum up to a non-negligible contribution of 82.6 %. All individual efficiencies and transmissions are in a similar range as for the C-band converter, thus, we do not provide a detailed breakdown. Including the transmission of the outsourced spectral filter system of 90.7 %, we obtain an EDI of 57 %. All numbers are given for the H-polarized component; for the V-polarized component we find deviations of the individual efficiencies and transmissions in the small percent regime due to slight asymmetries in the interferometer as well as polarization-dependent loss (cf. Sect. 3.2.3). For the same reasons, the maximum device efficiency is shifted to a higher pump power per arm as shown in Fig. 6.7b. Nevertheless, by careful alignment and an appropriate setting of the pump power in both arms to 175 mW (H) and 188 mW (V), we obtain equal efficiencies for both polarization components. Note that we require much less pump power to achieve maximum conversion efficiency compared to the C-band (625 mW) and O-band converter (695 mW). This is mainly caused by two reasons: first, the normalized coupling constant η_{nor} is proportional to the frequencies of input and converted light, i.e. η_{nor} is larger for the present wavelength combination. Second, the WG cross section is decreased compared to the other converters resulting in higher field intensities and accordingly in a reduced demand for pump power.
The total detected background count-rate R_{bcr}, composed of CIB and the DCR of both SNSPDs ($R_{\mathrm{dcr}} = 116\,\mathrm{cps}$), at different total pump powers is presented in Fig. 6.7c (black data points). In analogy to the C-band converter, we observe a nonlinear course of the ASR background due to up-conversion of ASR in the WG. Based on the model from Sect. 3.2.3 we fit the data according to Eq. 3.17 with the coefficient α_{asr} as free parameter (black solid line) yielding an excellent agreement with the data. As expected, at the operating point marked by the dashed green line where the conversion efficiency has its maximum, R_{bcr} is reduced by roughly 50 % compared to the case without the nonlinear contribution (black dashed line). There we detect $R_{\mathrm{bcr}} = 793\,\mathrm{cps}$; if we subtract the SNSPD dark-counts and divide the number by the average SDE of 34 %, we end up at a generated CIB rate of $R_{\mathrm{cib,\,gen}} = 667\,\mathrm{cps}/0.34 = 1990\,\mathrm{cps}$. This is slightly higher than the anticipated rate of 1510 cps calculated in Sect. 6.3.2. The difference is most probably caused by the OSA, which has not been calibrated with respect to the absolute power scale for several years. Moreover, the power density of the OSA is calculated for a Gaussian distribution, whereas we have a Lorentzian filter window, which may also explain the discrepancy.
Despite the high CIB compared to the 854 nm-converters, it is low enough to achieve a SBR of 32.3 for single photons emitted by the Rb-atom quantum node (see Sect. 7.2.2). If "SBR-critical" measurements are performed, a slight improvement at the cost of device efficiency is possible since η_{dev} and R_{bcr} scale in different ways. The theoretically expected scaling of the SBR is calculated as

$$\mathrm{SBR} = \frac{\beta \cdot \eta_{\mathrm{dev}}(P)}{R_{\mathrm{bcr}}(P)} \tag{6.3}$$

and shown as red solid line in Fig. 6.7c. The parameter β is a scaling factor, which is adjusted until the measured SBR of 32.3 (red dot) is hit at the operating point. We find that a slight improvement to $\mathrm{SBR} \approx 35$ is possible at roughly 80 % of the maximum efficiency. However, for simplicity reasons the converter was operated at maximum

efficiency throughout the course of this work.
All numbers for efficiency and background as well as the respective curves in Fig. 6.7b & c are measured with the converter in lab 1. The second converter in lab 2 features almost identical properties, so we here renounce a detailed presentation of the results. The converter has a device efficiency of 57.4 % and a few percent more background because a higher overall pump power is required to achieve the maximum conversion efficiency in both arms. Note that we do not present results from a quantum process tomography. In fact, QPT was performed with one of the converters revealing process fidelities similar to the C-band converter, however, we do not gain further insight by the process matrices.

6.4 Summary and discussion

In this chapter we presented a complete QFC system to extend an existing metropolitan quantum network link based on two traps for single Rb-atoms. We presented the planned experiment – telecom-heralded atom-atom entanglement over 20 km of fiber – and derived a series of design criteria to achieve a sufficiently good performance in terms of conversion metrics as well as stability and reliability of the pump laser. The whole system is constructed on mobile stand-alone platforms to be transportable and compact enough for an integration into the network link. A master laser platform provides frequency-stabilized light with absolute stabilities of about 1 MHz for alignment and pumping of the DFG-process. The distribution of a single pump laser offers the advantage of frequency indistinguishability of the converted photons. Two PPQFCDs in Sagnac configuration translate input light at 780 nm to the telecom S-band at 1522 nm employing a pump laser at 1600 nm. This wavelength combination is the best trade-off between the availability of a reliable laser system (diode laser with good spectral properties and EDFAs to provide enough power) and the impact of CIB. The dominant background process of the present wavelength combination is anti-Stokes Raman scattering due to the comparably small spectral distance between pump and target wavelength of only $-317.8\,\mathrm{cm}^{-1}$. We quantified ASR scattering by measuring spectra around the target wavelength from which we estimated a background count-rate per spectral width of 41.4 cps/MHz. To achieve a feasible SBR in the network link, a spectral filtering stage with a broadband suppression and a narrow filter width of 27.3 MHz was implemented. The generated background count-rate of the converter was measured with the SNSPDs to be 1990 cps at the operating point, which corresponds to 73 cps/MHz. The disagreement to the value extracted from the spectra stems from leakage through the filter outside the transmission window as well as uncertainties in the power calibration of the spectrometer. The EDI was measured to be 57 %, comparable to that of the C-band converter for 854 nm. The QFC system is complemented by a fourth platform to perform a photonic Bell-state measurement as well as projective measurements at telecom wavelengths.
We again finish the chapter by assessing the QFC system with our criteria to scale-up QFCDs for quantum networks listed in Tab. 6.1. If we take a look at the conversion metrics, we find that the PPQFCDs feature a similar performance as the C-band converter except for the CIB. So we can add check marks to the device efficiency and process fi-

Table 6.1. Requirements and figures of merit to scale-up QFCDs for quantum networks: Performance of the QFC system for an Rb-atom quantum network link.

Figure of merit/Requirement	QFC system
High external device efficiency	✔
Low conversion-induced background	✔✘
High process fidelity of qubit conversion	✔
High frequency and power stability (pump)	✔
Reliable 24/7-operation (pump)	✔
Turn-key pump laser system	✔
Compact and transportable system	✔
Stand-alone system and operation	✔
Integration into 19-inch racks	✘
Integration on a single chip	✘
Bi-directional operation (SHG and DFG)	✔✘
Photon bandwidth manipulation	✘
Conversion to multiple frequency channels	✘
Dispersion cancellation	✘

delity with the same arguments as in Sect. 3.4. Although the background is low enough to demonstrate atom-photon entanglement over 20 km with a SBR of about 25, future applications, e.g. device-independent certification or QKD, might require larger SBRs. Therefore, we add a check mark and a x-mark to this item. We already mentioned in Sect. 6.1 that the QFC system has been designed in particular with respect to a highly-reliable frequency-stabilized pump laser system consisting of turn-key components. The same holds for the compactness, transportability and stand-alone operation: to perform the experiment in the next chapter, the QFC system was transported to Munich and integrated into the atom experiment without significant intricacies, hence we add check marks to all those items. As for the C-band converter, all items in the categories "Miniaturized devices" and "Advanced functionalities" are technically feasible, but not yet implemented. In principle, a bi-directional operation is possible with the Sagnac configuration, however, the converter generates up-converted ASR background at 780 nm with a similar intensity as the ASR at 1522 nm. Thus, additional narrowband spectral filtering is required.

Chapter 7

Long-distance distribution of atom-photon entanglement at telecom wavelength

Contributions: The experiments in this chapter have been performed at the Ludwig-Maximilians-Universität Munich in the labs of Prof. Harald Weinfurter (H.W.).
Matthias Bock (M.B.), Tim van Leent (T.v.L.) and Robert Garthoff (R.G.) conceived the experiment and analyzed the data with advice and technical support from Kai Redeker, Wenjamin Rosenfeld (W.R.) and Wei Zhang (all LMU Munich except M.B.). The QFCD was operated by M.B. while the atom trap was operated by T.v.L and R.G. The experiments were jointly supervised by H.W., W.R. and Prof. Christoph Becher.

The main results in this chapter are published in Phys. Rev. Lett. **124**, 010510 (2020).

In this chapter we present entanglement between a single trapped atom and a telecom photon that traveled through fibers up to 20 km length, which is an intermediate step towards the realization of the full long-distance quantum network link illustrated in Fig. 6.1. To this end, the complete QFC system introduced in the previous chapter was transported to the LMU Munich and installed in the labs of Harald Weinfurter. All experiments in this chapter were performed with the atom trap in lab 1 (see Fig. 6.1c). This chapter is organized as follows: first we introduce the ^{87}Rb quantum network link, the schemes for entanglement generation and atomic-state readout, the experimental sequence and the coherence properties of the atomic qubit (Sect. 7.1). The experimental setup and the control sequences were developed over the years by several members of the Weinfurter group, hence, a profound description can be found in the PhD theses of K. Redeker [270], D. Burchardt [271], N. Ortegel [272], and J. Hofmann [268] (the first two theses contain the most recent description). In Sect. 7.2 we show the combined

experimental setup including PPQFC as well as the results on long-distance atom-photon entanglement.

7.1 Single trapped Rubidium atoms as quantum nodes

7.1.1 Overview

In the context of this thesis we employ neutral ^{87}Rb-atoms. Rubidium is an alkaline atom with a single valence electron and possesses, accordingly, a hydrogen-like energy level structure. Fig. 7.1a shows the relevant energy levels of the valence electron: it has a long-lived ground state $5^2S_{1/2}$ and two short-lived excited states $5^2P_{1/2}$ and $5^2P_{3/2}$ with lifetimes of 26.70(4) ns and 26.24(4) ns, respectively. Excited and ground states are separated by optical dipole transitions at 795 nm and 780 nm labeled as D1- and D2-line. The nuclear spin of $I = 3/2$ results in a hyperfine splitting with respect to the quantum number F associated with the total angular momentum. Additionally, each hyperfine state consists of $2F + 1$ Zeeman sublevels with quantum number m_f ranging from $-F$ to F. The atomic qubit, which will be entangled with an emitted photon later on, is encoded in two Zeeman sublevels of the ground state $|\downarrow\rangle = |S_{1/2}, F = 1, m_\mathrm{F} = -1\rangle$ and $|\uparrow\rangle = |S_{1/2}, F = 1, m_\mathrm{F} = +1\rangle$. In contrast to the trapped-ion QNN, we typically do not apply strong magnetic bias fields along the quantization axis, but only small fields in the order of tens of mG. Hence, the Zeeman sublevels only reveal a small energy difference and we do not observe Larmor precession on the time scale of the length of the photon.
The colored arrows in Fig. 7.1a represent resonant and off-resonant laser beams, which are applied to the atom for different purposes. The cooling, repump and far off-resonant dipole trap (at 852 nm) lasers are employed for cooling and trapping, the pump 1-1 and 2-1 are required for initial-state preparation by optical pumping, the excitation laser for the generation of atom-photon entanglement, and the cycling, readout and ionization lasers for the atomic-state readout. All beams are generated by five lasers in total: three frequency-stabilized diode lasers of which two at 780 nm and one at 795 nm, a homebuilt free-running diode laser amplified by a commercial tapered amplifier delivering a few hundreds of mW at 852 nm, and a pulsed diode laser at 473 nm for ionization. Note that two diode lasers at 780 nm are sufficient since the total hyperfine splitting between the $P_{3/2}$ states $F' = 0$ and $F' = 3$ is around 500 MHz and can be conveniently covered by AOMs. Only the large ground-state splitting of nearly 6.8 GHz as well as laser power issues makes two individual lasers necessary.

A simplified schematic setup of the atom trap is shown in Fig. 7.1b. Single Rb-atoms are trapped using a far off-resonant tightly focused optical dipole trap (ODT) [273] within a ultra-high vacuum (UHV) glass cell. A dispenser provides a flux of hot Rb atoms emitted into the trapping region of the ODT. The ODT features a depth of the potential well of about $k_\mathrm{B} \cdot 1\,\mathrm{mK}$ (for comparison: the depth of ion traps is >10000 K), so the atoms are too hot and their density is too low to be trapped in the shallow ODT potential at room temperature. To this end, we cool and confine a cloud of several thou-

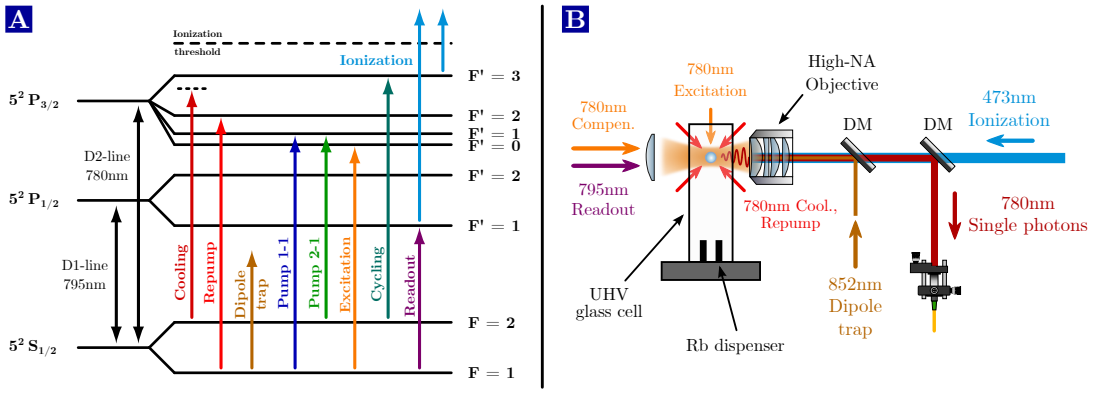

Figure 7.1. Level scheme of neutral ^{87}Rb-atoms and atom trap. **(A)** The relevant electronic energy levels of ^{87}Rb-atoms including the hyperfine but excluding the Zeeman splitting. The colored arrows denote the relevant optical transitions addressed by lasers. All lasers operate at the D1-line at 795 nm or the D2-line at 780 nm except the far off-resonant dipole trap laser at 852 nm and the ionization laser at 473 nm. Details on the purpose of each laser are given in the main text. **(B)** Simplified experimental setup of the atom trap.

sand atoms in a small volume with a diameter of roughly 1 mm with a magneto-optical trap (MOT) [274]. In the MOT the atoms are cooled in three dimensions to a few tens of µK via Doppler cooling with six beams (one pair of counter-propagating beams per direction) as well as polarization gradient cooling. Doppler cooling is performed on the cycling transition $S_{1/2}, F = 2 \Leftrightarrow P_{3/2}, F' = 3$ using the cooling laser being red-detuned by 18 MHz. Due to off-resonant excitation to $F' = 2$ the atom can decay to $S_{1/2}, F = 1$, which is a dark-state in the cooling cycle. To maintain the cycle, we additionally overlap the cooling with the repump laser to repump the atoms from $S_{1/2}, F = 1$ into the cooling/cycling transition. To spatially confine the cold atoms, coils outside the vacuum cell arranged in an anti-Helmholtz configuration generate a magnetic quadrupole field, whose field gradient leads to a position-dependent Zeeman shift. In combination with a circular polarization of the six laser beams, this results in a force towards the trap center in each direction.

The ODT is generated by a single far red-detuned Gaussian laser beam at 852 nm being focused down to a waist of 2 µm with a custom designed high-NA objective (NA = 0.4). Due to the high power of the dipole trap beam ($\approx$ 50 mW), the atoms in the focus experience a light shift of the dipole transition depending on the power of the beam, which leads to a position-dependent potential. In case of red-detuned lasers the potential is attractive, i.e. there is a force towards the highest field intensity, which confines the atom in three dimensions in the focal region of the beam. The strong focusing of the laser beam has another desired effect, namely the so-called collisional blockade effect: in the small trapping volume collisions between the atoms are the dominant loss mechanism. This prohibits trapping of more than one atom. Note that the axial confinement is one order of magnitude weaker compared to the radial one because of the geometry of the Gaussian laser beam. Depending on the trap laser power, the radial and axial trap frequencies are $\omega_{\mathrm{rad}} = 2\pi \cdot 65...92$ kHz and $\omega_{\mathrm{ax}} = 2\pi \cdot 9...13$ kHz, respectively. With

these techniques we achieve lifetimes of $\tau_{\text{life}} \approx 3.5\,\text{s}$ in the dipole trap.
The collection of fluorescence photons from the atom relies on a confocal microscope configuration employing the same objective as the dipole trap. The photons are separated from the dipole laser (and from the ionization laser, which is also focused onto the atom with the objective) with dichroic mirrors and coupled to a SM fiber. The photons are guided to the BSM and detected by a set of four APDs. The APDs detect either photons scattered by the cooling and pump lasers or single photons entangled with the atoms in order to analyze atom-photon entanglement[1] or generate atom-atom entanglement by employing an entanglement swapping protocol. The photons scattered by the cooling laser are necessary to distinguish if an atom is in the trap, which is part of the loading sequence as well as the atomic-state readout. The trap also features in-vacuum channel electron multipliers in order to perform fast state readout in $< 1\,\mu\text{s}$ (instead of 40 ms in case of fluorescence detection) for a loophole-free Bell test [112, 275]. However, for the sake of simplicity we rely on the more robust fluorescence readout during all experiments in this chapter. Note that the current high-NA objective has been immediately implemented before the experiments in this chapter and features a collection efficiency increased by a factor 2.5 compared to previous experiments.
In analogy to the experiments with the trapped-ion QNN, we have to compensate the unitary polarization rotation between the atom and the photon projection setup. To this end, a laser at 780 nm at the same frequency as the emitted photons, named compensation laser, is sent from the backside of the trap through the whole setup to the BSM. Its polarization is modulated in time with 10 Hz between V and D using a liquid crystal variable retarder (LCR). Motorized flip mirrors in front of the photon projection setup reflect the light to a polarimeter. The compensation is performed either with manual polarization controllers (lab 1) or in an automatized manner employing a dynamic polarization controller in combination with a gradient descent algorithm (lab 2). In fact, two polarization states are sufficient to compensate for arbitrary unitary rotations in the case of negligible PDL.

7.1.2 Generation and analysis of atom-photon entanglement

The timeline of the experimental sequence for entanglement generation and verification is illustrated in Fig. 7.2a. We start with loading an atom into the dipole trap, i.e. the MOT and dipole trap laser are switched on until we record an increase of the integrated fluorescence counts (40 ms time window) above a certain threshold. This procedure may take up to 1 s; afterwards the MOT coils are switched off and the atom is cooled for 350 µs. Subsequently, we perform 3 µs of optical pumping to the state $|S_{1/2}, F = 1, m_{\text{F}} = 0\rangle$ employing the pump 1-1 and 2-1 lasers with appropriate polarizations [271]. Next, atom-photon entanglement is generated according to the scheme sketched in Fig. 7.2b: a resonant laser pulse with a FWHM of 22 ns excites the atom to the state $|P_{3/2}, F^{'} = 0, m_{\text{F}} = 0\rangle$ with a probability of about 80 % [270]. The short-lived excited state ($\tau = 26.24\,\text{ns}$) spontaneously decays back to one of the three ground states

[1] The measurement of atom-photon entanglement requires projection to different bases, which is realized by additional motorized waveplates in the BSM

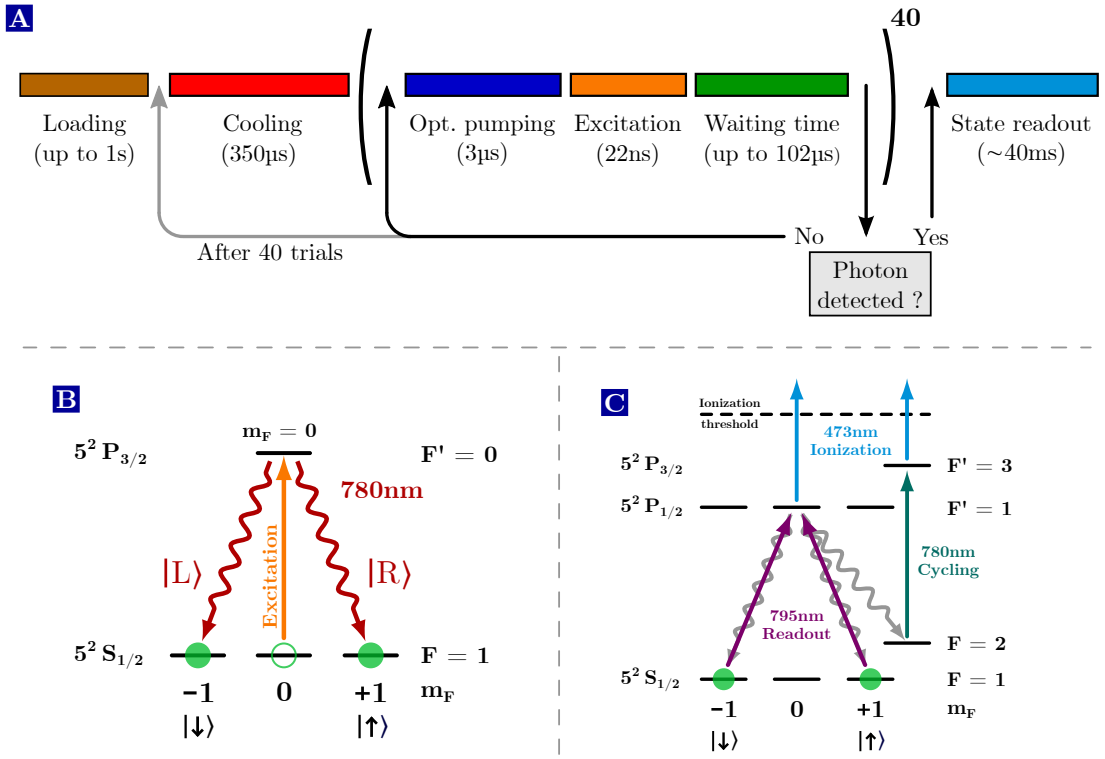

Figure 7.2. Entanglement generation scheme, atomic-state readout and experimental sequence. **(A)** Timeline of the experimental sequence. After loading and cooling we do 40 excitation tries consisting of optical pumping, excitation and a waiting time depending on the fiber length. If a photon is detected, we proceed with the atomic-state readout, otherwise another excitation trail or cooling is conceived. **(B)** Atom-photon entanglement at 780 nm is generated via spontaneous decay after resonant excitation to the state $|P_{3/2}, F^{'} = 0, m_F = 0\rangle$ with a π-pulse at 780 nm. **(C)** The atomic-state readout is based on Zeeman-state selective ionization employing a linear-polarized laser at 795 nm and an ionization laser at 473 nm. If the atom is ionized, it leaves the dipole trap, which can be discriminated via fluorescence detection. To avoid false events due to the undesired decay to $|S_{1/2}, F = 2\rangle$ before ionization, an additional cycling laser at 780 nm excites the atom to the state $|P_{3/2}, F^{'} = 3\rangle$, which is ionized, too.

under emission of a $\sigma^{+/-}$- or π-polarized photon. For collection along the quantization axis we only detect $\sigma^{+/-}$-polarized photons since π-polarized photons destructively interfere at the facet of the SM fiber. Equal CGCs of the two σ-polarized decay paths result in a maximally entangled state between the atomic qubit and the photon polarization

$$
\begin{aligned}
|\Psi\rangle_{\mathrm{ape}} &= \sqrt{\frac{1}{2}}\left(|\downarrow, L\rangle + |\uparrow, R\rangle\right) \\
&= \sqrt{\frac{1}{2}}\left(|-_{\mathrm{x}}, V\rangle + |+_{\mathrm{x}}, H\rangle\right) = \sqrt{\frac{1}{2}}\left(|+_{\mathrm{y}}, A\rangle + |-_{\mathrm{y}}, D\rangle\right). \qquad (7.1)
\end{aligned}
$$

After excitation, a variable waiting time up to 102 µs is introduced. Its duration depends on the fiber length, which determines the travel time of the photon to the detector. If we record an event by one of the single-photon detectors within a hardware-gated time window, the atomic-state readout is initialized. In case of no click the excitation sequence is restarted with optical pumping. After 40 excitation tries without a detected photon, there is an intermediate 350 µs long cooling step to avoid negative influences on the lifetime in the trap or the atomic coherence due to heating by the resonant pump and excitation pulses.
The scheme of the atomic-state readout based on Zeeman-selective ionization is shown in Fig. 7.2c: it starts with a linear-polarized readout pulse at 795 nm to transfer the population from a selected superposition state to the excited state $|P_{1/2}, F^{'} = 1, m_{\mathrm{F}} = 0\rangle$. Simultaneously, we sent a laser pulse at 473 nm to the atom, which exclusively ionizes the excited state. An ionized atom immediately leaves the dipole trap, i.e. we can distinguish if the selected ground-state superposition has been excited or not via fluorescence detection. Due to the short lifetime of the excited state the atom might decay to $|S_{1/2}, F = 2\rangle$ before ionization resulting in a false decision. Thus, an additional cycling laser at 780 nm transfers the population to the state $|P_{3/2}, F^{'} = 3\rangle$, which is ionized, too. The state-selectivity relies on coherent effects in the coupled three-level lambda-type system, namely the existence of dark- and bright-states in the ground state being related to coherent population trapping. In our case, the tuning knob is the polarization of the readout laser, which we define as superposition of H- and V-polarized light

$$J_{\mathrm{Readout}} = \cos(\alpha) \cdot V + e^{-i\varphi} \sin(\alpha) \cdot H. \tag{7.2}$$

Accordingly, we can derive two orthogonal atomic superposition states of which one is transferred to the excited state by the readout pulse (bright-state) and the other is not (dark-state):

$$|\Psi\rangle_{\mathrm{Bright}} = \cos(\alpha)\frac{1}{\sqrt{2}}(|\downarrow\rangle + |\uparrow\rangle) - \sin(\alpha)\frac{i}{\sqrt{2}}e^{i\varphi}(|\downarrow\rangle - |\uparrow\rangle) \tag{7.3}$$

$$|\Psi\rangle_{\mathrm{Dark}} = \sin(\alpha)\frac{1}{\sqrt{2}}(|\downarrow\rangle + |\uparrow\rangle) + \cos(\alpha)\frac{i}{\sqrt{2}}e^{i\varphi}(|\downarrow\rangle - |\uparrow\rangle). \tag{7.4}$$

The most intuitive example is purely circular-polarized light, e.g. σ^+-light with $\alpha = \pi/4$ and $\varphi = \pi/2$. In this case, the bright- (dark-) state is $|\downarrow\rangle$ ($|\uparrow\rangle$), which is consistent with the selection rules since σ^+-polarized light cannot excite the state $|\uparrow\rangle$ to $|P_{1/2}, F^{'} = 1, m_{\mathrm{F}} = 0\rangle$. Consequently, a readout of atomic superposition bases requires a linear-polarized readout pulse. It is straightforward to verify that H/V readout light corresponds to the bright- (dark-) states $|-/+\rangle_{\mathrm{x}}$ ($|+/-\rangle_{\mathrm{x}}$), while D/A corresponds to $|-/+\rangle_{\mathrm{y}}$ ($|+/-\rangle_{\mathrm{y}}$). The fidelity of this readout scheme is 97 %, limited by off-resonant excitation of the dark-state to $|P_{1/2}, F^{'} = 2\rangle$ and a mixture of the bright- and dark-state caused by spontaneous decay from the excited to the ground state before ionization. It is important to note that population in the third ground state $|m_0\rangle = |S_{1/2}, F = 1, m_{\mathrm{F}} = 0\rangle$ is excited and ionized, too. Thus, the readout scheme can be considered as a projective measurement to the dark-state. During the experiments,

we measure the atomic state only in superposition bases albeit full state reconstruction additionally requires readout in the eigenbasis. However, we will see later that it is still possible to estimate a lower bound of the fidelity with an appropriate model.

7.1.2.1 Coherence properties of the atomic qubit

In analogy to the trapped-ion experiments we employ two Zeeman states with different m_{F}-numbers as atomic qubit. Hence, the qubit is prone to magnetic-field noise. However, several effects render the situation in the Rb-atom QNN more complex. In the following we briefly explain the decoherence mechanisms and the techniques to counteract those.

The first issue arises from the fact that we have a spin-1 system in the ground state with the states $|\downarrow\rangle$, $|\uparrow\rangle$ and $|m_0\rangle = |S_{1/2}, F = 1, m_{\mathrm{F}} = 0\rangle$. For a magnetic field in z-direction, these states are eigenstates resulting in a Larmor precession of the phase of an initially prepared superposition state. Accordingly, the effect of field noise in z-direction is the same as described in Sect. 4.1.1 for the trapped-ion qubit, namely shot-to-shot dephasing. The situation is different for fields in x- or y-direction: now the eigenstates are superposition states of $|\downarrow\rangle$, $|m_0\rangle$ and $|\uparrow\rangle$. Calculating the temporal evolution of the qubit superposition states $|+\rangle_{\mathrm{x}}$ and $|-\rangle_{\mathrm{x}}$, which are initially prepared at time $t = 0$, in a magnetic field $\pm B_{\mathrm{x}}$ yields

$$|+\rangle_{\mathrm{x}}(t) = |+\rangle_{\mathrm{x}}(0) \tag{7.5}$$

$$|-\rangle_{\mathrm{x}}(t) = |-\rangle_{\mathrm{x}}(0)\cos(\omega_{\mathrm{L}}t) \pm i|m_0\rangle\sin(\omega_{\mathrm{L}}t). \tag{7.6}$$

We find that $|+\rangle_{\mathrm{x}}$ is an eigenstate being insensitive to x-fields (comparable to $|m_0\rangle$ in a z-field), whereas $|-\rangle_{\mathrm{x}}$ is a superposition of the two field-dependent eigenstates. This results in a population transfer between $|-\rangle_{\mathrm{x}}$ and $|m_0\rangle$. Since the state $|m_0\rangle$ is ionized during the atomic-state readout, x-field noise is detected as false events and therefore a source of decoherence of the state $|-\rangle_{\mathrm{x}}$. However, the observation of this decoherence depends on the basis of the atomic-state readout. If we assume for instance a H-polarized readout pulse (readout angle: $\alpha = 90°$), the state $|-\rangle_{\mathrm{x}}$ is the bright state and ionized anyway, i.e. population transfer to $|m_0\rangle$ does not lead to false events. In contrast, a readout with V-polarized light ($\alpha = 0°$) features $|-\rangle_{\mathrm{x}}$ as dark-state and is, accordingly, maximally sensitive to x-field noise. All other readout bases can be described as superpositions of H and V, so noise partly influences these bases with respect to their overlap with V.

The calculation for a magnetic field $\pm B_{\mathrm{y}}$ in y-direction is performed in a similar way, yielding

$$|+\rangle_{\mathrm{x}}(t) = |+\rangle_{\mathrm{x}}(0)\cos(\omega_{\mathrm{L}}t) \mp |m_0\rangle\sin(\omega_{\mathrm{L}}t). \tag{7.7}$$

$$|-\rangle_{\mathrm{x}}(t) = |-\rangle_{\mathrm{x}}(0). \tag{7.8}$$

The result is the same except that $|+\rangle_{\mathrm{x}}$ and $|-\rangle_{\mathrm{x}}$ are swapped. Accordingly, y-field noise only affects the state $|+\rangle_{\mathrm{x}}$ and is primarily detected for a readout angle of $\alpha = 90°$, while readout at $\alpha = 0°$ is insensitive to noise.

Static and time-dependent magnetic fields with different strengths and frequency components can originate from a series of external sources, e.g. the earth magnetic field, the subway being in close proximity to the lab (60 m), or electrical devices and power supplies around the trap. In order to compensate for these external fields, an active stabilization is implemented: a magnetic-field sensor is placed in close proximity to the atom (2 cm) to measure the magnetic fields in all three directions. With the help of three coil pairs around the trap, which are arranged in Helmholtz configuration, we can apply magnetic fields in all three directions. Hence, we can stabilize the fields at the position of the atom to arbitrary values (max. ± 500 mG) using a PID loop with a bandwidth of 200 Hz with an uncertainty of < 0.5 mG rms.
Apart from external sources, a major contribution to the decoherence emerges from the dipole trap. In particular, two effects lead to an additional effective magnetic field

$$\vec{B}_{\text{eff}}(\vec{r}) = \frac{\pi c^2 \Gamma}{2\omega_0^3 \mu_{\text{B}}} \left(\frac{1}{\Delta_{2,\text{F}}} - \frac{1}{\Delta_{1,\text{F}}} \right) \cdot \begin{pmatrix} 0 \\ P_{\text{long}}(\vec{r}) \\ P_{\text{ODT}} \end{pmatrix} \cdot I(\vec{r}) \tag{7.9}$$

with Γ and ω_0 being the decay rate and transition frequency of the central D-line, $1/\Delta_{2,\text{F}}$ ($1/\Delta_{1,\text{F}}$) the detuning of the ODT with respect to the D1-(D2-)line, and $I(\vec{r})$ the intensity profile of the focused ODT laser. The first effect occurs if the ODT is not perfectly linear polarized but slightly elliptical, for instance caused by birefringence of the objective or glass cell. The ellipticity is quantified by P_{ODT}; for linear polarized light P_{ODT} equals zero, whereas $P_{\text{ODT}} = \pm 1$ for circular polarization. The consequence of an elliptically polarized ODT is a Zeeman-state dependent AC Stark-shift, which can be considered as an effective magnetic field in z-direction (see Eq. 7.9). This contribution is reduced to < 1 mG by a careful adjustment of the ODT polarization in combination with a stabilization of the air temperature in the box containing the atom trap to 0.1 K to avoid temperature-induced birefringence. The value of < 1 mG is lower than the external magnetic fields and in the same order as the uncertainty of the magnetic-field stabilization.
The second effect is related to the appearance of longitudinal electric-field components $E_{\text{z}}(\vec{r})$ in the focal region of the ODT. These field components are caused by the tight focusing and even occur if the laser is initially purely linear-polarized. A detailed calculation reveals that the (desired) component $E_{\text{x}}(\vec{r})$ has a phase shift unequal to zero with respect to $E_{\text{z}}(\vec{r})$, i.e. the resulting polarization can be considered as an elliptical polarization of a light field propagating in y-direction. This elliptical polarization – labeled as $P_{\text{long}}(\vec{r})$ – depends on the relative amplitude and phase of $E_{\text{x}}(\vec{r})$ and $E_{\text{z}}(\vec{r})$, and induces just like P_{ODT} a Zeeman-state dependent AC Stark-shift. Accordingly, we obtain an effective magnetic field $B_{\text{long}}(\vec{r})$ in y-direction, which is proportional to $P_{\text{long}}(\vec{r}) \cdot I(\vec{r})$ (see Eq. 7.9). Regarding the atomic coherence, we identify a few important properties of $B_{\text{long}}(\vec{r})$: first, B_{long} is zero in the y-z-plane at x = 0, which includes the optical axis, and has its maximum at $x \approx 1/\sqrt{2}\,\omega_0$ and y = z = 0. Second, the absolute values of B_{long} are plane symmetric with respect to the y-z-plane at x = 0, but the phase of $E_{\text{z}}(\vec{r})$ has different signs for positive and negative x-values. Hence, the direction of B_{long} is inverted on both sides of the y-z-plane. Since we do not cool the atom to the

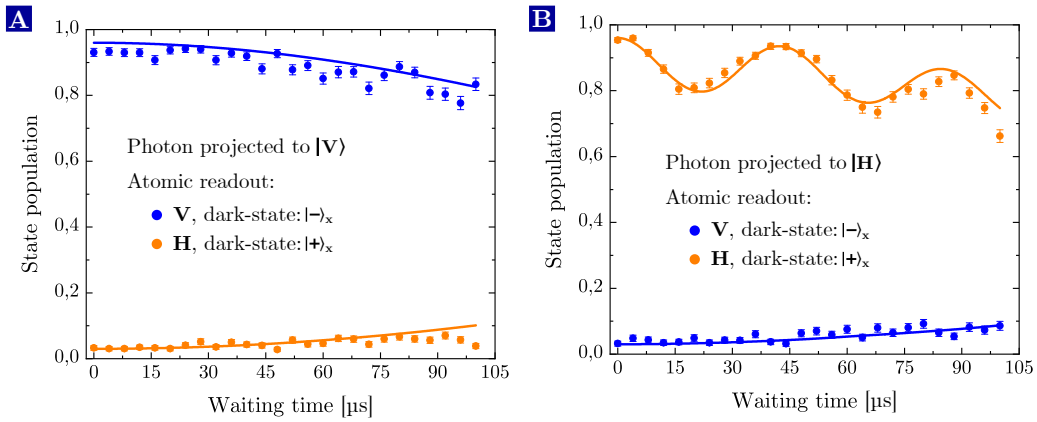

Figure 7.3. Coherence properties of single Rb-atoms. The time evolution of atomic superposition states. The atoms are initially prepared in $|\Psi\rangle(0) = |-\rangle_x$ **(A)** and $|\Psi\rangle(0) = |+\rangle_x$ **(B)** via generation of atom-photon entanglement and subsequent projection of the photon to $|V\rangle$ and $|H\rangle$, respectively. The y-axis denotes the population of the dark-state, which equals $|-\rangle_x$ for a V-polarized readout pulse (blue dots) and $|+\rangle_x$ for H (orange dots). The solid lines are simulations [276]. The loss of contrast at longer waiting times is caused by decoherence due to magnetic-field noise. If the photon is projected to $|H\rangle$ and the readout-laser polarization set to H, magnetic fields in y-direction stemming from the elliptical polarization of the ODT-light near the focus are clearly visible. After each transverse oscillation period of the atom in the ODT ($\approx 42\,\mu s$), the state rephases and the original coherence is restored.

motional ground state, it oscillates in the harmonic trap potential with an amplitude determined by its thermal energy. The initial energy obeys a thermal distribution and is different for each atom, i.e. each atom moves along different trajectories. The latter is relevant for the state evolution of the atomic qubit in the optically induced effective y-fields, thus, we obtain decoherence on a time-scale of the transverse oscillation period. However, due to the sign change of B_{long}, the temporal evolution of the state cancels out after one full transverse oscillation period. At this time the atoms rephase, i.e. the accumulated phase goes to zero independent of the particular atom trajectory. A perfect rephasing only occurs if the atom merely moves in transverse direction, however, since it also oscillates in z-direction – roughly with a ten times lower frequency – the rephasing becomes worse for multiple oscillation periods. Moreover, the trap is not perfectly harmonic, which results in energy-dependent trap frequencies and smears out the sharp rephasing points.

A measurement of the coherence properties is shown in Fig. 7.3. If the photon is projected to $|V\rangle$ the atom ends up in $|-\rangle_x$ (Fig. 7.3a). A state readout with H- or V-polarized light at 795 nm at different waiting times yields the time-dependent dark-state populations (orange and blue dots). They show decoherence on a time scale of a few hundreds of µs due to z- and x-field noise. The solid lines are simulations based on the atomic dynamics [276]. In contrast, if the atom is projected to $|+\rangle_x$, it is sensitive to noise in y-direction In case of a readout with V-polarized light. As expected we identify an oscillatory behavior of the orange data points with a rephasing point at roughly

45 µs. Note that it is difficult to give a single number for the coherence time due to the non-isotropic influence of the different effects.
We further improve the coherence shown in Fig. 7.3a by applying a guiding field in y-direction in the order of a few tens of mG to suppress the influence of field noise in the other two directions. A guiding field in y-direction is feasible since huge fields stemming from the dipole trap, which are hard to compensate for, are present in the direction anyway. Note that the guiding field leads to Larmor oscillations of the curves in Fig. 7.3b. Thus, the guiding field amplitude is set to a value where the high-contrast points of the Larmor oscillation exactly overlap with the rephasing time determined by the transverse trap frequency. Additionally, via control of the dipole trap power and the guiding field amplitude, we can shift the high-contrast points in time to match them for instance to the waiting time associated with a certain fiber length.

7.2 Atom-photon entanglement over up to 20 km of fiber

7.2.1 Experimental setup

In order to demonstrate atom-photon entanglement over long fiber distances, we combine the trapped-atom QNN with part of the previously described QFC system as depicted in Fig. 7.4. The fiber-coupled photons emitted by the atom first pass a MEMS switch (SN-2x2-4, *Sercalo microtechnology*), which guides the photons either to a single APD or to the PPQFCD. The switch is necessary because we collect fluorescence photons at 780 nm for entanglement generation as well as for the loading sequence and state readout, which rely on photons scattered by the cooling, pump and repump lasers, with the same objective. This is uncritical at 780 nm since we are able to detect all photons with the APDs. However, the narrowband spectral filters of the QFC system only possess significant transmission for photons emitted on the excitation transition, i.e. we cannot utilize the SNSPDs for atom trapping and state readout. Accordingly, it is necessary to implement a switch, which guides the photons to a single APD during the loading sequence and state readout, or to the PPQFCD during the excitation sequence. To solve this issue, we tested several approaches: we first used an AOM as a fast switch, but its thermal properties negatively influenced the polarization stability. Although the AOM was operated in a pulsed mode with a tiny duty cycle, we observed time-dependent relative polarization rotations between the photons and the compensation laser. This results in a phase uncertainty of the entangled state and consequently in a decrease of fidelity. Another approach were partially-reflecting beam splitters to extract – at the cost of SBR – 10 % of the fluorescence photons for trapping and state readout. The lower amount of fluorescence photons was still sufficient to clearly distinguish if an atom is in the trap with APDs featuring a DCR of < 10 cps. Unfortunately, this approach suffered from up-converted anti-Stokes Raman background at 780 nm, which went back into the input arm of the converter, was reflected at various optical elements in the trap, and generated additional background counts on the single APD. Despite the poor overall transmission, the background level was measured to be as high as the fluorescence level. We modified the single APD with the monolithic filter cavities already built in the pho-

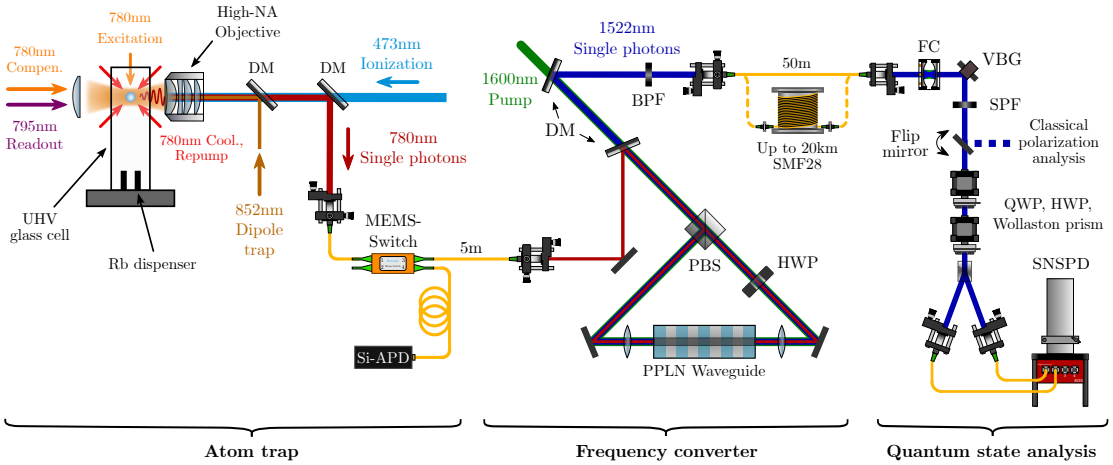

Figure 7.4. Setup for long-distance atom-photon entanglement. Schematic representation of the joint setup for atom-photon entanglement over up to 20 km of fiber. It combines the atom trap, the frequency converter and the quantum state analysis for telecom photons.

ton pair source in Sect. 3.3. At 780 nm they provide a finesse of 150 and a linewidth of 500 MHz. Although the up-converted ASR background was suppressed, the additional losses caused by the cavity ($T \approx 70\,\%$) further decreased the overall fluorescence level. This led to an increased amount of false decisions, in particular for long waiting times where we effectively cool less and therefore scatter less photons. A third approach was a second set of optics for fluorescence collection placed at the backside of the trap. Due to a limited optical access it was not possible to built a setup for collection into a SM fiber, but only into a multi-mode fiber. This led to a large background fluorescence level due to stray light from the cooling lasers rendering state detection impossible.
The best and most robust option was the above mentioned MEMS switch, since up-converted ASR background is completely suppressed due to a negligible cross-talk between the channels (> 100 dB suppression). Its major disadvantage is the switching time of about 1 ms. It hinders the detection of fluorescence photons generated during cooling and optical pumping, which are typically recorded to verify that the atom did not fall out of the trap during the excitation sequence. This is not an issue for atom-photon entanglement, since the high event rate results in a high probability to detect a photon in a 200 ms time window being well below the lifetime of the atom in the trap (even for the large waiting time of 102 µs at 20 km of fiber). Thus, we rarely loose the atom during the excitation sequence. However, it becomes critical for atom-atom entanglement where the event rate is several orders of magnitude lower. To allow for atom-atom entanglement with MEMS switches, the sequence has to be modified at the cost of event rate, e.g. with intermediate 20 ms long checking periods after 120 ms of excitation tries. During the excitation sequence, the emitted photons are sent to the PPQFCD and afterwards coupled to a 50 m long fiber connecting the atom lab to another lab where the BSM and SNSPDs are located. Additionally, we can insert 10 km and 20 km of spooled fibers into this path. To avoid polarization drifts in the long fibers, the spools are placed

within the temperature-stabilized box containing the atom trap. The stability of 0.1 K has proved to be sufficient to eliminate drifts to perform overnight measurements taking several hours. The 50 m long fiber is directly connected to one of the two branches of the BSM – without the fiber-BS and polarization controllers – for spectral filtering and state analysis. Note that the automatized polarization compensation was not yet operational during the experiments in this chapter. Instead we used the polarimeter as monitor for a manual compensation. Finally, the photons are detected by the SNSPDs as described in the previous chapters.

7.2.2 Results

We measured atom-telecom-photon entanglement in three different configurations: after 50 m (A), 10 km (B), and 20 km (C) fiber length. Furthermore, a reference measurement at 780 nm (R) was performed to assess the influence of the QFC. In measurements R and A we implemented an electronic delay of about 51 µs between a photon detection event and the atomic-state readout to mimic the waiting time of the 10 km-fiber. Hence, the influence of decoherence on the fidelity is comparable among R, A and B. The results are displayed in Fig. 7.5; the appropriate numbers are summarized in Tab. 7.1.
In all measurements we achieve an entanglement generation rate of 35 events per minute, mainly limited by the loading time of about 1 s, since we loose the atom during the state readout in roughly half of the cases. Note that for our parameters (repetition rate, success probability, loading rate) the generation rate is not sensitive to the success probability, i.e. the probability to detect a photon per excitation attempt. The photon wavepackets of measurements A, B and C, each containing >15000 events collected within a few hours, are shown in Fig. 7.5 on the left. Fits of the exponential decay reveal excited-state lifetimes of 26.7(6) ns, 26.0(4) ns and 26.4(5) ns being in good agreement with the literature value of 26.24(4) ns [263]. For the further evaluation we post-select events in a 50 ns-window (marked by blue dashed lines) corresponding to about 74 % of the total photon wavepacket. This window was chosen to obtain a good tradeoff between the number of detected events and the SBR. From the post-selected data we calculate success probabilities of $p_{\mathrm{suc}}^{(R)} = 3.764 \times 10^{-3}$, $p_{\mathrm{suc}}^{(A)} = 1.276 \times 10^{-3}$, $p_{\mathrm{suc}}^{(B)} = 0.221 \times 10^{-3}$ and $p_{\mathrm{suc}}^{(C)} = 0.173 \times 10^{-3}$. As a consistency check, we estimate the theoretically expected probabilities as

$$
\begin{aligned}
p_{\mathrm{suc,theo}}^{(A)} &= p_{\mathrm{suc}}^{(R)} \cdot T_{\mathrm{mems}} \cdot \eta_{\mathrm{dev}} \cdot T_{\mathrm{filter}} \cdot T_{\mathrm{proj}} \cdot \eta_{\mathrm{snspd,\,A}}/\eta_{\mathrm{apd}} = 0.83 \times 10^{-3}, \\
p_{\mathrm{suc,theo}}^{(B)} &= p_{\mathrm{suc,theo}}^{(A)} \cdot T_{\mathrm{fib,10\,km}} \cdot T_{\mathrm{fib,fib}} \cdot \eta_{\mathrm{snspd,\,BC}}/\eta_{\mathrm{snspd,\,A}} = 0.23 \times 10^{-3}, \\
p_{\mathrm{suc,theo}}^{(C)} &= p_{\mathrm{suc,theo}}^{(B)} \cdot T_{\mathrm{fib,20\,km}}/T_{\mathrm{fib,10\,km}} = 0.16 \times 10^{-3},
\end{aligned}
\tag{7.10}
$$

taking into account the transmissions of the MEMS switch ($T_{\mathrm{mems}} = 75\,\%$), projection setup ($T_{\mathrm{proj}} = 92.2\,\%$), 10 km-fiber ($T_{\mathrm{fib,10\,km}} = 63\,\%$), 20 km-fiber ($T_{\mathrm{fib,20\,km}} = 42.0\,\%$) and further fiber-fiber connectors ($T_{\mathrm{fib,fib}} = 90\,\%$) as well as the EDI ($\eta_{\mathrm{dev}} = 57\,\%$), the photon transmission of the filter system ($T_{\mathrm{filter}} = 81.8\,\%$), and the average quantum efficiencies of the APDs ($\eta_{\mathrm{apd}} \approx 50\,\%$) and SNSPDs ($\eta_{\mathrm{snspd,\,A}} = 34\,\%$ for measurement

A, $\eta_{\text{snspd, BC}} = 17\,\%$ for measurement B and C). We find a good agreement for measurements B and C, whereas the measured success probability for A is higher than expected. We attribute this to drifts of the laser powers in the atomic-state preparation and excitation cycles, which were thoroughly optimized before measurement A and might have been non-perfect during the other measurements. The same observation is valid for the SBR: in principle, the SBR should be similar for all telecom measurements because the main background contribution, CIB, is attenuated in the fibers just like the converted photons. In particular, we operated the SNSPDs during measurements B and C at a lower bias current where the DCR is reduced by one order of magnitude (cf. Sect. 3.1.3), i.e. we even expect a slightly higher SBR. We do not observe this in the measured values listed in Tab. 7.1, being related to the discrepancies in the success probabilities. We confirm this via the theoretical values, which are determined by the probabilities p_{bg} to detect a background count in the 50 ns-window, and given as

$$\begin{aligned}
\text{SBR}^{(A)}_{\text{theo}} &= \frac{p^{(A)}_{\text{suc}}}{p^{(A)}_{\text{bg}}} = \frac{p^{(A)}_{\text{suc}}}{50\,\text{ns}\cdot\left(R^{(A)}_{\text{cib, det}} + R^{(A)}_{\text{dcr, snspd1+2}}\right)} = 32.1,\\
\text{SBR}^{(B)}_{\text{theo}} &= \frac{p^{(B)}_{\text{suc}}}{50\,\text{ns}\cdot\left(R^{(B/C)}_{\text{cib, det}}\cdot T_{\text{fib,10\,km}}\cdot T_{\text{fib,fib}} + R^{(B/C)}_{\text{dcr, snspd1+2}}\right)} = 21,\\
\text{SBR}^{(C)}_{\text{theo}} &= \frac{p^{(C)}_{\text{suc}}}{50\,\text{ns}\cdot\left(R^{(B/C)}_{\text{cib, det}}\cdot T_{\text{fib,20\,km}}\cdot T_{\text{fib,fib}} + R^{(B/C)}_{\text{dcr, snspd1+2}}\right)} = 23.7,
\end{aligned} \tag{7.11}$$

with $R^{(A)}_{\text{dcr, snspd1+2}} = 116\,\text{cps}$, $R^{(B/C)}_{\text{dcr, snspd1+2}} = 18\,\text{cps}$, $R^{(A)}_{\text{cib, det}} = 0.34 \times 1990\,\text{cps} = 677\,\text{cps}$ and $R^{(B/C)}_{\text{cib, det}} = 0.5 \times R^{(A)}_{\text{cib, det}}$. All values agree well with the measured ones, the slight underestimation may result from different operating points of the QFCD at lower pump powers. Note that the background is – in contrast to the converters for 854 nm – dominated by CIB being a factor 6-12 stronger than the detector dark-counts.

To verify atom-photon entanglement, we measure the photon polarization state in the two linear bases $|H\rangle/|V\rangle$ and $|D\rangle/|A\rangle$ at different atomic readout angles α by varying the 795 nm laser polarization. Actually, the density matrix reconstruction via QST also requires projective measurements in $|R\rangle/|L\rangle$, which is currently not possible for technical reasons. However, the two linear bases are enough for an estimation of the fidelity. The respective atom-photon state correlations for measurements A, B and C are illustrated in Fig. 7.5 on the right side. The data points denote the population of the dark-state of a given readout angle (quoted in Fig. 7.5a below the x-axis) conditioned on the detection of a photon in a certain basis setting. The occurrence of oscillations in all settings with $\pi/2$ phase shifts already indicates the presence of entanglement. We quantify this by fitting the data with sinusoidal curves (solid lines) to obtain the visibilities. The fits reveal that the visibility for a projection of the photon to $|V\rangle$ (atom in $|-\rangle_{\text{x}}$, red curves) is almost the same in each measurement (A: 89.9(14) %, B: 88.1(14) %, C: 90.6(10) %), while all other visibilities decrease with increasing fiber

Table 7.1. Results of the four atom-photon entanglement measurements. R is a reference measurement at 780 nm while A, B and C denote measurements at 1522 nm in different configurations. They are related to the figures shown in Fig. 7.5a/b/c.

Measurement	**(R)**	**(A)**	**(B)**	**(C)**
Wavelength	780 nm	1522 nm	1522 nm	1522 nm
Fiber length	5 m	50 m	10 km	20 km
Readout delay	51 µs	51 µs	51 µs	102 µs
Success probability	3.764×10^{-3}	1.276×10^{-3}	0.221×10^{-3}	0.173×10^{-3}
SBR	934.2	32.3	23.2	25.1
Estimated fidelity	89.7(7) %	88.1(11) %	84.2(10) %	78.9(13) %
Bell parameter	2.49(3)	2.41(3)	2.37(4)	2.12(5)

length. This is explained by a loss of atomic coherence: as mentioned in Sect. 7.1.2, we apply a guiding field in y-direction to suppress magnetic-field noise in x- and z-direction, i.e. the atomic state $|-\rangle_x$ is insensitive to field noise on our time-scale. In contrast, the state $|+\rangle_x$ is affected by the y-fields stemming from the transverse oscillation in the trap being the dominant decoherence effect. Although the waiting time coincides with one of the rephasing points, we suffer from the non-perfect rephasing (see Fig. 7.3b). Note that the minimum data point of the $|H\rangle$-curve at the readout angle $\alpha = 0°$ is not affected by decoherence since we do not detect y-field noise for $\alpha = 0°$ (cf. Sect. 7.1.2). The curves for projection to $|D\rangle/|A\rangle$ are also prone to decoherence because the resulting atomic state has an overlap with $|+\rangle_x$. Moreover, the readout angles $\alpha = 45°$ and $\alpha = 135°$ where the maximum/minimum points are located also possess a contribution from $\alpha = 0°$, i.e. decoherence is observed in the maximum and minimum points. A similar outcome is expected for a projection to $|R\rangle/|L\rangle$ with the same argument.
Subsequently, we calculate the average visibility V_{avg} as the mean value of the visibilities of all six basis states. To this end, we assume the visibilities in the third basis $|R\rangle/|L\rangle$ to be equal to the $|D\rangle/|A\rangle$ basis. We find (estimated) average visibilities of 87.4(13) %, 85.8(13) %, 81.1(12) % and 74.7(16) % for measurements R, A, B, and C, respectively. In order to estimate the Bell-state fidelity from V_{avg}, we model the state in the 2×3 space spanned by $|R\rangle$, $|L\rangle$ and $|\downarrow\rangle$, $|m_0\rangle$, $|\uparrow\rangle$ as

$$\rho = V_{\text{avg}} |\Psi\rangle \langle\Psi|_{\text{ape}} + \frac{1}{6}(1 - V_{\text{avg}})\mathbb{1} \tag{7.12}$$

with $|\Psi\rangle_{\text{ape}}$ being the desired atom-photon entangled state. The third ground state $|m_0\rangle$ has to be taken into account since it can be populated by means of magnetic field noise in x- or y-direction. In Eq. 7.12 we assume isotropic decoherence towards white noise in the 2×3 space, which is not fully correct in our case, but justifiable since we consider all six basis states for the average fidelity. Accordingly, a lower bound of the

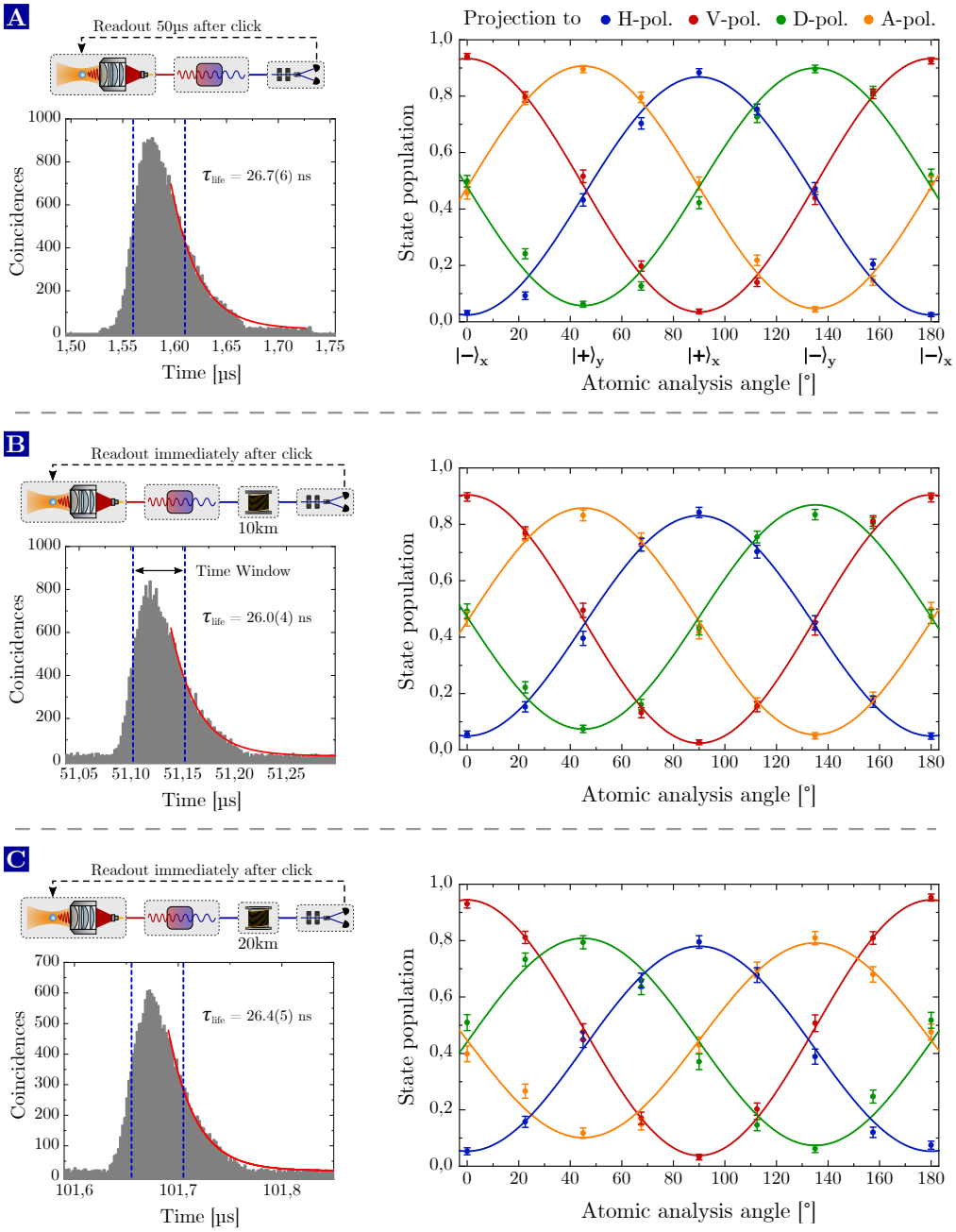

Figure 7.5. Verification of atom-photon entanglement over several kilometers of fiber. Results of atom-photon entanglement measurements after **(A)** 50 m of fiber including an additional electronic delay of 50 µs before the state readout, **(B)** 10 km and **(C)** 20 km of fiber. On the left side, each subfigure displays a small schematic picture of the setup as well as the photon wavepacket with the 50 ns time windows containing the data, which are post-selected for the evaluation. On the right side the atom-photon state correlations in two photonic superposition bases ($|H\rangle/|V\rangle$ and $|D\rangle/|A\rangle$) for different readout angles of the atomic-state analysis are plotted. The solid lines are sinusoidal fits; from their visibility we estimate the overlap fidelity.

fidelity with $|\Psi\rangle_{\text{ape}}$ is given by

$$\mathcal{F} \geq \langle\Psi|\,\rho\,|\Psi\rangle_{\text{ape}} = \frac{1}{6} + \frac{5}{6}V_{\text{avg}}, \tag{7.13}$$

yielding fidelities of $\geq 89.7(7)\,\%$ (R), $88.1(11)\,\%$ (A), $84.2(10)\,\%$ (B) and $78.9(13)\,\%$ (C). Note that we do not apply any background subtraction throughout this chapter. The fidelity without QFC is limited by imperfections of the atomic-state readout (3%) and the atomic coherence (7%). A comparison of measurement R and A with fidelities of $89.7(7)\,\%$ and $88.1(11)\,\%$, respectively, yields the influence of the QFC in terms of SBR and process fidelity since waiting time and fiber distance are quite similar. According to Eq. 2.56, we expect a loss of fidelity of $1.9\,\%$, which is supported by the experimental data within the error bars. In measurement B, the reduction in fidelity to $84.2(10)\,\%$ is larger than anticipated merely from the SBR ($2.7\,\%$). The remaining $3\,\%$ are most probably caused by drifts in the experiment, e.g. polarization rotations in the (unstabilized) long fiber, magnetic fields, or laser power of the pump and excitation beams. The different fidelities of measurements B of $84.2(10)\,\%$ and C of $78.9(13)\,\%$ can be attributed to the decoherence of the atomic qubit caused by the longer waiting time. Hence, for atom-photon entanglement over 20 km the decoherence contributes in total $11\,\%$ in fidelity loss while the SBR is responsible for $2.5\,\%$.
Additionally, all four measurements include the basis settings to measure the CHSH Bell parameter S: $|H\rangle/|V\rangle$ and $|D\rangle/|A\rangle$ for the photons, and $\alpha = 22.5°$ and $\alpha' = 157.5°$ for the atomic-state readout. We obtain S-parameters of $S^{(R)} = 2.49(3)$, $S^{(A)} = 2.41(3)$, $S^{(B)} = 2.37(4)$ and $S^{(C)} = 2.12(5)$, which reveal a clear violation of Bell's inequality.

7.3 Summary and discussion

To sum up, we demonstrated in this chapter entanglement between a Zeeman qubit in the $5^2S_{1/2}, F = 1$ ground-state manifold of a single trapped Rb-atom and the polarization state of a telecom photon traveled through up to 20 km of fiber. To this end, we modified an existing Rb-atom QNN with part of the QFC system introduced in Chap. 6. In the combined setup we achieved success probabilities, i.e. the probability of a photon detection event per excitation try, of 1.276×10^{-3} directly behind the PPQFC, 0.221×10^{-3} after 10 km and 0.173×10^{-3} after 20 km of fiber. The numbers are consistent with the individual efficiencies and transmissions and mainly limited by the collection efficiency from the atom ($\approx 1\,\%$), the EDI ($57\,\%$) and the average SDE of the SNSPDs ($\approx 34\,\%$ for the measurement behind the PPQFCD, $\approx 17\,\%$ for the measurements with the long fibers). An optimization of the success probability by a factor 5-6 is possible by employing state-of-the-art SNSPDs with efficiencies $> 80\,\%$ and the replacement of some lossy fiber components (MEMS switch, fiber-fiber connectors). Note that the success probabilities are comparable to those of the trapped-ion QNN in Chap. 4 and, hence, in the typical order of magnitude of free-space QNNs equipped with high-NA objectives for photon collection (cf. Sect. 4.3). The generation rate in all measurements – including those with the long fibers – is limited by the loading rate of the trap to 35 events per minute. This results from a saturation effect since the success

probabilities are high enough that the atom is likely to be shot out of the trap during the state analysis in below a second after loading. The rate is a few orders of magnitude lower compared to other QNNs, however, the influence of the loading rate is heavily diminished for atom-atom entanglement. There the success probability is proportional to the square of the current probabilities and therefore low enough to avoid the saturation effect.
In the measurements including QFC we achieved SBRs between 23.2 and 32.3, again in good agreement with the success probabilities and expected background in the photonic detection. The main contribution to the background is CIB, which is the reason that the SBR is not significantly reduced in the measurements with the long fibers since it also suffers from the same attenuation in the fibers. The remaining fluctuations are caused by drifts in the setup affecting the success probability. Causing a loss of fidelity of about 3 %, the SBR can be considered as the main obstacle for advanced device-independent protocols since it is non-trivial to improve it in the current setup.
Finally, we analyzed the atom-photon entanglement without QFC and with QFC after 50 m, 10 km and 20 km of fiber. From joint projective measurements of atom and photon we calculated the Bell parameter and estimated lower bounds of the fidelity with the expected Bell state. At short fiber distances (but with an electronic delay between a photon detection event and the state analysis corresponding to the waiting time of 10 km fiber) we obtained values of $\mathcal{F} \geq 89.7(7)\,\%$, $S = 2.49(3)$ without QFC and $\mathcal{F} \geq 88.1(11)\,\%$, $S = 2.41(3)$ with QFC. Here the loss of fidelity is explained by the limited SBR. After 10 km and 20 km of fiber we measured $\mathcal{F} \geq 84.2(10)\,\%$, $S = 2.37(4)$ and $\mathcal{F} \geq 78.9(13)\,\%$, $S = 2.12(5)$, respectively. While all numbers are reduced because of drifts, we clearly see the influence of the atomic coherence at 20 km, which accounts for a fidelity loss of 11 % in total.
For future, more demanding experiments the SBR and the coherence time must be improved. Regarding the SBR, one possibility is a even higher NA of the objective to improve the collection efficiency. A further reduction of Raman background by at least one order of magnitude could be realized by operating the PPLN waveguide at cryogenic temperatures $< 100\,\mathrm{K}$ (see Sect. 2.1.2). Despite promising recent results demonstrating SHG at cryogenic temperatures [277], this approach still adds complexity and a large technical overhead to the QFCDs. Another possibility are smaller filter bandwidths, however, an improvement of the SBR by one order of magnitude is not even realistic employing ideal single-photon detectors because the filter starts to absorb the emitted photons at the same time (see Sect. 6.3.3). An alternative is to change the target wavelength to the telecom O-band by utilizing e.g. the DFG-process to 1/780 nm - 1/1930 nm = 1/1310 nm with a thulium-based laser system as pump source [82]. The large spectral separation between pump and target wavelength of $-2450\,\mathrm{cm}^{-1}$ suppresses ASR background by several orders of magnitude and makes spectral filtering to the MHz-regime unnecessary. However, due to the large attenuation of the 1930 nm light in fibers ($\approx$ 20dB/km) it is not possible to use a single master laser, but independent TDFLs must be stabilized to ultra-stable high-finesse cavities.
To improve the coherence time, several strategies can be applied: first, the dominant contribution at the present time-scale ($< 1\,\mathrm{ms}$) stems from the position-dependent effec-

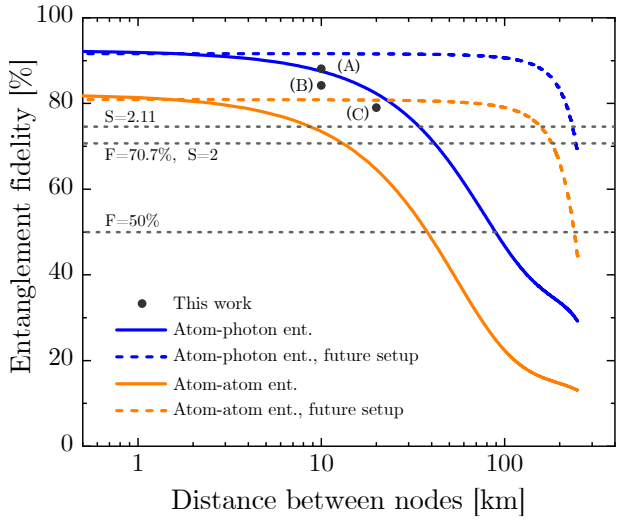

Figure 7.6. Expected atom-photon and atom-atom entanglement fidelities. Simulated entanglement fidelities at different fiber lengths for the current setup as well as a future one with an improved atomic coherence. The black data points represent the measurements in this chapter. While the SBR and the imperfect atomic-state readout limit the fidelity at short distances, the atomic coherence is the limiting factor at longer distances >10 km. The loss of fidelity at distances >100 km for the improved setup stems from detector dark-counts.

tive magnetic fields in the dipole trap. This effect can be circumvented by a standing-wave dipole trap to spatially confine the atom much stronger (see e.g. [104]). Beyond this, the influence of external magnetic field noise could be suppressed via a μ-metal shield or by decoupling the qubit from magnetic fields employing a combination of a Raman transfer to (first-order) magnetically-insensitive clock states (e.g. the states $|S_{1/2}, F = 1, m_F = +1\rangle$ and $|S_{1/2}, F = 2, m_F = -1\rangle$) and a spin-echo sequence [278]. It has been shown that these approaches enable coherence times up to a few hundreds of milliseconds, which is enough to enable atom-photon entanglement over 100 km without significant decoherence.

An estimation of the expected atom-photon (blue curves) and atom-atom (orange curves) entanglement fidelities at different fiber lengths is shown in Fig. 7.6. The gray dashed lines denote three important threshold of the fidelity, namely the classical threshold at 50 % as well as two values where the Bell parameter surpasses 2.0 and 2.11. The latter are related to the violation of Bell's inequality and the threshold to allow for self-testing of the quantum network link, respectively [220, 221]. The solid lines are calculated for the current setup (the results of measurements A, B and C are shown as black dots), while the dashed lines assume a future setup with an improved atomic coherence. At small fiber lengths, the dashed and solid lines overlap since the fidelities are mainly limited by the imperfect atomic-state readout and the SBR. We find that self-testing is possible until 5 km and a loophole-free Bell test until 10 km even with the current setup. With the future setup, this can be extended to about 100 km. For longer fibers, detector dark-counts are the main source of background, which results in a quick decrease of the fidelities.

Chapter 8

Summary and Outlook

In the first part of this chapter we will summarize the most important experimental results presented throughout this thesis. In the second part, we give an outlook on the next reasonable steps towards robust long-distance quantum network links capable of establishing high-fidelity entanglement between remote matter qubits. On that account, we suggest further improvements of our QFC devices and illustrate possible atom and ion experiments. Furthermore, we present some ideas to perform self-testing of our QFCDs, realize hybrid entanglement between two dissimilar quantum network nodes (QNN), and to demonstrate the preservation of nonclassical, negative Wigner functions during QFC.

8.1 Summary

The core of the work presented in this thesis was the development of in total four high-performance polarization-preserving quantum frequency converters to equip trapped-atom QNNs with a telecom interface that brings long-distance quantum networks in reach. In particular, we focused on trapped $^{40}Ca^{+}$-ions and neutral ^{87}Rb-atoms with transition wavelengths at 854 nm and 780 nm, respectively, which we connected to the telecom O-, C- and S-band. On top of the construction and characterization of the QFC devices, we performed a series of experiments combining those with the trapped-atom QNNs or an entangled photon pair source to establish photon-photon entanglement distributed over up to 40 km of fiber, light-matter entanglement over up to 20 km of fiber and a quantum state transfer from a matter qubit onto a photonic qubit at telecom wavelengths. We here sum up the most important achievements:

PPQFC devices for $^{40}Ca^{+}$-ion network nodes. We designed, constructed and characterized two PPQFCDs connecting the Ca-ion emission wavelength 854 nm to the telecom O-band at 1310 nm and C-band at 1550 nm (in the following, all numbers are listed in this order). Both converters rely on the nonlinear-optical process of difference-frequency generation in a PPLN waveguide employing strong cw pump lasers at 2456 nm and 1904 nm, respectively. To overcome the polarization dependency, the waveguides

are inserted into polarization interferometers, either arranged in a single-crystal Mach-Zehnder (O-band converter) or an intrinsically phase-stable Sagnac configuration (C-band converter). Both devices were characterized with respect to their efficiencies, conversion-induced background, and polarization-preserving properties. We measured external device efficiencies of 26.5 % and 57.2 %. While the O-band converter compares well with other state-of-the art QFCDs, the efficiency of the C-band converter is about a factor two above these numbers, which has been achieved by an optimization routine to allow for high waveguide-coupling efficiencies as well as improved optical components featuring low losses. Undesired nonlinear processes (O-band converter) induced by the pump laser and anti-Stokes Raman scattering (C-band converter) of the pump in the waveguide result in conversion-induced background, which has been quantified to 11.4 cps and 24 cps after spectral filtering down to 25 GHz and 250 MHz, respectively. Taking the higher external device efficiency of the C-band converter into account, both numbers are comparable with respect to their influence on the SBR and allow for SBRs of > 200 assuming state-of-the-art trapped-ion QNNs. The preservation of arbitrary polarization states of the input light was confirmed by means of quantum process tomography. We found process fidelities of up to 99.75 % and 99.85 % with a high long-term stability over several hours in which the fidelity never drops below 99.5 % and 99.75 %. These numbers are above the best achieved light-matter entanglement fidelities and therefore not a limiting factor as of yet. Moreover, we confirmed by simulations that imperfections of the PPQFCD do not significantly decrease the fidelities. Instead, the observed limitations are caused by a non-perfect compensation of the polarization rotation of the whole setup or polarization drifts in a 90 m long fiber connecting different labs. Eventually, we demonstrated the conversion of nonclassical light, namely polarization-entangled frequency-degenerated photon pairs at 854 nm emitted by a cavity-enhanced SPDC source, which delivers 5×10^4 $^{\text{pairs}}/_{\text{s·mW}}$ ion-resonant photon pairs with a fidelity of about 98 %. Via PPQFC of the idler photons, we measured photon-photon entanglement in three different configurations: directly after PPQFC, after PPQFC and 20 km of fiber, and after 40 km of fiber via back-reflection and two-stage PPQFC. In all measurements, we obtained background-corrected fidelities with the $|\Psi^-\rangle$ Bell-state above 97.4 % and purities above 97 %, which proves preservation of polarization entanglement during PPQFC. Without background subtraction we measured fidelities between 74 % and 79 %, being still clearly above the classical threshold of 50 %. All values are consistent with the measured SBRs around 2 limited by accidental coincidences of the source.

Ion-telecom-photon entanglement and ion-to-telecom photon state transfer. We performed two experiments to demonstrate basic operations of a quantum network by combining a trapped-ion QNN with the PPQFC connecting 854 nm to the telecom O-band. We started with the generation of entanglement between an atomic Zeeman qubit and the polarization state of a telecom photon. We first characterized the ion-photon entanglement at 854 nm without QFC, which we create with a rate of 256 Hz and a SBR of 29.5, limited by the collection efficiency and detector dark-counts, respectively. Due to different Clebsch-Gordan coefficients of the transitions, the entangled

state is not a Bell state, but an asymmetric state with a maximum Bell-state fidelity of about 97 %. Nevertheless, quantum state tomography of the ion-photon state reveals Bell-state fidelities of 95.4(2) % and 93.4(2) % with and without background subtraction, being in good agreement with the measured purity and SBR and clearly above the classical threshold of 50 %. The fidelities with respect to the asymmetric state are even > 96 %. In the next step, we combined ion trap and O-band converter and created ion-telecom photon entanglement with a rate of 43.5 Hz and a SBR of 24.3. In this measurement, the background is still mainly determined by detector dark-counts, but has a minor contribution (6.5 %) stemming from conversion-induced background. We proved preservation of light-matter entanglement after PPQFC by means of fidelities with a Bell-state above 92 % and the asymmetric state above 95 %. The loss of fidelity of 0.6 % and 1.1 % (with and without background subtraction) compared to the values without QFC can be explained by the process fidelity, polarization drifts in the fibers and the reduced SBR. Eventually, we employed the converter to introduce polarization-dependent losses in order to compensate for the unequal Clebsch-Gordan coefficients. With this method, we increased the Bell-state fidelities to > 93.4 % without and 97.8(1) % with background subtraction, respectively.
In the second experiment we implemented a quantum state transfer from an atomic Zeeman qubit onto the polarization state of a telecom photon utilizing the same setup as for ion-photon entanglement. The protocol relies on the preparation of an initial qubit in the $D_{5/2}$-manifold followed by excitation and photon emission on the 854 nm-transition and subsequent PPQFC to the O-band. The protocol succeeds with probabilities of 1.35 $\times 10^{-4}$ (854 nm) and 5.1 $\times 10^{-5}$ (1310 nm) per excitation try, which is in good agreement considering the accumulated impact of all individual efficiencies and transmissions. We characterized the protocol via quantum process tomography and found process fidelities > 93.2 % at 854 nm and > 91 % at 1310 nm, mainly limited by the atomic coherence, SBR and back-decay to the initial qubit. The results were confirmed by measurements of the average fidelities extracted from the single-qubit density matrices of the photonic output state.

PPQFC system for ^{87}Rb-atom network nodes. With the experience and techniques developed for the converter transducing 854 nm to 1310 nm, we designed a complete QFC system to extend an elementary quantum network link based on single ^{87}Rb-atoms by a telecom interface connecting 780 nm to the S-band at 1522 nm. The design is based on several criteria to meet the requirements determined by the network link in terms of conversion metrics and pump laser stability/reliability, as well as to allow for full transportability and the integration into the network link. The system consists of four mobile platforms, whose design and characterization was presented in Chap. 6. The first platform contains two frequency-stabilized lasers at 780 nm and 1600 nm with a long-term stability of about 1 MHz, which serve as master lasers for alignment, benchmarking and pumping of the PPQFCDs. The two PPQFCDs (one for each atom trap) are constructed in Sagnac configuration and represent the second and third platform. The nonlinear waveguides are designed for the DFG-process 1/780 nm - 1/1600 nm = 1/1522 nm and were characterized in terms of their spectral and temperature tuning

properties in order to find suitable operating points. We investigated the spectra and power density of the dominant background source of this wavelength combination – anti-Stokes Raman scattering – and designed a narrowband filter system based on these findings. Via a combination of interference filters, a Bragg grating and a frequency-stabilized Fabry-Pérot cavity, we achieved a bandwidth of 27.3 MHz with a suppression window of several hundreds of nanometers, and an overall transmission of 90.7 %. This enabled external device efficiencies of 57 % and generated conversion-induced background count-rates of about 2000 cps for both QFC devices. The fourth platform features the filtering system, which has been separated from the QFC platforms for technical reasons, and the optical components to perform an automatized compensation of the polarization rotation in the whole setup as well as projective measurements of the converted photons or a photonic Bell-state measurement.

Distribution of atom-photon entanglement over 20 km of fiber. Finally, the integration of the QFC system into the existing network link in Munich enabled the distribution of atom-photon entanglement over up to 20 km of fiber. We gave an overview of the Rb-atom QNN with a focus on the experimental sequence, the coherence properties of the atomic Zeeman qubit, and the joint setup featuring the atom trap and QFCD. We analyzed atom-photon entanglement in four different configurations: at 780 nm and after PPQFC at 1522 nm – each with an electronic delay corresponding to the waiting time of 10 km of fiber before the projective measurement of the atomic state – as well as after 10 km and 20 km of spooled fibers. From TCSPC measurements of the converted photon wavepacket we derived success probabilities to detect a photon per excitation trial between 0.173×10^{-3} and 1.276×10^{-3}, and SBRs between 23.2 and 32.3 being in good agreement with the reference measurement at 780 nm, all individual efficiencies and transmissions, and the detected background. The latter has a major contribution from conversion-induced background ($\approx 95\,\%$) and a minor one from detector dark-counts ($\approx 5\,\%$). We verified entanglement via projective measurements of the atomic and photonic qubit in several basis settings, from which we calculated the Bell parameter and estimated a lower bound of the Bell-state fidelity. We obtained fidelity bounds between 90 % at 780 nm and 79 % after 20 km of fiber. The loss of fidelity stems from the limited SBR and the atomic coherence caused by the waiting time of about 100 µs associated with the travel time of the photon through the fibers. Nevertheless, all fidelities are well above the classical threshold of 50 % as well as 70.7 %, which corresponds to a Bell parameter of 2. The latter is supported by the measured Bell parameters ranging from 2.12(5) to 2.49(3).

8.2 Outlook and future prospects

Further development of the QFC devices. The next steps in the development of the QFCDs for 780 nm and 854 nm are determined by the open issues listed in the tables of requirements and figures of merit presented in Sect. 2.3, 3.4 and 6.4. The integration into a 19-inch rack is currently approached in our group. While the lasers, electrical components and the projection setup can be conveniently mounted in a rack,

the main obstacle is the space requirement of the Sagnac interferometer. To this end, the optimization algorithm of the trichroic waveguide coupling has already been revised by T. Bauer to simultaneously find the parameters for best possible coupling and minimal distances between waveguide and fiber-couplers. This enabled the construction of the Sagnac interferometer on a breadboard, which fits into a 19-inch rack. The integration on a single chip with butt-coupled fibers at the entrance and exit represents a much more challenging task. In principle, all essential ingredients, among them on-chip polarization-dependent QFC, which relies on reverse-proton-exchanged waveguides to realize butt-coupling of fibers, S-bends as well as wavelength-dependent directional couplers [82, 222, 223], or polarization control of single photons employing electro-optical components attached to Ti-indiffused waveguides [279, 280] were demonstrated on LN chips. However, combining all components – each featuring low losses – on a chip with the additional constraint on a certain wavelength combination and simultaneous phasematching in more than one poled region is expected to be non-trivial. Photon bandwidth manipulation could be implemented either with dispersion-engineered QFC [224], chirped pump pulses, or via an electro-optic time lens [281]. However, these techniques are so far restricted to certain wavelength combinations and/or to bandwidths in the GHz regime. The reason is that all techniques rely on dispersion, which is negligible in the case of MHz-broad photons. The same argument renders dispersion cancellation unnecessary, even for several hundreds of km fiber MHz-broad photons are not significantly broadened [225]. Conversion to multiple frequency channels within the phasematching bandwidth can be easily achieved with more than one seed laser or fast frequency-tuning using an AOM or EOM. The main obstacle are the narrowband filters at the telecom wavelength. This could be solved by choosing the network protocol mentioned in Chap. 5, which relies on emission and absorption of photons by the QNNs. Here the absorptive QNN acts as a spectral filter, i.e. filtering at telecom wavelengths is not required [158].

Another direction is the development of two-stage frequency converters for QNNs based on color centers in diamond. The majority of the color centers currently explored as QNNs possess transition wavelengths between 500 nm and 750 nm (e.g. nitrogen-vacancy: 637 nm, silicon-vacancy: 737 nm, germanium-vacancy: 602 nm, tin-vacancy: 620 nm). DFG-processes connecting the telecom C-band to these wavelengths require pump laser wavelengths between 970 nm and 1410 nm, i.e. we are not in the long-wavelength pumping regime anymore and may suffer from a comparable large amount of background (see e.g. [141,142,192]). One possible solution to avoid narrowband spectral filtering is a two-step process: by using a pump laser with double the wavelength, we convert the input light in one waveguide to an intermediate wavelength and in a second waveguide to 1550 nm. Two examples: for the silicon-vacancy center emitting at 737 nm and the tin-vacancy at 620 nm the pump lasers have to operate around 2815 nm and 2067 nm, respectively. Both can be generated with Cr^{2+}:ZnSe/S lasers and enable conversion-induced background rates comparable to those of the C-band and O-band converters.

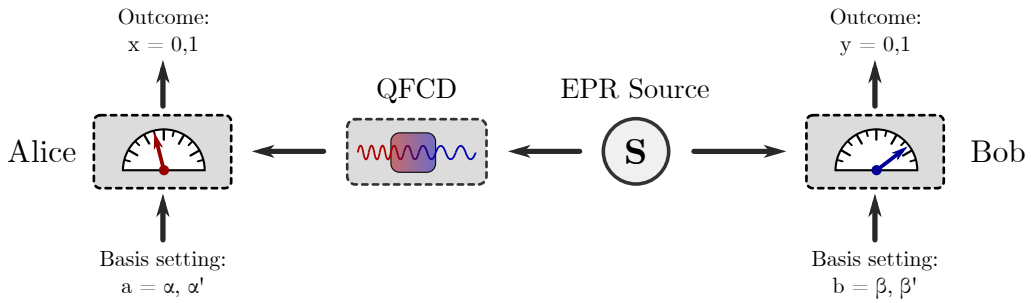

Figure 8.1. Self-testing of a quantum frequency converter.

Self-testing of frequency converters. During the last years, it has been theoretically proposed to employ Bell's theorem to perform a so-called self-testing or device-independent certification of building blocks for quantum computers or quantum networks, such as quantum states and measurements [282,283] as well as quantum channels or entangling gates [220]. Considering our frequency converters as such a building block, and in particular as a one-qubit identity channel, we can apply the protocol described by Sekatski et al. [220] to perform self-testing of our QFCDs. The basic idea relies on a (loophole-free) Bell test experiment since the measurement of the S-parameter can be performed – in contrast to quantum state or process tomography – device-independently. This means that no prior knowledge about the functionality of the channel is required and that we only make minimal assumptions on the input state and the measurement setup, e.g. in terms of Hilbert space dimension or calibration of the projection/detection setup (both are for instance necessary assumptions for a state tomography). The scheme to certify a QFC device is sketched in Fig. 8.1: an EPR source generates entangled Bell-states. One of the qubits is sent to Bob, while the other qubit passes the QFC and is detected at Alice's side. From measurements of the Bell parameter of the input and output state, i.e. with and without QFC, we can calculate the self-testing fidelity of the quantum channel. The detailed analysis presented in [220,284] reveals that the Bell parameter of the output state must significantly surpass a threshold of 2.11 to obtain a self-testing fidelity larger than zero.

Our idea for an experimental realization employs the C-band converter together with the trapped-ion QNN as EPR source generating atom-photon entangled states with high fidelity. The qubit on Bob's side is the atomic qubit, while the emitted photonic qubit can be directly characterized at 854 nm, or frequency-converted and measured at 1550 nm. However, two obstacles hinder the experimental realization of the original proposal. First, a device-independent certification necessitates the closure of the detection loophole, i.e. we have to collect, convert and detect a photon with more than 71 % efficiency (assuming an efficiency of 100 % for the atomic qubit). Without advanced schemes such as heralded qubit amplification [285,286] this threshold is far out of reach with the current setup. To this end, it has been proposed to perform self-testing under the fair sampling assumption, which is not fully device-independent anymore and requires further assumptions on the detection system [287], but still preferable compared to tomographic methods. The second issue is related to the asymmetric state

being generated by the trapped-ion QNN. In principle, all bounds on the fidelity mentioned above are calculated for maximally entangled Bell states, however, a modification of the protocol in [220] allows for robust self-testing with non-Bell states with higher demands on the Bell parameter of the output state [288]. Another possibility is to introduce state-dependent loss (e.g. in the QFCD as shown in Sect. 4.2) to compensate for the asymmetry. During the final stage of the preparation of this thesis, we performed experiments in this direction yielding a Bell parameter of 2.670(36) after frequency conversion including the compensation for the asymmetric state, which is a first evidence that self-testing of our QFCDs is feasible.

Further experiments with trapped-ion network nodes. The first obvious experiments are the retake of the experiments in Chap. 4 and 5 including 20 km fiber utilizing a recently developed spin-echo sequence, the C-band converter, and a set of state-of-the-art SNSPDs with $> 70\,\%$ SDE and < 10 cps DCR being delivered in the near future. Moreover, by combining the trapped-ion QNN with the cavity-enhanced SPDC source and the C-band converter, it is possible to employ heralded absorption [131] to realize heralded ion-telecom-photon entanglement [204] or a teleportation-based quantum state transfer of an atomic Zeeman qubit onto a telecom photon [261]. On a longer perspective, one could aim at experiments including a second ion, either in the same trap or in a second remote trap. Two ions in the same trap along with the possibility to collect and couple photons from each ion to individual fibers as well as entangling gates between the ions, enable the implementation of a single-sequential repeater node [289], being realistic already with the currently available ion trap. In contrast, remote entanglement of two ions relies on quantum interference of the photons from both traps and requires optical cavities in order to generate Fourier-limited photons.

Extending the network link in Munich: towards long-distance atom-atom entanglement, device-independent protocols and multiple network nodes. The next step in Munich is the demonstration of telecom-heralded atom-atom entanglement over several kilometers of spooled fibers as illustrated in Fig. 6.1. First promising results obtained during the final stage of this thesis revealed the successful creation of telecom-heralded atom-atom entanglement over 700 m of fiber (i.e. without km long fibers but with QFC) with a Bell parameter of about 2.2, and over 22 km with $S = 2.08$. This confirms that the BSM at telecom wavelengths as well as the automatized compensation of the polarization rotation works. Furthermore, a Bell parameter of 2.2 with sufficient statistics allows for self-testing of the network link according to the protocol in [221]. However, the demonstration of device-independent QKD [251] requires a Bell parameter of about 2.4, which calls for an improvement of either the SBR or the fidelity of the atomic-state readout (cf. Sect. 7.3). Going beyond spooled fibers, a further atom trap can be constructed at the Max-Planck-Institut für Quantenoptik (MPQ) in Garching, which is about 20 km apart from the LMU. Although we can mimic this experiment already with the current setup by inserting spooled fibers into the photonic channel and the classical communication channels of the herald and synchronization signals, the step towards deployed fibers will surely provide some challenges. Regarding the QFC

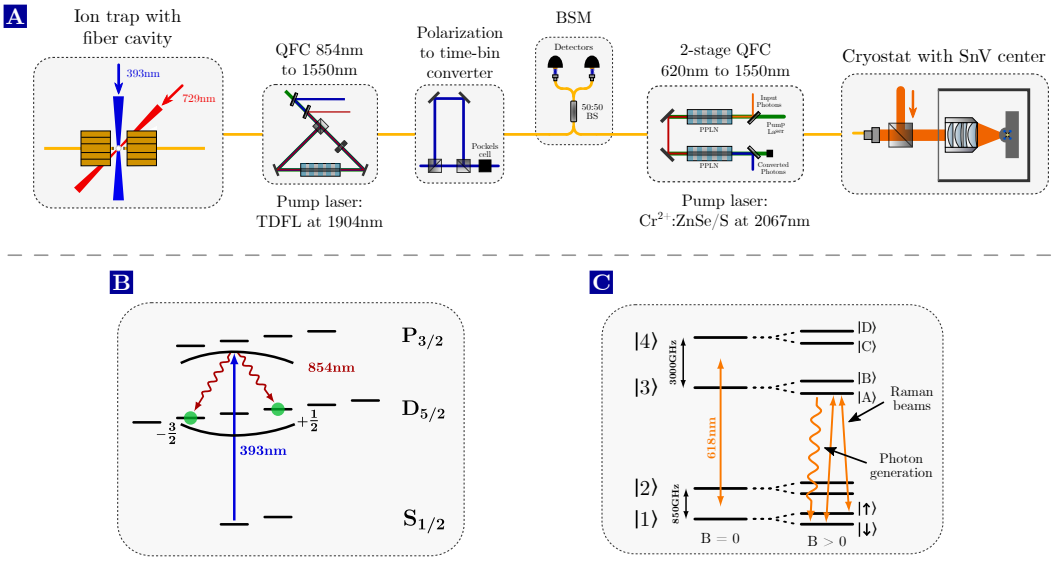

Figure 8.2. Entanglement of a trapped ion and a SnV center in diamond. **(A)** The scheme to entangle a Ca-ion with a SnV-center via QFC to a common bus wavelength at 1550 nm. Further details will be given in the main text. **(B)** Level scheme of the Ca-ion: ion-photon entanglement is generated between two Zeeman states and the photon polarization with a cavity-QED system. **(C)** Level scheme of the SnV-center: the qubit states are two Zeeman states of the lower ground state. Spin-photon entanglement is generated in the time-bin degree of freedom by means of Raman transitions and resonant excitation.

system, it might be necessary to investigate the linewidth of the 1600 nm laser on a millisecond time-scale. Since the laser is most probably not exactly located between the atom traps, a broadening of the linewidth to 1 MHz already causes a significant decrease of the HOM visibility. Thus, it might be necessary to narrow the linewidth by means of a high-finesse ultra-low expansion cavity or a self-heterodyne technique. On a longer perspective one could think about more than two QNNs via a connection to the cavity-based Rb-atom QNNs of the group of G. Rempe at the MPQ. Experiments in this direction include the entanglement of three single-atom QNNs, a three-node network with a central node featuring two atoms coupled to one cavity [107] or the storage of photons from the free-space QNNs in a recently-developed heralded quantum memory based on crossed fiber-cavities [253].

Towards hybrid entanglement: entangling a trapped ion with a color center in diamond. A further idea for a novel experiment aims at the entanglement or a quantum state transfer between dissimilar network nodes, e.g. between atomic and solid-state systems. Only in few cases a solid-state system can be found whose system wavelength exactly matches (or can be tuned to) the atomic wavelength; possible candidates are for instance quantum dots [290, 291] or ZnO semiconductor defects [292]. In general, the transition wavelengths of the nodes are different and QFC to a common bus wavelength can be applied as mentioned in the introduction. As an example, we could aim for the entanglement of a trapped $^{40}Ca^{+}$-ion Zeeman-qubit with the spin state of a

negatively-charged tin-vacancy center in diamond (SnV^-, details see e.g. [293, 294]) via a BSM at 1550 nm. The proposed scheme is shown in Fig. 8.2: the experiment has three major requirements: a trapped-ion QNN where the ion is coupled to a short fiber cavity, a SnV^--center QNN capable of generating spin-photon entanglement, and a QFC system to convert the photons emitted by both QNNs to 1550 nm in a qubit-preserving way. A major difficulty in connecting dissimilar systems are the unequal spectral properties of the photons apart from the central wavelength, mainly their linewidth and temporal profile. Fortunately, the SnV^- center has a natural linewidth around 20 MHz, being in a similar range as the 854 nm-transition linewidth of 23 MHz. In the ideal case (no further broadening mechanisms), this guarantees sufficiently large HOM interference contrasts ($> 90\,\%$) without the need for strong temporal filtering.
In the trapped-ion QNN, entanglement can be generated employing a scheme comparable to the one described in Chap. 4. However, we already mentioned that back-decay via the 393 nm-transition hinders the generation of lifetime-limited photons. Thus, an optical cavity to drive cavity-mediated Raman transitions is required. Since the emitted photons should possess linewidths in the order of the natural linewidth, a cm long cavity as in [59] with linewidths in the kHz-regime is not recommended. Instead, a short fiber cavity (e.g. $L \approx 250\,\mu m$, Finesse: ≈ 30.000) is advisable. Note that such a cavity is too broad to individually address Zeeman levels of the $D_{5/2}$-manifold via Raman transitions, thus, a suitable combination of detuning from the excited state and 393 nm-laser polarization must be identified to obtain Bell states.
The SnV^- center features two ground and two excited states with energy differences of about 850 GHz and 3000 GHz, mainly caused by spin-orbit coupling (see Fig. 8.2c). The line center of the four dipole-allowed transitions is at around 618 nm. The usage of the two ground states as qubit states is not advised due to fast (ps time-scale) phonon-mediated thermalization processes, which causes a fast decay of the population from the upper to the lower ground state (the inverse process is unlikely at 2 K since phonons at 850 GHz are frozen-out). Hence, a magnetic field is applied, which splits each state in two orthogonal spin states. Phonon-mediated transitions between these states are forbidden (except phonon-mediated transitions via the upper ground state, which could be minimized by operating at 2 K and with an appropriate Zeeman splitting), i.e. we can encode a qubit in the two spin states of the lower ground state. Unfortunately, due to selection rules of the optical transitions between ground and excited states, it is not feasible to directly create spin-photon entanglement in the polarization degree of freedom. A common choice for color centers in diamond is the time-bin degree of freedom, where the protocol works as follows: after optical pumping to the state $|\downarrow\rangle$, a balanced superposition between $|\downarrow\rangle$ and $|\uparrow\rangle$ is created by means of Raman transitions (manipulation of the qubit states via microwaves would also work, but has proven challenging with group-IV vacancy centers due to the high power required for driving the transition interfering with the cooling inside a (dilution) cryostat [295, 296]). Next, a single photon is generated on the optical transition $|\downarrow\rangle \leftrightarrow |A\rangle$ via π-pulse excitation on the same transition. After a waiting time sufficiently longer than the excited state lifetime, the population of the qubit states is inverted by a π-pulse on the Raman transition, and another photon is generated in the same way as mentioned above. This

results in entanglement between the spin qubit and the time-bin of the photon. Note that it would be desirable to generate time-bin entangled photons in the trapped-ion QNN as well, however, this requires a narrow cavity where Raman transitions between individual Zeeman states can be driven.
The QFC system and BSM works as follows: for the photons emitted by the ion we employ the C-band converter (see Sect. 3.2), while the SnV^--photons at 620 nm can be converted to 1550 nm in the above mentioned two-stage process with a Cr^{2+}:ZnSe/S-laser operating at 2067 nm. The respective DFG-processes are 1/620 nm - 1/2067 nm = 1/886 nm and 1/886 nm - 1/2067 nm = 1/1550 nm. Indistinguishability of the converted photons with respect to the center wavelength can be ensured by a frequency stabilization of both pump lasers, either via transfer-locks or detection of the frequency-doubled pump light with a state-of-the-art wavelength meter with 2 MHz absolute accuracy (model WS8-2, *High Finesse*). The BSM at 1550 nm can be conveniently performed in the time-bin degree of freedom as the fast recovery time of SNSPDs makes only two detectors necessary to measure Ψ^- and Ψ^+ Bell states [297]. Since the photons from the ion are entangled with respect to their polarization, the entanglement has to be converted to time-bin. To this end, the standard configuration consisting of an unbalanced Mach-Zehnder interferometer with two PBS to separate the two polarization components in time, and a subsequent Pockels cell, which rotates the polarization of one of the photons by 90° to equalize the polarization of both, is inserted before the BSM.

Preservation of nonclassical Wigner functions during QFC. We mentioned in the introduction, that the preservation of various classical and nonclassical properties of photons during QFC has been already demonstrated. However, one important property remained elusive so far, the nonclassical Wigner function of a single-photon Fock state. The latter is the quasi-probability distribution of the quantum state in phase space spanned by the quadratures X and P, which features for a single-photon Fock state a rotationally symmetrical shape with negative values around the center (see e.g. [298]). Wigner functions are commonly measured via balanced homodyne detection. There the challenge is that losses between the single-photon source and detectors, which result in an increase of the zero-photon contribution in the photon statistics, diminish the negativity of the Wigner function. In fact, a total loss 50 % is the threshold where the Wigner function becomes non-negative, thus, even the combination of our QFC devices with highly-efficient single-photon sourced based on SPDC [298] or single atoms in optical cavities [299] is not efficient enough to be above this threshold. For this reason, it was up to now only possible to verify the preservation of non-negative, loss-tolerant Wigner functions of squeezed states during QFC [300]. One way out is an alternative measurement technique developed by Laiho et al. [301]: in the case of a rotationally symmetrical Wigner function, it is possible to probe that of a pulsed single-photon source point by point. To this end, Laiho et al. employed loss-tolerant photon-number resolving detectors to measure the photon statistics of a single-photon Fock state generated by a heralded SPDC source at different displacements α. From the photon statistics, the value of the Wigner function for a certain displacement, which corresponds to the distance to

the origin in phase space, can be calculated. A variation of the displacement thus allows for a point by point probing. They utilized time-multiplexed detectors (TMD), which are capable of resolving the photon number of pulsed sources with standard binary detectors [302], however, also more recently developed superconducting transition edge sensors (TES) would allow for this task. The preservation of negative Wigner functions during QFC employing this loss-tolerant technique could be performed as follows: we start with a pulsed heralded single-photon source operating at 780 nm or 854 nm, similar to that in [301], where a mode-locked titanium sapphire laser is frequency-doubled and subsequently down-converted in a KTP waveguide. The signal photons are converted with one of the QFCDs described in this thesis and detected with a TMD for telecom wavelengths or a TES. The required displacement is in [301] realized by overlapping a small fraction of the pump laser of the source (attenuated to the single-photon level) in different intensities with the single photons on a fiber-based PBS. To measure the ideal Wigner function of a Fock state, it is important that the pump laser has a large spectral, spatial and temporal overlap with the photons (verified by HOM interference), thus, in the scheme including QFC the pump laser of the source must be frequency-converted to telecom wavelengths, too. To this end, a second QFCD for 854 nm or 780 nm, where the particular waveguide is chosen to obtain the best spectral overlap with the first QFCD, can be utilized.

Appendices

Appendix **A**

Calculation of the process matrix from the Choi-matrix

The maximum-likelihood estimation presented in Sect. 2.2.4 outputs the Choi-matrix S, which is isomorphic to the positive map $\mathcal{E}$ describing the process, but less intuitive and descriptive than the process matrix χ associated with $\mathcal{E}$. Thus, we here present how to transform the S-matrix to the χ-matrix representation. As a reminder, the quantum process is described by the map $\mathcal{E}$

$$\rho_{\mathrm{out}} = \mathcal{E}\left(\rho_{\mathrm{in}}\right) = \sum_{\mathrm{m,n}\,=\,1}^{4} \chi_{\mathrm{mn}}\, \sigma_{\mathrm{n}}\, \rho_{\mathrm{in}}\, \sigma_{\mathrm{m}}^{\dagger} \tag{A.1}$$

with χ_{mn} being the entries of the process matrix and $\sigma_{\mathrm{n/m}}$ the Pauli matrices. However, the Pauli matrices are only one possible basis and we can rewrite the map $\mathcal{E}$ in a different basis. In fact, if we choose a particular orthogonal basis A_n with

$$A_1 = \begin{pmatrix} 1 & 0 \\ 0 & 0 \end{pmatrix} \quad A_2 = \begin{pmatrix} 0 & 1 \\ 0 & 0 \end{pmatrix} \quad A_3 = \begin{pmatrix} 0 & 0 \\ 1 & 0 \end{pmatrix} \quad A_3 = \begin{pmatrix} 0 & 0 \\ 0 & 1 \end{pmatrix}, \tag{A.2}$$

we find that the matrix elements χ_{mn} are identical to the entries of the S-matrix. Hence, we can describe $\mathcal{E}$ as

$$\rho_{\mathrm{out}} = \mathcal{E}\left(\rho_{\mathrm{in}}\right) = \sum_{\mathrm{m,n}\,=\,1}^{4} S_{\mathrm{mn}}\, A_{\mathrm{n}}\, \rho_{\mathrm{in}}\, A_{\mathrm{m}}^{\dagger} \tag{A.3}$$

and calculate the process matrix χ from the S-matrix (and vice versa) via a basis transformation. To this end, we write the A-matrices as linear combination of Pauli matrices

$$A_{\mathrm{i}} = \sum_{\mathrm{j}\,=\,1}^{4} M_{\mathrm{ji}} \sigma_{\mathrm{j}} \tag{A.4}$$

with M_{kl} being the entries of the transformation matrix M. For a given set of two bases, we can calculate these entries via

$$M_{\mathrm{kl}} = \frac{1}{2} \mathrm{Tr}\left(\sigma_{\mathrm{k}} A_{\mathrm{l}}\right). \tag{A.5}$$

Inserting Eq. A.4 into Eq. A.3 yields

$$\rho_{\mathrm{out}} = \sum_{\mathrm{m,n}\,=\,1}^{4} S_{\mathrm{mn}}\, A_{\mathrm{n}}\, \rho_{\mathrm{in}}\, A_{\mathrm{m}}^{\dagger} = \sum_{\mathrm{m,n}\,=\,1}^{4} S_{\mathrm{mn}} \left(\sum_{\mathrm{i}\,=\,1}^{4} M_{\mathrm{in}} \sigma_{\mathrm{i}} \right) \rho_{\mathrm{in}} \left(\sum_{\mathrm{j}\,=\,1}^{4} M_{\mathrm{jm}}^{*} \sigma_{\mathrm{j}}^{\dagger} \right)$$

$$= \sum_{\mathrm{i,j}\,=\,1}^{4} \left(\sum_{\mathrm{m,n}\,=\,1}^{4} M_{\mathrm{in}}\, S_{\mathrm{mn}}\, M_{\mathrm{jm}}^{*} \right) \sigma_{\mathrm{i}}\, \rho_{\mathrm{in}} \sigma_{\mathrm{j}}^{\dagger} = \sum_{\mathrm{i,j}\,=\,1}^{4} \chi_{\mathrm{ij}}\, \sigma_{\mathrm{i}}\, \rho_{\mathrm{in}} \sigma_{\mathrm{j}}^{\dagger}. \tag{A.6}$$

Thus, we obtain the following expression to transform the S-matrix into the χ-matrix utilizing the transformation matrix M:

$$\chi = M\, S\, M^{\dagger} \tag{A.7}$$

Appendix B

Infrared-pumped optical parametric oscillator at 2456 nm

The laser system at 2456 nm to drive the DFG-process in the O-band converter is made up of a home-built cw optical parametric oscillator (OPO) being is a modified version of the device presented in the PhD thesis of A. Lenhard [169]. A detailed description of OPOs in general as well as all components and a characterization of those can be found there. All essential components (e.g. cavity mirrors, dichroic mirrors, PPLN crystal) are identical to [169], we solely changed the mechanical design to improve power and frequency stability, and the optical setup since the Ytterbium-doped fiber amplifier (YDFA), which provides the pump light of the OPO, has been replaced by a new model equipped with a different collimator.
The optical setup is illustrated in Fig. B.1. The OPO is pumped by a diode laser at 1081 nm (DL Pro, *Toptica Photonics*). Part of the light is coupled to a single-mode fiber connected to a wavemeter for coarse adjustment of the wavelength. The remaining light is coupled to a fiber-based isolator, which is connected to a YDFA (*LEA Photonics*) providing maximal 15 W output power. The amplified light passes two magnifying telescopes with magnifications of 3 (f_1 =50 mm, f_2 = 150 mm) and 2 (f_1 =75 mm, f_2 =150 mm), and a combination of HWP and PBS for power control. Another lens with $f = 84$ mm couples the pump light to the four-mirror ring cavity arranged in Bow-tie configuration. The heart of the OPO is a 40 mm long temperature-stabilized PPLN crystal with seven poling periods (Λ = 31.7µm ... 32.7µm), which allows for tuning of the idler wavelength from 2310 nm to 2870 nm. The cavity mirrors are mounted on top-adjustable mirror mounts to be able to align the cavity without having to open the housing (see Fig. B.1b). Wavelength tuning of the OPO is achieved by changing the poling period, the crystal temperature, the position of an intra-cavity etalon or the cavity length using a piezo actuator. The output light at 2456 nm is collimated with a spherical AR-coated CaF_2-lens with $f = 125$ mm, separated from the remaining pump light with a DM and guided in free-space to the O-band converter. To monitor the idler wavelength, we measure the pump wavelength and the erroneously generated (non-phasematched) SFG light of the pump and the intra-cavity signal field around 693 nm using a wavemeter.

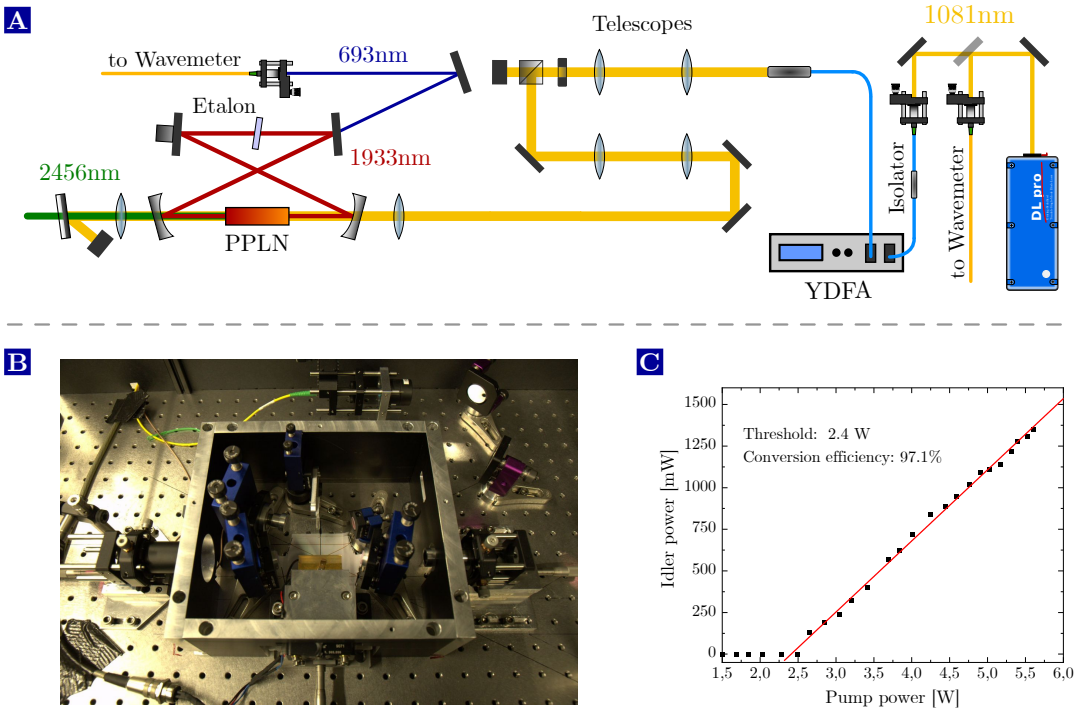

Figure B.1. Setup and output power of the optical parametric oscillator. **(A)** Experimental setup of the OPO to generate laser light at 2456 nm. **(B)** Photograph of the OPO cavity. During operation the OPO is covered by a lid not shown in the figure. **(C)** Idler power versus pump power.

During all experiments in this thesis, the OPO was operated at 2456 nm using a poling period of $\Lambda = 32.6\,\mu\text{m}$ at a crystal temperature of 49°C. A measurement of the idler power in dependence on the pump power is displayed in Fig. B.1c. A stable operation of the OPO in terms of power and idler wavelength is possible until an output power of 1.3 W (measured directly behind the dichroic mirror, this correspond to about 750 mW at the beginning of the QFCD). From a linear fit we extract a laser threshold of 2.4 W and a photon conversion efficiency of 97.1 %, which verifies a proper alignment of the OPO and is consistent with the performance of previous versions of the device.

Appendix C

Density matrices of photon-photon entanglement without background-subtraction

In Fig. C.1 we show the density matrices of the photon-photon entangled states reconstructed from raw data without background subtraction (in contrast to Fig. 3.16 which contains only the background-subtracted matrices). The entangled photons at 854 nm are produced by a SPDC source and frequency-converted in different measurement schemes. The schemes are sketched in the left column of Fig. C.1. In detail, we measured

(I) entanglement between two 854 nm-photons generated directly by the source without QFC with a fidelity of $\mathcal{F} = 76.9(3)\,\%$ and a purity of $\mathcal{P} = 61.9(4)\,\%$.

(II) entanglement between a 854 nm-photon and a frequency-converted photon at 1550 nm with $\mathcal{F} = 78.7(1)\,\%$ and $\mathcal{P} = 65.9(1)\,\%$.

(III) entanglement between a 854 nm-photon and a frequency-converted photon traveled through 20 km of fiber with $\mathcal{F} = 74.0(1)\,\%$ and $\mathcal{P} = 58.2(1)\,\%$.

(IV) entanglement between two 854 nm-photons while the second photon was down-converted to 1550 nm, traveled through 40 km of fiber, and again up-converted to 854 nm in the same QFCD. We achieved $\mathcal{F} = 75.8(3)\,\%$ and $\mathcal{P} = 61.8(4)\,\%$.

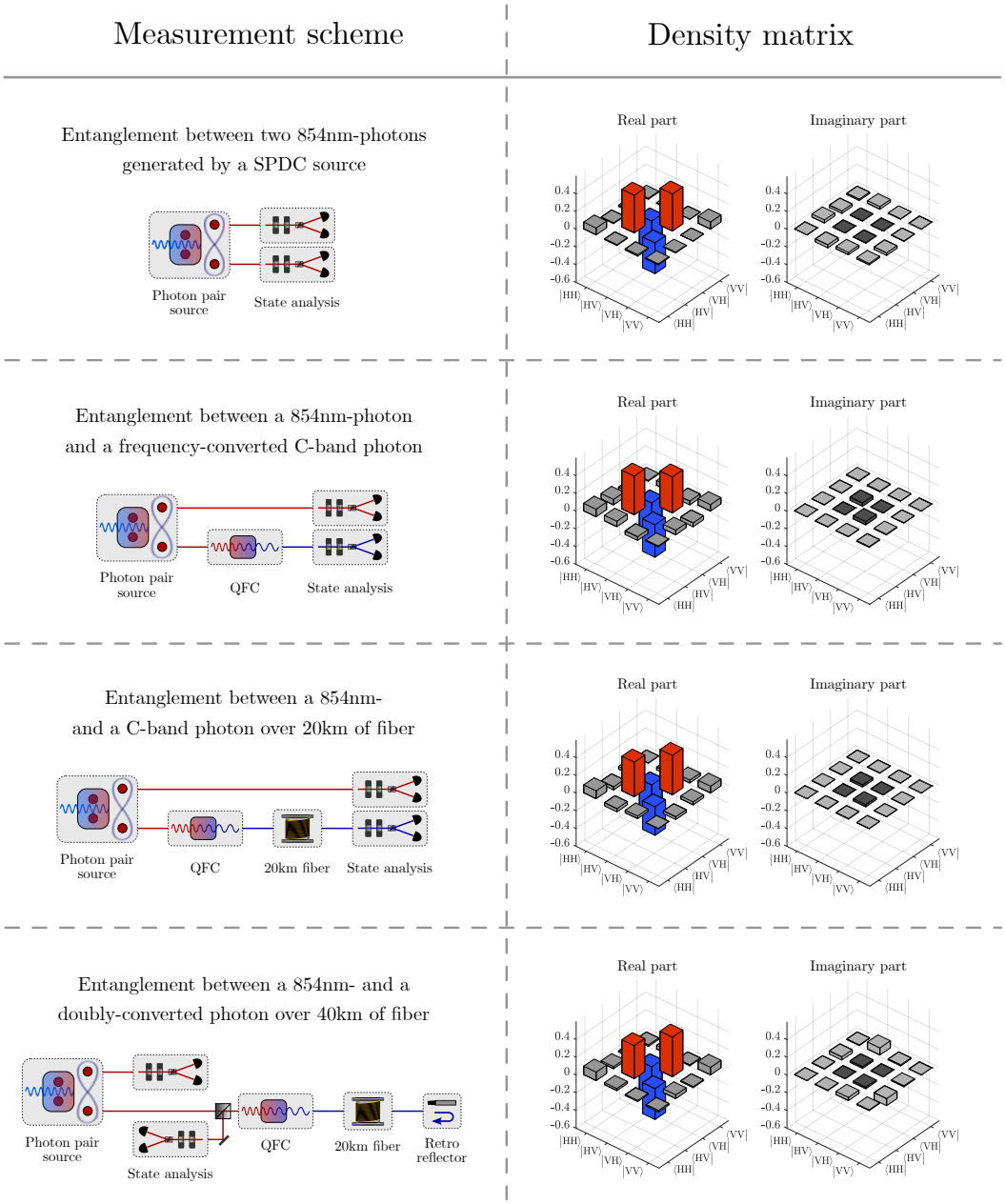

Figure C.1. Preservation of photon-photon entanglement during PPQFC. The measured density matrices for different measurement schemes without background subtraction. All density matrices correspond to Ψ^- Bell-states.

Appendix D

Photographs of the QFC system for Rb-atom wavelengths

Here we show a series of photographs of the QFC system for the Rb-atom quantum network link. As mentioned in Sect. 6.1, it consists of four mobile platforms: the master laser platform, two PPQFCDs and a platform which incorporates the BSM and the spectral filters.

Figure D.1. The master laser platform.

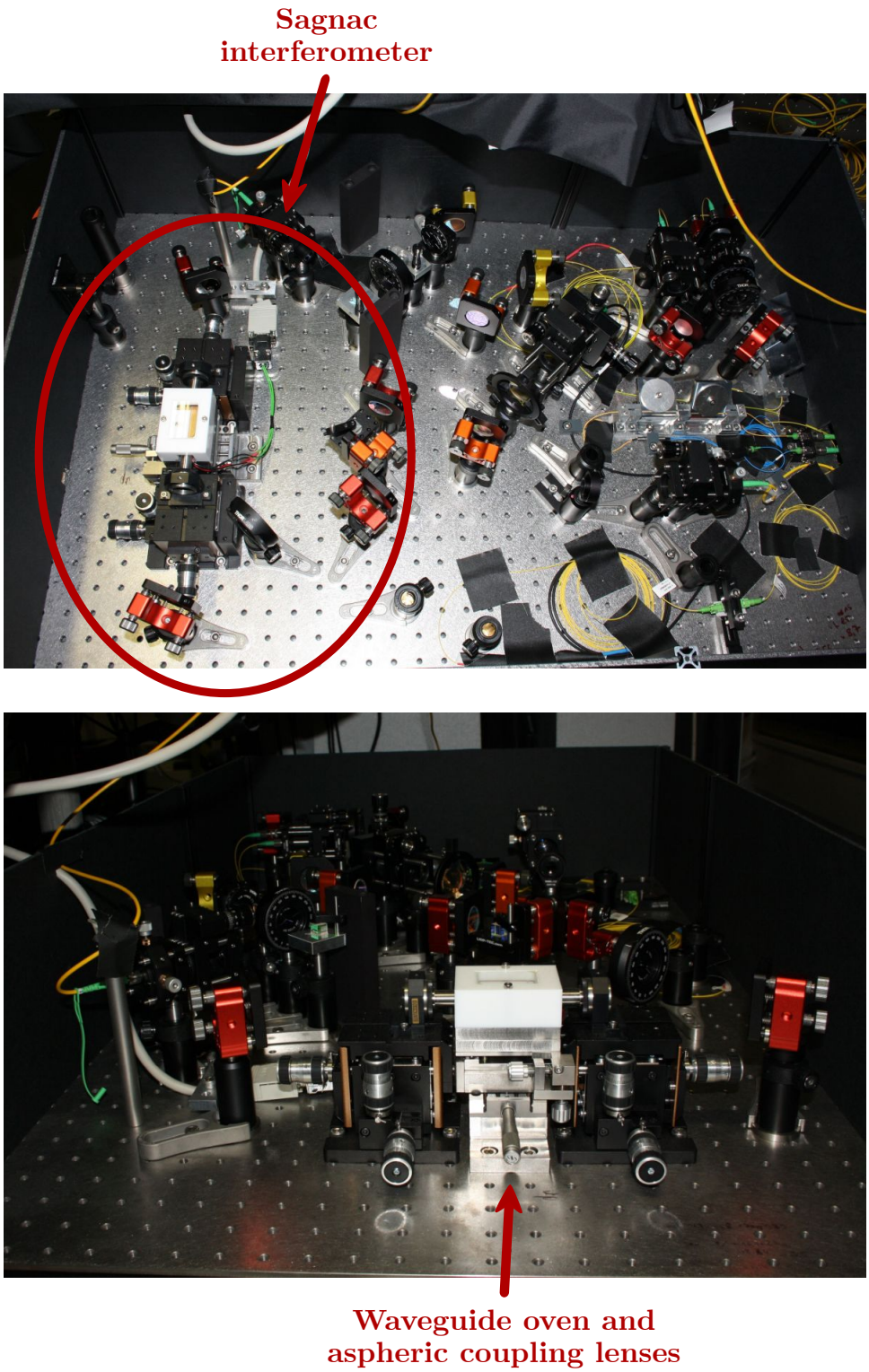

Figure D.2. Sagnac-type polarization-preserving QFCD

Figure D.3. Platform containing the BSM and spectral filtering system.

References

[1] M. A. Nielsen and I. L. Chuang, *Quantum Computation and Quantum Information* (Cambridge University Press, 2010), 7th ed.

[2] D. P. DiVincenzo, "The Physical Implementation of Quantum Computation," Fortschritte der Physik **48**, 771–783 (2000).

[3] J. P. Dowling and G. J. Milburn, "Quantum technology: the second quantum revolution," Philos. Trans. R. Soc. A **361**, 1655–1674 (2003).

[4] A. Acín, I. Bloch, H. Buhrman, T. Calarco, C. Eichler, J. Eisert, D. Esteve, N. Gisin, S. J. Glaser, F. Jelezko, S. Kuhr, M. Lewenstein, M. F. Riedel, P. O. Schmidt, R. Thew, A. Wallraff, I. Walmsley, and F. K. Wilhelm, "The European Quantum Technologies Roadmap," New J. Phys. **20**, 080201 (2018).

[5] M. F. Riedel, D. Binosi, R. Thew, and T. Calarco, "The European quantum technologies flagship programme," Quantum Sci. Technol. **2**, 030501 (2017).

[6] Y. Alexeev, D. Bacon, K. R. Brown, R. Calderbank, L. D. Carr, F. T. Chong, B. DeMarco, D. Englund, E. Farhi, B. Feerman, A. V. Gorshkov, A. Houck, J. Kim, S. Kimmel, M. Lange, S. Lloyd, M. D. Lukin, D. Maslov, P. Maunz, C. Monroe, J. Preskill, M. Roetteler, M. J. Savage, and J. Thompson, "Quantum Computer Systems for Scientic Discovery," arXiv:1912.07577 (2019).

[7] P. W. Shor, "Polynomial-time algorithms for prime factorization and discrete logarithms on a quantum computer," SIAM J. Comput. **26**, 1484–1509 (1997).

[8] L. K. Grover, "A fast quantum mechanical algorithm for database search," 28th Annual ACM Symposium on the Theory of Computing pp. 212–219 (1996).

[9] F. Arute, K. Arya, R. Babbush, D. Bacon, J. C. Bardin, R. Barends, R. Biswas, S. Boixo, F. G. S. L. Brandao, D. A. Buell, B. Burkett, Y. Chen, Z. Chen, B. Chiaro, R. Collins, W. Courtney, A. Dunsworth, E. Farhi, B. Foxen, A. Fowler, C. Gidney, M. Giustina, R. Graff, K. Guerin, S. Habegger, M. P. Harrigan, M. J. Hartmann, A. Ho, M. Hoffmann, T. Huang, T. S. Humble, S. V. Isakov, E. Jeffrey, Z. Jiang, D. Kafri, K. Kechedzhi, J. Kelly, P. V. Klimov, S. Knysh, A. Korotkov, F. Kostritsa, D. Landhuis, M. Lindmark, E. Lucero, D. Lyakh, S. Mandra, J. R. McClean, M. McEwen, A. Megrant, X. Mi, K. Michielsen, M. Mohseni, J. Mutus,

O. Naaman, M. Neeley, C. Neill, M. Y. Niu, E. Ostby, A. Petukhov, J. C. Platt, C. Quintana, E. G. Rieffel, P. Roushan, N. C. Rubin, D. Sank, K. J. Satzinger, V. Smelyanskiy, K. J. Sung, M. D. Trevithick, A. Vainsencher, B. Villalonga, T. White, Z. J. Yao, P. Yeh, A. Zalcman, H. Neven, and J. M. Martinis, "Quantum supremacy using a programmable superconducting processor," Nature **574**, 505–510 (2019).

[10] M. H. Devoret and R. J. Schoelkopf, "Superconducting Circuits for Quantum Information: An Outlook," Science **339**, 1169–1174 (2013).

[11] P. Schindler, D. Nigg, T. Monz, J. T. Barreiro, E. Martinez, S. X. Wang, S. Quint, M. F. Brandl, V. Nebendahl, C. F. Roos, M. Chwalla, M. Hennrich, and R. Blatt, "A quantum information processor with trapped ions," New J. Phys. **15**, 123012 (2013).

[12] D. Kielpinski, C. Monroe, and D. Wineland, "Architecture for a large-scale ion-trap quantum computer," Nature **417**, 709–711 (2002).

[13] R. P. Feynman, "Simulating physics with computers," Int. J. Theor. Phys. **21**, 467–488 (1982).

[14] J. I. Cirac and P. Zoller, "Goals and opportunities in quantum simulation," Nat. Phys. **8**, 264–266 (2012).

[15] A. Aspuru-Guzik, A. D. Dutoi, P. J. Love, and M. Head-Gordon, "Simulated Quantum Computation of Molecular Energies," Science **309**, 1704–1707 (2005).

[16] R. Blatt and C. F. Roos, "Quantum simulations with trapped ions," Nat. Phys. **8**, 277–284 (2012).

[17] C. Gross and I. Bloch, "Quantum simulations with ultracold atoms in optical lattices," Science **357**, 995–1001 (2017).

[18] H. Bernien, S. Schwartz, A. Keesling, H. Levine, A. Omran, H. Pichler, S. Choi, A. S. Zibrov, M. Endres, M. Greiner, V. Vuletić, and M. D. Lukin, "Probing many-body dynamics on a 51-atom quantum simulator," Nature **551**, 579–584 (2017).

[19] A. Aspuru-Guzik and P. Walther, "Photonic quantum simulators," Nat. Phys. **8**, 285–291 (2012).

[20] A. D. Ludlow, M. M. Boyd, J. Ye, E. Peik, and P. O. Schmidt, "Optical atomic clocks," Rev. Mod. Phys. **87**, 637 (2014).

[21] S. S. Y. Chua, B. J. J. Slagmolen, D. A. Shaddock, and D. E. McClelland, "Quantum squeezed light in gravitational-wave detectors," Class. Quantum Grav. **31**, 183001 (2014).

[22] L. Pezzè, A. Smerzi, M. K. Oberthaler, R. Schmied, and P. Treutlein, "Quantum metrology with nonclassical states of atomic ensembles," Rev. Mod. Phys. **90**, 035005 (2018).

[23] T. Nagata, R. Okamoto, J. L. O'Brien, K. Sasaki, and S. Takeuchi, "Beating the Standard Quantum Limit with Four-Entangled Photons," Science **316**, 726–729 (2007).

[24] G. Balasubramanian, I. Y. Chan, R. Kolesov, M. Al-Hmoud, J. Tisler, C. Shin, C. Kim, A. Wojcik, P. R. Hemmer, A. Krueger, T. Hanke, A. Leitenstorfer, R. Bratschitsch, F. Jelezko, and J. Wrachtrup, "Nanoscale imaging magnetometry with diamond spins under ambient conditions," Nature **455**, 648–651 (2008).

[25] P. Maletinsky, S. Hong, M. S. Grinolds, B. Hausmann, M. D. Lukin, R. L. Walsworth, M. Loncar, and A. Yacoby, "A robust scanning diamond sensor for nanoscale imaging with single nitrogen-vacancy centres," Nat. Nanotechnol. **7**, 320–324 (2012).

[26] N. Gisin, G. Ribordy, W. Tittel, and H. Zbinden, "Quantum Cryptography," Rev. Mod. Phys. **74**, 145–195 (2002).

[27] F. Xu, X. Ma, Q. Zhang, H.-K. Lo, and J.-W. Pan, "Secure quantum key distribution with realistic devices," Rev. Mod. Phys. **92**, 025002 (2020).

[28] S. Pirandola, U. L. Andersen, L. Banchi, M. Berta, D. Bunandar, R. Colbeck, D. Englund, T. Gehring, C. Lupo, C. Ottaviani, J. Pereira, M. Razavi, J. S. Shaari, M. Tomamichel, V. C. Usenko, G. Vallone, P. Villoresi, and P. Wallden, "Advances in Quantum Cryptography," arXiv:1906.01645 (2019).

[29] H. J. Kimble, "The Quantum Internet," Nature **453**, 1023–1030 (2008).

[30] S. Wehner, D. Elkouss, and R. Hanson, "Quantum internet: A vision for the road ahead," Science **362**, eaam9288 (2018).

[31] https://qutech.nl/2018/10/18/qutech-researchers-put-forward-a-roadmap-for-quantum-internet development/.

[32] A. K. Ekert, "Quantum cryptography based on Bell's theorem," Phys. Rev. Lett. **67**, 661 (1991).

[33] R. Ursin, F. Tiefenbacher, T. Schmitt-Manderbach, H. Weier, T. Scheidl, M. Lindenthal, B. Blauensteiner, T. Jennewein, J. Perdigues, P. Trojek, B. Ömer, M. Fürst, M. Meyenburg, J. Rarity, Z. Sodnik, C. Barbieri, H. Weinfurter, and A. Zeilinger, "Entanglement-based quantum communication over 144 km," Nat. Phys. **3**, 481–486 (2007).

[34] T. Honjo, S. W. Nam, H. Takesue, Q. Zhang, H. Kamada, Y. Nishida, O.Tadanaga, M. Asobe, B. Baek, R. Hadfield, S. Miki, M. Fujiwara, M. Sasaki, Z.Wang, K. Inoue, and Y. Yamamoto, "Long-distance entanglement-based quantum key distribution over optical fiber," Opt. Express **16**, 19118–19126 (2008).

[35] J. Yin, Y.-H. Li, S.-K. Liao, M. Yang, Y. Cao, L. Zhang, J.-G. Ren, W.-Q. Cai, W.-Y. Liu, S.-L. Li, R. Shu, Y.-M. Huang, L. Deng, L. Li, Q. Zhang, N.-L. Liu, Y.-A. Chen, C.-Y. Lu, X.-B. Wang, F. Xu, J.-Y. Wang, C.-Z. Peng, A. K. Ekert, and J.-W. Pan, "Entanglement-based secure quantum cryptography over 1,120 kilometres," Nature **582**, 501–505 (2020).

[36] A. Acín, N. Brunner, N. Gisin, S. Massar, S. Pironio, and V. Scarani, "Device-Independent Security of Quantum Cryptography against Collective Attacks," Phys. Rev. Lett. **98**, 230501 (2007).

[37] U. Vazirani and T. Vidick, "Fully Device-Independent Quantum Key Distribution," Phys. Rev. Lett. **113**, 140501 (2014).

[38] G. Murta, S. B. van Dam, J. Ribeiro, R. Hanson, and S. Wehner, "Towards a realization of device-independent quantum key distribution," Quantum Sci. Technol. **4**, 035011 (2019).

[39] N. H. Nickerson, J. F. Fitzsimons, and S. C. Benjamin, "Freely Scalable Quantum Technologies Using Cells of 5-to-50 Qubits with Very Lossy and Noisy Photonic Links," Phys. Rev. X **4**, 041041 (2014).

[40] D. Cuomo, M. Caleffi, and A. S. Cacciapuoti, "Towards a Distributed Quantum Computing Ecosystem," IET Quant. Commun. **1**, 3–8 (2020).

[41] A. Broadbent, J. Fitzsimons, and E. Kashefi, "Universal blind quantum computation," in "2009 50th Annual IEEE Symposium on Foundations of Computer Science," (2009), pp. 517–526.

[42] S. Barz, E. Kashefi, A. Broadbent, J. F. Fitzsimons, A. Zeilinger, and P. Walther, "Demonstration of Blind Quantum Computing," Science **335**, 303–308 (2012).

[43] J. F. Fitzsimons, "Private quantum computation: an introduction to blindquantum computing and related protocols," NPJ Quantum Inf. **3**, 23 (2017).

[44] P. Kómár, E. M. Kessler, M. Bishof, L. Jiang, A. S. Sørensen, J. Ye, and M. D. Lukin, "A quantum network of clocks," Nat. Phys. **10**, 582–587 (2014).

[45] P. Kómár, T. Topcu, E. M. Kessler, A. Derevianko, V. Vuletić, J. Ye, and M. D. Lukin, "Quantum Network of Atom Clocks: A Possible Implementation with Neutral Atoms," Phys. Rev. Lett. **117**, 060506 (2016).

[46] E. T. Khabiboulline, J. Borregaard, K. D. Greve, and M. D. Lukin, "Optical Interferometry with Quantum Networks," Phys. Rev. Lett. **123**, 070504 (2019).

[47] E. T. Khabiboulline, J. Borregaard, K. D. Greve, and M. D. Lukin, "Quantum-assisted telescope arrays," Phys. Rev. A **100**, 022316 (2019).

[48] M. Takeoka, S. Guha, and M. M. Wilde, "Fundamental rate-loss tradeoff for optical quantum key distribution," Nat. Commun. **5**, 5235 (2014).

[49] S. Pirandola, R. Laurenza, C. Ottaviani, and L. Banchi, "Fundamental limits of repeaterless quantum communications," Nat. Commun. **8**, 15043 (2017).

[50] M. Lucamarini, Z. L. Yuan, J. F. Dynes, and A. J. Shields, "Overcoming the rate–distance limit of quantum key distribution without quantum repeaters," Nature **557**, 400–403 (2018).

[51] J. Yin, Y. Cao, Y.-H. Li, S.-K. Liao, L. Zhang, J.-G. Ren, W.-Q. Cai, W.-Y. Liu, B. Li, H. Dai, G.-B. Li, Q.-M. Lu, Y.-H. Gong, Y. Xu, S.-L. Li, F.-Z. Li, Y.-Y. Yin, Z.-Q. Jiang, M. Li, J.-J. Jia, G. Ren, D. He, Y.-L. Zhou, X.-X. Zhang, N. Wang, X. Chang, Z.-C. Zhu, N.-L. Liu, Y.-A. Chen, C.-Y. Lu, R. Shu, C.-Z. Peng, J.-Y. Wang, and J.-W. Pan, "Satellite-based entanglement distribution over 1200 kilometers," Science **356**, 1140–1144 (2017).

[52] W. K. Wootters and W. H. Zurek, "A single quantum cannot be cloned," Nature **299**, 802–803 (1982).

[53] H.-J. Briegel, W. Dür, J. I. Cirac, and P. Zoller, "Quantum Repeaters: The Role of Imperfect Local Operations in Quantum Communication," Phys. Rev. Lett. **81**, 5932–5935 (1998).

[54] N. Sangouard, C. Simon, H. de Riedmatten, and N. Gisin, "Quantum repeaters based on atomic ensembles and linear optics," Rev. Mod. Phys. **83**, 33–80 (2011).

[55] D. Bouwmeester, J.-W. Pan, K. Mattle, M. Eibl, H. Weinfurter, and A. Zeilinger, "Experimental quantum teleportation," Nature **390**, 575–579 (1997).

[56] M. Żukowski, A. Zeilinger, M. A. Horne, and A. K. Ekert, "Event-ready-detectors Bell experiment via entanglement swapping," Phys. Rev. Lett. **71**, 4287 (1993).

[57] J.-W. Pan, D. Bouwmeester, H. Weinfurter, and A. Zeilinger, "Experimental Entanglement Swapping: Entangling Photons That Never Interacted," Phys. Rev. Lett. **80**, 3891 (1998).

[58] B. B. Blinov, D. L. Moehring, L.-M. Duan, and C. Monroe, "Observation of entanglement between a single trapped atom and a single photon," Nature **428**, 153–157 (2004).

[59] A. Stute, B. Casabone, P. Schindler, T. Monz, P. O. Schmidt, B. Brandstätter, T. E. Northup, and R. Blatt, "Tunable ion–photon entanglement in an optical cavity," Nature **485**, 482–485 (2012).

[60] D. L. Moehring, P. Maunz, S. Olmschenk, K. C. Younge, D. N. Matsukevich, L.-M. Duan, and C. Monroe, "Entanglement of single-atom quantum bits at a distance," Nature **449**, 68–71 (2007).

[61] D. Hucul, I. V. Inlek, G. Vittorini, C. Crocker, S. Debnath, S. M. Clark, and C. Monroe, "Modular entanglement of atomic qubits using photons and phonons," Nat. Phys. **11**, 37–42 (2015).

[62] J. Volz, M. Weber, D. Schlenk, W. Rosenfeld, J. Vrana, K. Saucke, C. Kurtsiefer, and H. Weinfurter, "Observation of Entanglement of a Single Photon with a Trapped Atom," Phys. Rev. Lett. **96**, 030404 (2006).

[63] T. Wilk, S. C. Webster, A. Kuhn, and G. Rempe, "Single-Atom Single-Photon Quantum Interface," Science **317**, 488–490 (2007).

[64] J. Hofmann, M. Krug, N. Ortegel, L. Gérard, M. Weber, W. Rosenfeld, and H. Weinfurter, "Heralded Entanglement Between Widely Separated Atoms," Science **337**, 72–75 (2012).

[65] S. Ritter, C. Nölleke, C. Hahn, A. Reiserer, A. Neuzner, M. Uphoff, M. Mücke, E. Figueroa, J. Bochmann, and G. Rempe, "An elementary quantum network of single atoms in optical cavities," Nature **484**, 195–200 (2012).

[66] E. Togan, Y. Chu, A. S. Trifonov, L. Jiang, J. Maze, L. Childress, M. V. G. Dutt, A. S. Sørensen, P. R. Hemmer, A. S. Zibrov, and M. D. Lukin, "Quantum entanglement between an optical photon and a solid-state spin qubit," Nature **466**, 730–734 (2010).

[67] H. Bernien, B. Hensen, W. Pfaff, G. Koolstra, M. S. Blok, L. Robledo, T. H. Taminiau, M. Markham, D. J. Twitchen, L. Childress, and R. Hanson, "Heralded entanglement between solid-state qubits separated by three metres," Nature **497**, 86–90 (2013).

[68] B. Hensen, H. Bernien, A. E. Dréau, A. Reiserer, N. Kalb, M. S. Blok, J. Ruitenberg, R. F. L. Vermeulen, R. N. Schouten, C. Abellán, W. Amaya, V. Pruneri, M. W. Mitchell, M. Markham, D. J. Twitchen, D. Elkouss, S. Wehner, T. H. Taminiau, and R. Hanson, "Loophole-free Bell inequality violation using electron spins separated by 1.3 kilometres," Nature **526**, 682–686 (2015).

[69] P. C. Humphreys, N. Kalb, J. P. J. Morits, R. N. Schouten, R. F. L. Vermeulen, D. J. Twitchen, M. Markham, and R. Hanson, "Deterministic delivery of remote entanglement on a quantum network," Nature **558**, 268–273 (2018).

[70] C. T. Nguyen, D. D. Sukachev, M. K. Bhaskar, B. Machielse, D. S. Levonian, E. N. Knall, P. Stroganov, R. Riedinger, H. Park, M. Lončar, and M. D. Lukin, "Quantum Network Nodes Based on Diamond Qubits with an Efficient Nanophotonic Interface," Phys. Rev. Lett. **123**, 183602 (2019).

[71] M. K. Bhaskar, R. Riedinger, B. Machielse, D. S. Levonian, C. T. Nguyen, E. N. Knall, H. Park, D. Englund, M. Lončar, D. D. Sukachev, and M. D. Lukin, "Experimental demonstration of memory-enhanced quantum communication," Nature **580**, 60–64 (2020).

[72] K. D. Greve, L. Yu, P. L. McMahon, J. S. Pelc, C. M. Natarajan, N. Y. Kim, E. Abe, S. Maier, C. Schneider, M. Kamp, S. Höfling, R. H. Hadfield, A. Forchel, M. M. Fejer, and Y. Yamamoto, "Quantum-dot spin-photon entanglement via frequency downconversion to telecom wavelength," Nature **491**, 421–425 (2012).

[73] W. B. Gao, P. Fallahi, E. Togan, J. Miguel-Sanchez, and A. Imamoglu, "Observation of entanglement between a quantum dot spin and a single photon," Nature **491**, 426–430 (2012).

[74] A. Delteil, Z. Sun, W. B. Gao, E. Togan, S. Faelt, and A. Imamoğlu, "Generation of heralded entanglement between distant hole spins," Nat. Phys. **12**, 218–223 (2016).

[75] R. Stockill, M. J. Stanley, L. Huthmacher, E. Clarke, M. Hugues, A. J. Miller, C. Matthiesen, C. L. Gall, and M. Atatüre, "Phase-Tuned Entangled State Generation between Distant Spin Qubits," Phys. Rev. Lett. **119**, 010503 (2017).

[76] L.-M. Duan, M. D. Lukin, J. I. Cirac, and P. Zoller, "Long-distance quantum communication with atomic ensembles and linear optics," Nature **414**, 413–418 (2001).

[77] A. Seri, A. Lenhard, D. Rieländer, M. Gündoğan, P. M. Ledingham, M. Mazzera, and H. de Riedmatten, "Quantum Correlations between Single Telecom Photons and a Multimode On-Demand Solid-State Quantum Memory," Phys. Rev. X **7**, 021028 (2017).

[78] N. Sinclair, E. Saglamyurek, H. Mallahzadeh, J. A. Slater, M. George, R. Ricken, M. P. Hedges, D. Oblak, C. Simon, W. Sohler, and W. Tittel, "Spectral Multiplexing for Scalable Quantum Photonics using an Atomic Frequency Comb Quantum Memory and Feed-Forward Control," Phys. Rev. Lett. **113**, 053603 (2014).

[79] Y.-F. Pu, N. Jiang, W. Chang, H.-X. Yang, C. Li, and L.-M. Duan, "Experimental realization of a multiplexed quantum memory with 225 individually accessible memory cells," Nat. Commun. **8**, 15359 (2017).

[80] C. W. Chou, H. de Riedmatten, D. Felinto, S. V. Polyakov, S. J. van Enk, and H. J. Kimble, "Measurement-induced entanglement for excitation stored in remote atomic ensembles," Nature **438**, 828–832 (2005).

[81] Z.-S. Yuan, Y.-A. Chen, B. Zhao, S. Chen, J. Schmiedmayer, and J.-W. Pan, "Experimental demonstration of a BDCZ quantum repeater node," Nature **454**, 1098–1101 (2008).

[82] Y. Yu, F. Ma, X.-Y. Luo, B. Jing, P.-F. Sun, R.-Z. Fang, C.-W. Yang, H. Liu, M.-Y. Zheng, X.-P. Xie, W.-J. Zhang, L.-X. You, Z. Wang, T.-Y. Chen, Q. Zhang, X.-H. Bao, and J.-W. Pan, "Entanglement of two quantum memories via fibres over dozens of kilometres," Nature **578**, 240–245 (2020).

[83] B. Jing, X.-J. Wang, Y. Yu, P.-F. Sun, Y. Jiang, S.-J. Yang, W.-H. Jiang, X.-Y. Luo, J. Zhang, X. Jiang, X.-H. Bao, and J.-W. Pan, "Entanglement of three quantum memories via interference of three single photons," Nat. Photon. **13**, 210–213 (2019).

[84] K. Kutluer, M. Mazzera, and H. de Riedmatten, "Solid-State Source of Nonclassical Photon Pairs with Embedded Multimode Quantum Memory," Phys. Rev. Lett. **118**, 210502 (2017).

[85] C. Laplane, P. Jobez, J. Etesse, N. Gisin, and M. Afzelius, "Multimode and Long-Lived Quantum Correlations Between Photons and Spins in a Crystal," Phys. Rev. Lett. **118**, 210501 (2017).

[86] M. G. Puigibert, M. F. Askarani, J. H. Davidson, V. B. Verma, M. D. Shaw, S. W. Nam, T. Lutz, G. C. Amaral, D. Oblak, and W. Tittel, "Entanglement and nonlocality between disparate solid-state quantum memories mediated by photons," Phys. Rev. Research **2**, 013039 (2020).

[87] C. Kurz, P. Eich, M. Schug, P. Müller, and J. Eschner, "Programmable atom-photon quantum interface," Phys. Rev. A **93**, 062348 (2016).

[88] C. Kurz, M. Schug, P. Eich, J. Huwer, P. Müller, and J. Eschner, "Experimental protocol for high-fidelity heralded photon-to-atom quantum state transfer," Nat. Commun. **5**, 5527 (2014).

[89] L. J. Stephenson, D. P. Nadlinger, B. C. Nichol, S. An, P. Drmota, T. G. Ballance, K. Thirumalai, J. F. Goodwin, D. M. Lucas, and C. J. Ballance, "High-Rate, High-Fidelity Entanglement of Qubits Acrossan Elementary Quantum Network," Phys. Rev. Lett. **124**, 110501 (2020).

[90] V. Krutyanskiy, M. Meraner, J. Schupp, V. Krcmarsky, H. Hainzer, and B. P. Lanyon, "Light-matter entanglement over 50 km of optical fibre," NPJ Quantum Inf. **5**, 72 (2019).

[91] S. Begley, M. Vogt, G. K. Gulati, H. Takahashi, and M. Keller, "Optimized Multi-Ion Cavity Coupling," Phys. Rev. Lett. **116**, 223001 (2016).

[92] Y. Wang, M. Um, J. Zhang, S. An, M. Lyu, J.-N. Zhang, L.-M. Duan, D. Yum, and K. Kim, "Single-qubit quantum memory exceeding ten-minute coherence time," Nat. Photon. **11**, 646–650 (2017).

[93] C. Langer, R. Ozeri, J. D. Jost, J. Chiaverini, B. DeMarco, A. Ben-Kish, R. B. Blakestad, J. Britton, D. B. Hume, W. M. Itano, D. Leibfried, R. Reichle, T. Rosenband, T. Schaetz, P. O. Schmidt, and D. J. Wineland, "Long-Lived Qubit Memory Using Atomic Ions," Phys. Rev. Lett. **95**, 060502 (2005).

[94] T. Ruster, C. T. Schmiegelow, H. Kaufmann, C. Warschburger, F. Schmidt-Kaler, and U. G. Poschinger, "A long-lived Zeeman trapped-ion qubit," Appl. Phys. B **122**, 254 (2016).

[95] P. Wang, C.-Y. Luan, M. Qiao, M. Um, J. Zhang, Y. Wang, X. Yuan, M. Gu, J. Zhang, and K. Kim, "Single ion-qubit exceeding one hour coherence time," arXiv:2008.00251 (2020).

[96] C. J. Ballance, T. P. Harty, N. M. Linke, M. A. Sepiol, and D. M. Lucas, "High-Fidelity Quantum Logic Gates Using Trapped-Ion Hyperfine Qubits," Phys. Rev. Lett. **117**, 060504 (2016).

[97] J. P. Gaebler, T. R. Tan, Y. Lin, Y. Wan, R. Bowler, A. C. Keith, S. Glancy, K. Coakley, E. Knill, D. Leibfried, and D. J. Wineland, "High-Fidelity Universal Gate Set for $^{9}Be^{+}$ Ion Qubits," Phys. Rev. Lett. **117**, 060505 (2016).

[98] A. Erhard, J. J. Wallman, L. Postler, M. Meth, R. Stricker, E. A. Martinez, P. Schindler, T. Monz, J. Emerson, and R. Blatt, "Characterizing large-scale quantum computers via cycle benchmarking," Nat. Commun. **10**, 5347 (2019).

[99] A. C. Hughes, V. M. Schäfer, K. Thirumalai, D. P. Nadlinger, S. R. Woodrow, D. M. Lucas, and C. J. Ballance, "Benchmarking a high-fidelity mixed-species entangling gate," Phys. Rev. Lett. **125**, 080504 (2020).

[100] N. Kalb, A. A. Reiserer, P. C. Humphreys, J. J. W. Bakermans, S. J. Kamerling, N. H. Nickerson, S. C. Benjamin, D. J. Twitchen, M. Markham, and R. Hanson, "Entanglement distillation between solid-state quantum network nodes," Science **356**, 928–932 (2017).

[101] M. Zwerger, B. P. Lanyon, T. E. Northup, C. A. Muschik, W. Dür, and N. Sangouard, "Quantum repeaters based on trapped ions with decoherence-free subspace encoding," Quantum Sci. Technol. **2**, 044001 (2017).

[102] I. V. Inlek, C. Crocker, M. Lichtman, K. Sosnova, and C. Monroe, "Multispecies Trapped-Ion Node for Quantum Networking," Phys. Rev. Lett. **118**, 250502 (2017).

[103] A. Reiserer and G. Rempe, "Cavity-based quantum networks with single atoms and optical photons," Rev. Mod. Phys. **87**, 1379–1418 (2015).

[104] A. Reiserer, C. Nölleke, S. Ritter, and G. Rempe, "Ground-State Cooling of a Single Atom at the Center of an Optical Cavity," Phys. Rev. Lett. **110**, 223003 (2013).

[105] A. Reiserer, N. Kalb, G.Rempe, and S. Ritter, "A quantum gate between a flying optical photon and a single trapped atom," Nature **504**, 237–240 (2014).

[106] P. Samutpraphoot, T. Dordević, P. L. Ocola, H. Bernien, C. Senko, V. Vuletić, and M. D. Lukin, "Strong Coupling of Two Individually Controlled Atoms via a Nanophotonic Cavity," Phys. Rev. Lett. **124**, 063602 (2020).

[107] S. Welte, B. Hacker, S. Daiss, S. Ritter, and G. Rempe, "Photon-Mediated Quantum Gate between Two Neutral Atoms in an Optical Cavity," Phys. Rev. X **8**, 011018 (2018).

[108] K. M. Maller, M. T. Lichtman, T. Xia, Y. Sun, M. J. Piotrowicz, A. W. Carr, L. Isenhower, and M. Saffman, "Rydberg-blockade controlled-NOT gate and entanglement in a two-dimensional array of neutral-atom qubits," Phys. Rev. A **92**, 022336 (2015).

[109] H. Levine, A. Keesling, A. Omran, H. Bernien, S. Schwartz, A. S. Zibrov, M. Endres, M. Greiner, V. Vuletić, and M. D. Lukin, "High-Fidelity Control and Entanglement of Rydberg-Atom Qubits," Phys. Rev. Lett. **121**, 123603 (2018).

[110] I. S. Madjarov, J. P. Covey, A. L. Shaw, J. Choi, A. Kale, A. Cooper, H. Pichler, V. Schkolnik, J. R. Williams, and M. Endres, "High-fidelity entanglement and detection of alkaline-earth Rydberg atoms," Nat. Phys. **16**, 857–861 (2020).

[111] "Corning, SMF-28 ULL Optical Fiber, Datasheet (2020)," .

[112] W. Rosenfeld, D. Burchardt, R. Garthoff, K. Redeker, N. Ortegel, M. Rau, and H. Weinfurter, "Event-Ready Bell Test Using Entangled Atoms Simultaneously Closing Detection and Locality Loopholes," Phys. Rev. Lett. **119**, 010402 (2017).

[113] E. Saglamyurek, J. Jin, V. B. Verma, M. D. Shaw, F. Marsili, S. W. Nam, D. Oblak, and W. Tittel, "Quantum storage of entangled telecom-wavelength photons in an erbium-doped optical fibre," Nat. Photon. **9**, 83–87 (2015).

[114] M. F. Askarani, M. G. Puigibert, T. Lutz, V. B. Verma, M. D. Shaw, S. W. Nam, N. Sinclair, D. Oblak, and W. Tittel, "Storage and Reemission of Heralded Telecommunication-Wavelength Photons Using a Crystal Waveguide," Phys. Rev. Appl. **11**, 054056 (2019).

[115] I. Craiciu, M. Lei, J. Rochman, J. M. Kindem, J. G. Bartholomew, E. Miyazono, T. Zhong, N. Sinclair, and A. Faraon, "Nanophotonic Quantum Storage at Telecommunication Wavelength," Phys. Rev. Appl. **12**, 024062 (2019).

[116] A. M. Dibos, M. Raha, C. M. Phenicie, and J. D. Thompson, "Atomic Source of Single Photons in the Telecom Band," Phys. Rev. Lett. **120**, 243601 (2018).

[117] M. Raha, S. Chen, C. M. Phenicie, S. Ourari, A. M. Dibos, and J. D. Thompson, "Optical quantum nondemolition measurement of a single rare earth ion qubit," Nat. Commun. **11**, 1605 (2020).

[118] B. Merkel, A. Ulanowski, and A. Reiserer, "Coherent and Purcell-Enhanced Emission from Erbium Dopants in a Cryogenic High-Q Resonator," Phys. Rev. X **10**, 041025 (2020).

[119] B. Casabone, C. Deshmukh, S. Liu, D. Serrano, A. Ferrier, T. Hümmer, P. Goldner, D. Hunger, and H. de Riedmatten, "Dynamic control of Purcell enhanced emission of erbium ions in nanoparticles," arXiv:2001.08532 (2020).

[120] M. Uphoff, M. Brekenfeld, G. Rempe, and S. Ritter, "An integrated quantum repeater at telecom wavelength with single atoms in optical fiber cavities," Appl. Phys. B **122**, 46 (2016).

[121] Y. O. Dudin, A. G. Radnaev, R. Zhao, J. Z. Blumoff, T. A. B. Kennedy, and A. Kuzmich, "Entanglement of Light-Shift Compensated Atomic Spin Waves with Telecom Light," Phys. Rev. Lett. **105**, 260502 (2010).

[122] A. G. Radnaev, Y. O. Dudin, R. Zhao, H. H. Jen, S. D. Jenkins, A. Kuzmich, and T. A. B. Kennedy, "A quantum memory with telecom-wavelength conversion," Nat. Phys. **6**, 894–899 (2010).

[123] M. Benyoucef, M. Yacob, J. P. Reithmaier, J. Kettler, and P. Michler, "Telecom-wavelength (1.5 µm) single-photon emission from InP-based quantum dots," Appl. Phys. Lett. **103**, 162101 (2013).

[124] M. Anderson, T. Müller, J. Huwer, J. Skiba-Szymanska, A. B. Krysa, R. M. Stevenson, J. Heffernan, D. A. Ritchie, and A. J. Shields, "Quantum teleportation using highly coherent emission from telecom C-band quantum dots," NPJ Quantum Inf. **6**, 14 (2020).

[125] D. M. Lukin, M. A. Guidry, and J. Vučković, "Integrated quantum photonics with silicon carbide: challenges and prospects," arXiv:2010.15700 (2020).

[126] E. Saglamyurek, N. Sinclair, J. Jin, J. A. Slater, D. Oblak, F. Bussières, M. George, R. Ricken, W. Sohler, and W. Tittel, "Broadband waveguide quantum memory for entangled photons," Nature **469**, 512–515 (2011).

[127] J. Fekete, D. Rieländer, M. Cristiani, and H. de Riedmatten, "Ultranarrow-Band Photon-Pair Source Compatible with Solid State Quantum Memories and Telecommunication Networks," Phys. Rev. Lett. **110**, 220502 (2013).

[128] F. Bussières, C. Clausen, A. Tiranov, B. Korzh, V. B. Verma, S. W. Nam, F. Marsili, A. Ferrier, P. Goldner, H. Herrmann, C. Silberhorn, W. Sohler, M. Afzelius, and N. Gisin, "Quantum teleportation from a telecom-wavelength photon to a solid-state quantum memory," Nat. Photon. **8**, 775–778 (2014).

[129] A. Lenhard, M. Bock, J. Brito, S. Kucera, P. Eich, P. Müller, J. Eschner, and C. Becher, "Telecom-heralded single-photon absorption by a single atom," Phys. Rev. A **92**, 063827 (2015).

[130] M. Förtsch, J. U. Fürst, C. Wittmann, D. Strekalov, A. Aiello, M. V. Chekhova, C. Silberhorn, G. Leuchs, and C. Marquardt, "A versatile source of single photons for quantum information processing," Nat. Commun. **4**, 1818 (2013).

[131] N. Piro, F. Rohde, C. Schuck, M. Almendros, J. Huwer, J. Ghosh, A. Haase, M. Hennrich, F. Dubin, and J. Eschner, "Heralded single-photon absorption by a single atom," Nat. Phys. **7**, 17–20 (2011).

[132] P. Kumar, "Quantum frequency conversion," Opt. Lett. **15**, 1476–1478 (1990).

[133] J. Huang and P. Kumar, "Observation of quantum frequency conversion," Phys. Rev. Lett. **68**, 2153–2156 (1992).

[134] S. Zaske, A. Lenhard, and C. Becher, "Efficient Frequency Downconversion at the Single Photon Level from the Red Spectral Range to the Telecommunications C-Band," Opt. Express **19**, 12825–12836 (2011).

[135] J. S. Pelc, L. Ma, C. R. Phillips, Q. Zhang, C. Langrock, O. Slattery, X. Tang, and M. M. Fejer, "Long-wavelength-pumped upconversion single-photon detector at 1550 nm: performance and noise analysis," Opt. Express **19**, 21445–21456 (2011).

[136] M. T. Rakher, L. Ma, O. Slattery, X. Tang, and K. Srinivasan, "Quantum transduction of telecommunications-band single photons from a quantum dot by frequency upconversion," Nat. Photon. **4**, 786–791 (2010).

[137] S. Zaske, A. Lenhard, C. A. Keßler, J. Kettler, C. Hepp, C. Arend, R. Albrecht, W.-M. Schulz, M. Jetter, P. Michler, and C. Becher, "Visible-to-telecom quantum frequency conversion of light from a single quantum emitter," Phys. Rev. Lett. **109**, 147404 (2012).

[138] S. Ates, I. Agha, A. Gulinatti, I. Rech, M. T. Rakher, A. Badolato, and K. Srinivasan, "Two-Photon Interference Using Background-Free Quantum Frequency Conversion of Single Photons Emitted by an InAs Quantum Dot," Phys. Rev. Lett. **109**, 147405 (2012).

[139] T. Walker, K. Miyanishi, R. Ikuta, H. Takahashi, S. V. Kashanian, Y. Tsujimoto, K. Hayasaka, T. Yamamoto, N. Imoto, and M. Keller, "Long-Distance Single Photon Transmission from a Trapped Ion via Quantum Frequency Conversion," Phys. Rev. Lett. **120**, 203601 (2018).

[140] J. D. Siverns, J. Hannegan, and Q. Quraishi, "Neutral-Atom Wavelength-Compatible 780 nm Single Photons from a Trapped Ion via Quantum Frequency Conversion," Phys. Rev. Appl. **11**, 014044 (2019).

[141] A. Dréau, A. Tchebotareva, A. E. Mahdaoui, C. Bonato, and R. Hanson, "Quantum Frequency Conversion of Single Photons from a Nitrogen-Vacancy Center in Diamond to Telecommunication Wavelengths," Phys. Rev. Appl. **9**, 064031 (2018).

[142] N. Maring, D. Lago-Rivera, A. Lenhard, G. Heinze, and H. de Riedmatten, "Quantum frequency conversion of memory-compatible single photons from 606 nm to the telecom C-band," Optica **5**, 507–513 (2018).

[143] T. Kroh, A. Ahlrichs, B. Sprenger, and O. Benson, "Heralded wave packet manipulation and storage of a frequency-converted pair photon at telecom wavelength," Quantum Sci. Technol. **2**, 034007 (2017).

[144] H. Rütz, K.-H. Luo, H. Suche, and C. Silberhorn, "Quantum Frequency Conversion between Infrared and Ultraviolet," Phys. Rev. Appl. **7**, 024021 (2017).

[145] S. Tanzilli, W. Tittel, M. Halder, O. Alibart, P. Baldi, N. Gisin, and H. Zbinden, "A photonic quantum information interface," Nature **437**, 116–120 (2005).

[146] A. Lenhard, J. Brito, M. Bock, J. Eschner, and C. Becher, "Coherence and Entanglement Preservation of Frequency-Converted Heralded Single Photons," Opt. Express **25**, 11187–11199 (2017).

[147] R. Ikuta, Y. Kusaka, T. Kitano, H. Kato, T. Yamamoto, M. Koashi, and N. Imoto, "Wide-band quantum interface for visible-to-telecommunication wavelength conversion," Nat. Commun. **2**, 537 (2011).

[148] B. Kambs, J. Kettler, M. Bock, J. N. Becker, C. Arend, A. Lenhard, S. L. Portalupi, M. Jetter, P. Michler, and C. Becher, "Low-noise quantum frequency downconversion of indistinguishable photons," Opt. Express **24**, 22250–22260 (2016).

[149] L. Yu, C. M. Natarajan, T. Horikiri, C. Langrock, J. S. Pelc, M. G. Tanner, E. Abe, S. Maier, C. Schneider, S. Höfling, M. Kamp, R. H. Hadfield, M. M. Fejer, and Y. Yamamoto, "Two-photon interference at telecom wavelengths for time-bin-encoded single photons from quantum-dot spin qubits," Nat. Commun. **6**, 8955 (2015).

[150] R. Ikuta, H. Kato, Y. Kusaka, S. Miki, T. Yamashita, H. Terai, M. Fujiwara, T. Yamamoto, M. Koashi, M. Sasaki, Z. Wang, and N. Imoto, "High-fidelity conversion of photonic quantum information to telecommunication wavelength with superconducting single-photon detectors," Phys. Rev. A **87**, 010301 (2013).

[151] Z.-Y. Zhou, S.-L. Liu, Y. Li, D.-S. Ding, W. Zhang, S. Shi, M.-X. Dong, B.-S. Shi, and G.-C. Guo, "Orbital Angular Momentum-Entanglement Frequency Transducer," Phys. Rev. Lett. **117**, 103601 (2016).

[152] B. Albrecht, P. Farrera, X. Fernandez-Gonzalvo, M. Cristiani, and H. de Riedmatten, "A waveguide frequency converter connecting rubidium-based quantum memories to the telecom C-band," Nat. Commun. **5**, 3376 (2014).

[153] P. Farrera, N. Maring, B. Albrecht, G. Heinze, and H. de Riedmatten, "Nonclassical correlations between a C-band telecom photon and a stored spin-wave," Optica **9**, 1019–1024 (2016).

[154] R. Ikuta, T. Kobayashi, K. Matsuki, S. Miki, T. Yamashita, H. Terai, T. Yamamoto, M. Koashi, T. Mukai, and N. Imoto, "Heralded single excitation of atomic ensemble via solid-state-based telecom photon detection," Optica **3**, 1279–1284 (2016).

[155] A. Tchebotareva, S. L. N. Hermans, P. C. Humphreys, D. Voigt, P. J. Harmsma, L. K. Cheng, A. L. Verlaan, N. Dijkhuizen, W. de Jong, A. Dréau, and R. Hanson,

"Entanglement between a Diamond Spin Qubit and a Photonic Time-Bin Qubit at Telecom Wavelength," Phys. Rev. Lett. **123**, 063601 (2019).

[156] J. Weber, B. Kambs, J. Kettler, S. Kern, J. Maisch, H. Vural, M. Jetter, S. Portalupi, C. Becher, and P. Michler, "Two-photon interference in the telecom C-band after frequency conversion of photons from remote quantum emitters," Nat. Nanotechnol. **14**, 23–26 (2019).

[157] A. N. Craddock, J. Hannegan, D. P. Ornelas-Huerta, J. D. Siverns, A. J. Hachtel, E. A. Goldschmidt, J. V. Porto, Q. Quraishi, and S. L. Rolston, "Quantum Interference between Photons from an Atomic Ensemble and a Remote Atomic Ion," Phys. Rev. Lett. **123**, 213601 (2019).

[158] N. Maring, P. Farrera, K. Kutluer, M. Mazzera, G. Heinze, and H. de Riedmatten, "Photonic quantum state transfer between a cold atomic gas and a crystal," Nature **551**, 485–488 (2017).

[159] Q. Li, M. Davanço, and K. Srinivasan, "Efficient and low-noise single-photon-level frequency conversion interfaces using silicon nanophotonics," Nat. Photon. **10**, 406–414 (2016).

[160] X. Lu, G. Moille, Q. Li, D. A. Westly, A. Singh, A. Rao, S.-P. Yu, T. C. Briles, S. B. Papp, and K. Srinivasan, "Efficient telecom-to-visible spectral translation through ultralow power nonlinear nanophotonics," Nat. Photon. **13**, 593–601 (2019).

[161] A. Singh, Q. Li, S. Liu, Y. Yu, X. Lu, C. Schneider, S. Höfling, J. Lawall, V. Verma, R. Mirin, S. W. Nam, J. Liu, and K. Srinivasan, "Quantum frequency conversion of a quantum dot single-photon source on a nanophotonic chip," Optica **6**, 563–569 (2019).

[162] M. A. Albota, F. N. Wong, and J. H. Shapiro, "Polarization-independent frequency conversion for quantum optical communication," J. Opt. Soc. Am. B **23**, 918–924 (2006).

[163] S. Ramelow, A. Fedrizzi, A. Poppe, N. K. Langford, and A. Zeilinger, "Polarization-entanglement-conserving frequency conversion of photons," Phys. Rev. A **85**, 013845 (2012).

[164] V. Krutyanskiy, M. Meraner, J. Schupp, and B. P. Lanyon, "Polarisation-preserving photon frequency conversion from a trapped-ion-compatible wavelength to the telecom C-band," Appl. Phys. B **123**, 228 (2017).

[165] M. Bock, P. Eich, S. Kucera, M. Kreis, A. Lenhard, J. Eschner, and C. Becher, "High-fidelity entanglement between a single trapped ion and a telecom photon via quantum frequency conversion," Nat. Commun. **9**, 1998 (2018).

[166] R. Ikuta, T. Kobayashi, T. Kawakami, S. Miki, M. Yabuno, T. Yamashita, H. Terai, M. Koashi, T. Mukai, T. Yamamoto, and N. Imoto, "Polarization insensitive frequency conversion for an atom-photon entanglement distribution via a telecom network," Nat. Commun. **9**, 1997 (2018).

[167] F. Kaiser, P. Vergyris, A. Martin, D. Aktas, M. P. D. Micheli, O. Alibart, and S. Tanzilli, "Quantum optical frequency up-conversion for polarisation entangled qubits: towards interconnected quantum information devices," Opt. Express **27**, 25603–25610 (2019).

[168] T. van Leent, M. Bock, R. Garthoff, K. Redeker, W. Zhang, T. Bauer, W. Rosenfeld, C. Becher, and H. Weinfurter, "Long-Distance Distribution of Atom-Photon Entanglement at Telecom Wavelength," Phys. Rev. Lett. **124**, 010510 (2020).

[169] A. Lenhard, "Quantum photonic interfaces between atomic and telecommunication wavelengths," Ph.D. thesis, Universität des Saarlandes (2015).

[170] R. W. Boyd, *Nonlinear Optics* (Academic Press (Elsevier), 2008), 3rd ed.

[171] T. Suhara and M. Fujimura, *Waveguide Nonlinear-Optic Devices* (Springer, 2003).

[172] D. Marcuse, *Theory of Dielectric Optical Waveguides* (Academic Press (Elsevier), 1991), 2nd ed.

[173] S. Zaske, "Quantum Frequency Down-Conversion of Single Photons in Nonlinear Optical Waveguides," Ph.D. thesis, Universität des Saarlandes (2013).

[174] I. Shoji, T. Kondo, A. Kitamoto, M. Shirane, and R. Ito, "Absolute scale of second-order nonlinear-optical coefficients," J. Opt. Soc. Am. B **14**, 2268–2294 (1997).

[175] D. Roberts, "Simplified characterization of uniaxial and biaxial nonlinear optical crystals: a plea for standardization of nomenclature and conventions," IEEE J. Quantum Elect. **28**, 2057–2074 (1992).

[176] M. M. Fejer, G. A. Magel, D. H. Jundt, and R. L. Byer, "Quasi-Phase-Matched Second Harmonic Generation: Tuning and Tolerances," IEEE J. Quantum Elect. **28**, 2631–2654 (1992).

[177] T. Andres, P. Haag, S. Zelt, J.-P. Meyn, A. Borsutzky, R. Beigang, and R. Wallenstein, "Synchronously pumped femtosecond optical parametric oscillator of congruent and stoichiometric MgO-doped periodically poled lithium niobate," Appl. Phys. B **76**, 241–244 (2003).

[178] S. Zelt, "Erzeugung von periodischen Domanen in ferroelektrischen Kristallen und deren Anwendung in der nichtlinearen Optik," Ph.D. thesis, Technische Universität Kaiserslautern (2003).

[179] T. R. Volk, V. I. Pryalkin, and N. M. Rubinina, "Optical-damage-resistant $LiNbO_3$:Zn crystal," Opt. Lett. **15**, 996–998 (1990).

[180] Y. Furukawa, K. Kitamura, S. Takekawa, A. Miyamoto, M. Terao, and N. Suda, "Photorefraction in $LiNbO_3$ as a function of [Li]/[Nb] and MgO concentrations," Appl. Phys. Lett. **77**, 2494–2496 (2000).

[181] E. A. J. Marcatili, "Dielectric rectangular waveguide and directional coupler for integrated optics," Bell Labs Tech. J. **48**, 2071–2102 (1969).

[182] S. Blum, *Theoretische und experimentelle Untersuchungen der nichtlinearen Frequenzkonversion einzelner Photonen* (Diplomarbeit, Universität des Saarlandes, 2011).

[183] R. F. Schaufele and M. J. Weber, "Raman Scattering by Lithium Niobate," Phys. Rev. **152**, 705–708 (1966).

[184] J. S. Pelc, "Frequency Conversion of Single Photons: Physics, Devices, and Applications," Ph.D. thesis, Stanford University (2012).

[185] Y. Repelin, E. Husson, F. Bennani, and C. Proust, "Raman spectroscopy of lithium niobate and lithium tantalate. Force field calculations," J. Phys. Chem. Solids **60**, 819–825 (1999).

[186] M. Malyj and J. E. Griffiths, "Stokes/Anti-Stokes Raman Vibrational Temperatures: Reference Materials, Standard Lamps, and Spectrophotometric Calibrations," Appl. Spectrosc. **37**, 315–333 (1983).

[187] W. D. Johnston and I. P. Kaminow, "Temperature Dependence of Raman and Rayleigh Scattering in $LiNbO_3$ and $LiTaO_3$," Phys. Rev. **168**, 1045–1054 (1968).

[188] P. S. Kuo, J. S. Pelc, C. Langrock, and M. M. Fejer, "Using temperature to reduce noise in quantum frequency conversion," Opt. Lett. **43**, 2034–2037 (2018).

[189] J. S. Pelc, C. Langrock, Q. Zhang, and M. M. Fejer, "Influence of domain disorder on parametric noise in quasi-phase-matched quantum frequency converters," Opt. Lett. **35**, 2804–2806 (2010).

[190] J. S. Pelc, C. R. Phillips, D. Chang, C. Langrock, and M. M. Fejer, "Efficiency pedestal in quasi-phase-matching devices with random duty-cycle errors," Opt. Lett. **36**, 864–866 (2011).

[191] S. Tamura, K. Ikeda, K. Okamura, K. Yoshii, F.-L. Hong, T. Horikiri, and H. Kosaka, "Two-step frequency conversion for connecting distant quantum memories by transmission through an optical fiber," Jpn. J. Appl. Phys. **57**, 062801 (2018).

[192] P. C. Strassmann, A. Martin, N. Gisin, and M. Afzelius, "Spectral noise in frequency conversion from the visible to the telecommunication C-band," Opt. Express **10**, 14298–14307 (2019).

[193] M. Fox, *Quantum Optics: An Introduction* (Oxford University Press, 2006).

[194] D. F. V. James, P. G. Kwiat, W. J. Munro, and A. G. White, "Measurement of qubits," Phys. Rev. A **64**, 052312 (2001).

[195] M. Ježek, J. Fiurášek, and Z. Hradil, "Quantum inference of states and processes," Phys. Rev. A **68**, 012305 (2003).

[196] T. Monz, "Quantum information processing beyond ten ion-qubits," Ph.D. thesis, Universität Innsbruck (2011).

[197] H. P. Specht, "Einzelatom-Quantenspeicher für Polarisations-Qubits," Ph.D. thesis, Technische Universität München and Max-Planck-Institut fur Quantenoptik (2010).

[198] M. D. Bowdrey, D. K. L. Oi, A. J. Short, K. Banaszek, and J. A. Jones, "Fidelity of single qubit maps," Phys. Lett. A **294**, 258–260 (2002).

[199] A. Gilchrist, N. K. Langford, and M. A. Nielsen, "Distance measures to compare real and ideal quantum processes," Phys. Rev. A **71**, 062310 (2005).

[200] C. Nölleke, "Quantum state transfer between remote single atoms," Ph.D. thesis, Technische Universität München and Max-Planck-Institut fur Quantenoptik (2013).

[201] T. Baumgratz, A. Nüßeler, M. Cramer, and M. B. Plenio, "A scalable maximum likelihood method for quantum state tomography," New J. Phys **15**, 125004 (2013).

[202] J. B. Altepeter, E. Jeffrey, and P. Kwiat, *Advances In Atomic, Molecular, and Optical Physics* (Elsevier, 2005), vol. 52, chap. Photonic State Tomography, pp. 105 – 159.

[203] J. Řeháček, Z. Hradil, and M. Ježek, "Iterative algorithm for reconstruction of entangled states," Phys. Rev. A **63**, 040303 (2001).

[204] S. Kucera, "Experimental distribution of entanglement in ion-photon quantum networks: Photon-pairs as resource," Ph.D. thesis, Universität des Saarlandes (2019).

[205] I. L. Chuang and M. A. Nielsen, "Prescription for experimental determination of the dynamics of a quantum black box," J. Mod. Opt. **44**, 2455–2467 (1997).

[206] M.-D. Choi, "Completely positive linear maps on complex matrices," Linear Algebra Appl. **10**, 285–290 (1975).

[207] A. Einstein, B. Podolsky, and N. Rosen, "Can Quantum-Mechanical Description of Physical Reality Be Considered Complete?" Phys. Rev. **47**, 777–780 (1935).

[208] J. Bell, "On the Einstein-Podolsky-Rosen paradox," Physics **1**, 195–290 (1964).

[209] J. F. Clauser, M. A. Horne, A. Shimony, and R. A. Holt, "Proposed Experiment to Test Local Hidden-Variable Theories," Phys. Rev. Lett. **23**, 880–884 (1969).

[210] S. J. Freedman and J. F. Clauser, "Experimental Test of Local Hidden-Variable Theories," Phys. Rev. Lett. **28**, 938–941 (1972).

[211] A. Aspect, P. Grangier, and G. Roger, "Experimental Realization of Einstein-Podolsky-Rosen-Bohm Gedankenexperiment: A New Violation of Bell's Inequalities," Phys. Rev. Lett. **49**, 91–94 (1982).

[212] G. Weihs, T. Jennewein, C. Simon, H. Weinfurter, and A. Zeilinger, "Violation of Bell's Inequality under Strict Einstein Locality Conditions," Phys. Rev. Lett. **81**, 5039–5043 (1998).

[213] B. G. Christensen, K. T. McCusker, J. B. Altepeter, B. Calkins, T. Gerrits, A. E. Lita, A. Miller, L. K. Shalm, Y. Zhang, S. W. Nam, N. Brunner, C. C. W. Lim, N. Gisin, and P. G. Kwiat, "Detection-Loophole-Free Test of Quantum Nonlocality, and Applications," Phys. Rev. Lett. **111**, 130406 (2013).

[214] M. Giustina, M. A. M. Versteegh, S. Wengerowsky, J. Handsteiner, A. Hochrainer, K. Phelan, F. Steinlechner, J. Kofler, J.-A. Larsson, C. Abellán, W. Amaya, V. Pruneri, M. W. Mitchell, J. Beyer, T. Gerrits, A. E. Lita, L. K. Shalm, S. W. Nam, T. Scheidl, R. Ursin, B. Wittmann, and A. Zeilinger, "Significant-Loophole-Free Test of Bell's Theorem with Entangled Photons," Phys. Rev. Lett. **115**, 250401 (2015).

[215] L. K. Shalm, E. Meyer-Scott, B. G. Christensen, P. Bierhorst, M. A. Wayne, M. J. Stevens, T. Gerrits, S. Glancy, D. R. Hamel, M. S. Allman, K. J. Coakley, S. D. Dyer, C. Hodge, A. E. Lita, V. B. Verma, C. Lambrocco, E. Tortorici, A. L. Migdall, Y. Zhang, D. R. Kumor, W. H. Farr, F. Marsili, M. D. Shaw, J. A. Stern, C. Abellán, W. Amaya, V. Pruneri, T. Jennewein, M. W. Mitchell, P. G. Kwiat, J. C. Bienfang, R. P. Mirin, E. Knill, and S. W. Nam, "Strong Loophole-Free Test of Local Realism," Phys. Rev. Lett. **115**, 250402 (2015).

[216] M.-H. Li, C. Wu, Y. Zhang, W.-Z. Liu, B. Bai, Y. Liu, W. Zhang, Q. Zhao, H. Li, Z. Wang, L. You, W. Munro, J. Yin, J. Zhang, C.-Z. Peng, X. Ma, Q. Zhang, J. Fan, and J.-W. Pan, "Test of Local Realism into the Past without Detection and Locality Loopholes," Phys. Rev. Lett. **121**, 080404 (2018).

[217] M. A. Rowe, D. Kielpinski, V. Meyer, C. A. Sackett, W. M. Itano, C. Monroe, and D. J. Wineland, "Experimental violation of a Bell's inequality with efficient detection," Nature **409**, 791–794 (2001).

[218] S. Pironio, A. Acín, S. Massar, A. B. de la Giroday, D. N. Matsukevich, P. Maunz, S. Olmschenk, D. Hayes, L. Luo, T. A. Manning, and C. Monroe, "Random numbers certified by Bell's theorem," Nature **464**, 1021–1024 (2010).

[219] N. Brunner, D. Cavalcanti, S. Pironio, V. Scarani, and S. Wehner, "Bell nonlocality," Rev. Mod. Phys. **86**, 419–478 (2014).

[220] P. Sekatski, J.-D. Bancal, S. Wagner, and N. Sangouard, "Certifying the Building Blocks of Quantum Computers from Bell's Theorem," Phys. Rev. Lett. **121**, 180505 (2018).

[221] J.-D. Bancal, K. Redeker, P. Sekatski, W. Rosenfeld, and N. Sangouard, "Self-testing with finite statistics enabling the certification of a quantum network link," arXiv:1812.09117 (2018).

[222] J. S. Pelc, L. Yu, K. D. Greve, P. L. McMahon, C. M. Natarajan, V. Esfandyarpour, S. Maier, C. Schneider, M. Kamp, S. Höfling, R. H. Hadfield, A. Forchel, Y. Yamamoto, and M. M. Fejer, "Downconversion quantum interface for a single quantum dot spin and 1550-nm single-photon channel," Opt. Express **20**, 27510–27519 (2012).

[223] F. Ma, L.-Y. Liang, J.-P. Chen, Y. Gao, M.-Y. Zheng, X.-P. Xie, H. Liu, Q. Zhang, and J.-W. Pan, "Up-conversion single-photon detectors based on integrated periodically poled lithium niobate waveguides," J. Opt. Soc. Am. B **35**, 2096–2101 (2018).

[224] M. Allgaier, V. Ansari, L. Sansoni, C. Eigner, V. Quiring, R. Ricken, G. Harder, B. Brecht, and C. Silberhorn, "Highly efficient frequency conversion with bandwidth compression of quantum light," Nat. Commun. **8**, 14288 (2017).

[225] B. Kambs, "Quantum Frequency Conversion of Indistinguishable Photons from Independent Solid State Emitters," Ph.D. thesis, Universität des Saarlandes (2020).

[226] A. Lenhard, J. Brito, S. Kucera, M. Bock, J. Eschner, and C. Becher, "Single telecom photon heralding by wavelength multiplexing in an optical fiber," Appl. Phys. B **122**, 20 (2016).

[227] S. Aleksic, F. Hipp, D. Winkler, A. Poppe, B. Schrenk, and G. Franzl, "Perspectives and limitations of QKD integration in metropolitan area networks," Opt. Express **23**, 10359–10373 (2015).

[228] p. c. Götz Zinner (B. Halle Nachfl. GmbH, Berlin).

[229] B. A. Korzh, Q.-Y. Zhao, S. Frasca, J. P. Allmaras, T. M. Autry, E. A. Bersin, M. Colangelo, G. M. Crouch, A. E. Dane, T. Gerrits, F. Marsili, G. Moody, E. Ramirez, J. D. Rezac, M. J. Stevens, E. E. Wollman, D. Zhu, P. D. Hale, K. L. Silverman, R. P. Mirin, S. W. Nam, M. D. Shaw, and K. K. Berggren, "Demonstrating sub-3 ps temporal resolution in a superconducting nanowire single-photon detector," Nat. Photon. **14**, 250–255 (2018).

[230] I. E. Zadeh, J. W. N. Los, R. B. M. Gourgues, J. Chang, A. W. Elshaari, J. Zichi, Y. J. van Staaden, J. Swens, N. Kalhor, A. Guardiani, Y. Meng, K. Zou, S. Dobrovolskiy, A. W. Fognini, D. R. Schaart, D. Dalacu, P. J.Poole, M. E. Reimer, X. Hu,

S. F. Pereira, V. Zwiller, and S. N. Dorenbos, "A platform for high performance photoncorrelation measurements," arXiv:2003.09916 (2020).

[231] F. Marsili, V. B. Verma, J. A. Stern, S. Harrington, A. E. Lita, T. Gerrits, I. Vayshenker, B. Baek, M. D. Shaw, R. P. Mirin, and S. W. Nam, "Detecting single infrared photons with 93 % system efficiency," Nat. Photon. **7**, 210–214 (2013).

[232] C. M. Natarajan, M. G. Tanner, and R. H. Hadfield, "Superconducting nanowire single-photon detectors: physics and applications," Supercond. Sci. Tech. **25**, 063001 (2012).

[233] E. A. Dauler, M. E. Grein, A. J. Kerman, F. Marsili, S. Miki, S. W. Nam, M. D. Shaw, H. Terai, V. B. Verma, and T. Yamashita, "Review of superconducting nanowire single-photon detector system design options and demonstrated performance," Opt. Eng. **53**, 081907 (2014).

[234] T. Bauer, "Polarisationserhaltende Quantenfrequenzkonversion einzelner $^{40}Ca^{+}$-resonanter Photonen in das Telekom-C-Band," Master's thesis, Universität des Saarlandes (2019).

[235] P. E. Ciddor, "Refractive index of air: new equations for the visible and near infrared," Appl. Opt. **35**, 1566–1573 (1996).

[236] N. Maring, "Quantum Frequency Conversion for Hybrid Quantum Networks," Ph.D. thesis, ICFO - The Institute of Photonic Sciences, Barcelona (2018).

[237] J. Arenskötter, "Photonenpaarquelle für Einzelatom-Einzelphoton Wechselwirkung," Master's thesis, Universität des Saarlandes (2016).

[238] T. Kim, M. Fiorentino, and F. N. C. Wong, "Phase-stable source of polarization-entangled photons using a polarization Sagnac interferometer," Phys. Rev. A **73**, 012316 (2006).

[239] A. Fedrizzi, T. Herbst, A. Poppe, T. Jennewein, and A. Zeilinger, "A wavelength-tunable fiber-coupled source of narrowband entangled photons," Opt. Express **15**, 15377–15386 (2007).

[240] P. Palittapongarnpim, A. MacRae, and A. Lvovsky, "A Monolithic Filter Cavity for Experiments in Quantum Optics," Rev. Sci. Instrum. **83**, 066101 (2012).

[241] A. Ahlrichs, C. Berkemeier, B. Sprenger, and O. Benson, "A monolithic polarization-independent frequency-filter system for filtering of photon pairs," Appl. Phys. Lett. **103**, 241110 (2013).

[242] R. Valivarthi, M. G. Puigibert, Q. Zhou, G. H. Aguilar, V. B. Verma, F. Marsili, M. D. Shaw, S. W. Nam, D. Oblak, and W. Tittel, "Quantum teleportation across a metropolitan fibre network," Nat. Photon. **10**, 676–680 (2016).

[243] P. Eich, "Single-ion based quantum interfaces for quantum-network applications," Ph.D. thesis, Universität des Saarlandes (2019).

[244] C. Kurz, "Quantum networking with single ions and single photons interfaced in free space," Ph.D. thesis, Universität des Saarlandes (2015).

[245] J. Huwer, "Experimental tools for quantum networking operations with single photons and single ions," Ph.D. thesis, Universität des Saarlandes (2013).

[246] C. Schuck, F. Rohde, M. Almendros, M. Hennrich, and J. Eschner, "Two-color photoionization of calcium using SHG and LED light," Appl. Phys. B **100**, 765 (2010).

[247] F. Rohde, M. Almendros, C. Schuck, J. Huwer, M. Hennrich, and J. Eschner, "A diode laser stabilization scheme for ^{40} Ca^{+} single ion spectroscopy," J. Phys. B: At. Mol. Opt. Phys. **43**, 115401 (2010).

[248] H. Rütz, K.-H. Luo, H. Suche, and C. Silberhorn, "Towards a quantum interface between telecommunication and UV wavelengths: design and classical performance," Appl. Phys. B **122**, 13 (2016).

[249] T. A. Wright, R. J. A. Francis-Jones, C. B. E. Gawith, J. N. Becker, P. M. Ledingham, P. G. R. Smith, J. Nunn, P. J. Mosley, B. Brecht, and I. A. Walmsley, "Two-Way Photonic Interface for Linking the Sr^{+} Transition at 422 nm to the Telecommunication C Band," Phys. Rev. Appl. **10**, 044012 (2018).

[250] C. Schuck, W. H. P. Pernice, and H. X. Tang, "Waveguide integrated low noise NbTiN nanowire single-photon detectors with milli-Hz dark count rate," Sci. Rep. **3**, 1893 (2013).

[251] R. Schwonnek, K. T. Goh, I. W. Primaatmaja, E. Y.-Z. Tan, R. Wolf, V. Scarani, and C. C.-W. Lim, "Robust Device-Independent Quantum Key Distribution," arXiv:2005.02691 (2020).

[252] J. I. Cirac, P. Zoller, H. J. Kimble, and H. Mabuchi, "Quantum State Transfer and Entanglement Distribution among Distant Nodes in a Quantum Network," Phys. Rev. Lett. **78**, 3221–3224 (1997).

[253] M. Brekenfeld, D. Niemietz, J. D. Christesen, and G. Rempe, "A quantum network node with crossed optical fibre cavities," Nat. Phys. **16**, 647–651 (2020).

[254] A. Stute, B. Casabone, B. Brandstätter, K. Friebe, T. E. Northup, and R. Blatt, "Quantum-state transfer from an ion to a photon," Nat. Photon. **7**, 219–222 (2013).

[255] P. Kurpiers, P. Magnard, T. Walter, B. Royer, M. Pechal, A. A. J. Heinsoo and, Y. Salathé, S. Storz, J.-C. Besse, S. Gasparinetti, A. Blais, and A. Wallraff, "Deterministic quantum state transfer and remote entanglement using microwave photons," Nature **558**, 264–267 (2018).

[256] C. J. Axline, L. D. Burkhart, W. Pfaff, M. Zhang, K. Chou, P. Campagne-Ibarcq, P. Reinhold, L. Frunzio, S. M. Girvin, L. Jiang, M. H. Devoret, and R. J. Schoelkopf, "On-demand quantum state transfer and entanglement between remote microwave cavity memories," Nat. Phys. **14**, 705–710 (2018).

[257] P. Campagne-Ibarcq, E. Zalys-Geller, A. Narla, S. Shankar, P. Reinhold, L. Burkhart, C. Axline, W. Pfaff, L. Frunzio, R. J. Schoelkopf, and M. H. Devoret, "Deterministic Remote Entanglement of Superconducting Circuits through Microwave Two-Photon Transitions," Phys. Rev. Lett. **120**, 200501 (2018).

[258] A. Delteil, Z. Sun, S. Fält, and A. Imamoğlu, "Realization of a Cascaded Quantum System: Heralded Absorption of a Single Photon Qubit by a Single-Electron Charged Quantum Dot," Phys. Rev. Lett. **118**, 177401 (2017).

[259] M. Gündoğan, P. M. Ledingham, A. Almasi, M. Cristiani, and H. de Riedmatten, "Quantum Storage of a Photonic Polarization Qubit in a Solid," Phys. Rev. Lett. **108**, 190504 (2012).

[260] C. Clausen, F. Bussières, M. Afzelius, and N. Gisin, "Quantum Storage of Heralded Polarization Qubits in Birefringent and Anisotropically Absorbing Materials," Phys. Rev. Lett. **108**, 190503 (2012).

[261] J. Arenskötter, S. Kucera, M. Kreis, F. Brunei, P. Eich, P. Müller, and J. Eschner, "Atom-to-Photon State Mapping by Quantum Teleportation," in "Quantum Information and Measurement (QIM) V: Quantum Technologies, OSA Technical Digest," (Optical Society of America, 2019), paper T5A.71.

[262] T. Bauer, *Frequenzstabilisierung von Diodenlasern für Experimente zur Quantenfrequenzkonversion* (Bachelorarbeit, Universität des Saarlandes, 2017).

[263] D. A. Steck, "Rubidium 87 D Line Data," (2001, last revision 2019).

[264] F. Rohde, "Remote ion traps for quantum networking: Two-photon interference and correlations," Ph.D. thesis, ICFO - The Institute of Photonic Science/Universitat Politècnica de Catalunya (2009).

[265] S. Helmfrid and G. Arvidsson, "Influence of randomly varying domain lengths and nonuniform effective index on second-harmonic generation in quasi-phase-matching waveguides," J. Opt. Soc. Am. B **8**, 797–804 (1991).

[266] N. V. Sidorov, A. A. Yanichev, P. G. Chufyrev, M. N. Palatnikov, and B. N. Mavrin, "Raman spectra of photorefractive lithium niobate single crystals," J. Appl. Spectrosc. **77**, 110–114 (2010).

[267] N. Piro, "Controlled absorption of heralded single photons by a single atom: Towards entanglement distribution in quantum networks," Ph.D. thesis, ICFO - The Institute of Photonic Science/Universitat Politècnica de Catalunya (2010).

[268] J. Hofmann, "Heralded Atom-Atom Entanglement," Ph.D. thesis, Ludwig-Maximilians-Universität München (2013).

[269] W. Rosenfeld, F. Hocke, F. Henkel, M. Krug, J. Volz, M. Weber, and H. Weinfurter, "Towards Long-Distance Atom-Photon Entanglement," Phys. Rev. Lett. **101**, 260403 (2008).

[270] K. Redeker, "Entanglement of Single Rubidium Atoms: From a Bell Test Towards Applications," Ph.D. thesis, Ludwig-Maximilians-Universität München (2020).

[271] D. Burchardt, "A Rigorous Test of Bell's Inequality and Quantum Teleportation Employing Single Atoms," Ph.D. thesis, Ludwig-Maximilians-Universität München (2017).

[272] N. Ortegel, "State readout of single Rubidium-87 atoms for a loophole-free test of Bell's inequality," Ph.D. thesis, Ludwig-Maximilians-Universität München (2016).

[273] R. Grimm, M. Weidemüller, and Y. B. Ovchinnikov, "Optical Dipole Traps for Neutral Atoms," Adv. At. Mol. Opt. Phys. **42**, 95–170 (2000).

[274] E. L. Raab, M. Prentiss, A. Cable, S. Chu, and D. E. Pritchard, "Trapping of Neutral Sodium Atoms with Radiation Pressure," Phys. Rev. Lett. **59**, 2631–2634 (1987).

[275] F. Henkel, M. Krug, J. Hofmann, W. Rosenfeld, M. Weber, and H. Weinfurter, "Highly Efficient State-Selective Submicrosecond Photoionization Detection of Single Atoms," Phys. Rev. Lett. **105**, 253001 (2010).

[276] P. Koschmieder, "Efficient Control of Magnetic Fields in Single Atom Experiments," Master's thesis, Ludwig-Maximilians-Universität München (2019).

[277] M. Bartnick, M. Santandrea, J. P. Hoepker, F. Thiele, R. Ricken, V. Quiring, C. Eigner, H. Herrmann, C. Silberhorn, and T. J. Bartley, "Cryogenic second harmonic generation in periodically-poled lithium niobate waveguides," arXiv:2005.07500 (2020).

[278] M. Körber, O. Morin, S. Langenfeld, A. Neuzner, S. Ritter, and G. Rempe, "Decoherence-protected memory for a single-photon qubit," Nat. Photon. **12**, 18–21 (2018).

[279] K.-H. Luo, S. Brauner, C. Eigner, P. R. Sharapova, R. Ricken, T. Meier, H. Herrmann, and C. Silberhorn, "Nonlinear integrated quantum electro-optic circuits," Sci. Adv. **5**, eaat1451 (2019).

[280] A. Martin, O. Alibart, M. P. D. Micheli, D. B. Ostrowsky, and S. Tanzilli, "A quantum relay chip based on telecommunication integrated optics technology," New J. Phys. **14**, 025002 (2012).

[281] M. Karpinski, M. Jachura, L. J. Wright, and B. J. Smith, "Bandwidth manipulation of quantum light by an electro-optic time lens," Nat. Photon. **11**, 53–57 (2017).

[282] T. H. Yang, T. Vértesi, J.-D. Bancal, V. Scarani, and M. Navascués, "Robust and Versatile Black-Box Certification of Quantum Devices," Phys. Rev. Lett. **113**, 040401 (2014).

[283] C.-E. Bardyn, T. Liew, S. Massar, M. McKague, and V. Scarani, "Device-independent state estimation based on Bell's inequalities," Phys. Rev. A **80**, 062327 (2009).

[284] J. Kaniewski, "Analytic and Nearly Optimal Self-Testing Bounds for the Clauser-Horne-Shimony-Holt and Mermin Inequalities," Phys. Rev. Lett. **117**, 070402 (2016).

[285] N. Gisin, S. Pironio, and N. Sangouard, "Proposal for Implementing Device-Independent Quantum Key Distribution Based on a Heralded Qubit Amplifier," Phys. Rev. Lett. **105**, 070501 (2010).

[286] N. Bruno, V. Pini, A. Martin, B. Korzh, F. Bussières, V. Verma, S. W. Nam, R. Mirin, A. Lita, F. Marsili, N. Sangouard, H. Zbinden, N. Gisin, and R. Thew, "Heralded amplification of photonic qubits," Opt. Express **24**, 125–133 (2016).

[287] D. Orsucci, J.-D. Bancal, N. Sangouard, and P. Sekatski, "How post-selection affects device-independent claims under the fair sampling assumption," Quantum **4**, 238 (2020).

[288] S. Wagner, J.-D. Bancal, N. Sangouard, and P. Sekatski, "Device-independent characterization of quantum instruments," Quantum **4**, 243 (2020).

[289] D. Luong, L. Jiang, J. Kim, and N. Lütkenhaus, "Overcoming lossy channel bounds using a single quantum repeater node," Appl. Phys. B **122**, 96 (2016).

[290] N. Akopian, U. Perinetti, L. Wang, A. Rastelli, O. G. Schmidt, and V. Zwiller, "Tuning single GaAs quantum dots in resonance with a rubidium vapor," Appl. Phys. Lett. **97**, 082103 (2010).

[291] H. M. Meyer, R. Stockill, M. Steiner, C. L. Gall, C. Matthiesen, E. Clarke, A. Ludwig, J. Reichel, M. Atatüre, and M. Köhl, "Direct Photonic Coupling of a Semiconductor Quantum Dot and a Trapped Ion," Phys. Rev. Lett. **114**, 123001 (2015).

[292] J. F. Lilieholm, V. Niaouris, A. Kato, K.-M. C. Fu, and B. B. Blinov, "Photon-mediated entanglement scheme between a ZnO semiconductor defect and a trapped Yb ion," Appl. Phys. Lett. **117**, 154002 (2020).

[293] J. Görlitz, D. Herrmann, G. Thiering, P. Fuchs, M. Gandil, T. Iwasaki, T. Taniguchi, M. Kieschnick, J. Meijer, M. Hatano, A. Gali, and C. Becher, "Spectroscopic investigations of negatively charged tin-vacancy centres in diamond," New J. Phys. **22**, 013048 (2020).

[294] M. E. Trusheim, B. Pingault, N. H. Wan, M. Gündoğan, L. D. Santis, R. Debroux, D. Gangloff, C. Purser, K. C. Chen, M. Walsh, J. J. Rose, J. N. Becker, B. Lienhard, E. Bersin, I. Paradeisanos, G. Wang, D. Lyzwa, A. R.-P. Montblanch, G. Malladi, H. Bakhru, A. C. Ferrari, I. A. Walmsley, M. Atatüre, and D. Englund, "Transform-Limited Photons From a Coherent Tin-Vacancy Spin in Diamond," Phys. Rev. Lett. **124**, 023602 (2020).

[295] B. Pingault, D.-D. Jarausch, C. Hepp, L. Klintberg, J. N. Becker, M. Markham, C. Becher, and M. Atatüre, "Coherent control of the silicon-vacancy spin in diamond," Nat. Commun. **8**, 15579 (2017).

[296] J. N. Becker, "Silicon Vacancy Colour Centres in Diamond: Coherence Properties & Quantum Control," Ph.D. thesis, Universität des Saarlandes (2017).

[297] R. Valivarthi, I. Lucio-Martinez, A. Rubenok, P. Chan, F. Marsili, V. B. Verma, M. D. Shaw, J. A. Stern, J. A. Slater, D. Oblak, S. W. Nam, and W. Tittel, "Efficient Bell state analyzer for time-bin qubits with fast-recovery WSi superconducting single photon detectors," Opt. Express. **22**, 24497–24506 (2014).

[298] A. I. Lvovsky, H. Hansen, T. Aichele, O. Benson, J. Mlynek, and S. Schiller, "Quantum State Reconstruction of the Single-Photon Fock State," Phys. Rev. Lett. **87**, 050402 (2001).

[299] B. Hacker, S. Welte, S. Daiss, A. Shaukat, S. Ritter, L. Li, and G. Rempe, "Deterministic creation of entangled atom–light Schrödinger-cat states," Nat. Photon. **13**, 110–115 (2019).

[300] C. E. Vollmer, C. Baune, A. Samblowski, T. Eberle, V. Händchen, J. Fiurášek, and R. Schnabel, "Quantum Up-Conversion of Squeezed Vacuum States from 1550 to 532 nm," Phys. Rev. Lett. **112**, 073602 (2014).

[301] K. Laiho, K. N. Cassemiro, D. Gross, and C. Silberhorn, "Probing the Negative Wigner Function of a Pulsed Single Photon Point by Point," Phys. Rev. Lett. **105**, 253603 (2010).

[302] D. Achilles, C. Silberhorn, C. Śliwa, K. Banaszek, and I. A. Walmsley, "Fiber-assisted detection with photon number resolution," Opt. Lett. **28**, 2387–2389 (2003).

Publications

Research articles

Articles resulting from research work discussed in this thesis

- T. van Leent*, M. Bock*, R. Garthoff*, K. Redeker, W. Zhang, T. Bauer, W. Rosenfeld, C. Becher, and H. Weinfurter, "Long-distance distribution of atom-photon entanglement at telecom wavelength", Phys. Rev. Lett. **124**, 010510 (2020).
  *These authors contributed equally

- M. Bock*, P. Eich*, S. Kucera, M. Kreis, A. Lenhard, C. Becher, and J. Eschner, "High-fidelity entanglement between a trapped ion and a telecom photon via quantum frequency conversion", Nature Commun. **9**, 1998 (2018).
  *These authors contributed equally
  Among "Top 50 read physics articles of 2018 in Nature Communications."

- S. Kucera et al., "Direct and teleportation-based quantum state transfer from a trapped-ion qubit onto a telecom photon" (working title), *in preparation.*

- T. Bauer, M. Bock et al., "Photon-photon entanglement distribution over 40 km of fiber by two-step polarization-preserving quantum frequency conversion" (working title), *in preparation.*

Articles created during the time of my PhD which are not discussed in this thesis

- M. Bock, S. Kucera et al., "Self-testing of a high-performance quantum frequency converter via Bell's theorem" (working title), *in preparation.*

- M. Bock, A. Lenhard, C. Chunnilall, and C. Becher, "Highly efficient heralded single-photon source for telecom wavelengths based on a PPLN waveguide", Opt. Express **24**, 23992 (2016).

- B. Kambs, J. Kettler, M. Bock, J.N. Becker, C. Arend, A. Lenhard, S.L. Portalupi, M. Jetter, P. Michler, and C. Becher, "Low-noise quantum frequency down-conversion of indistinguishable photons", Opt. Express **24**, 22250 (2016).

Further articles

- A. Lenhard, J. Brito, M. Bock, C. Becher, and J. Eschner, "Coherence and Entanglement Preservation of Frequency-Converted Heralded Single Photons", Opt. Express **25**, 11187 (2017).
- A. Lenhard, J. Brito, S. Kucera, M. Bock, J. Eschner, and C. Becher, "Single telecom photon heralding by wavelength multiplexing in an optical fiber", Appl. Phys. B **122**:20 (2016).
- A. Lenhard, M. Bock, C. Becher, S. Kucera, J. Brito, P. Eich, P. Müller, and J. Eschner, "Telecom-heralded single-photon absorption by a single atom", Phys. Rev. A **92**, 063827 (2015).

Invited seminar talks

- M. Bock, "Polarization-Preserving Quantum Frequency Conversion for Trapped-Atom based Quantum Networks", *Group Seminar "Quantum Optics and Spectroscopy" R. Blatt, Leopold-Franzens-Universität Innsbruck, Austria, January 20, 2020.*
- M. Bock, "Polarization-Preserving Quantum Frequency Conversion for Trapped-Atom based Quantum Networks", *Group Seminar "3. Physikalisches Institut" J. Wrachtrup, Universität Stuttgart, Germany, October 15, 2019.*
- M. Bock, "Quantum frequency conversion of single photons as tool for quantum networks", *Group Seminar "Laser spectroscopy & quantum physics" T. Hänsch, Ludwigs-Maximilians-Universität, Munich, Germany, May 09, 2019.*
- M. Bock, "Quantum Frequency Conversion of single photons and photon pairs", *Group Seminar "Laser spectroscopy & quantum physics" T. Hänsch, Ludwigs-Maximilians-Universität, Munich, Germany, October 26, 2016.*

Contributed conference talks

- M. Bock, T. van Leent, R. Garthoff, K. Redeker, W. Zhang, T. Bauer, W. Rosenfeld, C. Becher, and H. Weinfurter, "Long-distance distribution of atom-photon entanglement at telecom wavelength", *Quantum Technology International Conference (QTech 2020), Online Conference, November 2-4, 2020.*

- M. Bock, P. Eich, S. Kucera, M. Kreis, A. Lenhard, C. Becher, and J. Eschner, "High-fidelity entanglement between a trapped ion and a telecom photon via quantum frequency conversion", *25th Central European Workshop on Quantum Optics (CEWQO), University of the Balearic Islands, Palma de Mallorca, Spain, May 21-25, 2018.*

- M. Bock, P. Eich, S. Kucera, M. Kreis, A. Lenhard, C. Becher, and J. Eschner, "High-fidelity entanglement between a trapped ion and a telecom photon via quantum frequency conversion", *DPG Spring Meeting (SAMOP), Friedrich-Alexander-Universität, Erlangen, Germany, March 04-09, 2018.*

- M. Bock, S. Kucera, J. Arenskötter, B. Kambs, S. Rühle, A. Lenhard, J. Eschner, and C. Becher, "Quantum Frequency Down-Conversion of $^{40}Ca^{+}$–Resonant Polarization–Entangled Photons to the Telecom O-Band", *CLEO/Europe-EQEC, Munich, Germany, June 23-27, 2017.*

- M. Bock, S. Kucera, J. Arenskötter, B. Kambs, S. Rühle, A. Lenhard, J. Eschner, and C. Becher, "Quantum Frequency Down-Conversion of Ca^{+}–Resonant Polarization–Entangled Photons to the Telecom O-Band", *Quantum Information and Measurement (QIM) IV, Université Pierre et Marie Curie, Paris, France, April 05-07, 2017.*

- M. Bock, S. Kucera, J. Arenskötter, B. Kambs, S. Rühle, A. Lenhard, J. Eschner, and C. Becher, "Quantum Frequency Down-Conversion of $^{40}Ca^{+}$–Resonant Polarization–Entangled Photons to the Telecom O-Band", *DPG Spring Meeting (SAMOP), Johannes Gutenberg-Universität, Mainz, Germany, March 06-10, 2017.*

- M. Bock, A. Lenhard, and C. Becher, "A Highly Efficient Heralded Single Photon Source for Telecom Wavelengths based on a PPLN Ridge Waveguide", *Single Photon Workshop, Geneva, Switzerland, July 13-17, 2015.*

- M. Bock, A. Lenhard, and C. Becher, "A Highly Efficient Heralded Single Photon Source for Telecom Wavelengths based on a PPLN Ridge Waveguide", *CLEO/Europe-EQEC, Munich, Germany, June 21-25, 2015.*

- M. Bock, A. Lenhard, and C. Becher, "A Highly Efficient Heralded Single Photon Source for Telecom Wavelengths based on a PPLN Ridge Waveguide", *DPG Spring Meeting (SAMOP), Ruprecht-Karls-Universität, Heidelberg, Germany, March 15-19, 2015.*

- M. Bock, A. Lenhard, and C. Becher, "Setup and Characterization of a Cavity-Enhanced SPDC-Photon Pair Source", *Greenhorn Meeting, Johannes Gutenberg-Universität, Mainz, Germany, September 09-12, 2014.*

Contributed conference posters

- M. Bock, S. Kucera, T. van Leent, R. Garthoff, K. Redeker, P. Eich, M. Kreis, W. Rosenfeld, T. Bauer, H. Weinfurter, J. Eschner, and C. Becher, "Polarization-preserving quantum frequency conversion as tool for long-distance quantum networks", *International Conference on Quantum Optics, Obergurgl, Tirol, Austria, February 23-29, 2020.*

- M. Bock, S. Kucera, R. Garthoff, T. van Leent, K. Redeker, P. Eich, M. Kreis, W. Rosenfeld, T. Bauer, H. Weinfurter, J. Eschner, and C. Becher, "Polarization-preserving quantum frequency conversion for entanglement distribution in quantum networks", *DPG Fall Meeting, Albert-Ludwigs-Universität, Freiburg, Germany, September 23-27, 2019.*

- M. Bock, S. Kucera, P. Eich, M. Kreis, A. Lenhard, J. Eschner, and C. Becher, "Polarization-preserving quantum frequency conversion for entanglement distribution in trapped-atom based quantum networks", *Quantum Information and Measurement (QIM) V, Sapienza University, Rome, Italy, April 04-06, 2019.*

- M. Bock, P. Eich, S. Kucera, M. Kreis, A. Lenhard, C. Becher, and J. Eschner, "High-fidelity entanglement between a trapped ion and a telecom photon via quantum frequency conversion", *662nd WE-Heraeus-Seminar "Quantum networks", Physikzentrum Bad Honnef, Germany, February 05-07, 2018.*

- M. Bock, P. Eich, S. Kucera, M. Kreis, A. Lenhard, C. Becher, and J. Eschner, "High-fidelity entanglement between a trapped ion and a telecom photon via quantum frequency conversion", *2nd Workshop for Quantum Repeaters and Networks, Seefeld, Austria, September 25-26, 2017.*

- M. Bock, A. Lenhard, and C. Becher, "A narrowband Photon Pair Source based on Spontaneous Parametric Down-Conversion", *DPG Spring Meeting (SAMOP), Humboldt University, Berlin, Germany, March 17-21, 2014.*

Danksagung

Getreu dem Motto “Das Beste kommt zum Schluss” möchte ich hier allen danken, ohne die diese Arbeit nicht möglich gewesen wäre. Der größte Dank geht an meinen Doktorvater Prof. Christoph Becher für die Aufnahme in seine Gruppe und die Möglichkeit an einem so spannenden und aktuellen Thema an vorderster Front mitarbeiten zu können. Ich hatte immer große Freiheiten im Labor und die Möglichkeit eigene Ideen einzubringen bei gleichzeitig voller Unterstützung (sowohl in wissenschaftlicher als auch in organisatorischer Hinsicht) und einem großen Vertrauen in mich (z.B. durch das frühe Einbinden in Planung und Koordination neuer Projekte). Deine motivierende Art hat uns angetrieben nie aufzugeben und immer mit Vollgas fokussiert auf ein Ziel hinzuarbeiten, dabei aber trotzdem den Blick auf das große Ganze zu behalten. Ich bin mir sicher, dass ich noch lang und in vielerlei Hinsicht von der mittlerweile fest etablierten “Saarbrücker Schule” profitieren werde. Prof. Wolfgang Tittel und Dr. Ben Lanyon möchte ich herzlich danken, dass sie sich bereit erklärt haben diese Arbeit zu begutachten.
Ein weiteres herzliches Dankeschön geht an die aktuellen und ehemaligen Mitglieder der AG Quantenoptik für die 1A Zusammenarbeit und die vielen lustigen Momente an oder außerhalb der Uni sowie auf zahlreichen Projektreffen, Konferenzreisen und DPG-Tagungen. Insbesondere möchte ich unser nichtlineares Team erwähnen. Meinem Doktorandenkollegen Benjamin Kambs möchte ich für die gute Stimmung im Büro, die vielen Diskussionen und seine – in guter Schelm-Manier – wohlplatzierten Scherze jeglicher Art danken. Benni hat zudem die wichtige Aufgabe des Kaffeemaschinen-Managers übernommen. Ich vermute mein Kaffeekonsum über die letzten Jahre ähnelt sehr den Covid19-Zahlen der USA: ein verspäteter Einstieg, dann aber ein rasanter Anstieg mit einer Reihe von immer höher werdenden Peaks während dem Paperschreiben sowie dem Zusammenschreiben dieser Arbeit[1]. Ein Dank geht auch an die “Altvorderen” und Begründer der nichtlinearen Optik in Saarbrücken, Sebastian Zaske und Andreas Lenhard. Insbesondere Andreas hat mir als Betreuer meiner Masterarbeit einen super Einstieg gegeben und enorm viel von seinem Wissen und Skills im Labor vermittelt. Ich hoffe wir konnten die nichtlineare Optik mit “High Performance” in eurem Sinne weiterführen. Ein weiterer Dank gilt meinen Bachelor- und Masterstudenten Tobias Bauer und Sebastian Rühle. Tobias wird die nichtlineare Optik als mein Nachfolger weiterführen, ich wünsche dir alles Gute und viel Erfolg für deine Promotion und hoffe natürlich auf neue Effizienzrekorde in der Konversion. Weiterhin möchte ich Alexan-

[1] Die Zukunft wird zeigen ob sich die Zahlen nach dem Abschluss dieser Arbeit Anfang November wieder auf einem normalen Niveau einpendeln werden.

der Bommer (Weihnachtswanderungsorganisationskomitee, Stimmungsmacher der AG), Johannes Görlitz (Weihnachtswanderungsorganisationskomitee, für jedes Party-Event zu haben), Philipp Fuchs (IT-Infrastruktur-Bewahrer, nicht endende Versorgung mit Kuchen und Süßigkeiten), Anna Breunig (Heim- und Gartenpartys), Dennis Herrmann (DPG-Laufrunde), Thomas Jung (herrlicher Zweckoptimismus) und Robert Morsch (Gesangseinlagen) danken. Ein dickes merci geht zudem an Benjamin Kambs, Tobias Bauer, Johannes Görlitz, Stephan Kucera, Philipp Fuchs und Tim van Leent für das (wie gewünscht strenge) Korrekturlesen dieser Arbeit.
Ich hatte das große Glück während der gesamten Doktorandenzeit mit fantastischen Kooperationspartnern zusammen arbeiten zu dürfen, den Hütern der Atom- und Ionenfallen. Der enorme Drive, unser Team-Spirit und die generelle Einstellung "Failure is not an option" sind maßgeblich für den Erfolg der meisten Experimente in dieser Arbeit verantwortlich.
Zum einen möchte ich Prof. Jürgen Eschner und seinem Team für die langjährige Kooperation und die 1A Zusammenarbeit danken. Vielen Dank an Jan Arenskötter für das Bereitstellen der Photonenpaarquelle und unsere gemeinsamen Experimente zum Verschränkungserhalt nach Konversion. Von Matthias Kreis habe ich viel Unterstützung bei den Cavitylockern bekommen; zudem hat er bei fast allen Experimenten im Hintergrund gewirkt, u.A. beim Erstellen von Sequenzen oder der Weiterentwicklung der Ionenfallen; vielen Dank. Eine besondere Freude war es mir mit Pascal Eich zusammenzuarbeiten. Pascal als hartnäckiger und konsequenter Pessimist ("Bei uns im Labor iss ääfach alles maximal beschissen", "Wie sieht die Messung aus? Beschissen nemm ich aan.") und ich als das absolute Gegenteil haben uns da hervorragend ergänzt. Das Hin-und-her spielen der Bälle sowie das gegenseitige Hochschaukeln haben zu jeder Menge lustiger Situationen geführt ("Här uff die ganze Geräte so zu lowe, immer wenn isch das mache gehn die kurz deno kabutt!"). Ich bin am Schluss aber doch froh und muss auch mit einer gewissen Genugtuung feststellen, dass der Optimismus gesiegt hat und alles so gut wie erhofft (z.T. sogar noch besser) funktioniert hat. Ein weiterer Dank geht an Stephan Kucera, eine stete Quelle neuer Ideen, mit dem ich nahezu die kompletten 6 Jahre zusammengearbeitet habe, und mit dem ich definitiv die optimistische Zeitrechnung, die unkomplizierte Art schnell Probleme zu lösen und den Spirit, dass wir das alles irgendwie zu Laufen bekommen, geteilt habe. Highlights waren sicher unsere Messsessions, bei denen wir trotz z.T. völliger Übermüdung immer noch überraschend effizient waren, vlt. wegen der erheiternden Mischung aus Erfreuen über jeden kleinen Fortschritt ("Ahh, das sieht gut aus; ein Traum.") und gegenseitigen Rumgemeckere. Aber auch das ein oder andere Feierabendbier/-whiskey, die vielen Konferenzreisen und gemeinsamen Skiausfahrten (sowohl privat als auch dienstlich verordnet in Obergurgl) werden mir in guter Erinnerung bleiben.
Zum anderen geht ein großes Dankeschön an Prof. Harald Weinfurter und sein Team an der LMU München, die mich für unser gemeinsames Projekt insgesamt 16 Wochen in ihre Gruppe aufgenommen haben. Wenjamin Rosenfeld war Senior-Postdoc am Experiment, mit ihm habe ich während der Planungsphase des Experiments viel zusammengearbeitet; vielen Dank für deinen großen Einsatz dieses Projekt zu realisieren und meine vielen Fragen zum Atomexperiment zu beantworten. Florian Fertig und Seb Ep-

pelt sind als Doktorand und Masterstudent kurz vor der zweiten Messsession neu zum Experiment dazu gestoßen, haben aber von Anfang an mit viel Elan und Begeisterung mitgezogen; ich bin mir sicher, dass die Verschränkung zwischen München und Garching mit eurem Einsatz funktionieren wird. Robert Garthoff hat als Senior-Doktorand viel Erfahrung und Ruhe mitgebracht und zudem das große Projekt der Modifizierung der Falle mit neuen Objektiven umgesetzt, ohne die alle Atom-Experimente in dieser Arbeit nicht durchführbar gewesen wären. Wei Zhang hat als Postdoc nicht nur eine enorme Hartnäckigkeit und Arbeitsmoral im Labor an den Tag gelegt, sondern mir auch den chinesischen Humor sowie die Dimension von "full" nach dem Essen nähergebracht. Die meisten Experimente habe ich mit Tim van Leent, der ebenfalls Doktorand am Atomexperiment ist, durchgeführt. Lustigerweise kann vieles, was ich oben über Stephan geschrieben habe, auch 1:1 auf Tim übertragen werden. Lediglich Tims Zeitrechnung ist noch deutlich optimistischer, trotz vollem Einsatz war "2 Minutes", "Almost there" oder "Today will be the day" nur fast immer einhaltbar. Vielen Dank zudem an euch alle für eure Gastfreundschaft inklusive einer Einführung in das gastronomische Angebot und die Kneipenlandschaft in München-Downtown sowie fast tägliche Besuche in verschiedenen Eisdielen. Zudem möchte ich der Generalin des Head Office, Frau Gabriele Gschwendtner, für die unkomplizierte Bereitstellung eines Schlüssels danken.
Ein großes Dankeschön geht an unsere Sekretärin Elke Huschens, ohne die wir (ich zumindest) sicher ziemlich verloren wären und die, ohne zu übertreiben, die Arbeit für zwei Sekretärinnen erledigt hat. Deine unumstößliche gute Laune (trotz vielen Situationen, die zum Verzweifeln waren) sowie die kleinen Kommentare mit spitzer Zunge kurz vor Verlassen des Büros werden mit definitiv in Erinnerung bleiben. Ich hoffe, dass es nach meinem Abschied ohne die vielen 1., 2. und letzten Mahnungen nicht zu langweilig geworden ist. Ich wünsche dir in jedem Fall alles Gute für deinen wohlverdienten Ruhestand und noch viel erlebnisreiche Reisen.
An dieser Stelle darf natürlich Michael Schmidts Team der feinmechanischen Werkstatt bestehend aus Titan Monosteri, Gereon "The Rock" Pink, Jürgen Pola, Peter Wagner, Didi und Armin Seel nicht fehlen (auch wenn diese in einer anderen Doktorarbeit schockierenderweise bereits einmal vergessen wurden). Ohne die zahlreichen präzise und oft in atemberaubender Geschwindigkeit (oft von dem "Lieblingsgesell" der AG Becher) gefertigten Bauteile wären viele unserer Aufbauten nicht realisierbar gewesen. Einige der Bauteile wurde sogar zu einem Exportschlager in den Freistaat Bayern und erfreuen sich dort größter Beliebtheit. In besonderer Erinnerung werden mir unsere halbjährlichen Meetings im Sommer und vor Weihnachten bleiben, bei denen wir immer ein tolles Programm auf die Beine gestellt haben (u.A. mit Gastauftritten von Marcel Reich-Ranicki Jr. zu verschiedenen literarischen Themen) und danach noch gemütlich auf 1-2 Bier mit Schwenker oder Fleischkäse zusammengekommen sind.
Nicht zu vergessen ist unser Monsieur Löw aus der Elektronikwerkstatt. Selbst das Abholen eines Widerstands konnte sich zu einem einstündigen Aufenthalt werden, da Monsieur Löw immer sehr unterhaltsame, ab und an aber auch ernste Geschichten auf Lager hatte. Die Bandbreite dabei war enorm: von Lebensweisheiten über die Demonstrationen von Kamptechniken oder das bashing einiger Bewohner des E26 Gebäudes war alles dabei. Ich danke ihnen für die zahlreichen Reparaturen von elektronischen Geräten

sowie die Möglichkeit ihr Equipment benutzen zu dürfen und mich in ihrem umfangreichen Lager bedienen zu dürfen. Auch ihnen wünsche ich alles Gute für den wohlverdienten Ruhestand. Mit dem Nachfolger Günni Schmidt hatte ich leider nur einen kleinen zeitlichen Überlapp, trotzdem war es mir immer eine Freude bei vielen kleinen Gelegenheiten über unsere gemeinsame Leidenschaft für Lauf- und Radmarathons zu quatschen (zudem war dies eine perfekte Gelegenheit das Schreiben dieser Arbeit etwas zu prokrastinieren). Ich bin mir aber sicher, dass Günnis frischer Wind, sein Enthusiasmus und seine Expertise noch viele Projekte der AG vorantreiben werden.
Das Leben wäre wohl etwas trist wenn es nur aus Uni bestehen würde, daher möchte auch eine großen Dank an meine Freunde in Auersmacher und den umliegenden Subgemeinden, von der KAS und aus meiner alten Schule für die notwendige Ablenkung bei zahlreichen Geburtstagen, Festen, Ausflügen, gemütlichem Beisammensein im Gasthaus, Skype-Kneipenabende oder sonstigen Events richten. Das Besondere in Auersmacher ist die sehr lebendige Vereinslandschaft, die natürlich einiges an zeitlichem Aufwand (und eigentlich den gesamten Jahresurlaub) für das ehrenamtliche Engagement erfordern, dafür aber ein Vielfaches an Lebensfreude zurückgeben. Danke hier an alle Musiker des Saar Wind Orchestras und Angehörige der freiwilligen Feuerwehr für die tolle Zeit. Besonders erwähnen möchte ich das Ferienfreizeit-Team unserer Kirchengemeinde: in keinem sonstigem "Urlaub" ist es wohl möglich ab der ersten Minute völlig abzuschalten und in einen im Vergleich zum normalen Leben orthogonalen Modus zu wechseln, vielen Dank an euch. Eine quantitative Analyse aller meiner Urlaubanträge würde vermutlich ergeben, dass die Ferienfreizeit die einzigen Urlaubstage zwischen Mitte April und Mitte November sind, der Rest ging komplett für den schönsten und geselligsten Sport der Welt drauf: Skifahren. Ob privat oder als Skilehrer in unserem Skiclub, ob Kaiserwetter mit fantastischem Paranoma in den Dolomiten oder Regen in La Brin, ob Ausbildungsfahrt oder LB-Skitour, ich habe bisher noch keinen einzigen gebrauchten Skitag erlebt, wofür ich alle Mitfahrern danken möchte. Alles in allem bin mir sicher: das vollständige Ausmaß an völlig verrückten und abgefahrenen Erlebnissen und Aktionen in all den Jahren würde an der Uni wohl doch für einiges an Erstaunen sorgen...
Das wichtigste im Leben ist die Familie, ein großer Dank geht daher an meine Eltern, die mich über die gesamte Zeit der Promotion voll unterstützt (sowohl moralisch als auch organisatorisch oder finanziell wenn es mit dem Doktorandengehalt in der Wintersaison mal etwas eng wurde), mich in meinem Tun bestärkt haben, und auch Verständnis hatten wenn es im Labor mal wieder etwas länger wurde. Nur durch eure Unterstützung war es mir möglich gleichzeitig an der Uni Vollgas zu geben und mich trotzdem noch in den Vereinen und Institutionen ehrenamtlich zu engagieren. Ebenso möchte ich insbesondere meine Schwester Annika, meinem Schwager Tobias, Opa Erwin und Inge sowie meiner Oma Maria, die den Abschluss dieser Promotion leider nicht mehr erleben durfte, sowie meiner restlichen Familie von ganzen Herzen für die vielen schönen Stunden bei Festen, Feiern und Geburtstagen (und nicht zu vergessen das traditionelle Mittagessen jeden Samstag bei Oma) und die kontinuierliche Unterstützung in den ganzen Jahren bedanken.